UNIVERSITÀ DEGLI STUDI DI MILANO

Dottorato di Ricerca in Scienze della Terra
Ciclo XXX

Experimental study of interconnectivity and grain boundary wetness of hydrous carbonatitic liquids in mantle peridotite

Ph.D. Thesis

Luca Samuele Capizzi
Matricola R11020

Tutor
Prof. Stefano Poli

Academic Year
2016-2017

Coordinator
Prof.ssa Elisabetta Erba

Co- Tutor
Prof.ssa Patrizia Fumagalli

Dr. Simone Tumiati

Table of Contents

Abstract

Carbon-bearing solids, fluids, and melts in the Earth's deep interior play an important role in the long-term carbon cycle. Carbonatite magmas have been suggested as important agents of mantle metasomatism and yet, their physical features are expected to control the mobility from the source region to shallow Earth. Carbonatites are known to form at relatively low temperatures and are very mobile, as controlled by their low viscosities and their ability to form an interconnected grain-edge melt at low melt fraction. The factors promoting migration and infiltration are the minimization of interfacial energy, the density and chemical gradients, the thermal diffusion. However, the mobility and infiltration rates of carbonatitic melts, together with their influence on the annealing of mantle peridotites are poorly constrained processes. Although natural carbonatitic melts are complex chemical systems with C-O-H species as a major component, previous work has been performed in anhydrous model systems.

Here we present a quantitative laboratory simulation of variables and processes controlling the ascent, mobility and connectivity of carbonatites in a model mantle material investigating the dihedral angle of hydrous carbonatitic liquids. We aim at comparing the texturally equilibrated volume proportions of volatile-rich carbonatitic melts with silicate melts in a partially molten peridotite, and and we examine whether carbonatitic liquids are always more wetting than silicate melts.

The percolation of carbonatitic liquids and the interconnectivity of melt pockets are investigated by placing a cylindrical dunite rod against a liquid reservoir. As peridotitic matrix we used a synthetic dunite starting from natural San Carlos olivine powder. Sintering has been performed in a single stage piston-cylinder apparatus at 0.8 GPa and 1200°C P-T conditions. The liquid reservoir has a dolomitic composition ($Ca_{0.541}$, $Mg_{0.389}$, $Fe_{0.069}$) CO_3 and uses free water as hydrous source (5 wt.% and 30% of the starting material). Time resolved infiltration experiments were performed employing an end loaded piston-cylinder apparatus, at T= 1200°C and P = 2.5 GPa. In order to account for the different roles of gravity, chemical diffusion and Ludwig-Soret diffusion we used two opposite capsule geometries.

Hydrous carbonatitic melt pockets were found along olivine grain boundaries; image analysis on electron back scattered and X-ray maps allow us quantifying the apparent dihedral angles between the liquid and olivine and to calculate the grain boundary wetness.

Experiments performed at 5 wt. % of water content and 3, 30 and 300 hours of run durations result in dihedral angles evolving from ~ 31° for 3 hours run, to ~ 41° for 300 hours run through ~ 34° for 30 hours run. The volume of liquid fraction infiltrated provides values of 10 vol.%, 8 vol.% and 2 vol.% for short, medium and long run duration experiments respectively. Experiments carried out at 30 wt. % of water content and 48 hours of durations show a dihedral angle values of almost 50° with a range of volume infiltrated melts between 4 to 9 vol. %. The experimental results indicate that dihedral angles progressively increase with increasing water dissolved from 25°-28° in anhydrous carbonatitic liquids up to 50° in water-rich carbonatitic liquids, and, as expected, the volume of interstitial liquid decreases with water increasing.

The increase of wetting angles is representative of a sintering process of the solid matrix, which evolves with time in the development of channels of pores, as highlighted relating the grain boundary wetness with fraction of liquid infiltrated. We suggest that the low grain boundary wetness measured may be due to a relatively low liquid-solid interfaces which develop with channelized liquid, and that channelization is promoted by chemical gradient, as established by a carbonatitic segregate in the silicate matrix.

If H_2O is available, we expect that H_2O strongly partitions into carbonatitic liquids. As a result, their dihedral angle may evolve up to 50°, a value which is significantly higher than that characterizing silicate melts at similar mantle conditions.

Chapter 1

Introduction

1.1. Carbonatitic magmas

Since the pioneering works of Streckeisen (1980), carbonatites are defined as intrusive and effusive igneous rocks which contain more than 50% of carbonate minerals and less than 20 wt.% of SiO_2 (Le Maitre, 2002) with high abundance of Sr, Ba, P and LREE (Nelson et al., 1988). Globally, both intrusive and extrusive carbonatites are distributed across all continents (Fig. 1.1).

Fig. 1.1. Global world distribution of carbonatites from Le Bas (1987).

Carbonatitic magmas are involved in many geological processes. There are many theories on the origins of carbonatites.

For many years carbonatites were thought to be remobilized limestone, marble or precipitates from hydrothermal solutions. During the geological mapping and geochemical and petrographic

studies it became clear that carbonatites are unlikely sedimentary or metasedimentary carbonate rocks and are represent complex igneous rocks. Trace element and isotope geochemistry confirmed that carbonatites are indeed igneous and mantle derived and not remobilized or assimilated limestone.

The composition of volatile-rich magmas derived from lherzolite vary with pressure, volatile content and temperature (Wendlandt and Eggler, 1980, Eggler, 1989, Wyllie and Lee, 1998). A volatile-free peridotite at various pressures produces komatiites, picrites, tholeiites and alkaline basalt. There is a general agreement that the composition of the volatile phase abundant in the mantle is dominated by C-O-H components and phases in this system may exist as CO_2-H_2O fluid mixtures. When these fluid species are present generate mantle lherzolite containing amphibole, phlogopite, dolomite and magnesite and any of which can affect the composition of melts produced at the lherzolite solidus. The presence of carbon dioxide at crustal o lithospheric mantle pressures converts silicates to carbonates. A temperature drop in the solidus is caused by the appearance of magnesite or dolomite as mantle phases (point Q in Fig. 1.2). The low percentage of partial melting at pressures higher than Q-point reflects the increased solubility of carbonate in the melt (Fig. 1.2). Introducing H_2O and CO_2 can produce dolomitic or carbonated phlogopite peridotites in the mantle at depths greater than 70 km producing primary carbonatite melts.

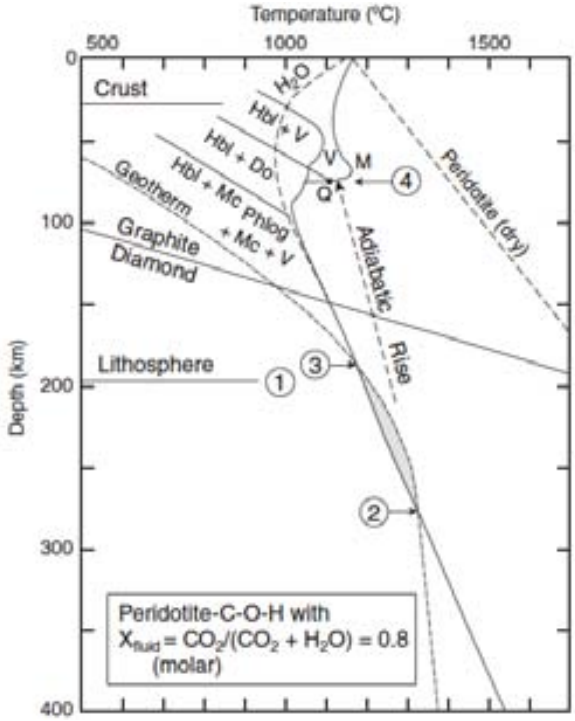

Fig. 1.2. Solidus curve for lherzolite- C-O-H system. Dashed curve represents H_2O-saturated and volatile-free peridotite solid and the shield geotherm (Wyllie, 1989).

Most carbonatites occur in stable continental intraplate settings, although some occur at continental margins and may be linked with orogeny or plate separation.

However, carbonatites have been proposed to be associated at other tectonic systems. Carbonatite melts by melting of carbonated eclogite in the upper mantle overlying peridotite to produce carbonate-bearing melts (Yaxley and Brey, 2004). Carbonatites are considered to generate in the lithospheric mantle as partial melts rising above mantle plume. If these melts stall, they can generate metasomatism in the mantle (Wyllie, 1995). In fact, chemical composition and low viscosity of carbonatitic melts make carbonatites a good metasomatic agent. Furthermore, carbonate metasomatism are observed in eclogitic xenoliths, implying a role of metasomatic carbonate fluids in subduction zones.

Percolation of carbonatitic melts through the mantle has been proposed by dissolution and precipitations process (Hammouda and Laporte, 2000) with percolation rates orders of magnitude higher than those estimated for basalt in the mantle. Such fast process implies a short residence time which may inhibit chemical interaction and metasomatism (Dalou et al., 2009). Evidence of relationship between carbonatite genesis and metasomatism is manifest in carbonate-bearing glimmerites with phlogopite, pyroxene and amphibole, across the globe (Rhodes and Dawson 1975; Dawson and Smith 1988, 1992; Rudnick et al. 1993; Dawson et al. 1995).

Among the different scenarios proposed, carbonatites have been also associated to MORB genesis. Via a transition from carbonatite to silicate melts (Hirose, 1997; Dasgupta et al., 2007a, 2007b; Foley et al., 2009) (Fig. 1.3).

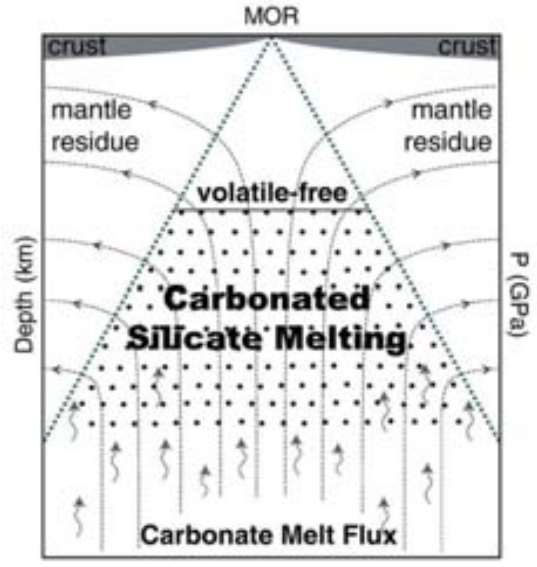

Fig. 1.3. Cartoon from Dasgupta and Hirschmann (2010) representing the carbonated silicate melt production beneath oceanic ridges. A flux of carbonatitic melt rising and inciting silicate melting of the shallow mantle.

Considering the carbonate stability field, at any pressure, carbonated silicate melting starts in a temperature interval at which dissolution of silicate begins in CO_2-rich carbonatitic fluid (Hirose, 1997; Dalton and Presnall, 1998; Moore and Wood, 1998; Gudfinnsson and Presnall, 2005; Dasgupta et al., 2007a, b; Brey et al., 2008; Fig. 1.3a) or a temperature at which an immiscible silicate melt appears with carbonatitic liquids (Hammouda, 2003; Dasgupta et al., 2006; Fig. 1.4b).

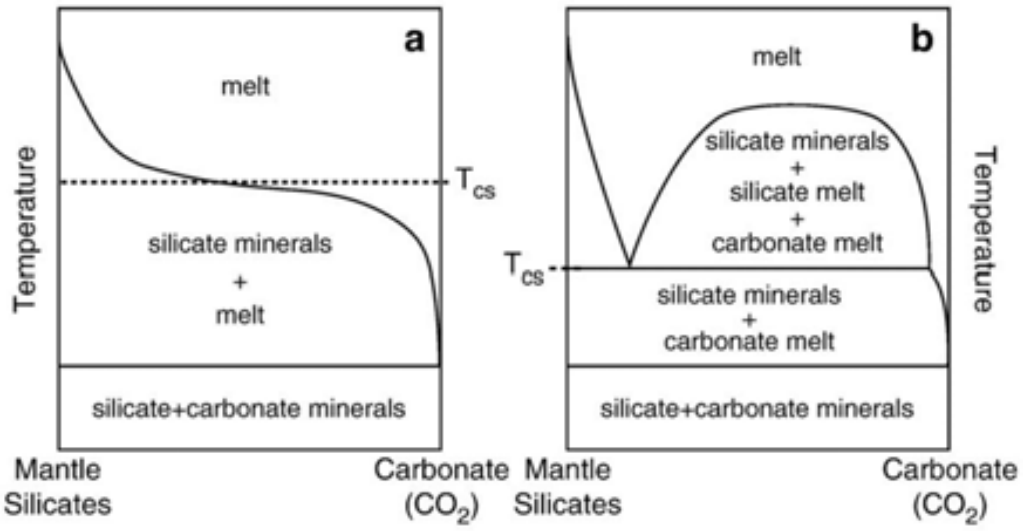

Fig. 1.4. Isobaric, $T - X$ sections. (a) The beginning of carbonated silicate melting through a miscible transition from a carbonatite melt at low T °C to a carbonated silicate melt at high T °C. (b) Coexistence between silicate and carbonatitic melts. These two melts appear immiscibly.

1.2. Physical properties of carbonate liquids

The physical properties of carbonate liquids related to carbonatitic magmas are widely discussed by Treiman (Treiman and Schedl, 1983; Treiman, 1989; Treiman, 1995).

The atomic structures of carbonate melts have been compared with the structure of silicate melts. Carbonatitic liquids are viewed as ionic liquids consisting of carbonate CO_3^{2-} molecular anions and metal cations bounded by ionic forces with inability to polymerize to form network structures. Therefore, they have a very low viscosity and are different from silicate melts, which have a network polymerized structure (Mysen, 1983; Fig. 1.5).

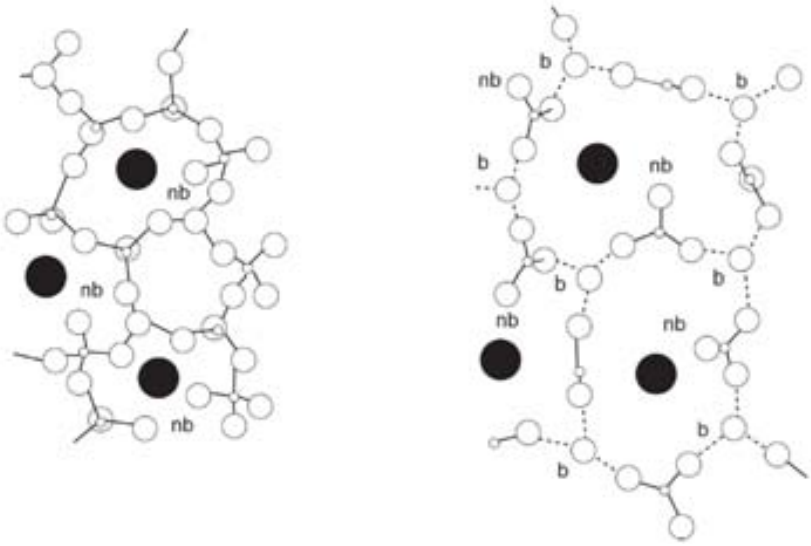

Fig. 1.5. Molecular bonding of silicate (on the left) and carbonate network (nb = nonbridging; b = bridging) (From Genge et al., 1995a).

The structure of water – saturated carbonate melts has been studied by Foustoukos and Mysen (2015) investigating calcite – H_2O, calcite – CaO – H_2O, magnesite – H_2O and magnesite – MgO – H_2O systems. The presence of water in the system involves development of hydroxyl bonds O---H – O. These bonds have been studied mainly in hydrated silicate melts highlighting negative effect on stability of the bond (Mysen, 2012). Foustoukos and Mysen (2015) noticed that a similar behaviour in the carbonate melts could reflect interactions with dissolved water dipoles (H – O---H – O) or interactions with CO_3^{2-} (O=C – O---H – O). Despite the difficulties in discriminating contribution between molecular water or structural water, it appears that the H_2O might be a stronger solvent in carbonate melt structure than in silicate melt structure promoting the solvation of trace elements and ionic species (Hamilton et al. 1989; Jones et al. 1995; Veksler and Keppler 2000; Dalou et al. 2009; Dasgupta et al. 2009; Veksler et al. 2012; Martin et al. 2013).

Sykes et al. (1992) carried out viscosity measurements in carbonatite melts on the calcite – magnesite ($CaCO_3$ – $MgCO_3$) binary system. Viscosity of a Ca-enriched carbonatite melt ($Ca_{0.7}Mg_{0.3}CO_3$) decreases from 0.6 Pa•s at 1200 °C to 0.08 Pa•s at 1300 °C. Temperature dependence of viscosity is small compared with silicate melts and the compositional dependence can be represented by linear isothermal conditions (Wolff, 1994), considering that the viscosities for Ca and Na-carbonatite at 800 °C are 0.08 and 0.008 Pa•s. For this reason, Jones et al. (1995), quoting Wolff (1994) suggest that the high viscosity measured by Sykes et al. (1992) must be due to the presence of a crystal mush or to incomplete melting while running experiment. Furthermore, Jones et al. (1995) and Dobson et al. (1996), considering previous literature data

and carrying out experiments at 4 GPa of pressure to measure density of $K_2(CaCO_3)_2$ and $K_2(MgCO_3)_2$, suggest that the pressure effect on viscosity is negligible (Table 1.1). Moreover, Kono et al. (2014) show a comparison of viscosity of carbonate and basaltic melts at high pressure in a previous study (Sakamaki et al., 2013) confirming that the carbonate melts viscosity values are much lower than basaltic melts values and that these values do not show any changes with pressure (Fig. 1.6a). These huge differences should yield a difference in the migration behaviour of these melts in the upper mantle (Fig. 1.6b).

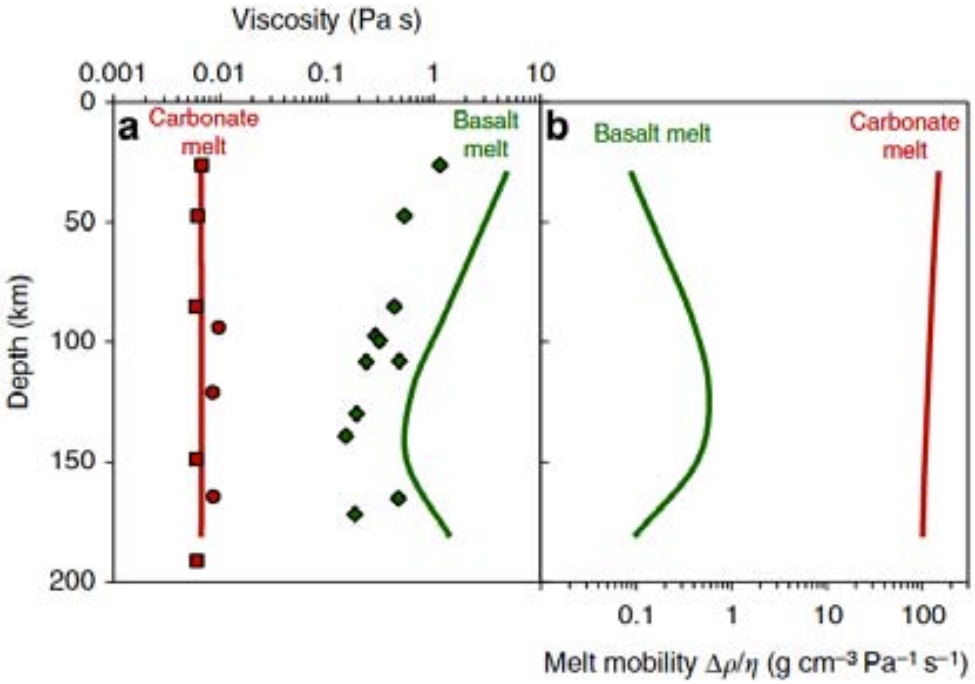

Fig. 1.6. (a) Viscosity of carbonate melts compared with those of basalt melts at their melting temperatures (1380 °C – 1790 °C and 1577 °C – 1827 °C respectively) at high pressure plotted with their viscosity along a geotherm (red and green line). (b) The mobility of carbonate and basaltic melts calculated by using viscosity and density of calcite with density of Fo_{90} (Circone and Agee, 1996) as solid rock (From Kono et al., 2014).

Reference	Composition	ρ (g/cm^3)	μ (Pa-s)	P (GPa)	T (°C)
Nesbit and Kelly (1977)	Natural carbonatite	2.20	---	---	---
Sykes et al. (1992)	$Ca_{0.7}Mg_{0.3}CO_3$	---	0.6	0.5	1200
			0.08	1	1300
Wolff (1994)	Ca-carbonatite	2.50	0.08	0	800
	Na-carbonatite	2.00	0.008	0	800
Genge et al. (1995)	$CaCO_3$	2.06	---	0.01	~1727
		2.90		10	~1327
Dobson et al. (1996)	$K_2(CaCO_3)_2$	2.06	---	0	859
	$K_2(CaCO_3)_2$	2.80	0.023	4	1050
	$K_2(MgCO_3)_2$	2.25	---	0	564
	$K_2(CaCO_3)_2$	2.75	0.032	2.5	950
	$K_2(CaCO_3)_2$	2.58	0.018	2.5	1150
	$K_2(MgCO_3)_2$	---	0.036	3	800
	$K_2(MgCO_3)_2$	---	0.022	3	900
	$K_2(MgCO_3)_2$	---	0.006	5.5	1200
	K_2CO_3	3.10	0.023	4	1500
	REE enriched carbonatite*	4.1	0.155	3	530
Liu et al. (2003)	$CaCO_3$	2.50	---	0	800
Liu et al. (2007)	K_2CO_3	2.18	---	4	1500
This study	$CaCO_3$	2.63	---	4	1750
	$MgCO_3$	2.72	---	4	1750
	$FeCO_3$	3.59	---	4	1750
	$Ca_{0.37}Mg_{0.53}Fe_{0.1}CO_3$	2.88	---	6.6	1245

Table. 1.1. Physical properties of carbonatitic melts.

The first calculation of density for carbonatitic magmas was carried out by Nesbitt and Kelly (1977) by studying magmatic inclusions in calcio-carbonatitic melt with SiO_2 > 15.7 wt.% content and calculating the carbonatitic melt density of ~ 2.2 g/cm^3. Wolff (1994) calculated a density value of Ca-carbonatite and Na-carbonatite of ~ 2.5 g/cm^3 and ~ 2.0 g/cm^3 respectively at atmospheric pressure and 800 °C. Genge et al. (1995a) predicted that $CaCO_3$ melt densities increase from ~ 2.06 g/cm^3 at atmospheric pressure to 2.9 g/cm^3 at 10 GPa of pressure, thus noting that changes in density with pressure are more significant than with temperature. At pressure relating to the depths of kimberlite source (~ 5 – 6 GPa), carbonate melts have density of about 2.5 – 2.6 g/cm^3, higher than those for $NaAlSi_3O_8$ melts. According to Genge et al. (1995a) the density measurements of Dobson et al. (1996) of $K_2(CaCO_3)_2$ between 2.5 to 4 GPa and $K_2(MgCO_3)_2$ at atmospheric pressure showing a density of 2.25 g/cm^3 for $K_2(MgCO_3)_2$ at 1 bar and ~ 550 °C pressure and temperature condition and 2.06 g/cm^3 for $K_2(CaCO_3)_2$ at 1 bar and 859 °C, while at 4 GPa and 1050°C the density of Ca end-member increases until 2.8 g/cm^3. Liu and Lange (2003) measured density for several carbonate liquids at atmospheric pressure and their results are in agreement with previous data except for $K_2(CaCO_3)_2$, whose density data show higher values compared with Dobson et al. (1996) values, probably due to different experimental techniques.

Variations in density can be used to estimate the isothermal compressibility and thermal expansivity of carbonate melts, and they generally increase with increasing temperature and decreasing pressure (Table 1.1). The isothermal compressibilities calculated show significant temperature variations at lower pressure (Genge et al., 1995b; Fig. 1.7).

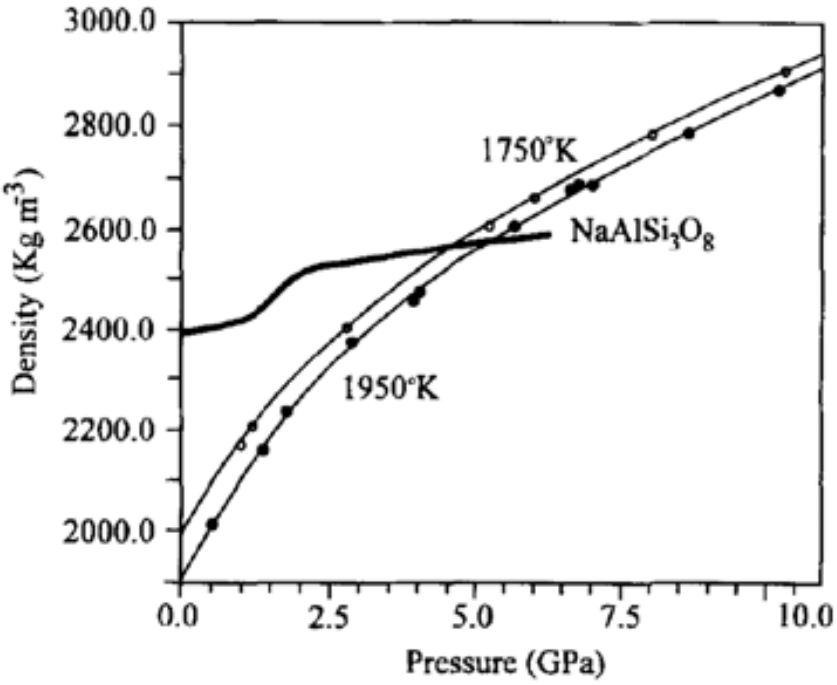

Fig. 1.7. Isothermal $CaCO_3$ density variation at 1750 °K and 1950 °K compared with $NaAlSi_3O_8$ melt.

Liu et al. (2007) carried out isothermal compressibility calculations on K_2CO_3 liquids at 1500 °C (Fig. 1.8a) noting that they drop rapidly with increasing pressure and that they can be compared with silicate liquids. In fact, at low or atmospheric pressure, carbonatitic liquid has a larger compressibility value than silicatic liquids like $CaAl_2Si_2O_8$ (An), and $CaMgSi_2O_6$ (Di) (Fig. 1.8b). The rapid drops with increasing pressure of compressibility of carbonate liquids do not allow density crossover with anorthite and diopside implying that carbonatitic melts remain buoyant to basaltic melts at upper mantle conditions.

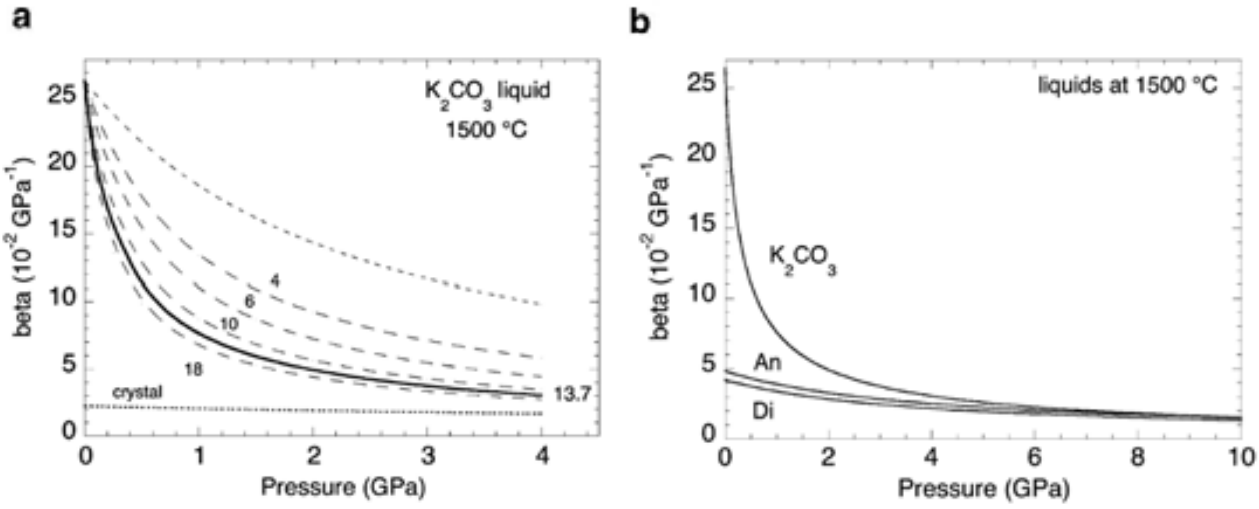

Fig. 1.8. (a) Isothermal compressibility of potassium carbonate at 1500 °C. (b) Comparison of isothermal compressibility variation between K_2CO_3, anorthite and diopside.

1.3. Chemical properties of carbonate liquids

Extrusive carbonatites are mostly calcio-carbonatites and to a lesser extent dolomitic carbonatites and alkaline natrocarbonatite (Woolley and Church, 2005; Jones et al,. 2013). Only 20% of carbonatites are associated with silicate rocks (Woolley and Kjarsgaard 2008).
Using a dominant modal carbonate mineral, they have been subdivided in calcite-, dolomite-carbonatites, on the basis of major element geochemistry, notably magnesium, calcium, iron (Woolley and Kempe, 1989; Fig. 1.9).

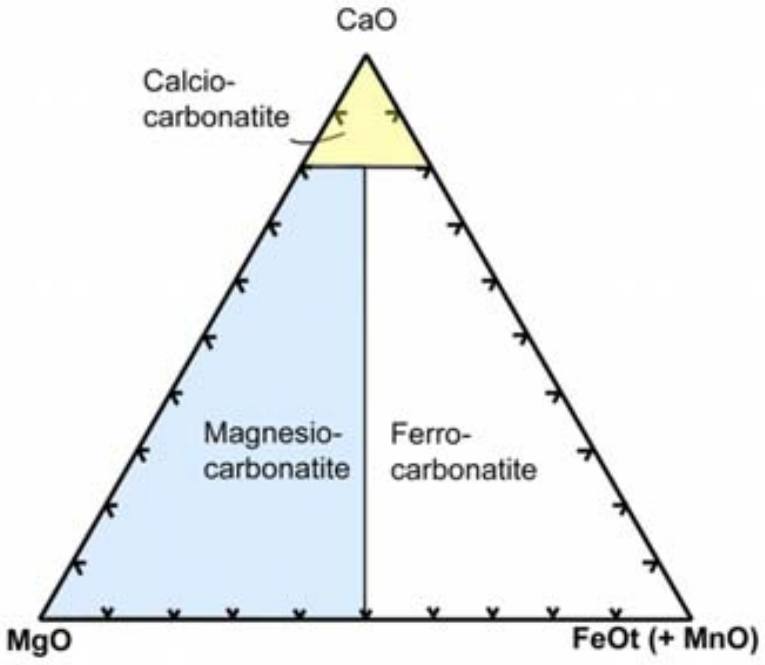

Fig. 1.9. Carbonatite classification diagram from Woolley and Kempe, 1989 modified by Jones et al., 2013.

Primary carbonatites are further divided into others subgroups in terms of mineralogical content, and genetically related to nephelinite, melilitite and kimberlite magmas.
Nephelinite carbonatites are represented by carbonatites with intrusive and extrusive rocks like ijoite, nepheline syenite and nephelinite and phonolite suite. Typically, phlogopite, olivine pyroxenites and dunites are absent in these rocks. Carbonatites contain mostly (Ca, Mg, Fe) carbonates, from calcite to siderite or ankerite through dolomite. Dolomite and calcite can be present in the same rocks.
Melilitite carbonatites are associated with plutonic and mantle rocks like melilitolites, perovskite pyroxenites and dunite. In this rock group ultramafic lamprophyres with the hypabyssal melilitite

facies are also included (Mitchell, 2005).

Effusive natural carbonatites could be an expression about chemistry of carbonatites. Magmas at Oldoinyio Lengai volcano (northern Tanzania), as observed by Dawson (1962), have a chemical composition of sodium carbonate for the 60% (Na_2O ~ 32 wt.%), 30% of calcite (CaO ~ 14 wt.%) and 10% of potassium carbonate (K_2O ~ 8.3 wt.%) and extremely low silica content (Dawson, 1989). In the natrocarbonatite of Oldoinyio Lengai the water content is negligible. Other carbonatites are calcio-, magnesio-, ferro-carbonatites with very low alkali content. Calcio-carbonatites were found on other African volcanoes (Bailey, 1960; Mariano and Roeder, 1983) and in Italy (Polino; Lupini and Stoppa, 1993).

These magmas have very low alkali content (< 1 wt.% of sodium and potassium), as indicated above. SiO_2 concentrations varying from 7.45 to 16.2 wt.%, whereas MgO varies from 3.27 to 8.55 wt.%. The range of CaO contents is greater than that for natrocarbonatite of Oldoinyio Lengai (CaO from 36 wt.% to 40.5 wt.%). FeO concentrations vary from ~ 1.3 to 4.5 wt.% and Fe_2O_3 contents ranging from 3.7 to 7.93 wt.%. The water contents are rarely provided and range from 1.2 to 3.45 wt.%. In effusive carbonatitic magmas, olivine, phlogopite, diopside, perovskite and apatite are present as xenocrysts in a groundmass of calcite, zirconium garnet, periclase, monticellite, chromium-spinel, ankerite, magnetite. Carbonatitic liquids are essentially made of calcite showing a negligible iron, magnesium, alkali and silica content and higher calcium concentrations (CaO ~ 52 – 54 wt.%) (Bailey, 1993 and reference therein).

Effusive magnesium-carbonatites are very rare and the rare analyses present were carried out quenched melt droplets in vent tuffsite in Runfunsa valley (Zambia) with high Mn-dolomite (MgO = 19 wt.% and CaO = 28.8 wt.%) (Bailey, 1989) (Table 1.2 and Table 1.3).

	SiO_2	TiO_2	Al_2O_3	Fe_2O_3	FeO	MnO	MgO	CaO	Na_2O	K_2O	P_2O_5	H_2O	CO_2	F	Cl	SO_3	SrO	BaO
1. Natrocarb. (Lengai)		0.11	0.09	0.28		0.04	0.53	13.9	32.2	8.27	0.90	tr.	34.7	2.93	4.21	2.18	1.53	1.04
2. Calcio-c (Kerimasi)	0.39	tr.	0.07	0.34		0.22	0.21	54.0	0.10	0.05	1.82		41.8				0.40	0.2
3. Calcio-c (Ft. Portal)	13.0	1.74	3.03	7.93	4.44	0.40	8.55	36.0	0.73	0.20	3.32	3.45	14.8	0.08			0.63	0.15
4. Calcio-c (Polino)	16.2	0.52	3.91	3.69	1.31	0.07	7.31	38.7	0.05	0.50	0.60	3.12	24.1					
5. Calcio-c (Kaiserstuhl)	0.45	0.03	0.15	0.98		0.41	0.36	52.6	0.04	0.50	1.56	1.16	39.8	0.54			0.67	0.15
6. Calcio-c (Emirates)	7.45	1.01	1.75	8.30	3.12	0.46	3.27	40.5	0.23	0.14	7.00	1.2	24.58					
7. Magnesio-c (Rufunsa)					0.49	1.56	19.0	28.8									1.10	

References
1. Dawson 1989, table 11.3, p. 269 (Anal. 1).
2. Mariano & Roeder 1983, table 1, p. 451 (Anal. 3).
3. Barker & Nixon 1989, table 5, p. 172 (Anal. 1) F value calculated from mode and mineral analyses.
4. Lupini & Stoppa in press.
5. Keller 1989, table 4.1, p. 79 (Anal. KB2).
6. Woolley *et al.* 1991, table 3, p. 1160 (Anal. Type 1, Mean).
7. Bailey 1989, table 1, p. 416 (Anal. 3: dolomite melt droplet).
c, carbonatite.

Table 1.2. Composition of effusive carbonatites and relative references (From Bailey, 1989).

Ref & Locality	Cognate minerals	Xenocrysts	Silicate melts in		Inference
			Complex	Province	
A Calcio-carbonatites					
1. Ft Portal (Uganda)	Cc, Cs, P, Ap, Mo	Ol, Di, Phl, Per, Ap	None	K u/m	Primary, direct eruption from mantle
2. Catanda (Angola)	Carbonates. Mainly Cc	Ol, Cr-Di, Cr-Sp, Phl, Kaer, Ap	None	Tinguaite (?)	Primary, direct
3. Polino (Italy)	Cc, Zr, (Mo)	Ol, Phl, Ol + Phl	None	K u/m	Primary, direct
4. U.A. Emirates	Cc, Cr-Sp		None	None	Primary direct
5. Khanneshin (Afghanistan)	Cc, Ank, Ba		Lc tephrite (minor)		Primary direct
6. Rufunsa	Cc, Cr-Sp	San	None	None	Primary, direct
7. Kaiserstuhl (Germany)	Cc, Mt, Ap		Melilitite*		Differentiate, high *T*
8 Kerimasi (Tanzania)	Cc		Melilitite*		Differentiate (?) High *T*
B. Magnesio-carbonatite					
6. Rufunsa (Zambia)	Dol, Cr-Sp	Phl	None	None	Primary Direct

* Silicate melt most closely related to carbonatite
Abbreviations: Cc, Calcite; Cs, spurrite; P, periclase; Ap, apatite; Ol, olivine; Di, diopside; Phl, phlogopite; Per, perovskite; Sp, spinel; Zr, zirconium garnet; Mo, monticellite; San, sanidine; Mt, magnetite; Dol, dolomite; Ank, ankerite; Ba, barite; Kaer, kaersutite; Lc, leucite; K u/m, potassic ultramafic lava.
References: 1, Barker & Nixon 1989; 2. Silva 1973; 3. Lupini & Stoppa in press; 4. Woolley *et al.* 1991; 5. Alkhazov *et al.* 1978; 6. Bailey 1990; 7. Keller 1981; 8. Mariano & Roeder 1983.

Table 1.3. Some localities where calcitic effusive rocks are closest to magmatic composition (From Bailey, 1989).

Carbonatites are associated with kimberlitic magmas, because some areas show calcite-carbonatite dykes associated with kimberlitic complex. Furthermore, several kimberlites contain primary carbonate (Dawson and Hawthorne, 1973). Kimberlites are commonly divided into "Group I" and "Group II" (Smith, 1983). These two groups are distinguished on trace element grounds like Ba/Nb, Th/Nb, La/Nb and Ce/Nb ratios indicating a more extensively metasomatized source for "Group II" (Smith, 1983; Becker and Le Roex, 2006).

Kimberlite magmas like calcio-carbonatite have low alkali contents (~ 0.2 and ~ 1.9 wt.% of Na_2O and K_2O respectively). The silica contents average is ~ 31 wt.% whereas MgO concentration varies between 18.6 and 33.3 wt.%. FeO average is ~ 10 wt.% and CaO ~ 10.7 wt.% varying between ~ 5 and 20 wt.%. Water content is defined as the difference between the loss of ignition (LOI) and CO_2 concentrations, and it reaches up to ~ 9 wt.%. These analysed kimberlites show olivine and phlogopite as phenocrysts and calcite, serpentine, ilmenite, perovskite and apatite (Becker and Le Roex, 2006).

Water plays an essential role in the generation of carbonatite and kimberlite magmas (Sokol and Kruk, 2015). Group I kimberlites and carbonatites represent low – H_2O sources. Hydrous volatile components may be generated in the mantle by hydrous phases at low pressure or by nominally anhydrous minerals (e.g. clinopyroxene); volatiles may interact with carbonated melt (Sokol et al., 2013). The kimberlite source can be inferred to contain small water contents as shown by

occurrence of MARID (Mica-Amphibole-Rutile-Ilmenite-Diopside; Dawson and Smith, 1977) xenoliths, even if water saturation is unlikely. MARID suite could be produced by interaction of alkali-rich fluid with peridotite or by fractionation of olivine in a kimberlitic magma with exsolution of carbonatite component (Sweeney et al., 1993).

Water is an important agent in carbonatite genesis because it is able to depress the carbonatites melting point and because it may be really crucial for the carbonatite magmas differentiation. Despite the relevance of H_2O for carbonatite magmatism, water solubility in carbonatite liquids is very poorly known (Keppler, 2003).

Carbonatite magmas usually consist of dolomite or calcite, but experimental evidence show that primary carbonatite contains Na- and K- amount (Wallace and Green, 1988). The first contributions on water solubility in carbonatite melts came from studies of Kostner van Groos (1990), who studied the Na_2CO_3-H_2O system. Experiments were conducted at *P* from 0.4-3.7 kbar and *T* from 100 to 925 °C using high-pressure differential thermal analysis (HP-DTA). The starting materials were pure Na_2CO_3 with less then 80 wt.% of water inserted into the capsule. For experiments with less then 85 and 92 wt.% of water a solution of Na_2CO_3 was used. DTA information peak represents the beginning of reaction and the peak temperature is related to maximum value for the reaction temperature. This technique was less precise for multicomponent system than in a one – component system because in multicomponent system the reactants are more than one and the reaction peak results broad instead of sharp. DTA curves show the increasing pressure effects on solidus and liquidus temperature.

The temperature of first peak represents solidus temperature, whereas the second peak with higher temperature than solidus represents high dissolution rate of Na_2CO_3 into the liquid. The experimental evidence from Kostner van Groos (1990) shows complete miscibility in the Na_2CO_3 – H_2O system above 500 °C and 1.5 kbar. Therefore, water solubility is expected to be very high. The composition of alkali rich CO_2 - H_2O fluids can be K-rich and Na-rich at pressure > 1.5 kbar but, at lower pressure, these fluids become K-rich and Na-poor. Therefore, Na solubility in carbonated alkali fluids decreases rapidly over a small pressure interval and Na increasing could result in the formation of Na-rich magma. Probably, the generation of kimberlites or carbonatites involves the reaction between mantle peridotite and alkali-rich CO_2 - H_2O supercritical fluids (Menzies and Wass, 1983; Bailey, 1984; Wendlandt, 1984; Roden and Murthy, 1985; Spera, 1987; Wyllie, 1987).

Keppler (2003) performed a water solubility study in a carbonate melt at *P* from 0.25-2.25 kbar and *T* of 900 °C. A melt composition consisting of 40 wt.% of $CaCO_3$, 40 wt.% of Na_2CO_3 and 20 wt.% of $MgCO_3$ was used, because Ca, Na and Mg are major constituents of carbonatite

melts. Since carbonatitic melts cannot be quenched (Genge et al., 1995a) it was impossible to use standard techniques to measure water solubility in silicate melts (Ihinger et al., 1994). For this reason, Keppler (2003) used a double-capsule method (Veksler and Keppler, 2000) in rapid-quench cold-seal (Boettcher and Kerrick, l97l) quenching the sample within 1-2 seconds. The composition of fluids was essentially water with dissolved carbonates. Starting material was enclosed in a platinum capsule and run at 1 kbar and 900 °C for a few days. After quench the Pt capsule was drilled in the upper part and closed in a bigger capsule with water and the instrument was preheated and pressurized at experimental desired conditions. After experimental run, the outer capsule was removed and the inner one was cleaned and put inside a larger platinum capsule to avoid loss of water. In order to account for the time for equilibrium, these experiments were performed at the same *P* and *T* conditions (1 kbar and 900 °C respectively) but with different run durations. The measure was performed by coulometric Karl-Fisher-Titration (Eberius, 1958). This procedure provides a capsule piercing before the measurement and positioning it in a furnace slowly heated to 1300 °C. This method is calibrated on the reaction $SO_2 + I_2 + 2\ H_2O = 4\ H^+ + 2\ I^- + SO_4^{2-}$.

The measurement results of Keppler (2003), related with typical water solubility in silicate melts values (Behrens, 1995), show extremely high water solubility in carbonatite liquids and these results are listed in Table 1.4. In fact, at only 0.225 GPa of pressure, water solubility measured is 14.39 wt.% and ~ 10 wt.% at only 0.1 GPa, almost three times for water solubility in silicate melts (Fig. 1.10). Water solubility measured in Na_2CO_3 – rich carbonates was extremely high due to complete miscibility of Na_2CO_3 at 1.5 kbar and 500 °C.

Run	*P* (kbar)	Duration (hours)	Weight ratio water/carbonate	Water content (wt%)
C15	1	1	5:7	9.68
C17	1	4	5:7	8.61
C18	1	8	5:7	10.12
C19	1	16	5:7	10.17
C21	1	2	5:7	10.24
C31	0.5	18	1:2	7.19
C33	1	19	1:2	11.19
C34	1.5	17	1:2	12.56
C35	1.25	3	1:2	8.22
C36	1.5	3	1:2	10.52
C38	2	4	1:2	13.03
C39	2.25	4	1:2	14.39
C41	0.5	3	1:2	6.45
C42	0.75	3	1:2	5.31
C43	1	4	1:2	9.42
C44	1.25	4	1:2	11.41
C45	0.25	2	1:7	2.64
C46	0.5	2	1:2	5.60
C48	1	2	1:2	8.13
C50	1.25	2	1:2	8.19
C52	1.75	2	1:2	9.12

Table 1.4. Experimental results on water solubility in carbonatitic melts at 900 °C (Keppler, 2003).

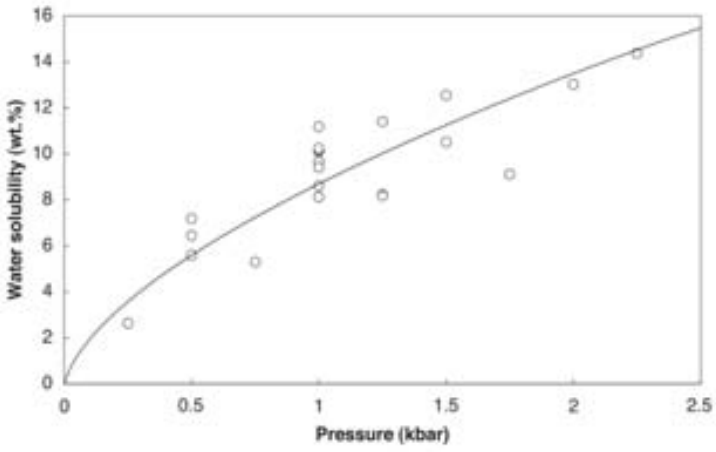

Fig. 1.10. Water solubility in a Ca – Na – Mg carbonate melts with pressure (Keppler, 2003).

1.4. Distribution and migration of liquids in a granular mantle

Migration of melts generated by partial melting of peridotite plays a crucial role in their segregation into larger masses that ascend and intrude overlying lithosphere as magmas.

Liquids can migrate through aggregates of mineral grains (rocks) by hydraulic fracturing or by porous flow involving movements of the liquid along grain boundaries considering the percolation as the principal process in presence of a mixture with a large contrast in properties like solid and liquid phases.

Consider a solid–liquid contact there are two types of interface at this contact: a solid–solid interface and a solid–liquid interface and each interface is associated with the interfacial energy.

Liquid phase sintered composite materials exhibit solid–solid and solid–liquid interfaces. In composite materials, melt particles represent a dispersed phase which is bounded with closed surfaces. The physical principle governing the grain scale melt distribution in partially molten rocks is the surface energy between grain and melt (Waff and Balau, 1979). For minerals with isotropic surface energies, the relative mineral–fluid interfacial energies can be described by dihedral angle θ (or wetting angle) between two grains and melt. Dihedral angle is critical to the distribution of melt in any partially molten material (Jurewicz and Jurewicz, 1986) and represents the intersection angle of two solid–fluid interfaces at the point of contact between grain boundary and liquid. (Bulau et al., 1979; von Bargen and Waff, 1986). The dihedral angle θ is related to the surface energies by:

$$\frac{\gamma_{\text{g-b}}}{\gamma_{\text{s-l}}} = \cos\frac{\theta}{2} \quad \text{(Eq. 1)}$$

where $\gamma_{\text{g-b}}$ is the grain boundary energy and $\gamma_{\text{s-l}}$ is the solid–liquid interfacial energy (Smith, 1964; Watson, 1982).

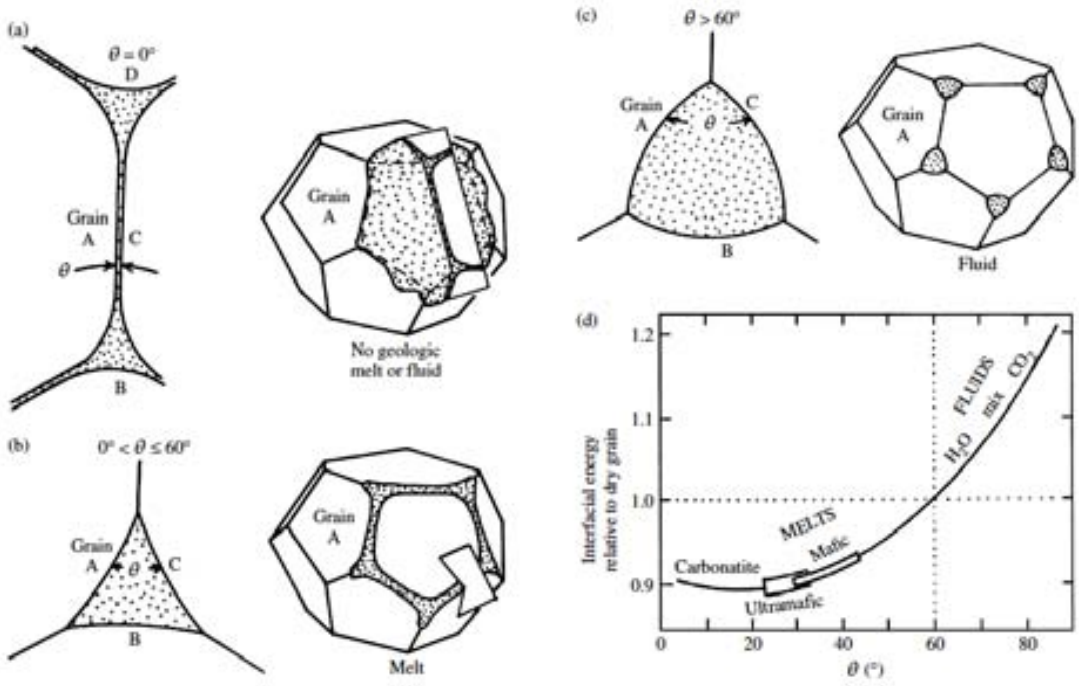

Fig. 1.11. Volumes of liquid in a grain aggregate distributed is a function of the relative interfacial energies of contacting phases. (a) For θ=0° the liquid wets the entire surface of grain A and its neighboring grains B, C, D forming thin film. (b) for 0 ° < θ < 60 ° melt is distributed in interconnecting strands with triangular cross sections that lie along three-grain edge junctions. (c) for θ > 60 ° small isolated packets of a fluid phase lie at grain corners. (d) Carbonatite melts and silicate melts of basaltic and ultramafic composition are stable along intergrain edges. H_2O-CO_2 fluids are stable along intergrain edges if in large volume whereas small volumes lie at grain corners (From Best, 1982).

Interfacial energies, which depend on liquid and crystal compositions and on *P*-*T* conditions, can be readily measured by experiment. Three cases are significant: if the dihedral angle is 0 ° ($\gamma_{g\text{-}b} > 2\gamma_{s\text{-}l}$) the grain boundaries are completely wetted reducing area of solid–solid contact (Fig. 1.11a). If 0° < θ < 60° solid–solid interfaces are stable and any melt fraction should form an interconnected channel along all grain edges (Fig. 1.11b). When θ > 60° melt forms a isolated pockets (Fig. 1.11c).

Fig. 1.11d shows the differences between carbonates, silicates liquids and water-rich and CO_2-rich fluids in terms of interfacial energies and dihedral angle values.

In particular, Cmiral et al. (2003) show that the local melt geometries in olivine-basalt aggregates are characterized by a variety of geometries as the wetting angle decreases: from large intersects (Fig. 1.12a), triple junctions with edge characterized by faceting (Fig. 1.12b), regular triple junctions (Fig. 1.12c) and thin layers or films (Fig. 1.12d).

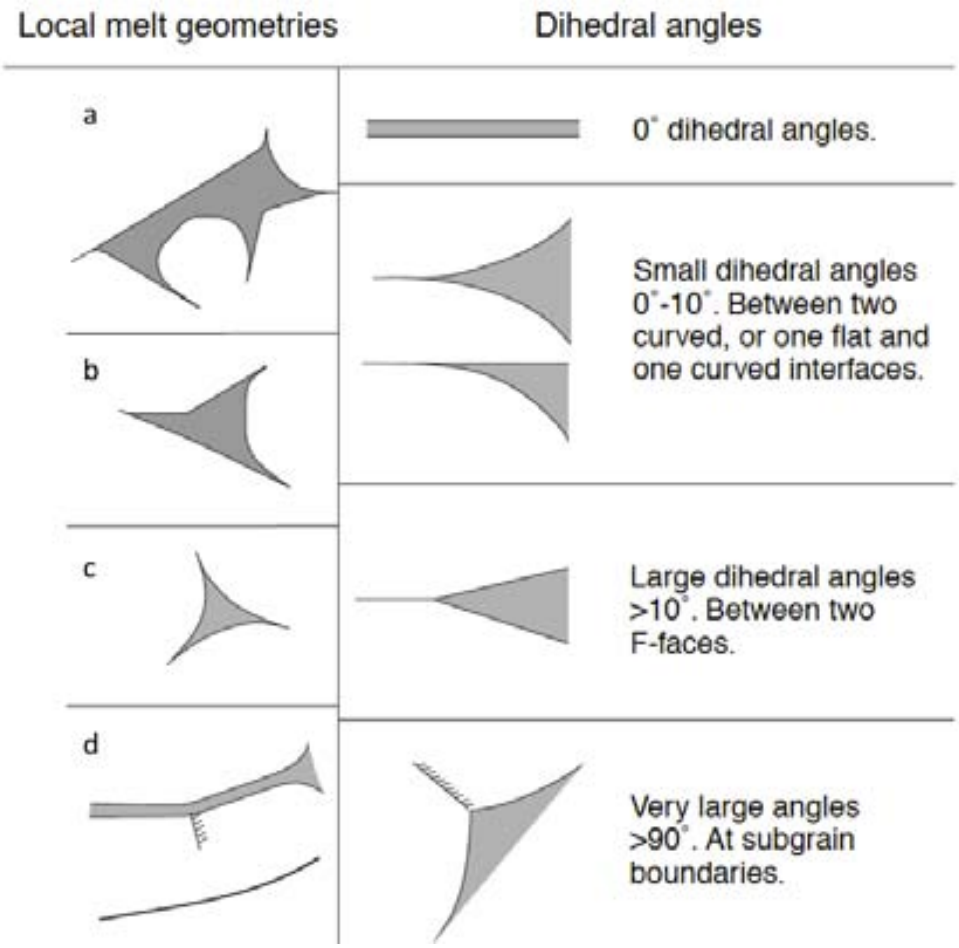

Fig. 1.12. Local melt geometries of melt fraction (grey) between olivine grains (white) related with dihedral angle (Cmiral et al., 2003).

The model for three-dimensional melt distribution based on surface tension equilibrium assumes grains of a fixed size with isotropic surface energy, and the predicted melt geometry has constant interfacial curvature independent of grain size and melt fraction (von Bargen and Waff, 1986). Consequently, the dihedral angle is independent of melt fraction. Furthermore, experimental observations indicate that melt forms not only triple junctions but also larger pockets surrounded by four or more grains with faceted crystal – melt interfaces (Waff and Faul, 1992; Faul, 1997). Therefore, experimental studies by Faul (1997) and Garapic et al. (2013) demonstrated that the melt geometry in partially molten systems cannot be characterized by dihedral angle alone. For these reasons, a parameter is needed to account for the variability of the melt geometry observed in partially molten rocks. This parameter is the grain boundary wetness ψ.

The grain boundary wetness ψ is defined as the ratio of solid–liquid boundary area over the total area of interphase boundaries by:

$$\psi = \frac{A_{sl}}{A_{sl}+A_{ss}} \text{ (Eq. 2)}$$

where A_{sl} is the solid–liquid and A_{ss} is the solid–solid interfacial areas of one grain (Yoshino et al., 2005). Since each grain boundary involves two crystals, it is necessary to use the factor "2" in front of A_{ss} and (Eq. 2) becomes:

$$\psi = \frac{A_{sl}}{A_{sl}+2A_{ss}} \text{ (Eq. 3)}$$

1.5. Objectives of this work

The goal of this work is a quantitative laboratory assessment of variables and processes controlling the ascent, mobility and connectivity of carbonatites in the mantle peridotite.

The project focuses on the experimental reproduction of rock textures resulting from the infiltration of hydrous carbonatitic liquids in ultramafic rocks at pressure and temperature conditions named above. We choose to investigate hydrous carbonatitic liquids at upper mantle conditions (P = 2.5 GPa and T = 1200 °C) by means of end-loaded piston cylinder apparatus experiments at the laboratory of Experimental Petrology, Department of Earth Sciences, University of Milan (Italy). Experiments were carried out considering the system $CaCO_3$ – $MgCO_3$ – $FeCO_3$ as representative of natural carbonate component of carbonatitic magmas, therefore neglecting here the role of alkali.

The objectives of this research are to investigate and verify differences in dihedral angle between hydrous (this work) and anhydrous carbonatitic liquids previously studied (Hunter and McKenzie, 1989; Watson et al., 1990; Minarik and Watson, 1995; Hammouda and Laporte, 2000). In addition to this, we compare the volume proportions of volatile–rich carbonatitic melts with silicate melts in partially molten peridotite (Yoshino et al., 2009), and with H_2O- or CO_2-rich fluids in peridotite and eclogite. Last, we will examine whether carbonatitic liquids are always more wetting than silicate melts.

Chapter 2

Experimental Background

2.1. Forces and factors promoting infiltration

2.1.1 Minimization interfacial energy

Most studies related to migration of liquids in the mantle invoke differential stress and gravity as force for melt migration (Shaw, 1980; Spera, 1980). Watson (1982) considered these factors certainly important to large–scale, but he focused his attention on surface energy for small–scale melt migration. Theoretically, at constant temperature and pressure conditions, neglecting buoyancy and differential pressure, the only driving force for melt migration is reduction in surface energy. In fact, if wetting lowers the surface free energy the melt will tend to penetrate the grain boundaries.

Therefore, melt infiltration will occur where grain–melt interfacial energy is low related to grain–grain interfacial energies. Melt might infiltrate crystals along planar surface or along triple junctions. Considering equilibrium setting, grains will be triple equiangular junction (120°) if the interfacial energies have the same value (Smith, 1964). Total interfacial energy, in this condition, can be expressed as:

$\gamma_{g\text{-}b} \cdot 3\, w\, l$,

where $\gamma_{g\text{-}b}$ represents isotropic solid–solid surface energies and w and l the dimensions.

The total interfacial energy when the grain edges are wet by melts becomes:

$$\gamma_{s\text{-}l} \cdot \frac{\sqrt{3}\left[\frac{\pi}{6} - \frac{\theta}{2}\right]}{sin\left[\frac{\pi}{6} - \frac{\theta}{2}\right]} \cdot 3\, w\, l ,$$

where $\gamma_{s\text{-}l}$ is the solid–liquid interface, and θ is the dihedral (or wetting) angle, that describes the intersection of two solid–liquids interfaces in contact at grain edge (Minarik and Watson, 1995; Fig. 2.1).

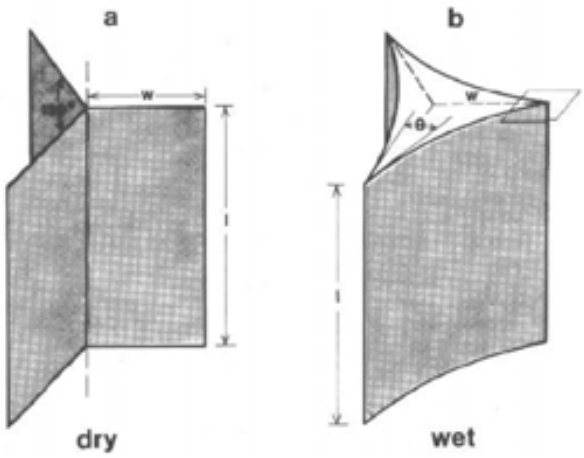

Fig. 2.1. (a) Schematic representation of grain edge in dry system. (b) Schematic representation of wet grain–edge (Watson, 1982).

Therefore, using (4), (5) and the wetting angle relation (1) mentioned above (see Section 1.4), Watson (1982) calculated total interfacial energies in a wet grain–edge as fraction of dry grain–edge for any value of wetting angle (Fig. 2.2).

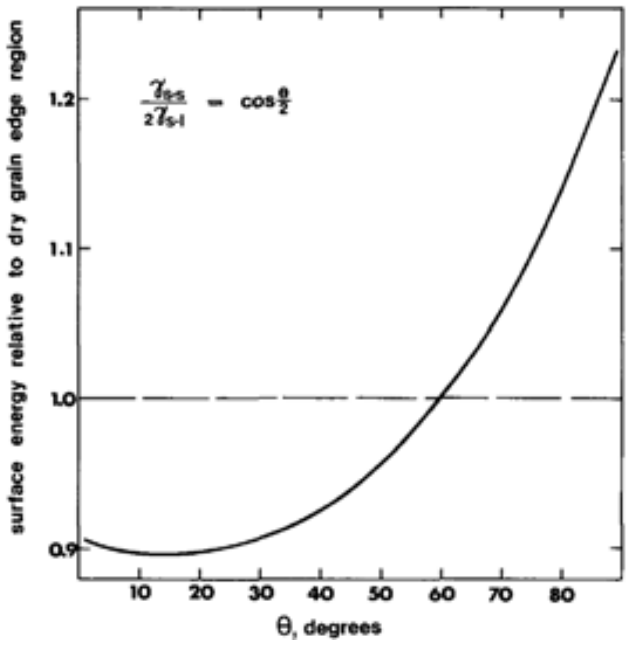

Fig. 2.2. Total interfacial energy represented against dihedral angle values (Watson, 1982).

Park and Yoon (1985) introduced the concept of a minimum–energy melt fraction in a crystal–melt system refers to a specific fluid fraction (ϕ_m) given by the sum of grain boundary energy ($\gamma_{g\text{-}b}$) and solid/liquid interfacial energy ($\gamma_{s\text{-}l}$). The minimum interfacial energy depends on dihedral angle θ and volume liquid fraction (Fig. 2.3). Assuming that the system is at equilibrium, and that the porosity is lower than the fraction defined by the minimum in the energy function the melt must infiltrate the rock in order to minimize the energy of the system (Watson, 1999).

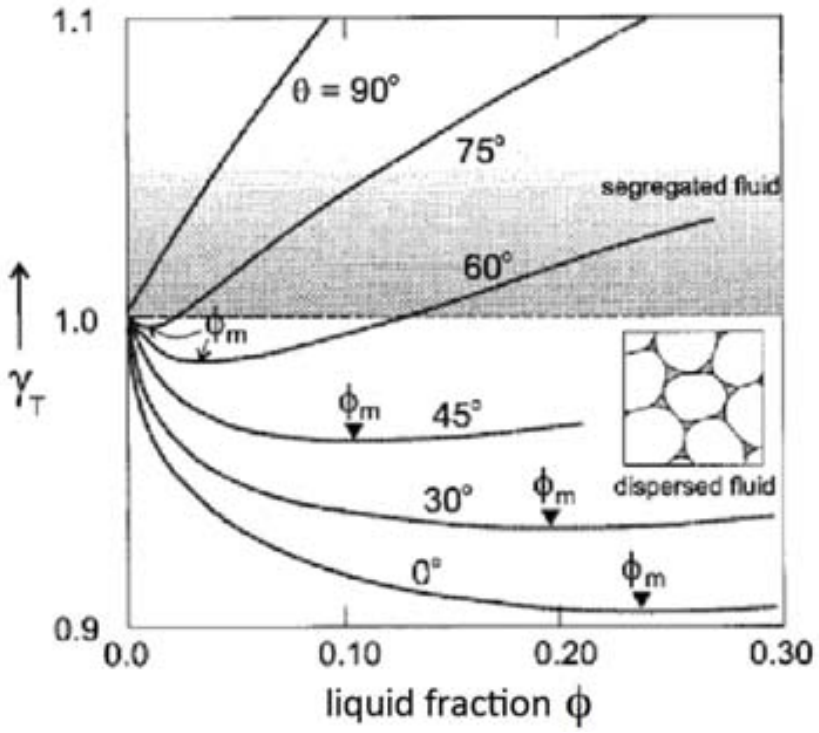

Fig. 2.3. Normalized total interfacial energy (γ_T) of a monomineralic rock related liquid fraction (ϕ) and dihedral angle values (Watson, 1999).

2.1.2 Soret effect – Thermal diffusion

Mass transport, diffusion in phases such as solutions or melts, by thermal gradients and solid – solid interface is a process observed by Soret (1879) placing salt solutions in a column within a temperature gradient. He observed and demonstrated how this solution develops a concentration gradient in two components. The chemical concentration of salt migrates at the cold part of column and the lighter element toward in the hotter part.

The same effect was observed by Walker and Delong (1982) and Lesher and Walker (1986) in high–temperature silicate melts (T > 1400 °C). In these silicate melts, calcium magnesium and iron become concentrated in the cooler part of temperature gradient, silica, sodium and

potassium in the hotter part instead. Soret diffusion is expected to occur in most experimental studies because of the intrinsic temperature distribution occurring in high-pressure assemblies, where the hot spot of the furnace usually corresponds to the location of the thermocouple junction.

2.1.3 Dissolution – (re-)precipitation mechanism

Dissolution – (re-)precipitation mechanism as a promoter of melt infiltration was invoked by Hammouda and Laporte (2000), performing experiments with dunite and Na_2CO_3 melt. They deduced that the melt infiltration proceeds by dissolution – precipitation mechanism. According to Hammouda and Laporte (2000) this process progresses in three step: first dunite dissolution occurs ahead of infiltration front creating new porosity and formation of interconnected melt channels allowing infiltration; secondly this dissolved material is transported by diffusion and it finally reaches the carbonatite inducing olivine growth at the carbonatite–dunite contact (Fig. 2.4).

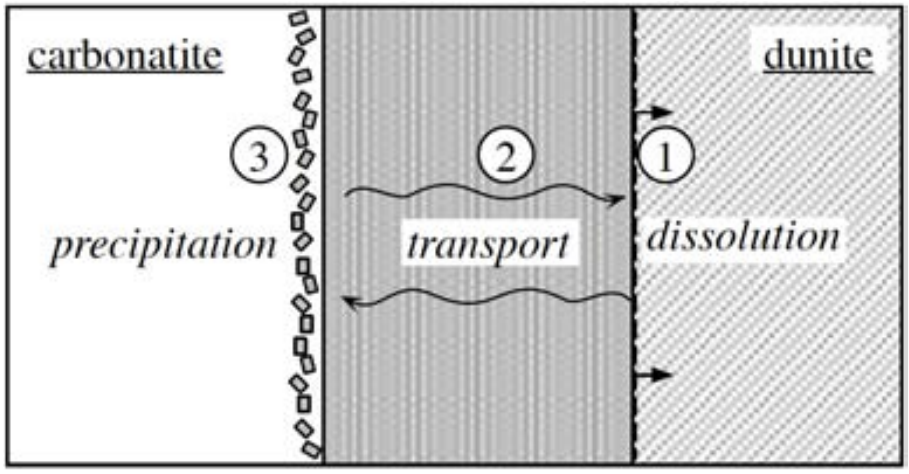

Fig. 2.4. Schematic representation of three step of dissolution – precipitation process in synthetic dunite from Hammouda and Laporte (2000).

2.1.4 Chemical gradients

Another factor promoting infiltration is the chemical gradient invoked by several authors (Takahashi, 1986; Lesher and Walker, 1988; Walker et al., 1988) in partially molten system and by Wark and Watson (2002) for systems bearing H_2O-CO_2 mixed fluids, the latter aimed at quantifying the role of migration of the mobile phase on pore geometry and permeability.

Wark and Watson (2002) observed experimentally that fluids (and therefore melts) become concentrated into elongated pores parallel to the thermal gradient. This channelization is responsible for an increase of permeability therefore affecting the transport properties of rocks at depth. Wark and Watson (2002) observed that channel morphology varied with rock type. In fact, this channelization of pores results the strongest for calcite + quartz + wollastonite with H_2O–CO_2 rich fluids, whereas it decreases in quartz and fluorite with H_2O–rich fluid, and it is weak for $CaCO_3$ + H_2O. This mechanism is therefore promoted not only by thermal gradient but also by strong gradients in fluid composition, especially XCO_2, i.e. gradients in concentration that, similarly to Soret effect, imply gradients in chemical potential.

2.2 Geometry and *P* – *T* conditions investigated in previous work

Experiments involving melt infiltrations in a mantle matrix have been carried out in several systems.

Watson and Brenan (1987) investigated experimentally the wetting characteristics of CO_2–H_2O fluids and fluid transport in different systems. The authors performed experiments by piston – cylinder apparatus at 1 GPa and a temperature range from 950 to 1150 °C and run time between 3 to 6 days. The analysed systems were quartz (glass and granular) + C-O-H fluids; clinopyroxene, orthopyroxene, feldspar and spinel–lherzolite + CO_2–H_2O rich fluids and olivine + pure H_2O or CO_2–rich fluids. For the dunite experiments they used a San Carlos olivine ground and sieved. As fluids source silver oxalate ($Ag_2C_2O_4$) was used to generate CO_2–rich fluid or oxalic acid ($C_2H_2O_4$) to obtain a 1:1 ratio of H_2O and CO_2 mixture.

Hunter and McKenzie (1989) focused on the equilibrium geometry of carbonate melts in mantle rocks. They carried out a melting experiment to determine the dihedral angle for dolomitic melt at 3 GPa and 1290 °C pressure and temperature conditions, above the solidus of carbonated peridotite. Starting material was a mixture of spinel lherzolite and dolomite powder in 4:1 ratio respectively. Natural spinel lherzolite was obtained by sieving a xenolith from San Carlos (ol 79 vol.%, opx vol.15 %, cpx vol.3 % and sp vol.3 %) while they used an iron free dolomite as a source for the carbonatitic melts.

Minarik and Watson (1995) proposed a study of interconnectivity of carbonatitic melt and they performed experiments at 3 GPa of pressure and 1300 °C of temperature. They used sodium

carbonate mixed with San Carlos olivine powder either placed separately or diluted in distilled water.

Cmiral et al., (1998) proposed a study focused on dihedral angle and melt geometry performing a detailed TEM analysis on olivine–basalt aggregates. As starting materials, they chose a San Carlos olivine and as basalt high purity oxides and carbonate with fayalite melted together into glass and then perform high $P - T$ experiments (1 GPa and ~ 1360 °C).

In order to establish the lithological partitioning of fluids and melts, Watson (1999) performed a large number of experiments in different systems using different pressure and temperature conditions. In fact, he evaluated the partitioning in aqueous fluids by conducting experiments in simple system like quartz/calcite + H_2O, quartz/fluorite + H_2O, quartz/clinopyroxene + H_2O, with water content ranging between 1.5 to 9 wt.%. For these runs the condition was 1 GPa and temperature from 700 to 950 °C. He carried out also an experimental survey involving a couple of peridotite (peridotite made of 85 vol.% of olivine and 15 vol.% of orthopyroxene and harzburgite with opx = 85 vol.% and ol = vol.15%) with morb basalt (SiO_2 ~ 50%). For such experiments he investigated a range of temperature from 1300 to 1350 °C at 1.5 GPa.

Hammouda and Laporte (2000) proposed a work to reproduce mantle impregnation by carbonatitic melts. For their experiments they used synthetic dunite prepared by sintering of synthetic forsterite crystals in a piston cylinder apparatus at 1 GPa and 1100 °C for five days. Then, infiltration experiment was performed at 1 GPa also and 1300 °C placing the sintered dunite with a forsterite saturated sodium carbonate as carbonatitic reservoir. Na_2CO_3 was used as source of melt because sodium carbonate is analogue with natural carbonatite in physical properties like viscosity and wetting behaviour.

Wark and Watson (2002) studied the chemical gradient of fluid/melt, the formation of channels and their variability by synthetizing monomineralic natural quartz + H_2O at 1 GPa and 800 °C pressure and temperature conditions, ultrapure fluorite + H_2O, calcite + quartz + H_2O (10:40 $CaCO_3$:SiO_2 ratio) at 1 GPa and 850 °C. Olivine + H_2O at 1.2 GPa and 1100 °C and in two experiments involving silicate melt at 1.5 GPa and 1300 °C they mixed a San Carlos olivine with 5 wt. % of morb basalt glass and in the other capsule dacite glass to examine effect of compositional gradient in the melt phase.

Yoshino et al. (2005) and Mu and Faul (2016) retrieved the features of grain boundary wetness (see section 1.4). Yoshino et al. (2005) prepared two different experimental setup performing piston cylinder experiments. 1) San Carlos olivine + different amount of morb glass (from 2 to 40 wt.%) to analyse wetness as a function of melt fraction at experimental conditions of 1 GPa and 1350 °C; 2) spinel lherzolite at P = 1 GPa and T = 1200–1350 °C to obtain different volume

liquid fraction. Instead Mu and Faul (2016) estimated grain boundary wetness of partially molten dunite performing only anhydrous experiments at 1 GPa and range temperature between 1250 and 1450 °C. As starting material, they used a solution–gelation from Fo_{90} olivine powder mixed with basaltic glass. The same Fo_{90} olivine powder mixed with basaltic glass was used by Garapic et al. (2013) for their experiments at 1 GPa and 1350 °C to make a study melt distribution in partially molten mantle rock using high–resolution image analysis.

2.3. A summary of phase relationships in carbonate – bearing model systems

Dalton and Presnall (1998) experimentally investigated the solidus of carbonated bulk compositions in a model Fe–free lherzolite in the system CaO – MgO – Al_2O_3 – SiO_2 – CO_2 (CMAS-CO_2) from 3 to 7 GPa at conditions where liquid coexists with olivine, orthopyroxene, clinopyroxene, garnet and carbonate. At these *P* – *T* conditions they showed two invariant points I_{1A} (2.6 GPa and 1230 °C) and I_{2A} (4.8 GPa and 1320 °C) representing the carbonatation reaction and consequently transition from CO_2–bearing to dolomite–bearing lherzolite and transition from dolomite–bearing to magnesite–bearing lherzolite. The dashed lines represent the position of reaction (Fig. 2.5).

In the pressure range investigated the composition of melts on the solidus are carbonatitic, with CO_2 > 40 wt.% and low SiO_2 (< 6 wt.%). The composition of carbonates in terms of Ca/(Ca+Mg) does not show variation with pressure. In the magnesite stability field (up to 4.8 GPa) the melt composition is mainly dolomitic with a systematic decrease of Ca–content with pressure. In the dolomite stability field (below 4.8 GPa) carbonate tends in calcitic composition with decreasing pressure (Fig. 2.6) suggesting that the composition is not dolomitic but magnesian calcite (Fig. 2.6).

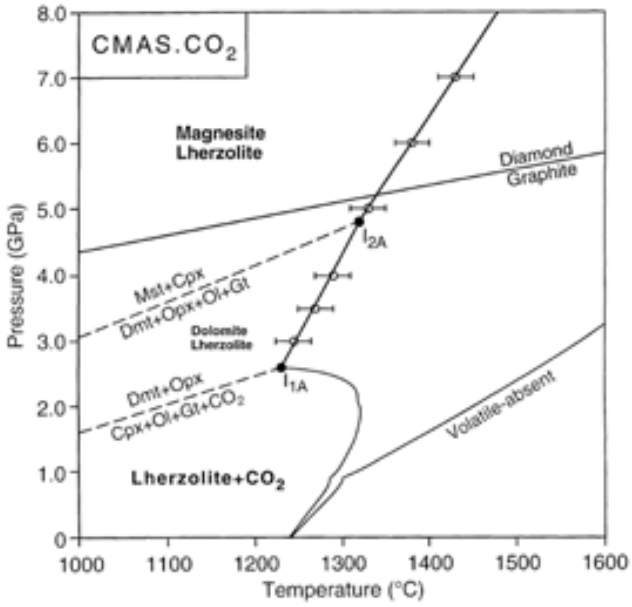

Fig. 2.5. Solidus curve for carbonated lherzolite in CMAS-CO_2 system determinate in Dalton and Presnall (1998) study. Dashed lines represent the position of reactions and their solid solutions. Phase abbreviations: Ol = olivine; Gt = garnet; Cpx = clinopyroxene; Opx = orthopyroxene, Dmt = dolomite; Mst = magnesite.

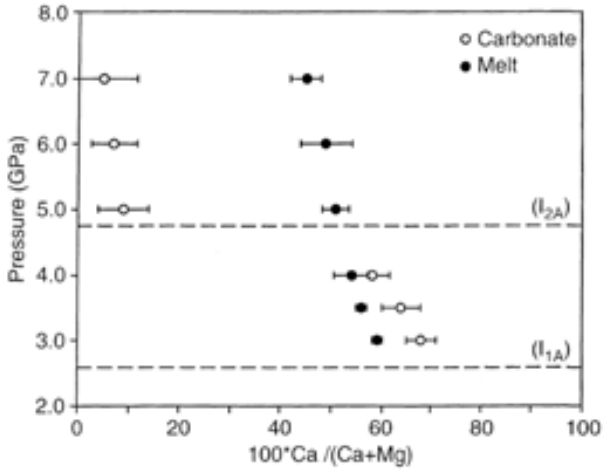

Fig. 2.6. Isothermal plot of pressure with Ca/ (Ca + Mg) ratio of crystalline carbonate and carbonate melt. Dashed lines represent the invariant point on the same CMAS-CO_2 system (Dalton and Presnall, 1998).

The complexities of the binary join $CaCO_3$–$MgCO_3$ and solid solutions therein at high pressure conditions were studied by Irving and Wyllie (1975) at 2.7 GPa, by Byrnes and Wyllie (1981) at 1 GPa and by Buob et al. (2006) at 6 GPa.

Between 1 to 2.7 GPa the decarbonation reaction involving periclase is replaced by congruent melting of magnesite. On the Ca–rich side it is possible to see the appearance of aragonite stability field at at high pressure (Fig. 2.7). The minimum in the liquidus surface indicates that the first fractions of carbonatitic melt have a Ca# [Ca/ (Ca + Mg)] moving from 0.7 to 0.5 with increasing pressure. A comparison of solidus temperatures and composition of minimum melts in the binary $CaCO_3$–$MgCO_3$ with more complex systems such as CMS.CO_2 (CaO – MgO – SiO_2 – CO_2, Canil and Scarfe, 1990), CMAS.CO_2 (Dalton and Presnall, 1998), and Na–poor carbonated eclogite (Yaxley and Brey, 2004), show similarities in phase relations on the solidus, and similar temperatures and melt composition (Fig. 2.8, Buob et al., 2006).

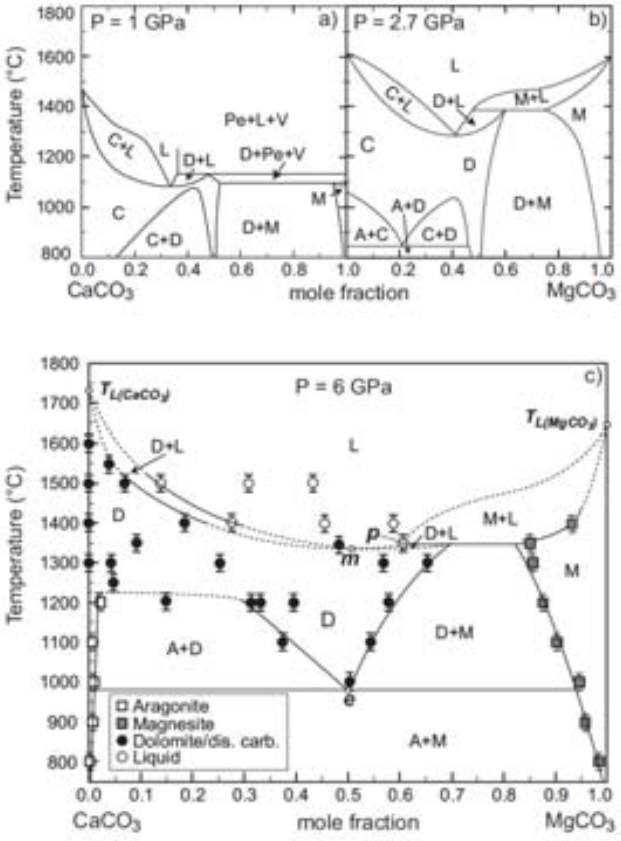

Fig. 2.7. $CaCO_3$ – $MgCO_3$ binary phase diagram at 1 GPa (a), 2.7 GPa (b) and at 6 GPa (c) (modified by Buob et al., 2006). Abbreviations: C = calcite; D = dolomite; M = magnesite; A = aragonite, Pe = periclase; L = liquid; V = vapor.

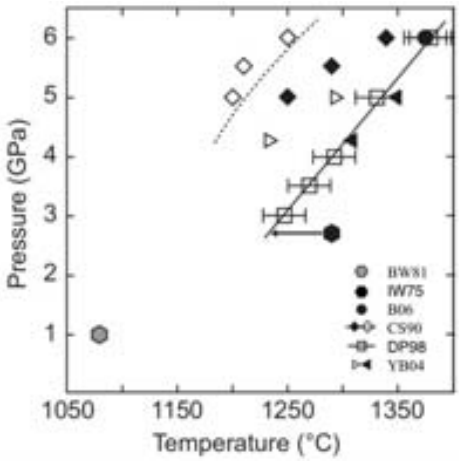

Fig. 2.8. Minimum melting temperature as a function of pressure.
Data from: BW81 = Byrnes and Wyllie, 1981; IW75 = Irving and Wyllie, 1975; B06 = Buob et al., 2006; CS90 = Canil and Scarfe, 1990; DP98 = Dalton and Presnall, 1998; YB04 = Yaxley and Brei, 2004.

Experiments performed by Tumiati et al. (2013) investigate a phlogopite- and C-O-H – bearing lherzolite at 900–1050 °C and 1.6 – 3.2 GPa, at fluid- and carbon- saturated conditions. Phase diagram from this study shows that at all $P - T$ conditions olivine, orthopyroxene and phlogopite are present, while garnet and spinel are present at pressure up to 2 GPa and < 2 GPa respectively. At pressure of 1.8 GPa and 1050 °C no carbonates are stable and carbon is present in the form of CO_2 in the fluid or as graphite. At pressures below 1.8–2.0 GPa there is the subsolidus dolomite stability field. Dolomite occurs with olivine, orthopyroxene, phlogopite and amphibole. From 1.8 GPa and 2.6 GPa the phase diagram is characterized by the occurrence of magnesite + dolomite, i.e. a two carbonates field. At higher pressure the only stable carbonate is magnesite coexisting with olivine, orthopyroxene, clinopyroxene, amphibole, phlogopite and garnet. Above amphibole out curve the only hydrous phase is phlogopite coexisting with magnesite, olivine, orthopyroxene, clinopyroxene and garnet until 2.6 GPa and 1040 °C pressure and temperature

conditions where the amphibole–out intersects solidus carbonate–silicate melt curve. Indeed melt is stable at temperatures above ≥ 1050 °C (Fig. 2.9).

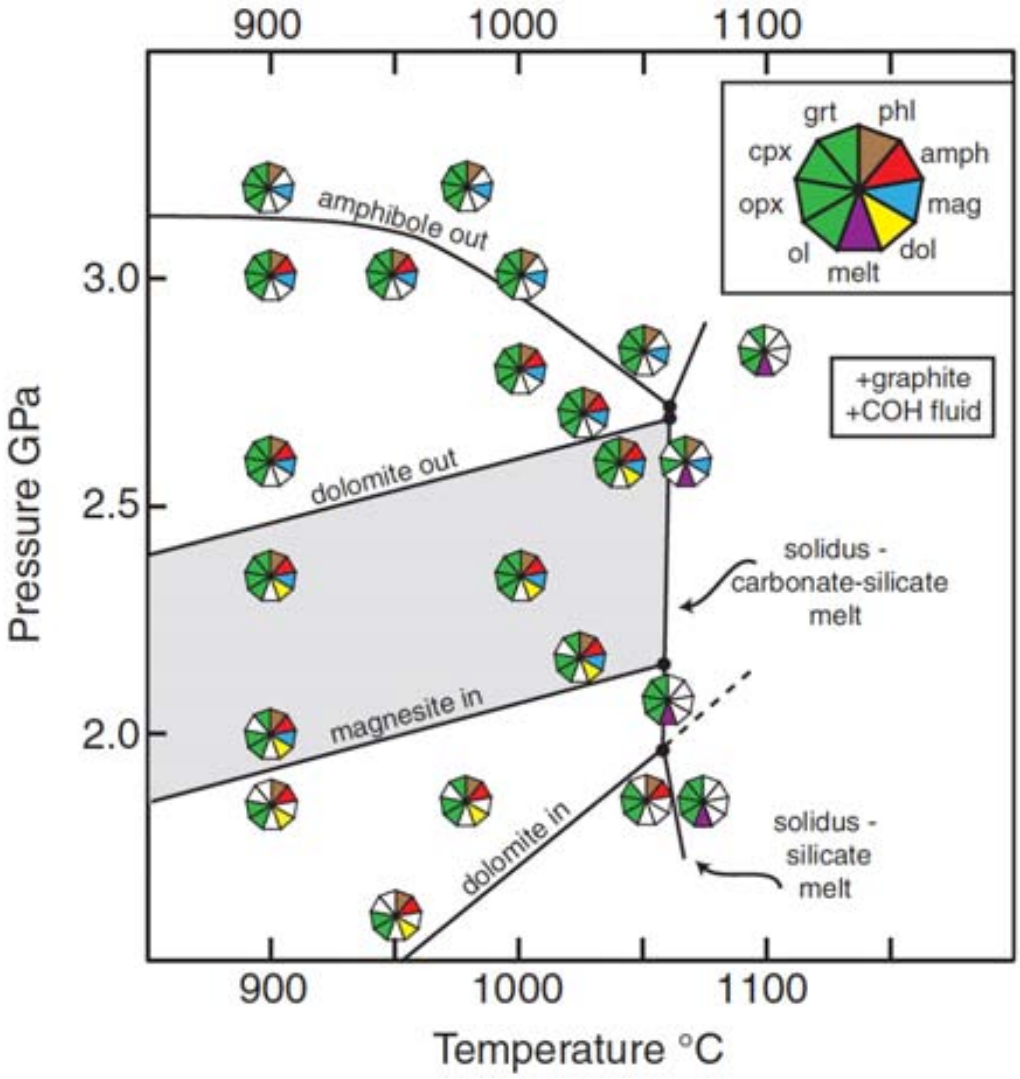

Fig. 2.9. Phase assemblage in K- doped lherzolite at COH- fluid – saturated conditions as a function of *P* and *T* (from Tumiati et al., 2013). Abbreviations: ol = olivine; opx = orthopyroxene; cpx = clinopyroxene; grt = garnet; phl = phlogopite; amph = amphibole; mag = magnesite; dol = dolomite.

Chapter 3

Experimental and Analytical procedures

In this section I present an overview of the experimental and analytical procedures to infiltrate hydrous carbonatitic melts in a model mantle dunite at high – pressure and high – temperature conditions, along with with a procedure to sinter dunite.
The description of the experimental and analytical facilities will also be provided.

3.1. Experimental procedures

3.1.1. Starting materials and geometries

For this experimental study we chose a synthetic dunite as a model mantle representative. The starting material was prepared from single crystals of natural San Carlos forsteritic olivine with Fo_{90} (San Carlos, Arizona; Fig. 3.1) for purity, clarity and lack of inclusions. These olivine crystals were crushed and sieved by use of boron carbide (B_4C) and agatha mortars to pass 64 μm and to keep 38 μm mesh sieves (Fig. 3.1).

SiO_2	FeO	MgO	CaO	P_2O_5	MnO	NiO	Total
40.81	9.55	49.42	<0.05	0	0.14	0.37	100.29

Fig. 3.1. San Carlos olivine single crystal and first crushing with B_4C mortar and final powder resulting in agatha mortar. Composition of San Carlos olivine from Jarosewich et al. (1980).

The choice of the melt sources depends on the required $P - T$ conditions, and on the occurrence of olivine as the solid buffering the liquidus surface.

Natural carbonatitic liquids in equilibrium with a mantle assemblages are mainly dolomitic. For this reason, according to phase diagram constraints of Tumiati et al. (2013) (see section 2.2, Fig. 2.9), a pressure and temperature of 2.5 GPa and 1200 °C is expected to stabilize a dolomitic hydrous liquid in equilibrium with a peridotitic mantle source. The choice of the starting liquids was performed by a mass balance of the dolomitic liquid stable with an olivine matrix used by Tumiati et al. (2013) (Table. 3.1).

	Carbonate-silicate melt		
Run:	ST15		
P (GPa):	2·60		
T (°C):	1060		
	mean value (821)	quench phase 1	quench phase 2
oxides (wt %)			
SiO_2	11·50	37·89	1·12
Al_2O_3	4·28	13·73	0·40
FeO	2·96	4·49	2·92
MgO	15·31	20·18	20·30
CaO	21·57	1·38	39·59
Na_2O	1·04	2·40	0·26
K_2O	1·16	4·74	0·12
Total	57·83	84·81	64·71

Table. 3.1. Melt composition of the carbonate – silicate melt determined for run ST15 at 2.6 GPa and 1060 °C pressure and temperature conditions from Tumiati et al. (2013).

We used several different mixtures of starting materials to obtain a dolomitic liquid composition and to avoid the problem of Fe – loss and periclase globules formation that are discussed in more detail below. The first mixture used (Mix.1) was obtained by mass balance calculation adopting reagent grade $CaCO_3$ as starting calcium carbonate, dolomite [Ca, $Mg(CO_3)_2$] from Bazena, Ivigtut siderite [$FeCO_3$], adding brucite [$Mg(OH)_2$] as a H_2O source. In the mass balance calculations, we obtained calcite = 34.77 wt.%, Bazena dolomite = 22.52 wt.%, Ivigtut siderite =

6.61 wt.% and brucite = 36.12 wt.% phases abundance. Re-ReO_2 buffer and graphite powder were added to buffer the redox conditions at relatively oxidizing conditions, therefore to prevent the formation of periclase (Table. 3.2).

The second mixture (Mix.2) was obtained by mass balance calculation considering as starting carbonates calcite, Pinerolo magnesite ($MgCO_3$) and Ivigtut siderite. The mass balance calculation shows as phases abundance $CaCO_3$ = 54.16 wt.%, $MgCO_3$ = 38.94 wt.% and $FeCO_3$ = 6.92 wt.% obtaining a dolomitic composition as shows in carbonate triangular diagram in Fig. 3.2.

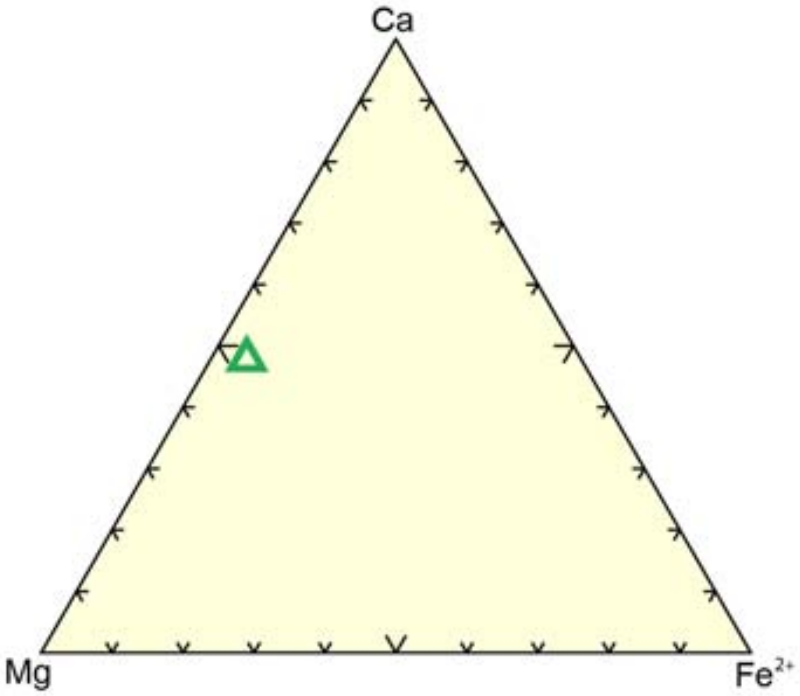

Fig. 3.2. Triangular Ca-, Mg-, Fe- carbonate diagram. Green triangle represents the dolomitic composition of phase proportions for starting material.

As hydrous source with Mix 2, we used free water added with μL–graduate syringe, or brucite + graphite powder, or brucite + quartz powder (1:1molar) + graphite powder to balance magnesium excess due to simultaneous presence of $MgCO_3$ and $Mg(OH)_2$ (Table. 3.2).

	Starting Materials	Phases abundance (wt. %)
Mix 1	$CaCO_3 + CaMg(CO_3)_2 + FeCO_3 + Mg(OH)_2$ $CaCO_3 + CaMg(CO_3)_2 + FeCO_3 + Mg(OH)_2 + Re - ReO_2$ $CaCO_3 + CaMg(CO_3)_2 + FeCO_3 + Mg(OH)_2 + Re - ReO_2 + Graphite_{powder}$	$CaCO_3 = 34.77$ $CaMg(CO_3)_2 = 22.52$ $FeCO_3 = 6.61$ $Mg(OH)_2 = 36.12$
Mix 2	$CaCO_3 + MgCO_3 + FeCO_3 + Water$ $CaCO_3 + MgCO_3 + FeCO_3 + Mg(OH)_2 + Graphite_{powder}$ $CaCO_3 + MgCO_3 + FeCO_3 + Mg(OH)_2 + SiO_2 + Graphite_{powder}$	$CaCO_3 = 54.16$ $MgCO_3 = 38.94$ $FeCO_3 = 6.92$ + $Water = 5\ \%\ or\ 30\ \%$ of carbonate mix powder $Mg(OH)_2 = 13.93$ of carbonate mix powder

Table. 3.2. Composition of the starting materials and relative abundances of phases (wt.%). Percentage of brucite was calculated to obtain 5% of water content considering the brucite composition of MgO = 69.11 % and H_2O = 30.89%.

The composition of C–saturated C-O-H melts and the oxidation state of the system are closely related. From a thermodynamic point of view, at oxidation states where graphite or diamond is stable, the speciation of a C – saturated C-O-H fluid is a function of oxygen fugacity (fO_2).

The range of fO_2 is large enough, but it is important to control the oxygen fugacity at conditions relatively oxidized to prevent the appearance of periclase and Fe–loss from starting materials to platinum capsule (Fig. 3.3).

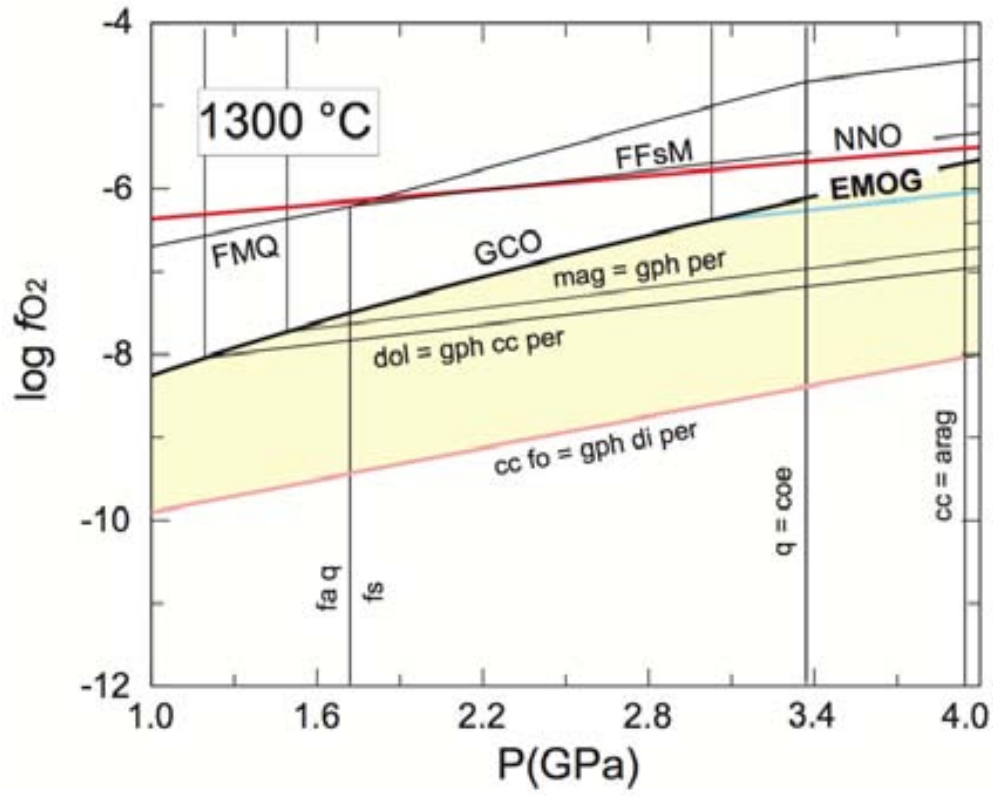

Fig. 3.3. Large fO_2 range graphite related to pressure at 1300 °C (Poli, personal communication).

By means of electron microprobe analysis, a strong iron loss was noted in the olivine (highlighted by iron – zonation of olivine crystals between rim and core) and consequently iron – enrichment on the platinum capsule. Fe–loss is discussed in more detail below. Furthermore, the formation of periclase globules either as a run product or as a quench precipitate due to a magnesium excess and reduction conditions, led us to adopt various capsule materials and different starting materials as mentioned above.

Pt – capsule at high temperature runs absorb considerable amounts of iron from sample and increasing temperature increase the amount of Fe – lost to the Pt – capsule (Johannes and Bode, 1978). In fact, considering the binary alloys formed by platinum and iron exists a complete range of γ-Fe, Pt solid solutions at high temperatures (Fredriksson and Sundman, 2001; Fig. 3.4).

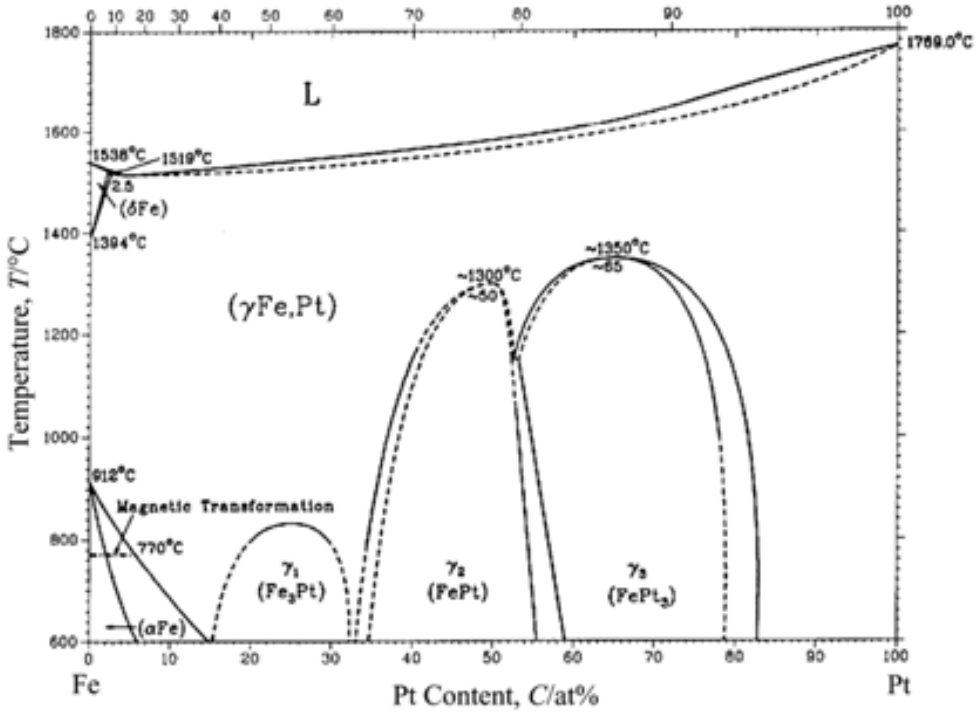

Fig. 3.4. Thermal equilibrium phase diagram of Fe – Pt alloy system that shows γ-Fe, Pt solid solution at high temperature (Wang et al., 2004 after Fredriksson and Sundman, 2001).

The iron – loss problem can be eliminated or reduced by choosing the appropriate capsule material. We decided to adopt a graphite sleeve inside the platinum capsule in order to control oxygen fugacity and contemporarily to have protection between starting material and platinum capsule to avoid Fe – loss (Fig. 3.5). The geometry used is summarized in Fig. 3.5a and Fig. 3.5b.

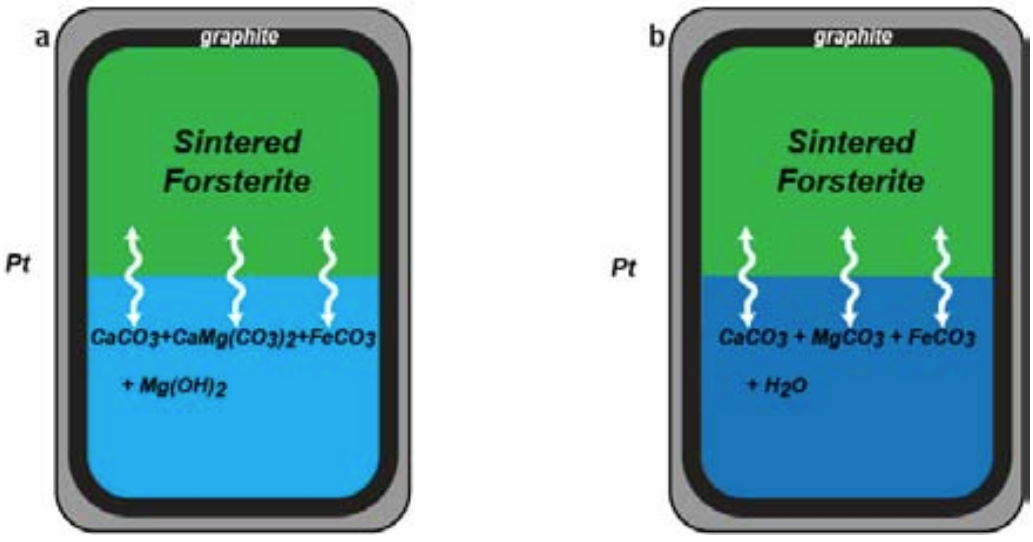

Fig. 3.5. Capsule geometries with platinum and graphite thick with Mix 1 ($CaCO_3$, $Ca,Mg(CO_3)_2$, $FeCO_3$ and $Mg(OH)_2$) (a) and Mix 2 ($CaCO_3$, $MgCO_3$, $FeCO_3$ and H_2O) (b).

Two experiments were performed using Gold – Palladium alloy capsule ($Au_{60}Pd_{40}$) without graphite sleeve (Fig. 3.6) as a sample container able to inhibit Fe – loss (Jakobsson, 2012).

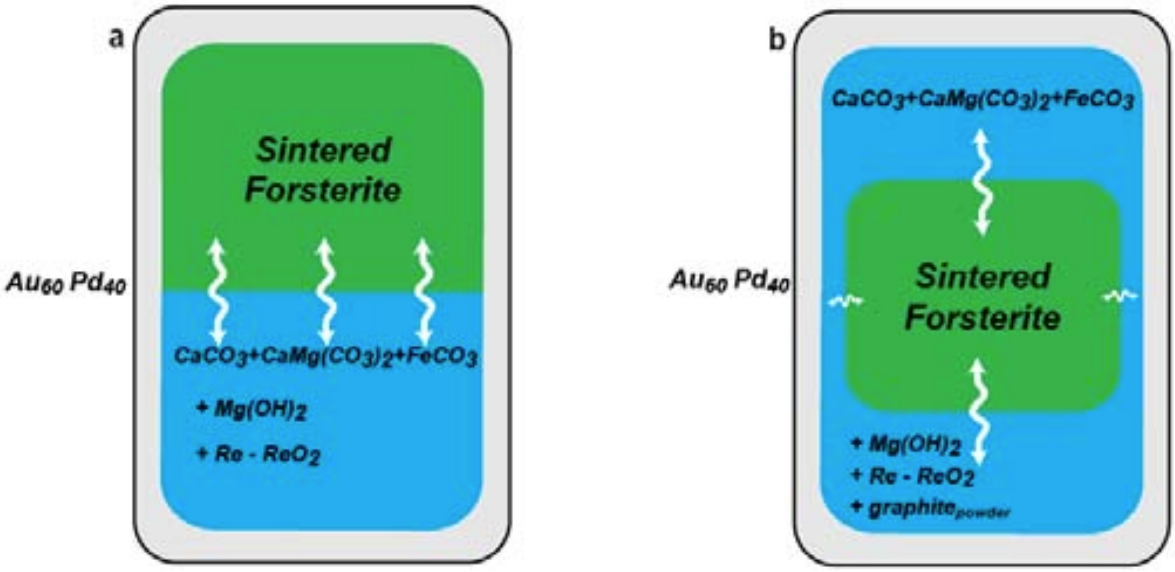

Fig. 3.6. Capsule geometries without graphite thick. (a) $Au_{60}Pd_{40}$ capsule with Mix 1 and brucite and Re-ReO_2 buffer; (b) $Au_{60}Pd_{40}$ capsule with sintered forsterite surrounded by Mix 1 and brucite, Re-ReO_2 buffer and graphite powder.

As the techniques mentioned above did not offer a solution to loss of iron, pre – conditioned platinum capsules (Fig. 3.9) were prepared.

Fig. 3.7. Gas Mixing furnace used for capsule preconditioning (Laboratory of Experimental Petrology of the University of Milan (Italy)).

The platinum capsules were conditioned placing them in an iridium crucible with a powder mixture made of granite doped with 15 wt.% of Fe_2O_3 powder. The preconditioning experiment was performed by means of a gas mixing furnace at 1350 °C (Fig. 3.7) for 24 hours at this controlled oxygen fugacity conditions:

$$\log fO_2 \qquad FMQ = -6.789$$

After preconditioning experiment, the resulting granitic glass (Fig. 3.8) was dissolved by means of $HF+HClO_4$ (7ml and 2 ml respectively) mixture at 250 °C.

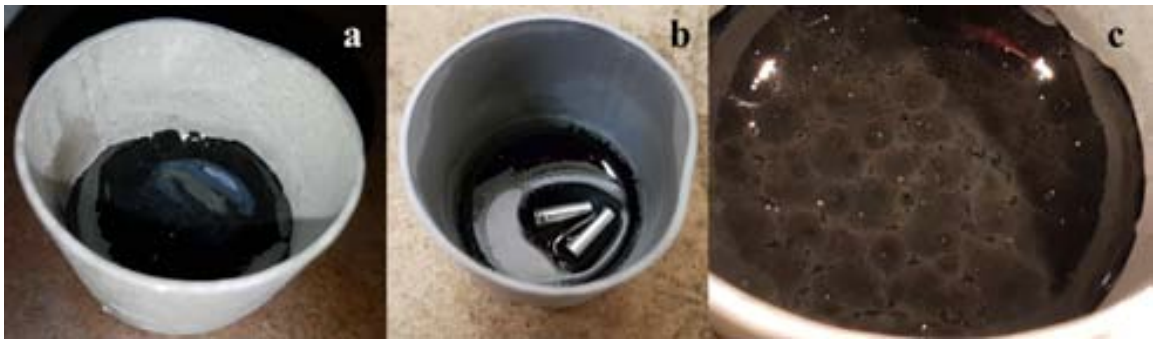

Fig. 3.8. Fe_2O_3 doped granitic glass resulting after gas mixing preconditioning inside iridium crucible. (c) Photo by stereoscope device.

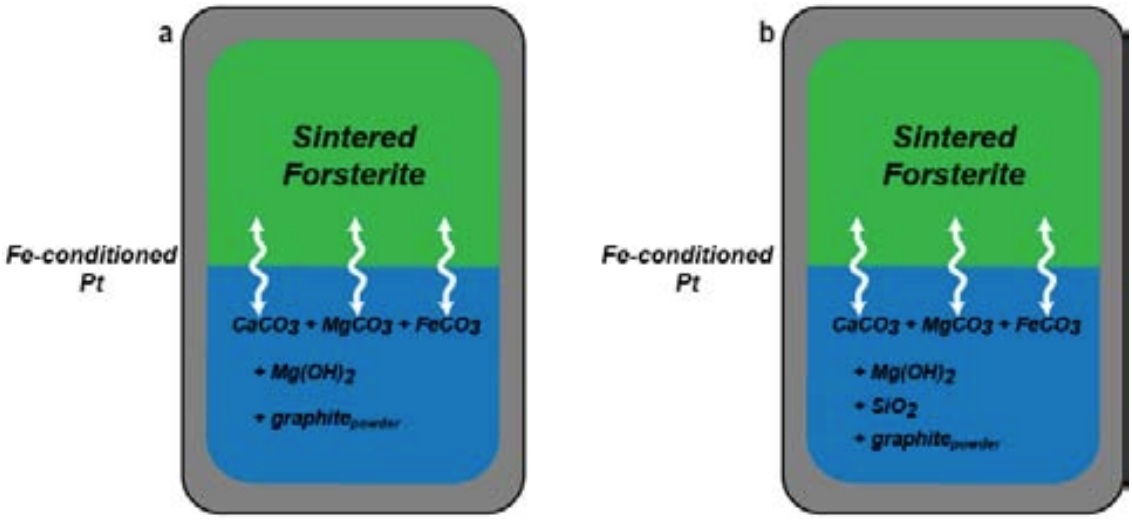

Fig. 3.9. (a) Fe-conditioned Pt capsule with Mix 2 with brucite and graphite powder; (b) Fe-conditioned Pt capsule with Mix 2 and brucite, SiO_2 and graphite powder.

Moreover, in order to account for the different roles of gravity and chemical and thermal diffusion, we used two different and opposite capsule geometries. First, placing the dunite rod at

the top of the capsule above the carbonate mix (Figs. 3.5a and b and 3.6a), then reversing the stack to have the carbonatitic reservoir at the top of the capsule, in experiments with platinum capsule and graphite cylindrical thick only (Fig. 3.10).

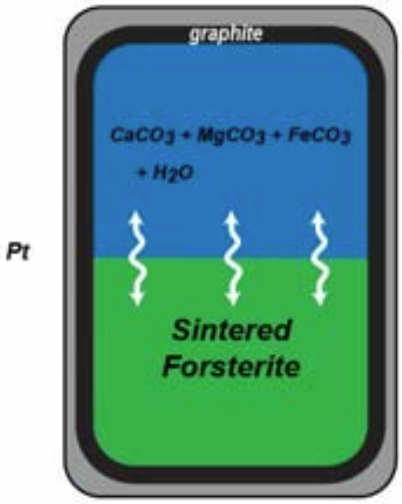

Fig. 3.10. Opposite capsule geometry with dunite rod below carbonatitic reservoir.

3.1.2. Experimental apparatus

a) Single stage piston – cylinder apparatus

In this study a Single stage piston – cylinder apparatus at the Laboratory of Experimental Petrology of the University of Milan (Italy) (Fig. 3.11) was employed to reach sintering of natural San Carlos forsterite (see section 3.1.1, Fig. 3.1). The single stage piston – cylinder used in these sintering has 100-ton press provided with 290 mm diameter oil – pressure ram that is used to transmit force to the smaller piston and it has a diameter of 22 mm. The assembly has 43 mm of length (Fig. 3.12) and it is contained in the bomb, which contains a tungsten carbide core supported by concentric rims of steel. Temperature is generated by a cylindrical furnace. The assembly is in contact with the upper piston by means of the top plug and electrically isolated by steel and pyrophyllite plug. Pressure calibration of this piston cylinder is based on the albite breakdown reaction (albite = jadeite + quartz; e.g. Johannes et al., 1971; Holland, 1980) and it is valid also when pyrex sleeve is coupled to NaCl sleeve. Pressure is controlled by an automated hydraulic system where the load is measured directly by a load cell.

Fig. 3.11. Single stage piston – cylinder apparatus at the Laboratory of Experimental Petrology of the University of Milan (Italy).

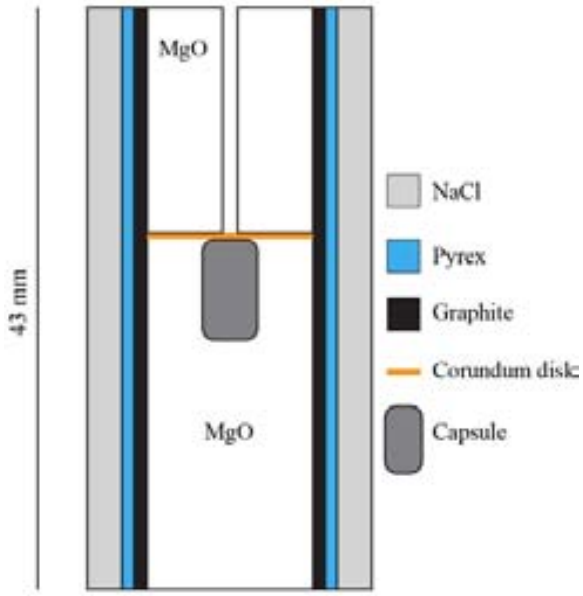

Fig. 3.12. NaCl-pyrex-graphite-MgO assembly configuration used for single stage piston – cylinder sintering runs.

b) End load and Rocking end load piston – cylinder apparatuses

In this research an end-load and an end-load rocking piston – cylinder apparatuses at the Laboratory of Experimental Petrology of the University of Milan (Italy) were employed to reach high – pressure and high temperature conditions in infiltrations experiments. The end-load press consists of an internally heated tungsten carbide pressure vessel supported by a steel ring.

Fig. 3.13. End – Load piston cylinder apparatus at the Laboratory of Experimental Petrology of the University of Milan (Italy).

The piston cylinder used for infiltration experiments has 1000-ton uniaxial press with 14 mm bore (Fig. 3.13; Boyd and England, 1960). The "bomb" is a steel matrix containing a tungsten-carbide core. The hole in its centre holds the pressure assembly. The end-load ram and the so-called bridge (upper part), under which the piston ram is hidden. The latter generates the pressure on the sample (Fig. 3.14).

Fig. 3.14. Mechanical scheme of end – load piston cylinder apparatus on the left; parts of end – load piston cylinder with bomb and bridge on the right (Image from http://users.unimi.it/spoli/).

The assembly has 34 mm of length and it is the same of single stage assembly except for the size (Fig. 3.15).

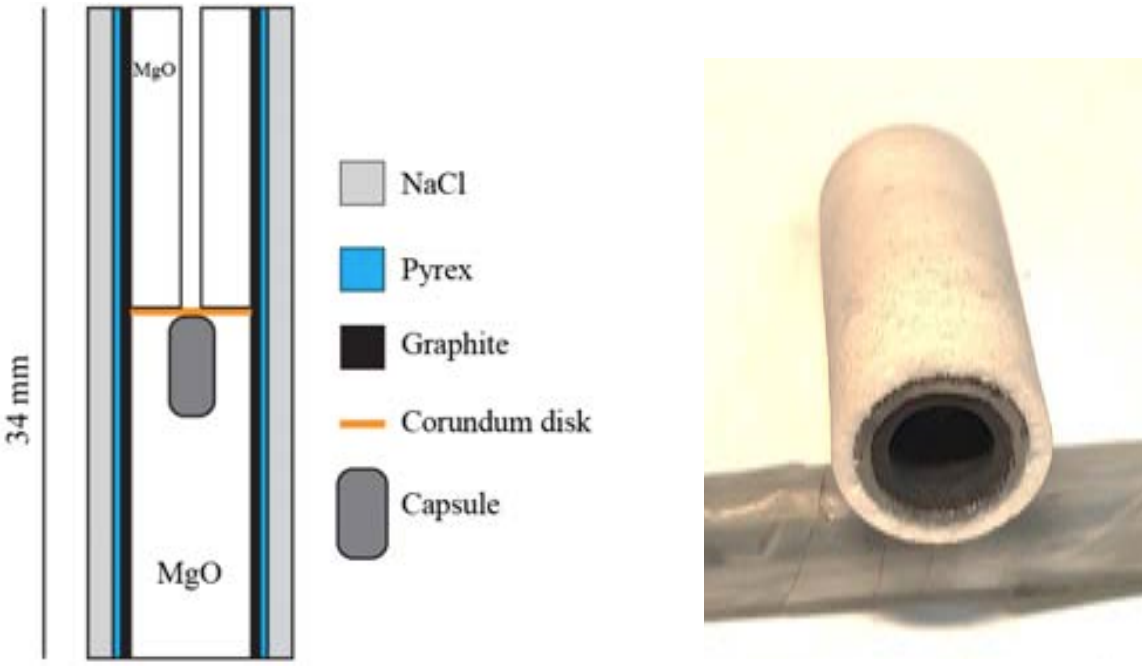

Fig. 3.15. NaCl-pyrex-graphite-MgO assembly configuration used for end load piston – cylinder infiltration runs. On the right NaCl-pyrex-graphite configuration.

The rocking piston – cylinder apparatus (Fig. 3.16) is an end – load piston cylinder which completes a rotation of 180° during runs thus inverting its position in the gravity field (Schmidt and Ulmer, 2004). It has 600-ton uniaxial press. The rocking piston – cylinder was developed to overcome the problem of inhomogeneity in mineral assemblage in fluid saturated experiments

(Stalder and Ulmer, 2001; Melekhova et al., 2007). The 180° rotation induce Rayleigh – Taylor instabilities forcing the fluid to migrate and causing rehomogenisation. Because it is a still end – load piston cylinder with same size parts of 1000-ton end – load piston cylinder apparatus, we use the same assembly dimensions and the same procedures. Pressure calibration of the end – load and rocking end – load piston cylinder apparatuses is based on the quartz to coesite transition at $P = 3.72$ and $T = 1000$ °C (Bose and Ganguly, 1995).

Fig. 3.16. End – Load rocking piston cylinder apparatus at the Laboratory of Experimental Petrology of the University of Milan (Italy). Orange part completes a rotation of 180 ° during runs.

3.1.3. Sintering of olivine pellets

Sintering experiments were conducted in a single different type of capsule geometry. Single molybdenum (Mo) capsule loaded with San Carlos Olivine powder (see section 3.1.1, Fig. 3.1) in an inner graphite capsule (Fig. 3.17).

Fig. 3.17. Molybdenum capsule geometry used for sintering experiments in a single stage piston – cylinder apparatus.

Sintering experiments were carried out in a single stage piston-cylinder apparatus as mentioned above, at pressure of 0.8 GPa and temperature of 1200 °C. We choose as assembly MgO rods drilled to accommodate the capsule and MgO rods drilled to accommodate the thermocouple. A corundum disk was placed at the top of the capsule to preserve and to avoid the contact with thermocouple. The furnace was a graphite heater surrounded by Pyrex glass and NaCl sleeve (Fig. 3.12). At the top of the entire assembly we used a pyrophyllite plug to ensure the electrical contact. Experiments were first heated to T= 400 °C with temperature rate of 50 °C/minute and then pressurized to the final pressure value of 0.8 GPa and finally heated to the final experimental temperature of 1200°C with temperature increase rate of 100 °C/minute. Temperature was measured with S-type thermocouple (Pt-$Pt_{90}Rh_{10}$).

These sintering experiments were performed for a variable run time from 30 hours to 5 days and were quenched by turning off the power.

After the experiments the Mo capsules were cut by means diamond saw to obtain dunite cylindrical rods to be used for infiltration experiments (Fig. 3.18).

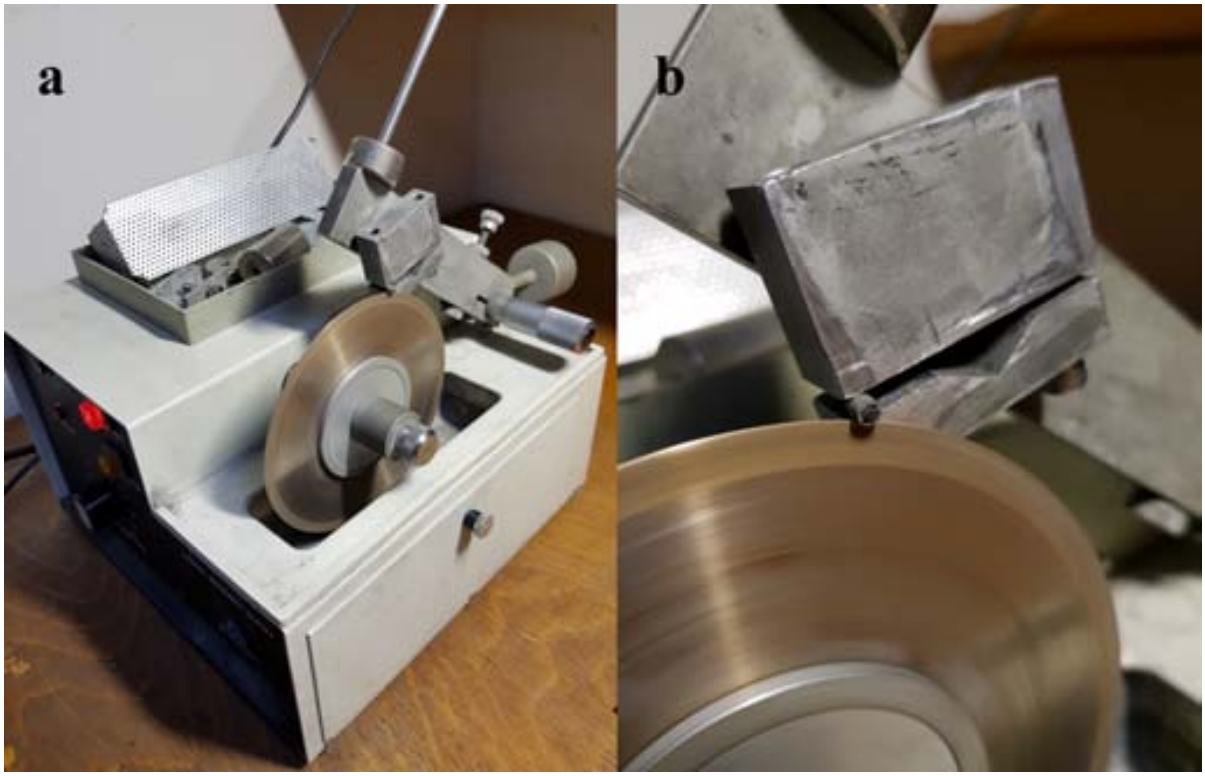

Fig. 3.18. Cutting of Mo capsule by means diamond saw (a); detail during cutting capsule (b).

3.1.4. Infiltration experiments

Infiltration experiments were performed in an end-loaded piston cylinder apparatus and in a rocking end-loaded piston cylinder apparatus at pressure of 2.5 GPa and temperature of 1200 °C except one experiment at 1100 °C (namely LSI_5). We carried out 19 time-resolved experiments with run times from 3 to 300 hours choosing an assembly made of MgO rods drilled for the capsule and at the top another MgO rods drilled to accommodate the thermocouple. Between these two MgO rods we placed a corundum disk to avoid the contact with thermocouple. Like the sintering experiments the MgO assembly was placed inside a graphite heater as furnace and surrounded by pyrex glass and NaCl sleeve (see section 3.1.2b; Fig. 3.15). The entire assembly was closed inside the "bomb". At the top of the assembly we used a pyrophyllite plug also to ensure the electrical contact with the graphite disk at the bottom of the entire assembly and the mylar disk at the top of the bomb.

Samples were first pressurized at P = 0.20 GPa and heated at T= 400 °C. Temperature rate was 50 °C/minute from ambient temperature to a target of 400 °C. Then samples were pressurized from 0.20 GPa of pressure to the final experimental pressure of 2.5 GPa in 20 minute and heated

from 400 °C until the final temperature value of 1200 °C with 100 °C/minute. Experiments were quenched by turning off the power and the quench rate was approximately 30 °C/second.
After experimental runs the capsules were extract from assemblies (Fig. 3.19a) and embedded in epoxy resin (Fig. 3.19b) and polished by means of sandpaper (320, 600, 1200, 2400 and 4000 μm size) and diamond paste (Fig. 3.19c) controlling the polish status by means of microscope and stereoscope device (Fig. 3.20) in order to perform EDS, WDS electron microprobe analysis, X-ray maps of elements and EBSD analysis.

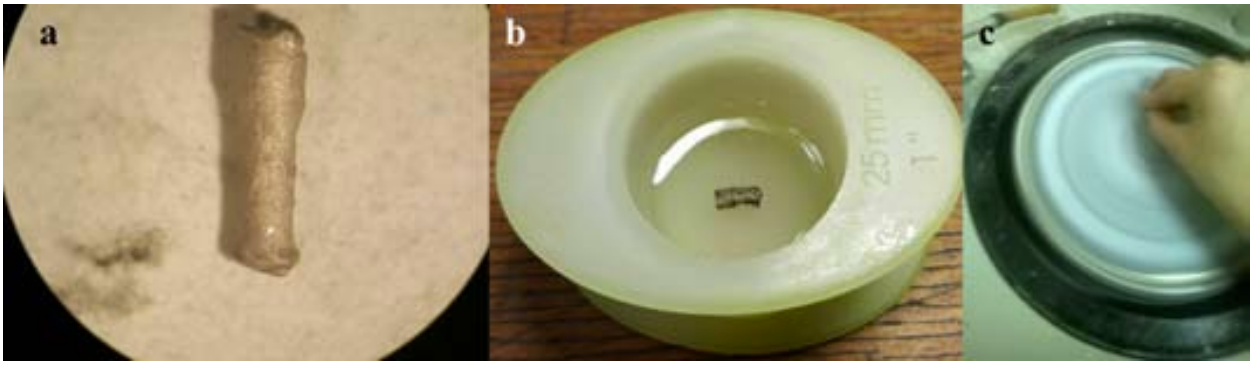

Fig. 3.19. Example of capsule after run experiment viewed by stereoscope device (a); capsule embedded in epoxy resin (b); polishing procedure by means of diamond paper (c).

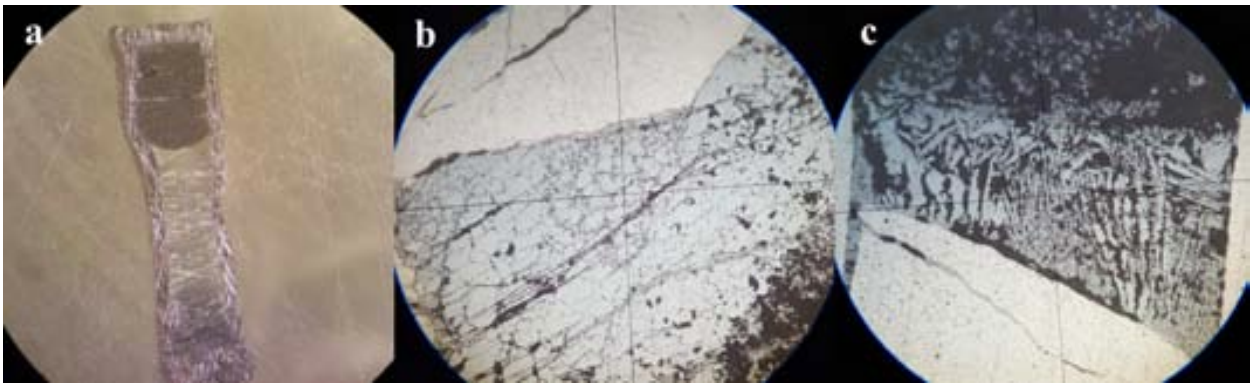

Fig. 3.20. Pt capsule without graphite thick with dunite rod at the top above carbonatitic melt after polishing procedure viewed by stereoscope device (a); dunite rod (b) and carbonatitic melt with typical dendritic texture (c) viewed by microscope after polishing procedure.

3.2. Analytical procedures

3.2.1. Electron Microprobe Analyzer (EMPA)

The Electron Microprobe Analyzer (EMPA) allows us to characterize chemically the run products and to obtain information of texturally features.

The EMPA analysis were performed at the Department of Earth Sciences, University of Milan. The electron microprobe instrument installed at our department is a Jeol JXA – 8200 Superprobe equipped with five WDS-wavelength-dispersive spectrometers, EDS and cathodoluminescence detector. The radius of Rowland circle is 140 mm for spectrometers 1, 2 and 3, bearing LDE1, LDE2, LDEB, TAP, PET and LiF crystals and 100 mm for spectrometers 4 and 5, bearing PETH and LIFH crystals. Natural and synthetic minerals were used as standards calibrated within 0.5 % at one standard deviation.

To characterize the mineral chemistry of our experiments with olivine, pyroxenes and carbonates I worked at 15 kV, 5 nA and beam size of 1 micron for individual grains, and 20 microns to estimate the bulk composition of carbonatite "melts", i.e. aggregates of quench precipitates. Elements and corresponding standards adopted for our experiments with olivines, pyroxenes and carbonates follow. Sodium: omphacite USNM110607 and albite; magnesium: olivine USNM2566; aluminium: anorthite USNM137041; calcium and silicon: wollastonite; chlorine: scapolite PSU62-1703; potassium: K-feldspar PSU-Or1A; titanium: ilmenite USNM96189; chromium: chromite USNM117075 and rodonite.

Furthermore, P10 gas-flow X-ray detectors were used for light elements on LDE and TAP-bearing spectrometers, and Xe-CO_2 sealed X-ray detectors on PET and LiF-bearing spectrometers to have high resolution X-Ray maps of elements operating at 15 kV of voltage, 5 nA, 7 msec of dwell time and 0.3 microns of step size.

3.2.2. Electron Back Scattered Diffraction (EBSD)

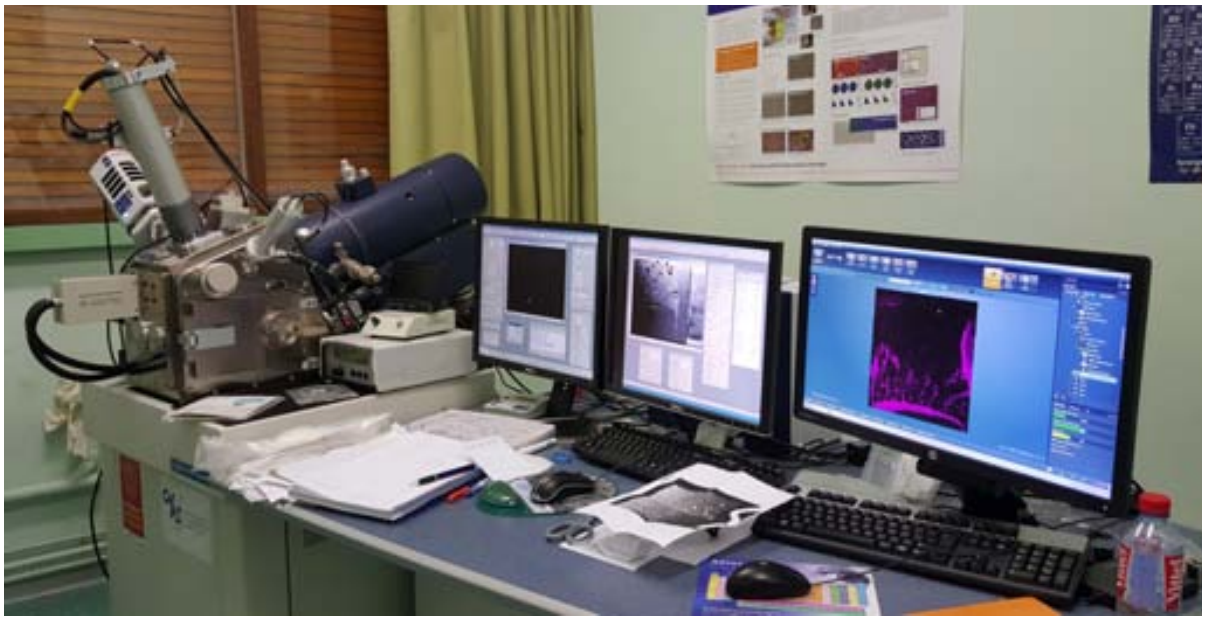

Fig. 3.21. Electron Back Scattered Diffraction (EBSD) at Géosciences Montpellier, University of Montpellier.

The EBSD analysis has been used to retrieve the misorientation of olivine grains, therefore to reconstruct grain boundaries. EBSD output images have been also used to estimate the size of olivine crystals and of quenched carbonate products. The EBSD analysis was performed at Géosciences Montpellier, University of Montpellier. The EBSD instrument installed at Géosciences Montpellier is a CamScan X500FE CrystalProbe (Fig. 3.21). Electron Backscatter Diffraction is a scanning electron microscope (SEM) based technique, which enables sample microstructure to be analysed, visualised and quantified. The data collected with EBSD is spatially distributed and is visualised in maps and images. EBSD is carried out on a specimen which is tilted between 60° and 70° from the horizontal, the optimum position for examining the microstructure using backscattered electrons. The area from which an EBSD pattern is acquired is approximately elliptical, with the major axis, which is perpendicular to the tilt axis, being some three times that of the minor axis (Humphreys, 1999). Electron beam working on 15 – 25 kV and 0.01 to 50 nA, from 8 to 45 mm working distance that determines spatial resolution and maximum specimen area, from 10 to 40 mm specimen to screen distance that determines solid angle.

We have been working at 15 kV with specimen tilted at 70° and speed of acquisition of ~ 940000.00 Hz and pixels size of 2.7 ~ μm. An example of EBSD image is given in Fig. 3.23, here used to discriminate olivine and carbonates grain – grain and liquid – grains boundaries. In

fact, in a crystal orientation map points with similar crystal orientations are shown in similar colours (Figs. 3.22 and 3.23).

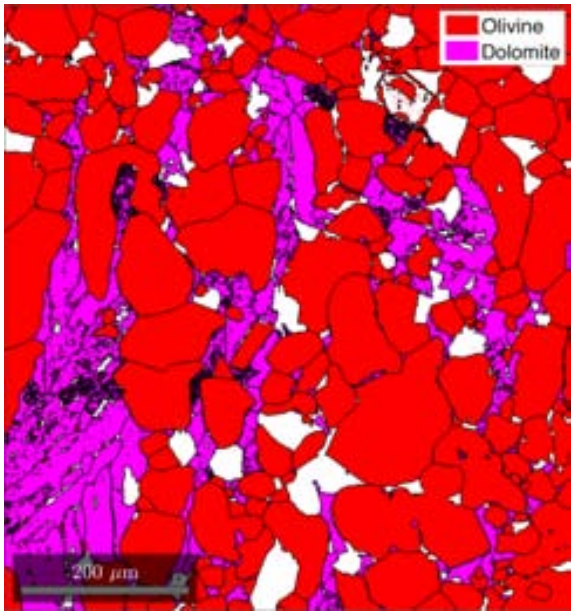

Fig. 3.22. Example of EBSD output image representative of olivine grain – grain and olivine – dolomite grain boundaries. Red colour represents olivine crystals and violet colour represents dolomite quenched melts.

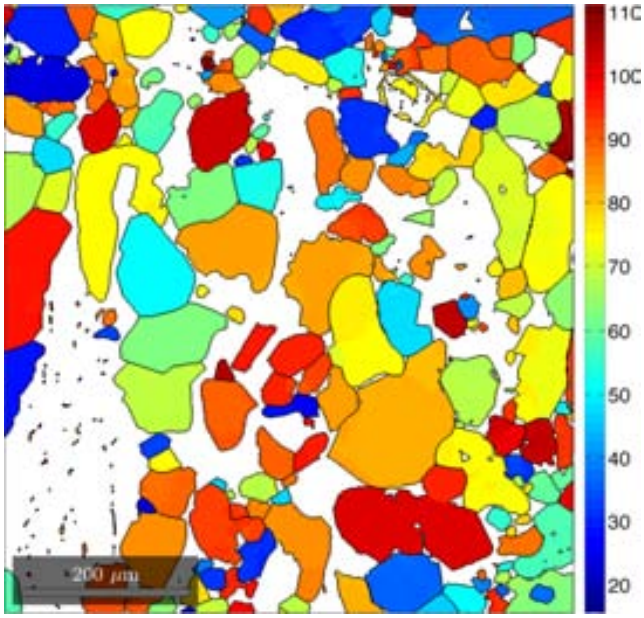

Fig. 3.23. Example of EBSD output image representative of olivine grain boundaries. Different and similar colours represent different or similar crystal orientations.

In these maps a grain is a region of the sample where the crystal orientation is the same within a certain orientation angle tolerance (for olivine segmentation angle is usually 10 degrees). Output EBSD data were cleaned by a software named "TANGO" and then processed by MTEX 4.1, a Matlab® toolbox (Bachmann et al., 2010) modified by David Mainprice and Benoit Ildefonse of Géosciences Montpellier, University of Montpellier.

3.2.3. Capsule-piercing device coupled with quadrupole mass spectrometry (QMS)

The volatile content in the experiment LSI_19 has been measured at the Laboratory of Experimental Petrology of the University of Milan using the capsule-piercing technique (Tiraboschi et al., 2016; Tumiati et al., 2017).

The device (Fig. 3.24) consists of a Teflon reactor where the capsule is punctured and the evolved gases are collected in a heated gas manifold system and transported to the QMS. Different mass/charge channels are monitored to retrieve the molar amount of the volatile species H_2O, CO_2, CH_4, CO, H_2, O_2 and N_2. The line and reactor preconditioning are

accomplished by performing vacuum/venting cycles, using ultrapure Ar as inert gas carrier. The volatile release occurs when the bottom part of the reactor is screwed upwards and the mill eventually pierces the capsule (Fig. 3.25).

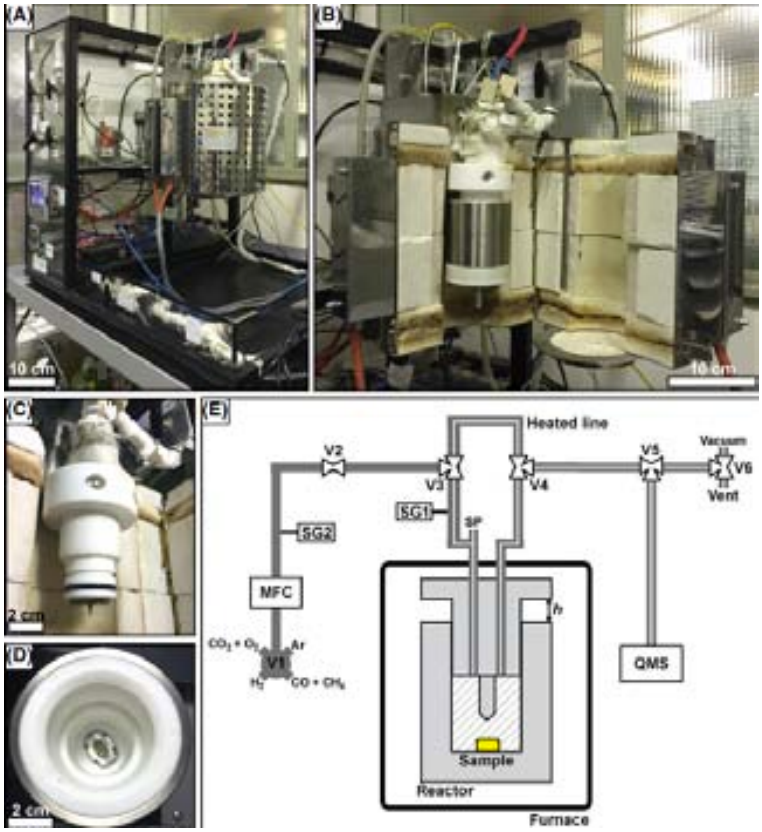

Fig. 3.24. Capsule-piercing device at Experimental Petrology Laboratory, University of Milan (Tiraboschi et al. (2016). (A) overview of the device; (B) reactor in the furnace; (C) steel mill mounted on the upper part of the reactor; (D) steel capsule holder placed in the bottom part of the reactor; (E) schematic drawing of the capsule-piercing device connected to the quadrupole mass spectrometer.
MFC = Mass Flow Controller; SG1 and SG2 = high-resolution pressure transducers; V1, V2, V3 and V4 = valves; SP = silicon septum; QMS = quadrupole mass spectrometer.

Fig. 3.25. Pierced capsule mounted in epoxy resin. Please note that the piercing technique does not affect the integrity of the capsule, allowing further investigations by means of electron microscopy and electron microprobe.

Chapter 4

Results

4.1. Run Table

Experimental conditions for each experiment are reported in Table 4.1 along with the observed mineral assemblage. All experimental runs were performed at 2.5 GPa and 1200 °C pressure and temperature conditions respectively. We also performed one experiment at P = 2.5 GPa and T = 1100 °C.

Electron – microprobe analyses and electron – microscopy observation will be presented in these sections where runs will be described on the basis of the observed textural features (section 4.2), mineral assemblage (section 4.3) and liquid distribution (section 4.4).

In section 4.5 the image analysis with dihedral angle measurements and characterization and grain boundary wetness and infiltrated volume liquid fraction observation will be presented.

Run	Capsule	Starting material + sinterized olivine	P (GPa)	T (°C)	Run time(h)	Stable products	Quenching products	Geometry (from top to bottom)
LSI_1	Pt+grph	cc+dol+sid+br	2.5	1200	90	ol+per	q-carb	Mix - Dunite
LSI_2	AuPd	cc+dol+sid+br+ Re-ReO_2	2.5	1200	<24	ol+cr-sp+per	q-carb	Buffer - Mix - Dunite
LSI_3	AuPd	cc+dol+sid+br+ Re-ReO_2+grph	2.5	1200	68	ol+per	ol/opx+q-carb	Buffer - Mix - Dunite
LSI_4	Pt+grph	cc+mag+sid+H_2O	2.5	1200	306	ol	q-carb	Mix - Dunite
LSI_5	Pt+grph	cc+mag+sid+H_2O	2.5	1100	241	ol+opx+cpx+carb	opx+cpx+q-carb	Mix - Dunite
LSI_6	Pt+grph	cc+mag+sid+H_2O	2.5	1200	3	ol	q-carb	Mix - Dunite
LSI_7	Pt+grph	cc+mag+sid+H_2O	2.5	1200	30	ol+Fe-per+cr-sp+carb	mag+q-carb	Mix - Dunite
LSI_8	Pt+grph	cc+mag+sid+H_2O	2.5	1200	30	...	...	Dunite - Mix
LSI_9	Pt+grph	cc+mag+sid+H_2O	2.5	1200	30	ol	ol/opx+l-carb	Dunite - Mix
LSI_10	Pt+grph	cc+mag+sid+H_2O	2.5	1200	3	ol+carb	opx+l-carb	Dunite - Mix
LSI_11	Pt+grph	cc+mag+sid+H_2O	2.5	1200	300	ol+grph	l-carb+ol	Dunite - Mix
LSI_12	Pt	cc+mag+sid+H_2O	2.5	1200	30	...	...	Dunite - Mix
LSI_13	Pt	cc+mag+sid+br+grph	2.5	1200	3	ol+cr-sp+Fe-per	l-carb	Dunite - Mix
LSI_14	Pt	cc+mag+sid+br+grph	2.5	1200	30	ol+per+Fe-per	ol/opx+l-carb	Dunite - Mix
LSI_15	Pt	cc+mag+sid+br+grph+qz	2.5	1200	30	ol+opx	l-carb	Dunite - Mix
LSI_16	Pt	cc+mag+sid+br+grph+qz	2.5	1200	30	ol+cpx+cr-sp	q-carb	Dunite - Mix
LSI_17	Pt	cc+mag+sid+br+grph+qz	2.5	1200	164	ol+opx	ol+q-carb+l-carb	Dunite - Mix
LSI_18	Pt+grph	cc+mag+sid+H_2O	2.5	1200	48	ol	ol/opx+l-carb	Mix - Dunite
LSI_19	Pt+grph	cc+mag+sid+H_2O	2.5	1200	47	ol	ol/opx+l-carb	Mix - Dunite

Table. 4.1. Run Table. Abbreviations: Pt = platinum; grph = graphite; AuPd = Aurum-Palladium; cc = calcite; dol = dolomite; sid = siderite; br = brucite; mag = magnesite; qz = quartz; ol = olivine; per = periclase; l-carb = carbonatitic liquid; q-carb = quench carbonates; cr-sp = chromium spinel; opx = orthopyroxene; cpx = clinopyroxene; Fe-per = ferropericlase.

4.2. Textural features

LSI_1

The first experiment (LSI_1) was performed using Pt capsule and a graphite sleeve (see section 3.1.1; Fig. 3.5). The mixture carbonate (calcite, dolomite, siderite) – brucite was placed above the dunite rod and run duration was 90 hours. The run charge shows several fractures due to a quenching process.

Olivine, periclase and quench products were observed in this experiment (Fig.4.1). Texture showed euhedral, subhedral and anhedral crystals of olivine. Texturally equilibrated olivine is present; BSE images show that the olivine grains did not underwent a significant growth as they show crystal size between 40 to > 100 μm, to be compared with size of the starting material (34-64 μm) (Fig.4.2 and 4.3). Triple junctions often occur between olivine grains indicating approach to equilibrium at *P-T* experimental conditions. Grain boundaries range from lobated to planar (Fig.4.2). Quench phases precipitated from the liquid consist of dendritic aggregates of carbonate characterized by intergrowth of feathery crystals because carbonate melts are not quenchable (Fig. 4.3). The carbonate feathers, and the olivine crystals often contains interstitial ferropericlase with a grain size ranging between 10 to >100 μm and lobated shape (Fig. 4.4).

To estimate the volume of carbonate, silicate and oxide phases in our experimental samples we used the comparison chart for volume percentage estimation (Terry and Chilingar, 1955) and this run charge approximatively has 2-3 vol.% of carbonate liquid phase and 97 vol.% of solid silicates (olivine) and periclase grains.

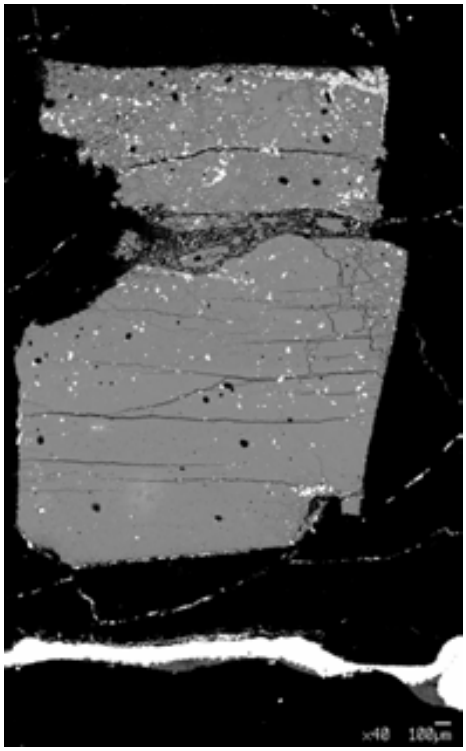

Fig. 4.1. BSE image of experimental run LSI_1.

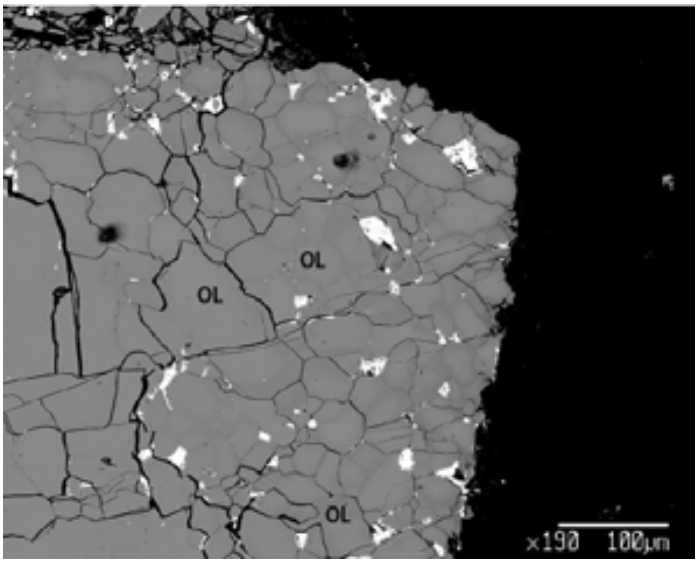

Fig. 4.2. Detail of olivine crystals of LSI_1 run.

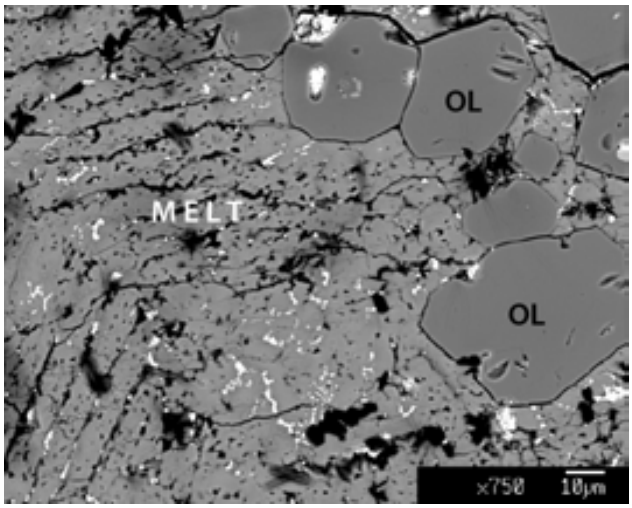

Fig. 4.3. BSE image of the dendritic carbonate liquids and olivine grains.

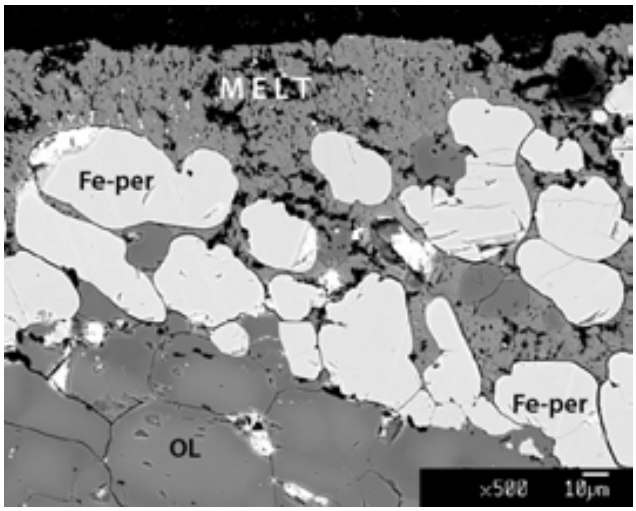

Fig. 4.4. BSE image of olivine grains, carbonate melt and ferropericlase globules.

LSI_2

This experiment was performed by placing the starting material directly into a $Au_{60}Pd_{40}$ capsule without graphite sleeve (See section 3.1.1; Fig. 3.6). To avoid the formation of periclase globules we used $ReReO_2$ buffer. The run time was of approximately 24 hours. Nonetheless, periclase formed with olivine, chromium-spinel, and quench products (Fig. 4.5).

Textural observations show polygonal anhedral and subhedral olivine grains. The crystal size is estimated in the range between 50 to > 100 μm. Triple junctions evidence equilibrium. Olivine crystals show zoning due to iron-loss. Smaller euhedral and subhedral olivine crystals are visible (size < 20 μm) in between larger olivine grains, often associated with infiltrated melt; most likely they are related to recrystallization processes or to reorganization of small olivine grains along the grain boundaries and the residual porosity left during sintering process (Fig. 4.6).

The quenching products are present as dendritic dolomitic carbonate characterized by growth of feathery crystals. From textural observations all the carbonate phases were completely melted. As evidenced by magnesium X-ray maps and BSE images ferropericlase and periclase globules are present in the carbonate melt, mostly with the same size of < 30 μm (Fig. 4.7) and rounded shape suggesting they represent a metastable phase.

Several subhedral Cr-spinel crystals occur inside the dunite rod between olivine grains probably due to primary inclusions in the San Carlos olivine (Fig. 4.8).

The fraction of carbonate liquid in the capsule is ~ 40 vol.% and the dunite with periclase globules ~ 60 vol.%.

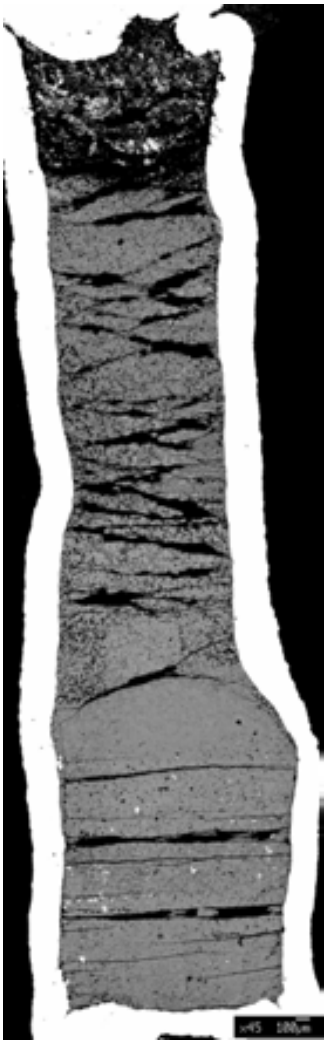

Fig. 4.5. BSE image of experimental run LSI_2.

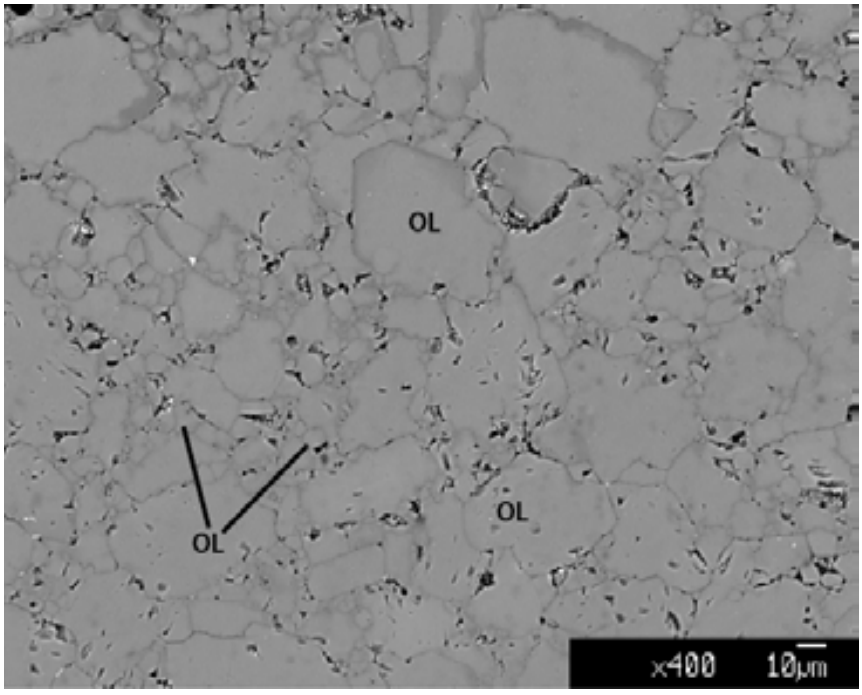

Fig. 4.6. BSE image of olivine grains from dunite rod and new smaller interstitial olivine.

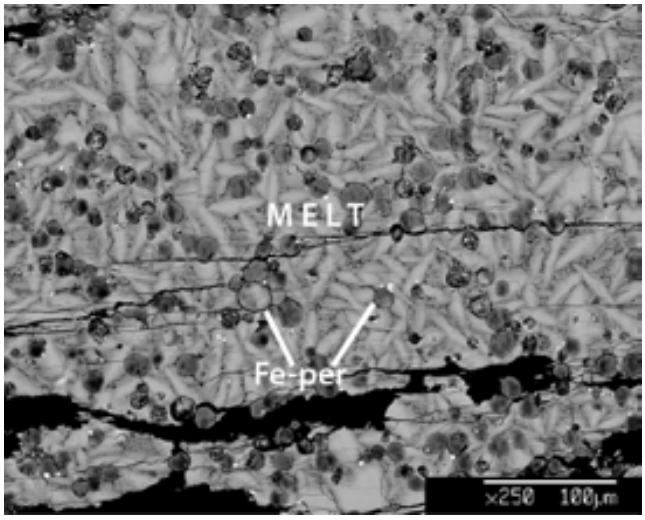

Fig. 4.7. BSE image of dendritic liquids and rounded ferropericlase globules.

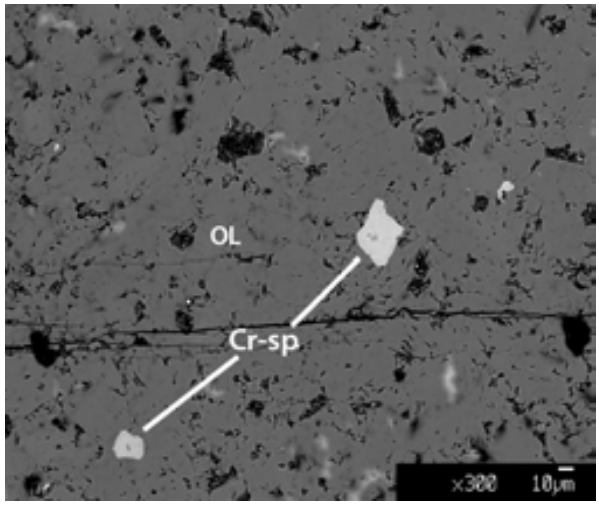

Fig. 4.8. BSE image of olivinic dunite rod and in light grey Cr-spinel crystals.

LSI_3

Experiment LSI_3 was performed with a different capsule setup, placing the dunite rod in a liquid reservoir using $ReReO_2$ and graphite powder, as redox buffer (See section 3.1.1; Fig. 3.6). The run time of this experiment was 68 hours at the same *P-T* conditions (Fig. 4.9).

Textural observations show again the presence of olivine grains with a strong zoning due to a loss of iron from core to rim. Grain boundaries (size > 50 μm) are undulated and in several cases planar. New olivine grains with a smaller size (< 10 μm) like LSI_2 sample (Fig. 4.10) are present between olivine interfaces or in aggregates.

Carbonate liquids are present at run conditions above and below the dunite rod because calcite or dolomite form with typical dendritic texture of quenched liquids (Fig. 4.11). Furthermore, by means of calcium X-ray maps it is possible to enhance little melt pockets inside the dunite rod representative of an infiltration flow. Texturally this liquid is characterized by intergrowth of feather crystals in dendritic aggregate. Moreover, carbonate dendrites at the bottom of the capsule present intergrowths with minor silicate phase having elongated tabular subhedral shape (Fig. 4.11). This phase could not be analysed for its small size by electron microprobe but was detected by means silicon X-ray map. At the bottom of the capsule these carbonate dendrites contain several periclase globules with a size in the order of 10-15 μm like LSI_2 sample (Fig. 4.12).

The fraction of carbonate liquid phase in the run charge is approximately 58 vol.% and the rest is represented by dunite and periclase.

Fig. 4.9. BSE image of experimental run LSI_3.

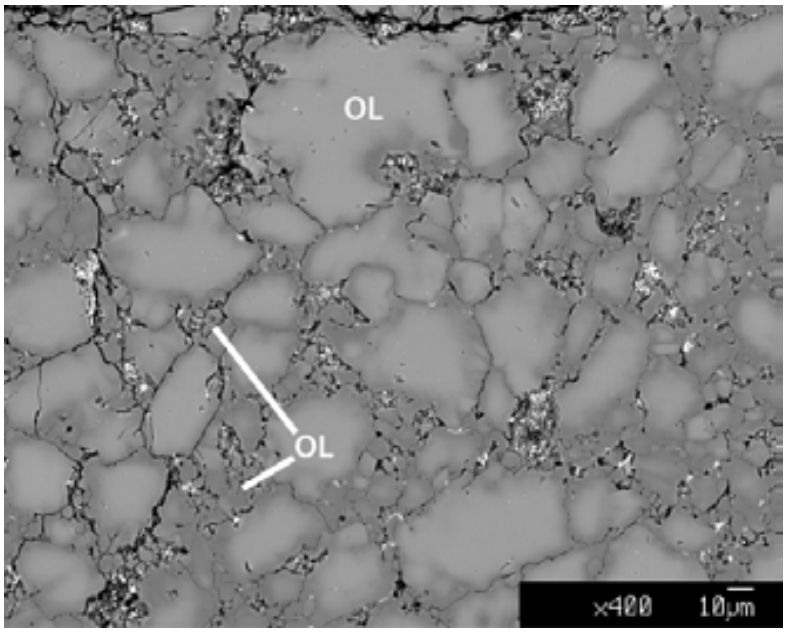

Fig. 4.10. BSE image of zoning olivine grains and new smaller interstitial olivine.

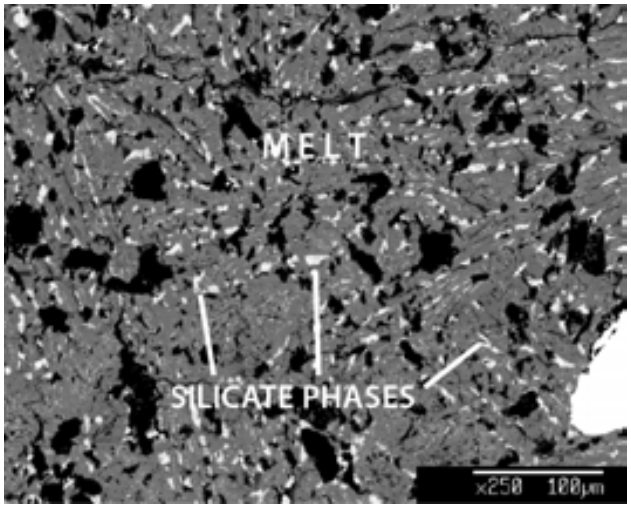

Fig. 4.11. BSE image of carbonate melt at the bottom of the capsule. Light grey are elongated silicate phase.

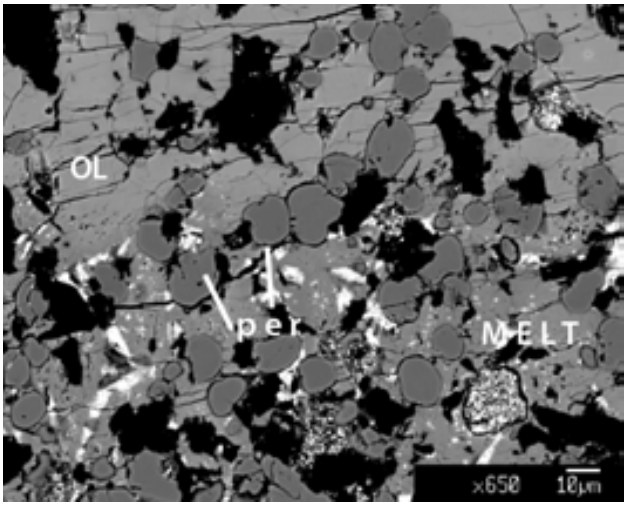

Fig. 4.12. BSE image of the bottom of the capsule that shows olivine – carbonate melt interface containing periclase rounded globules.

LSI_4

LSI_4 experiment was carried out with platinum capsule and graphite liner again like LSI_1 experiment. In this case we used mix 2 made of calcite, magnesite and siderite and as hydrous source free water (5 wt. %), placing this oxide mix above the dunite rod (see 3.1.1; table 3.2; Fig. 3.10). The run time experiment was of 306 hours (Fig. 4.13). Olivine and quench products were observed in this experiment.

Textural observations show polygonal euhedral and subhedral olivine grains with lobated and sharp grain boundaries. By means the EBSD analysis on this sample it was possible to perform a qualitative characterization of crystal size that showing the dimensions between 400 μm to ~ 40 μm as shown in Fig. 4.14 (in red olivine crystals and carbonatitic liquids in magenta color). Equilibrium texture is evidenced by 120 °C triple junctions. In this sample we do not observe significant loss of iron because the olivine grains are not zoned (Fig. 4.15).

The quenching products are present as dolomitic carbonate composition and they are characterized by feathery crystals in a typical dendritic quench texture (Fig. 4.15).

Carbonate melt is present inside the dunite rod as infiltrated liquids well evidenced by colored calcium X-ray map. Furthermore, using calcium X-ray map from electron microprobe, in orange/yellow it is possible to see how the run charge is divided into two zones with different liquid amount. Close to the olivine rod and carbonate mix, the liquid self-organizes a strong channelization, instead in the lower portion of the capsule that it is characterized by a smaller degree of melt infiltrated with more homogeneous liquid distribution (Fig. 4.16).

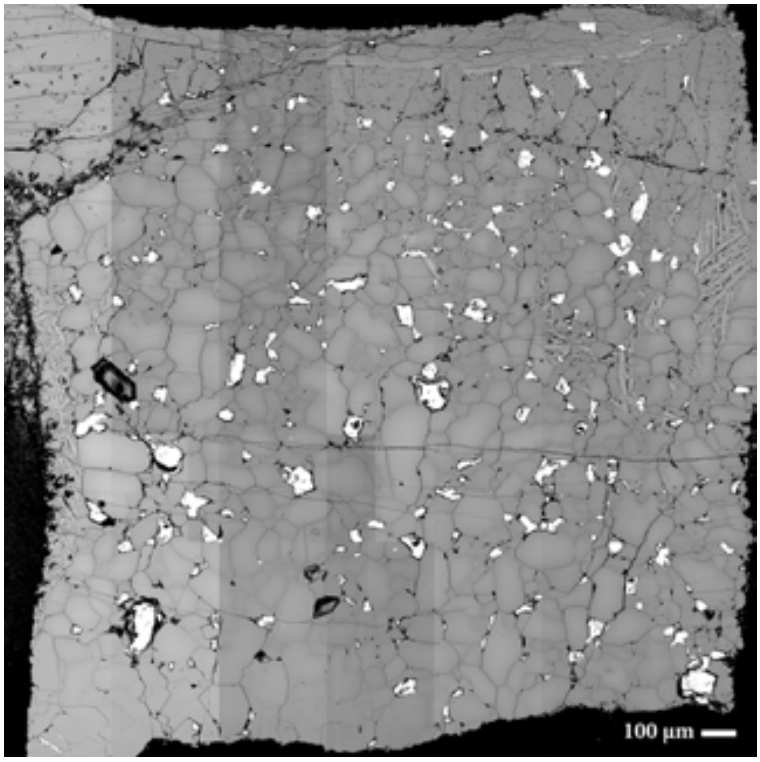

Fig. 4.13. BSE image of experimental run LSI_4.

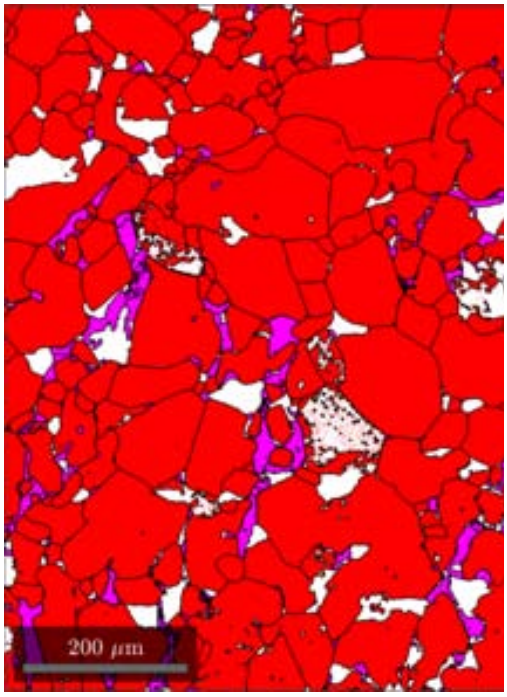

Fig. 4.14. EBSD image of detail of olivine crystals and theirs grain boundaries present in LSI_4 experiment.

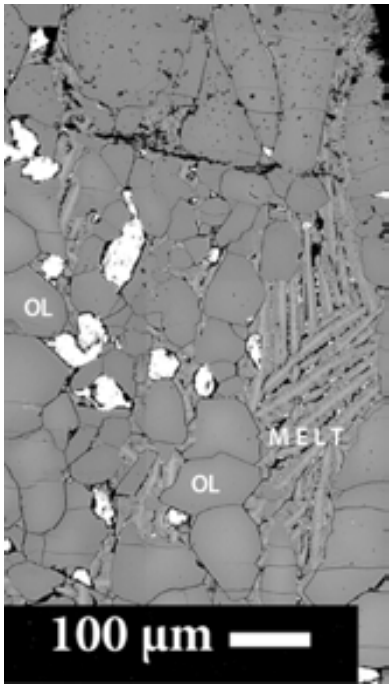

Fig. 4.15. BSE image of olivine and carbonate melt with a typical dendritic texture

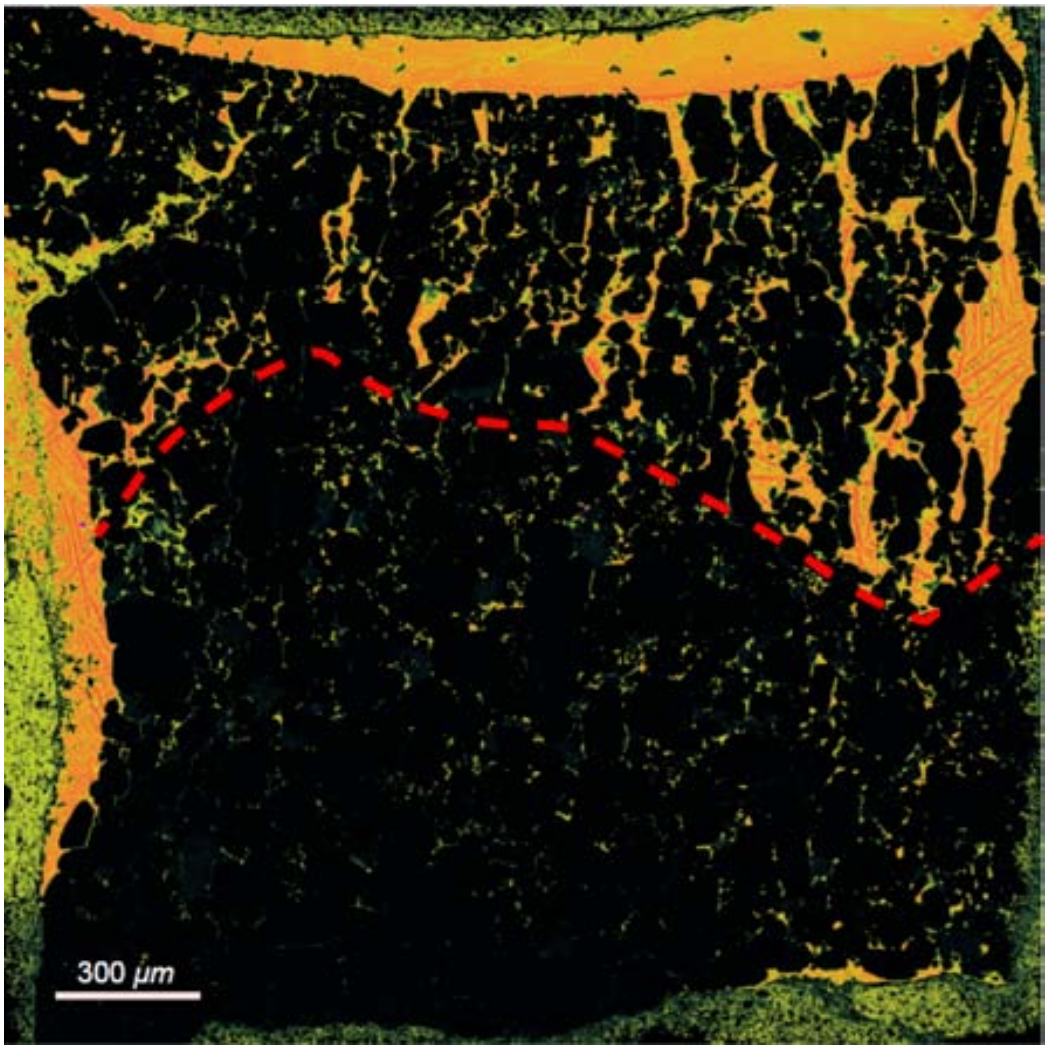

Fig. 4.16. Ca X-ray map of LSI_4 experiment that shows how this sample could be divided into two zones. At the top the carbonate melt forms a channelization, while at the bottom the infiltration is more homogeneous. Black = Dunite rod; Orange/Yellow = Carbonate melt.

LSI_5

This experiment was performed with the same capsule setup and the same starting material of LSI_4 experiment but with different experimental temperature, at 1100 °C. The run time was 241 hours.

Experimental products were olivine, orthopyroxene, clinopyroxene and carbonate grains (Fig. 4.17). Olivine results in a polygonal euhedral and subhedral texture with lobated or planar grain boundaries at 120° triple junctions. Olivine crystals show a strong zoning due to a loss of iron in rim respect to starting San Carlos olivine (Fig. 4.18).

Carbonate grains have approximately size of 10-20 μm and present a saccharoid structure with planar boundaries. These grains develop triple joints between grain boundaries (Fig. 4.19a). In many cases it is possible to see small carbonate melt pockets (size of < 10 μm) along the olivine grain boundaries (Fig. 4.19b).

Clinopyroxene has been observed as reaction rim between olivine and carbonate phases (Fig. 4.20a). Similarly, orthopyroxene is present as a melt-rock reaction phase forming an incipient symplectite near the olivine-carbonate mixture interphase (Fig. 4.20b); single crystals were previously described (Fig. 4.18b). The EBSD images allow us to define qualitatively the olivine and orthopyroxene grain size. Olivine shows sizes approximately between 40 to 250 μm and orthopyroxene ~ 60-70 μm (Fig. 4.18b). The silicate phases in the capsule are representative of ~ 73 vol.%, the carbonate grains are ~ 27 vol.%.

Fig. 4.17. BSE image of experimental run LSI_5 (P = 2.5 GPa and T = 1100 °C).

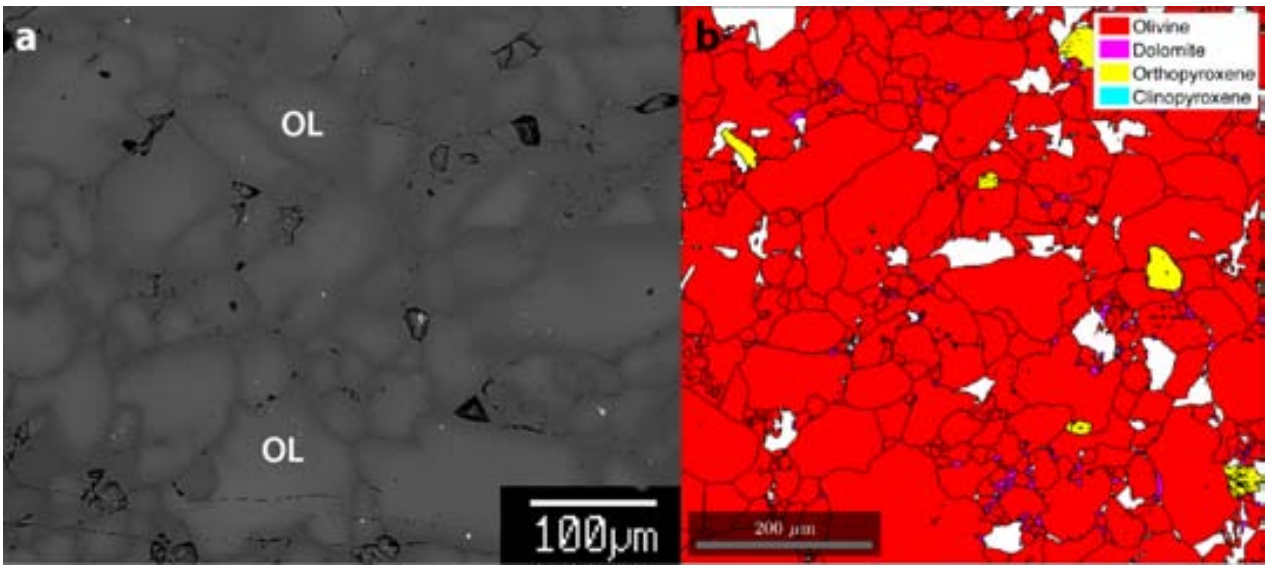

Fig. 4.18. (a) Detail of strong zoning olivine in the LSI_5 experiment; (b) EBSD image of olivine, orthopyroxene and quenching products (namely dolomite by Matlab® output image) boundaries.

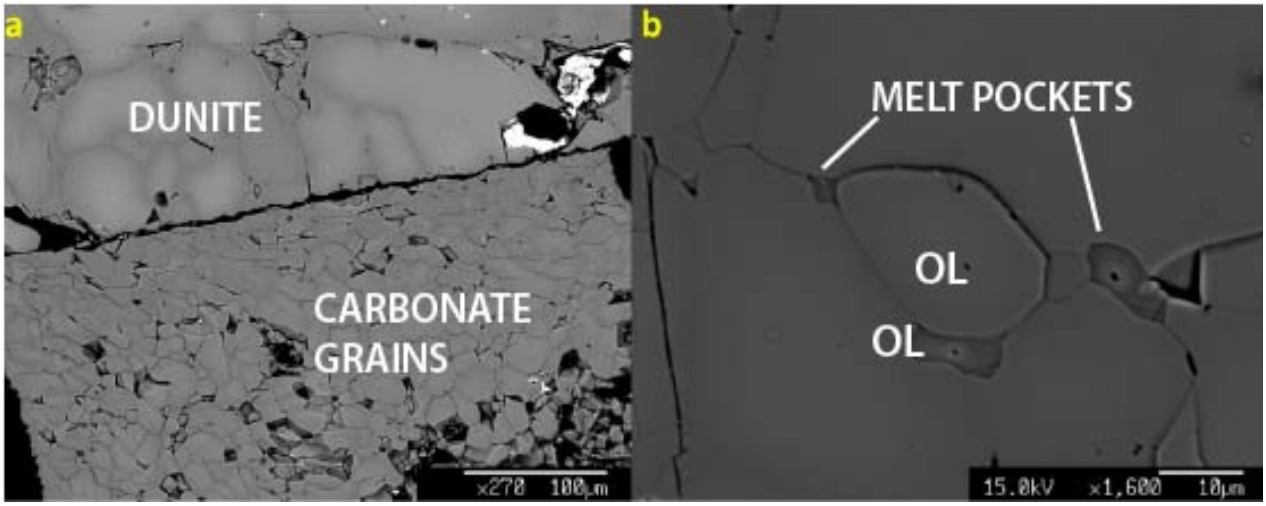

Fig. 4.19. BSE image of dunite rod – carbonate mix interface showing olivine and saccharoid carbonate grains (a); detail of melt pockets infiltrated into the dunite rod (b).

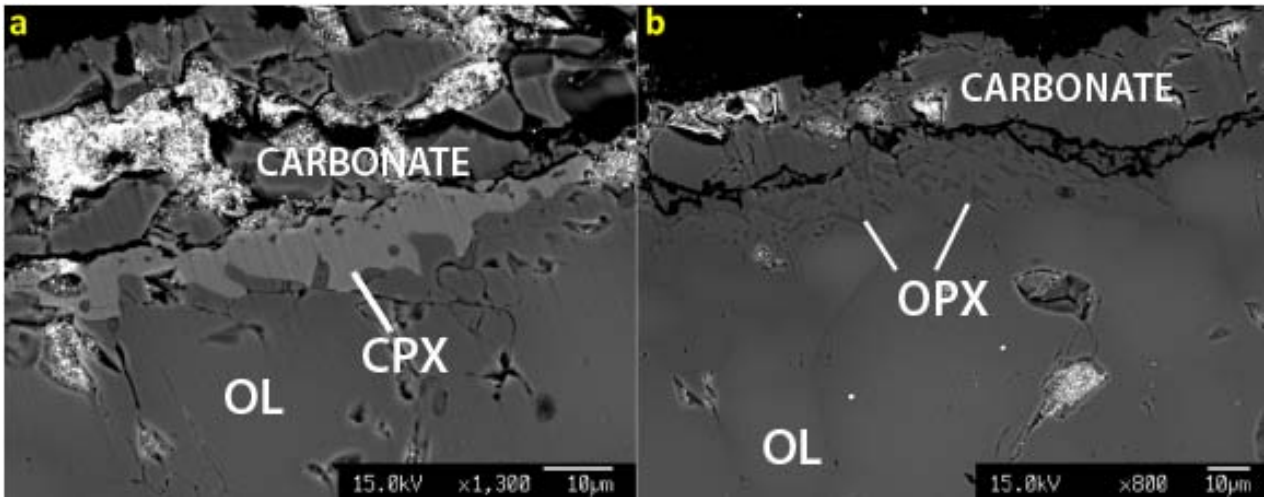

Fig. 4.20. Detail of the top of the capsule where it's possible to see the reaction rim between olivine and carbonate made of clinopyroxene (a); always at the top of the capsule it's possible to appreciate the formation of incipient orthopyroxene-olivine symplectite as melt-rock reaction phase (b).

LSI_6

LSI_6 was an experiment with the same conditions of LSI_4 except for the run time of 3 hours. The products run is olivine from dunite rod and quench carbonates. The volume of carbonate in the run charge is approximately 2/3 of the entire capsule (Fig. 4.21). These carbonates show ~ 30 vol.% of dendritic texture typical of a melt phase (Fig. 4.22b) and the rest, close to the dunite – carbonate mixture interface, seems to be a granular texture with saccharoid structure, straight boundaries and triple joint and grains size between 10 to 60 μm (Fig. 4.22a). Furthermore, by means of calcium X-ray maps it is possible to see carbonatitic melt phase infiltrated in the dunite rod (Fig. 4.23).

Dunite rod seems to be divided into two different portions. The lower part shows subhedral olivine grains with size from 50 μm to >> 100 μm and sharp edges. In the upper portion, subhedral and euhedral olivine crystals with size ~ 90/100 μm are present. Along grain boundaries small olivine crystals (5-20 μm) were recognized, due to recrystallization processes or reorganization of small olivine grains during sintering process (Fig. 4.24).

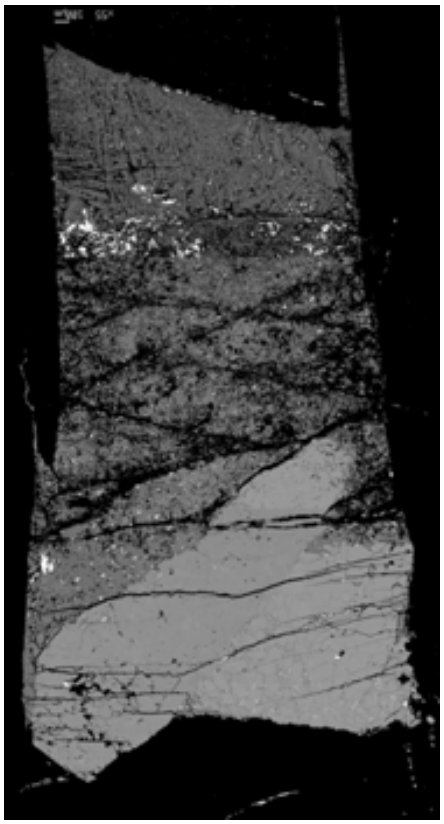

Fig. 4.21. BSE image of experimental run LSI_6.

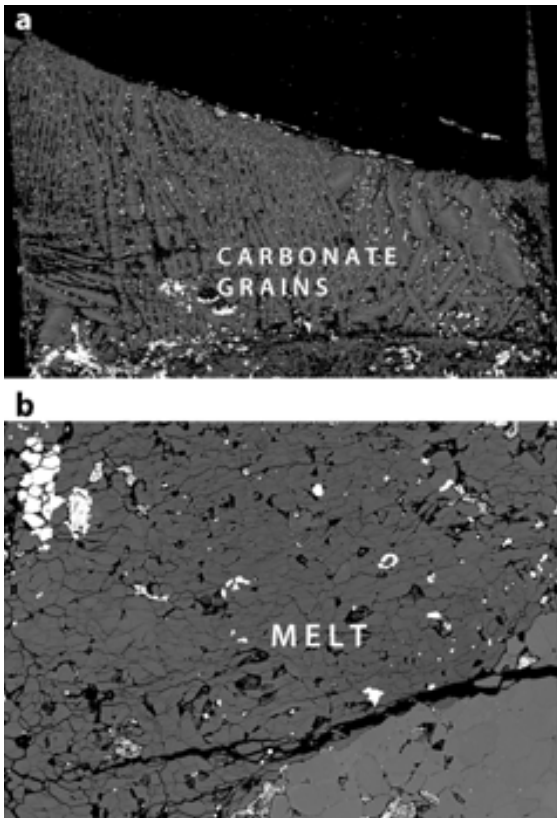

Fig. 4.22. BSE image that shows the carbonate granular grains at the olivine – carbonate interface (a) and the dendritic carbonate liquid texture (b).

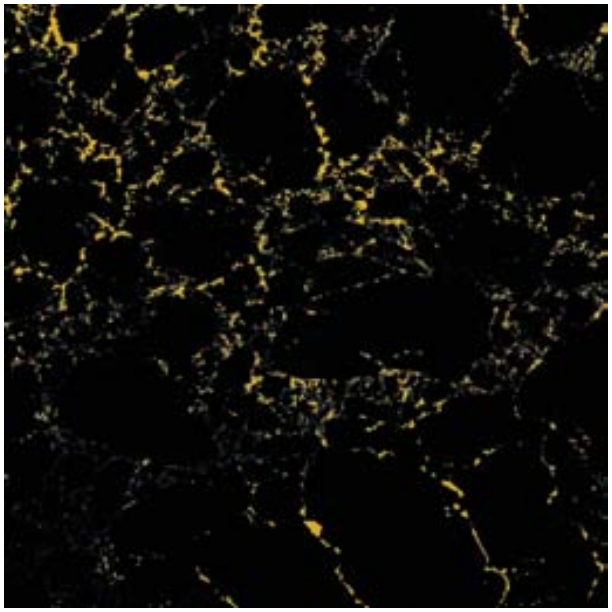

Fig. 4.23. Ca X-ray map shows clearly the carbonate (yellow) infiltrated into the dunite rod (black).

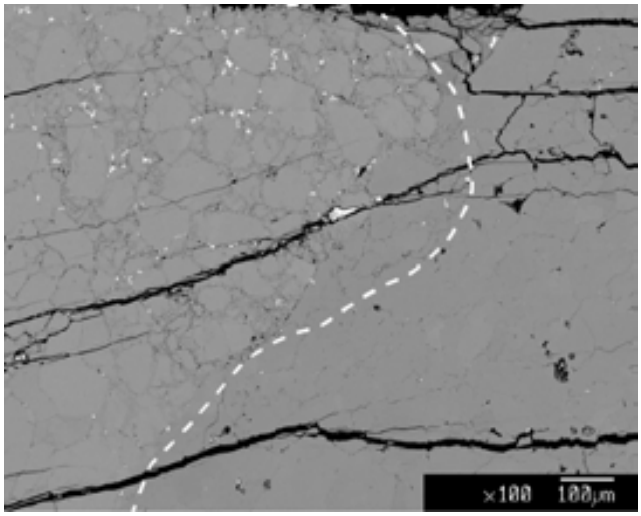

Fig. 4.24. Detail of dunite rod shows the presence (on the left) of little olivine grains along original olivine grain boundaries.

LSI_7

Olivine, ferropericlase, Cr-spinel, dolomite grains, magnesite and quenching carbonate were observed in this experiment (30 hours duration; Fig. 4.25).

Textural observations show subhedral olivine with lobated and straight shape. The size of this olivine is > 60 µm. Equilibrium is evidenced by the presence of triple junctions between olivine crystals and pronounced grain growth compared with starting San carlos olivine powder (Fig. 4.26a). Small crystals of Cr-spinel with planar edges are also present inside the dunite rod (~ 20-30 µm; Fig. 4.26b)

A carbonate liquid with typical dendritic quench structure is present at the top of the capsule, in the hotter zone (Fig. 4.27). At the interface between dunite rod and powder mixture, grains of subsolidus dolomitic carbonate with size < 30 µm (Fig. 4.27) are present. By means of calcium X-ray maps it is possible to see very little carbonate pockets inside the dunite rod between olivine grain boundaries and triple junctions. Furthermore, associated with subsolidus dolomitic carbonate composition there are aggregates of magnesite with size > 20 µm (Fig. 4.28a) and interstitials ferropericlase grains with lobated shape (5-40 µm) observed inside carbonate liquids and grains (Fig. 4.28b). The carbonatitic portion is representative of 55/60 vol.% of entire run charge.

Fig. 4.25. BSE image of experimental run LSI_7.

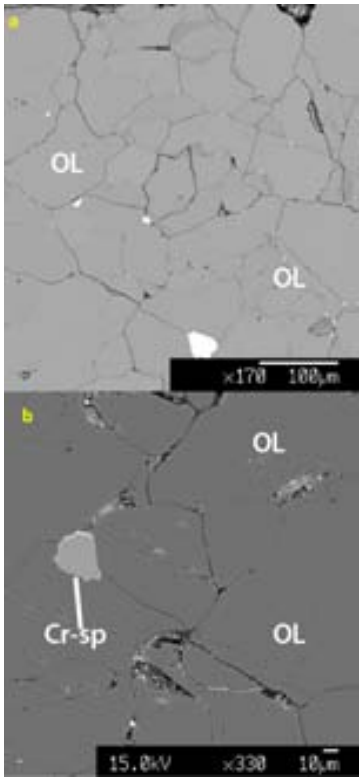

Fig. 4.26. Detail of olivine grain boundaries (a); Cr-spinel crystal into the dunite rod (b).

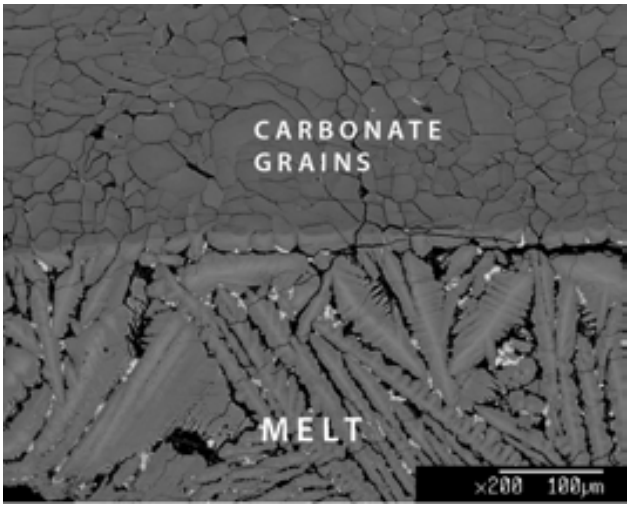

Fig. 4.27. BSE image of interface between granular and molten carbonates

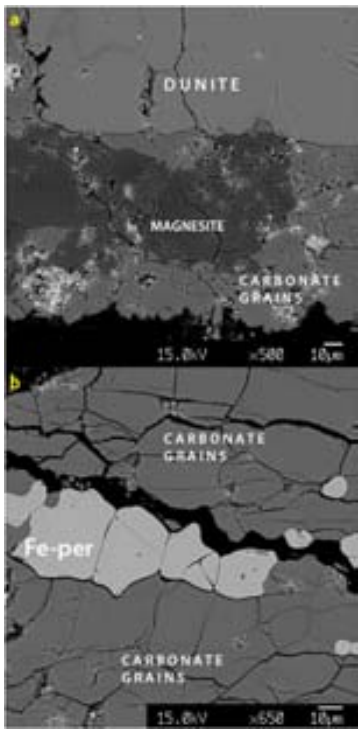

Fig. 4.28. BSE image of magnesite (a) and ferropericlase (b) presence into carbonate grains.

LSI_8

LSI_8 experiment was not characterized because during the polishing we lost the sample.

LSI_9

LSI_9 experiment was performed at same conditions and starting material of previous five experiments with run duration of 30 hours.

This capsule can be subdivided into 3 main parts (Fig. 4.29). At the top it is possible to see the dunite with olivine grains strongly zoned. These subhedral olivine grains underwent extensive growth respect to starting material and reach a size from 60 μm to > 220 μm (Fig. 4.30a). Triple junctions often occur between olivine grains indicating approach to equilibrium at pressure and temperature run conditions. Grain boundaries are lobated in some cases. Carbonatitic liquid is observed inside the dunite rod, as highlighted by calcium X-ray maps: carbonatitic pockets (orange) infiltrated in the peridotitic matrix (black) (Fig. 4.33).

At the bottom of the capsule there are olivine crystals that do not present zoning. These olivine grains, by means to dissolution-reprecipitation effects, parted from the original rod of dunite during the first step of experiment. By BSE image observation we can see that these grains have size > 100 μm and they are subhedral with lobated and straight shape (Fig. 4.30b).

Between dunite rod and big olivine grains at the bottom of the capsule there is carbonatitic melts with typical dendritic texture (Fig. 4.31a). In detail it is possible to appreciate the difference between the silicatic portion (light grey) and carbonate composition (dark grey) of this carbonatitic liquid inside the dendrite (Fig. 4.31b).

Within the carbonatitic liquid we found abnormal olivine grains characterized by growth up to a size between 500 μm to 800 μm. These olivine crystals present subhedral and perfect prismatic euhedral shape (Fig. 4.32). The carbonatitic dendrites represent ~ 80 % of volume of entire run charge, the rest are dunite rod and the olivine large grains in the middle and at the bottom of the capsule.

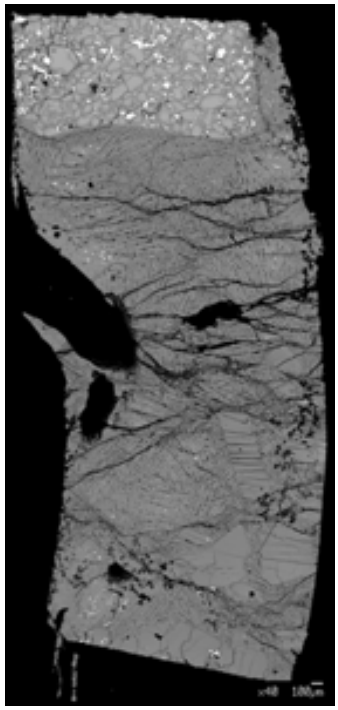

Fig. 4.29. BSE image of experimental run LSI_9.

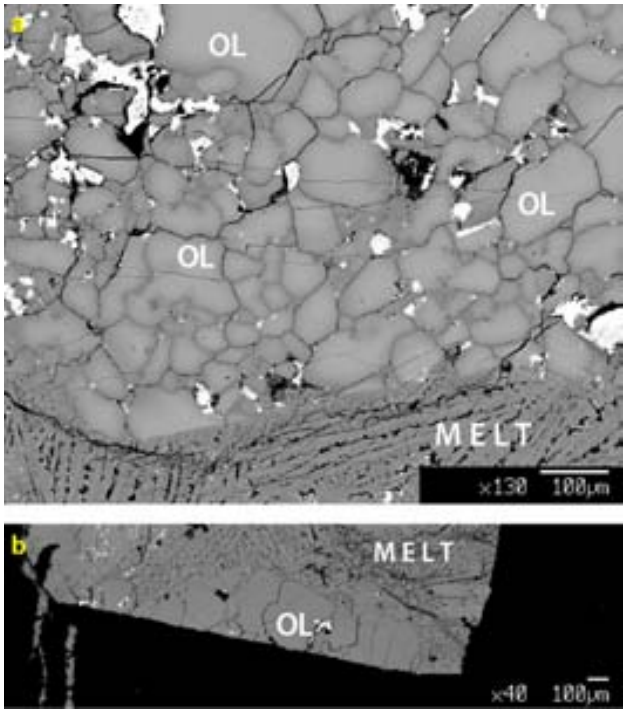

Fig. 4.30. Zoning olivine of dunite rod at the top of the capsule (a); not zoning big olivine grains at the bottom of the capsule (b).

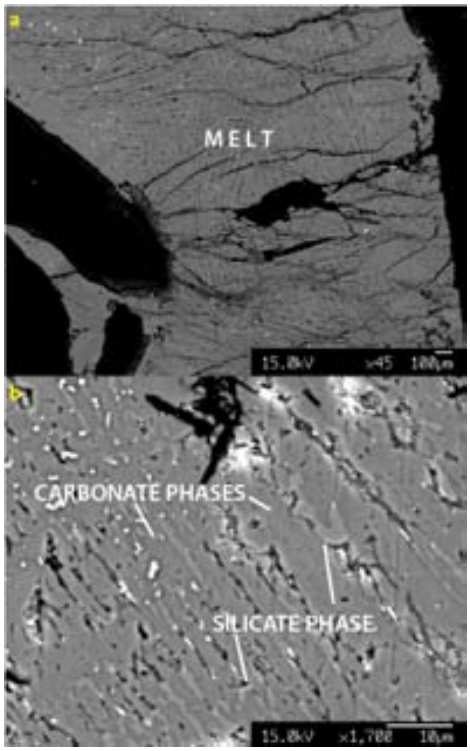

Fig. 4.31. Dendritic carbonatitic melt (a); detail of carbonatitic melt shows carbonate phases in dark grey and silicate phases in light grey (b).

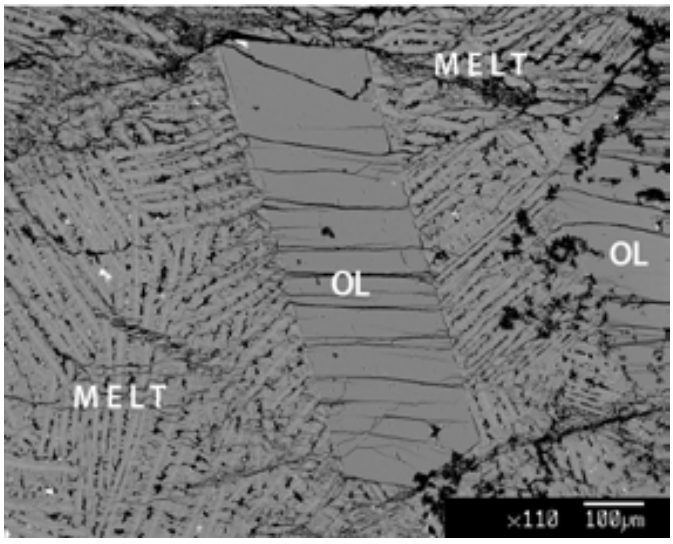

Fig. 4.32. Big grown olivine surrounded by carbonatitic melt.

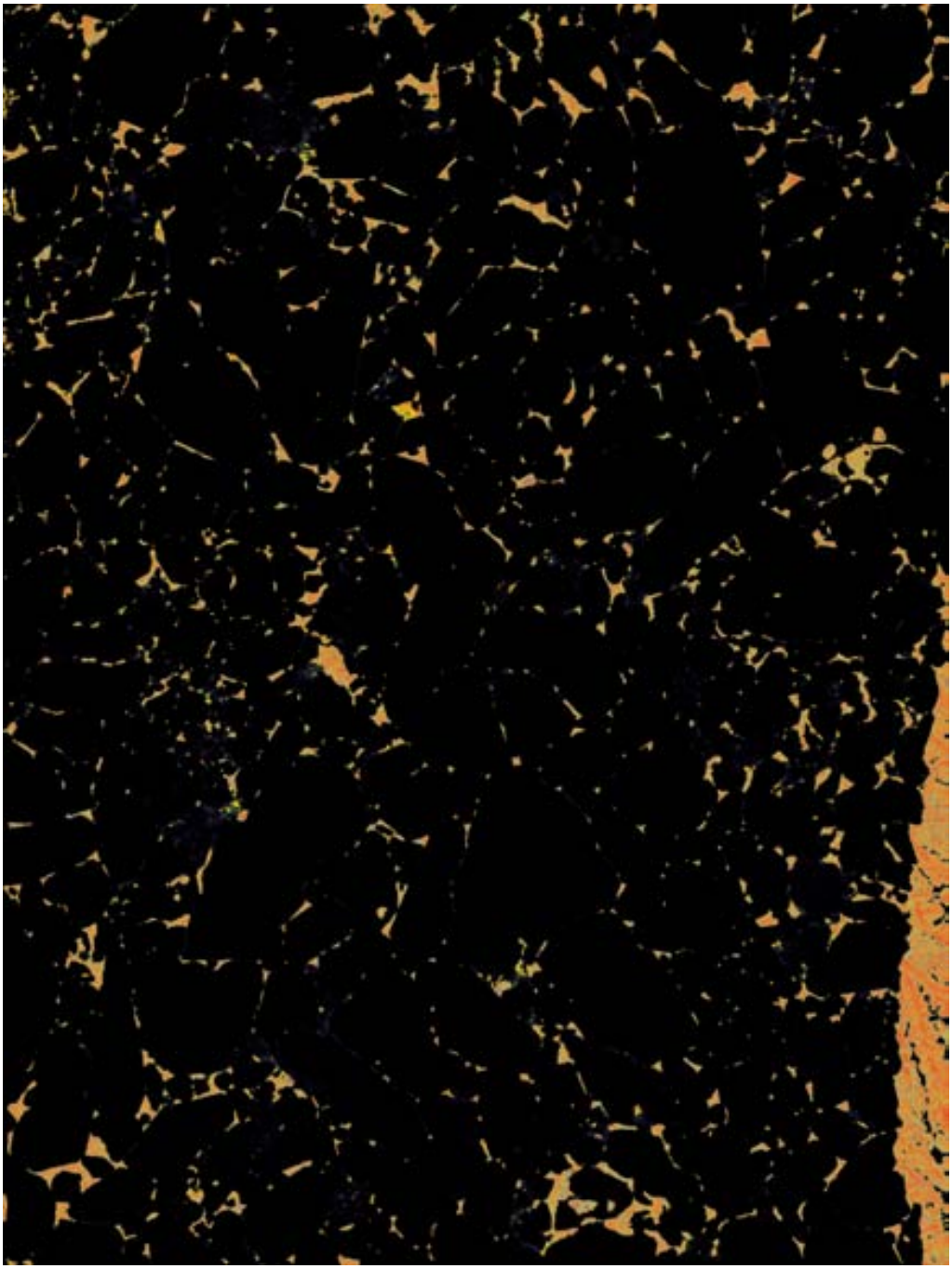

Fig. 4.33. Ca X-ray map shows the infiltration of carbonatitic liquid (orange/yellow) into the dunite rod (black).

LSI_10

This experiment was performed with same capsule setup and same starting material of the previous seven experiments. The run duration was of 3 hours. Olivine and quenching products were observed in this experiment (Fig. 4.34).

Textural observations of dunite rod show a strong zoning of olivine crystals. These olivine grains present prismatic euhedral shape with boundaries from lobated to planar, and development of triple junctions. Crystal size is from 50 μm to > 100 μm.

The quenching products are represented by carbonate grains with dendritic texture, as typical of carbonatitic liquids (Fig. 4.35). Dendritic textures representing liquid phase are close to carbonatitic reservoir and dunite rod; dendrites result from intergrowth of the silicatic and carbonate portions (Fig. 4.36). A subsolidus carbonate aggregate shows small grains with saccharoid structure and planar boundaries with developed triple joints and size from 7 μm to 40 μm (Fig. 4.35).

At the top of the capsule above the dunite rod there are aggregates of small euhedral crystals of zoned orthopyroxene with prismatic shape and size from 15 μm to < 5 μm (Fig. 4.37).

With the aid of calcium X-ray map, it was possible to observe the carbonatitic melt pockets infiltrated inside the dunite rod along olivine grain boundaries and between the triple junctions forming a well interconnected liquid network (Fig. 4.38).

The balance of silicate products is of approximatively 40 vol.% of entire capsule, consequently the carbonate is ~ 60 vol.% and almost all is represented by grains of carbonate with only 15 vol.% of liquid phase.

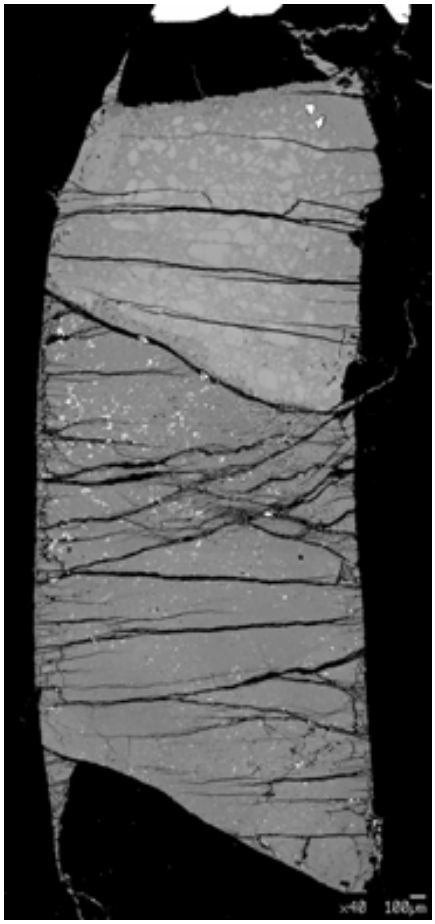

Fig. 4.34. BSE image of experimental run LSI_10.

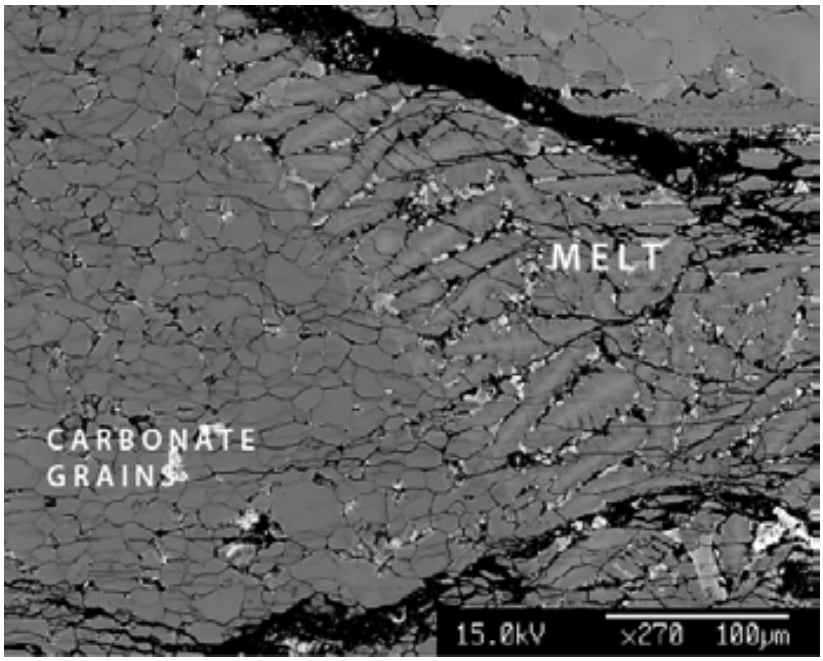

Fig. 4.35. Detail of interface between carbonate granules and molten carbonatite.

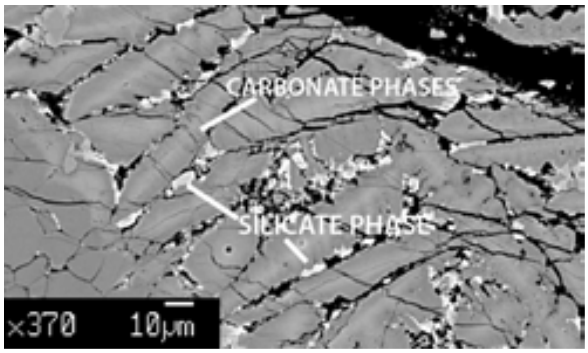

Fig. 4.36. Detail of carbonatitic melts with distinction between silicate (light grey) and carbonate (dark grey) phases.

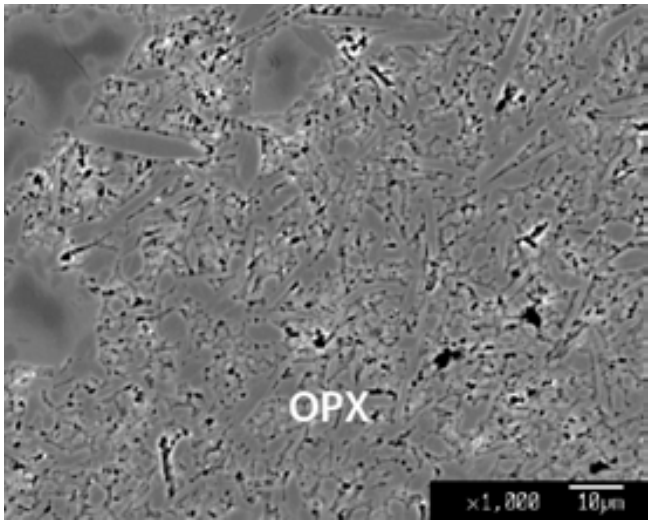

Fig. 4.37. Cumulate of elongated, prismatic orthopyroxene crystals.

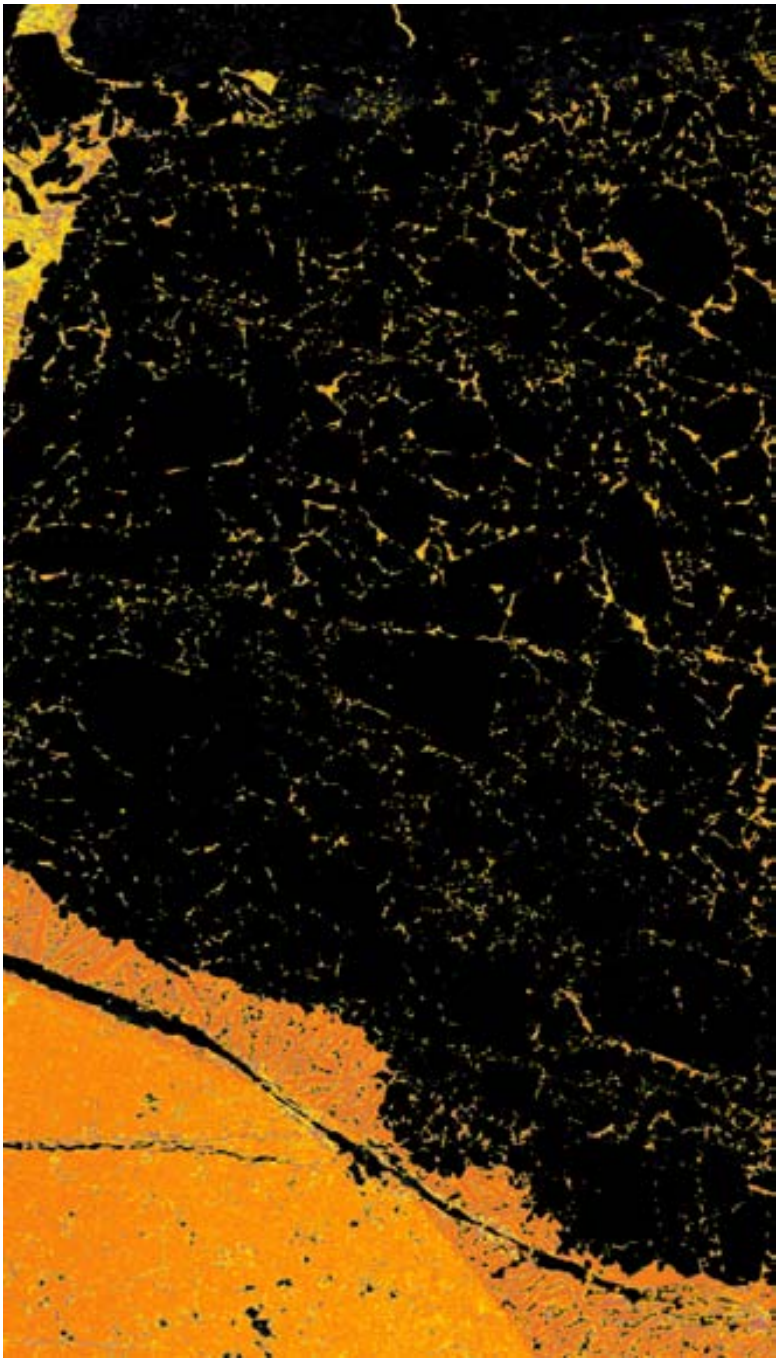

Fig. 4.38. Ca X-ray map shows in orange the carbonatitic phases, at the bottom the carbonate grains and at the interface with dunite the dendrites and into the dunite rod (black) the interconnected melt channel.

LSI_11

The experiment named LSI_11 was performed at the same conditions of LSI_10 but with run duration of 300 hours.

This capsule shows an almost complete loss of the dunite rod due to a strong dissolution-reprecipitation process (Fig. 4.39). The entire capsule presents carbonatitic melt with a typical dendritic structure (Fig. 4.40a) where it is possible to discriminate the carbonate and silicate phases (Fig. 4.40b). Subhedral olivine grains with size of ~ 100 μm representative of the original dunite rod (Fig. 4.41) are present at the bottom. In detail it is also possible to observe the formation of new olivine crystals surrounded by carbonatitic melt with elongated shape and length size of ~ 100 μm – 150 μm (Fig. 4.42 a and b). It is most remarkable the precipitation of large elongated platelets of graphite with dimensions from ~ 100 μm to > 900 ~ μm; Fig. 4.39.

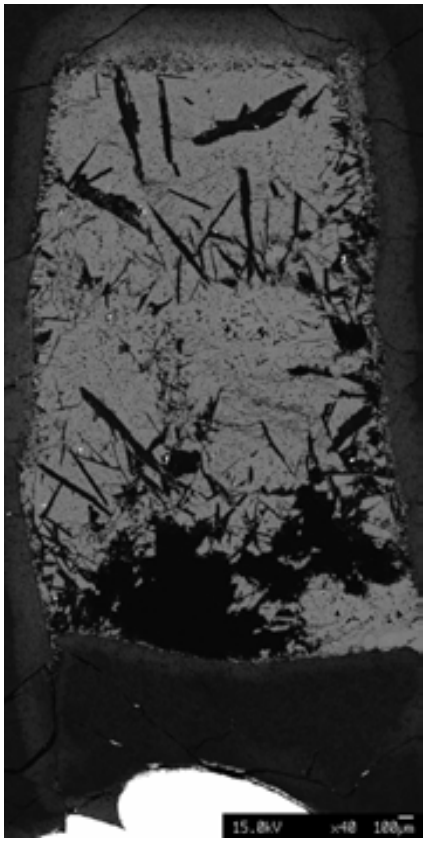

Fig. 4.39. BSE image of experimental run LSI_11.

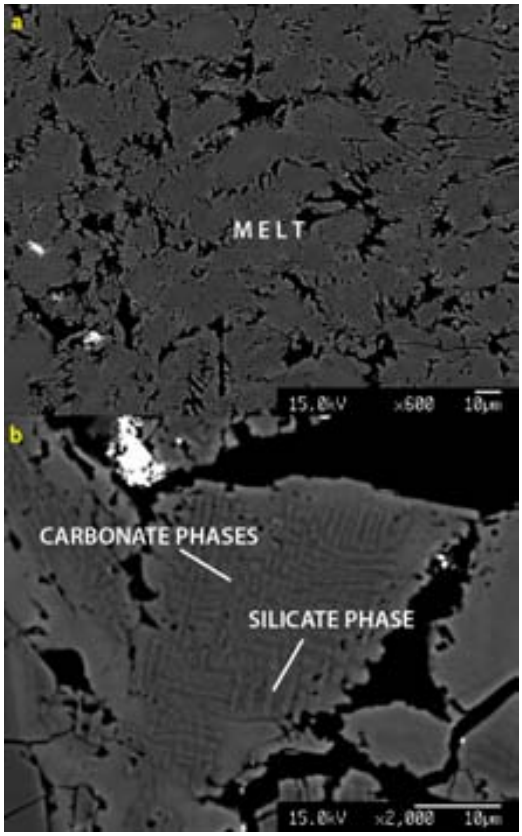

Fig. 4.40. Dendritic texture of carbonatitic melts (a) and detail of carbonate and silicate components of the liquid (b).

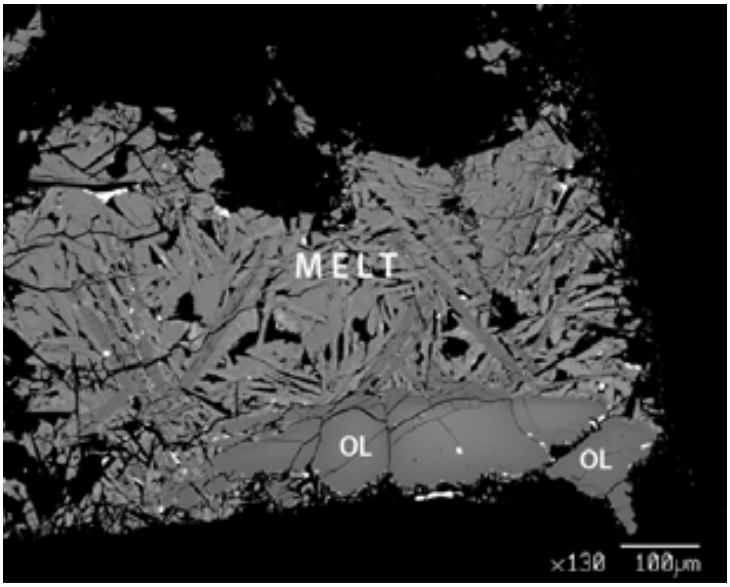

Fig. 4.41. The only olivine from original dunite rod placed at the top of the capsule below the carbonatite.

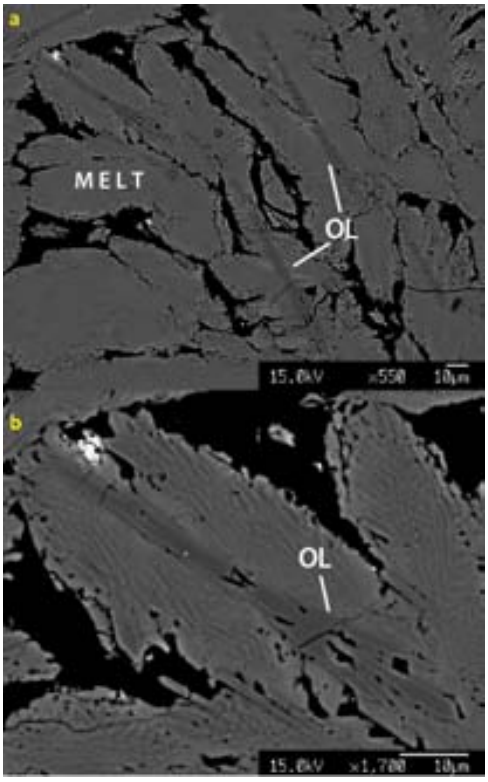

Fig. 4.42. Dendritic texture of carbonatite (a) and new elongated olivine inside the melt (a and b).

LSI_12

The LSI_12 experiment was performed using the same starting material of previous sample with run time of 30 hours. The capsule was only platinum preconditioned with basalt liquid at gas mixing furnace without graphite thick. This experiment was not considered for strong basaltic contamination due to preconditioning and the probable basaltic grains presence in the capsule. This contamination was found by EMPA analysis that showed the presence of basaltic phases containing Al_2O_3, TiO_2 and Na_2O.

LSI_13

LSI_13 experiment was performed using a platinum preconditioned (with basalt powder containing ~ 10 vol.% of Fe_2O_3) capsule without graphite thick and using calcite, Pinerolo magnesite and Ivigtut siderite as carbonate reservoir, adding brucite and graphite powder also to control oxygen fugacity (See 3.1.1 section, Fig. 3.9a). The run time of this experiment was of 3 hours.

Olivine, Cr-spinel, ferropericlase and quench products were observed (Fig. 4.43).

The dunite rod shows olivine grains with evident zoning due to a strong loss of iron during the run (Fig. 4.44). Grain growth of olivine powder is responsible for a size > 100 μm and subhedral and euhedral texture with lobated and planar shape. At the bottom of the dunite rod it is possible to appreciate the presence of euhedral olivine crystals. These grains do not show zoning and have a size between 80 μm to 120 μm. Several of these crystals are possibly related to dunite by dissolution-reprecipitation process (Fig.4.43). Furthermore, between olivine grain boundaries there is new small olivine (≤ 10 μm) with subhedral texture and from straight to lobated shape (Fig. 4.44)

The quench products are represented by typical dendritic texture of carbonatitic liquids (Fig. 4.45a) where several polygonal and rounded ferropericlase grains with size of ≤10 μm (Fig. 4.45b) are present. The carbonatitic melts are present inside the dunite rod as infiltrated melt pockets between olivine grain boundaries and triple junctions (Fig. 4.47).

By means of Cr X-ray maps it was possible to observe the Cr-spinel presence as crystalline aggregate (Fig. 4.46).

The carbonatitic liquids respect to total of run charge is almost 40 vol.%.

Fig. 4.43. BSE image of experimental run LSI_13.

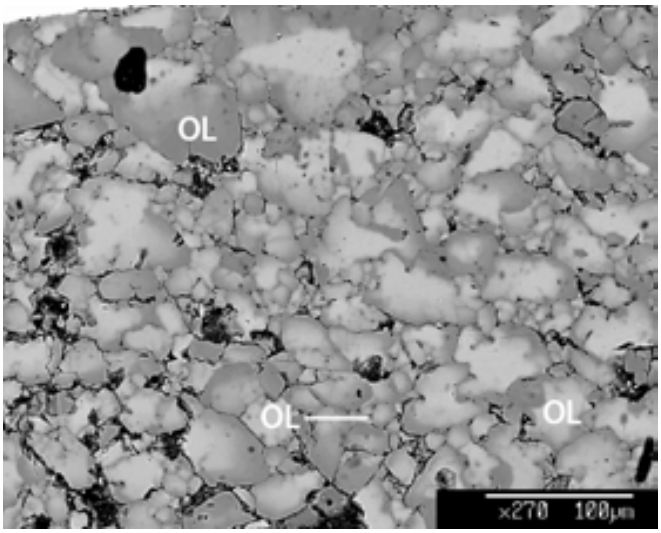

Fig. 4.44. Detail of strong zoning olivine crystals.

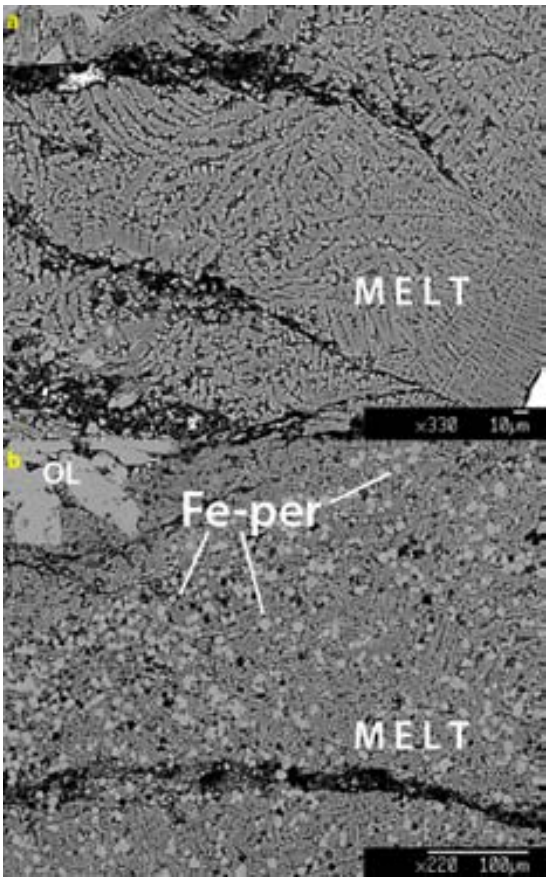

Fig. 4.45. Dendritic texture of liquid (a) and detail of ferropericlase surrounded by carbonatitic melts.

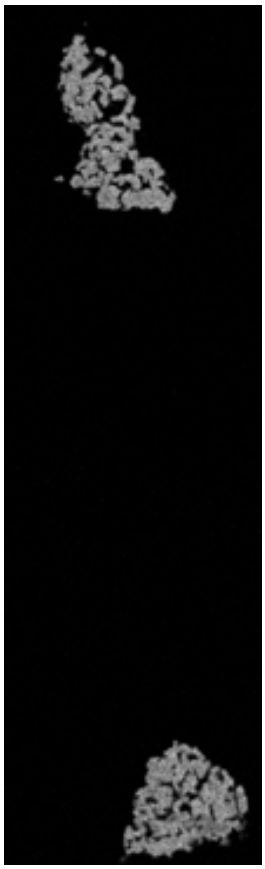

Fig. 4.46. Cr X-ray map that shows the Cr-spinel presence.

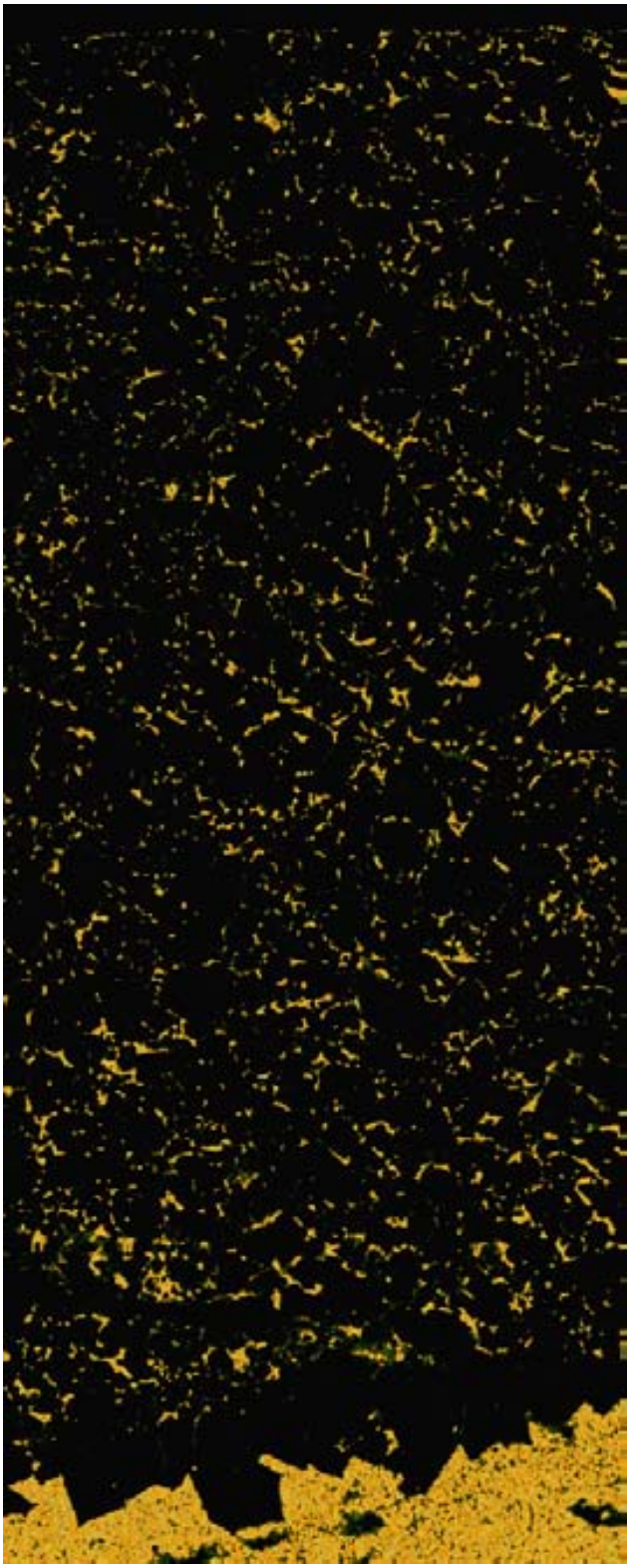

Fig. 4.47. Ca X-ray map shows in orange the carbonatitic melts infiltrated as channel or melt pockets along the olivine grain boundaries.

LSI_14

The setup of LSI_14 experiment is the same of LSI_13 except for the run time of 30 hours.
Olivine, periclase, ferropericlase and quench carbonatitic liquid phases are present in this capsule (Fig. 4.48).
The olivine crystals of the upper part of dunite rod show zoning due to loss of iron and smaller size (≥ 100 μm, Fig. 4.49a) than olivine grains at the bottom of dunite rod (from 100 μm to ~ 400 μm, Fig. 4.49b). The olivine grains have euhedral and subhedral shape with planar faces.
Inside the dunite rod there are the periclase grains infiltrated and stabilized along the olivine grain boundaries or inside the triple junctions into the dunite rod (Fig. 4.49a and b). Ferropericlase was found in the dunite – carbonatite interface as a band of polygonal grains with size from 50 μm to > 100 μm (Fig. 4.50).
The carbonatitic liquids, representative approximatively of 40 vol.% of entire run charge have a typical dendritic texture and filaments with little spherical silicate droplets (Fig. 4.51a and b).

Fig. 4.48. BSE image of experimental run LSI_14.

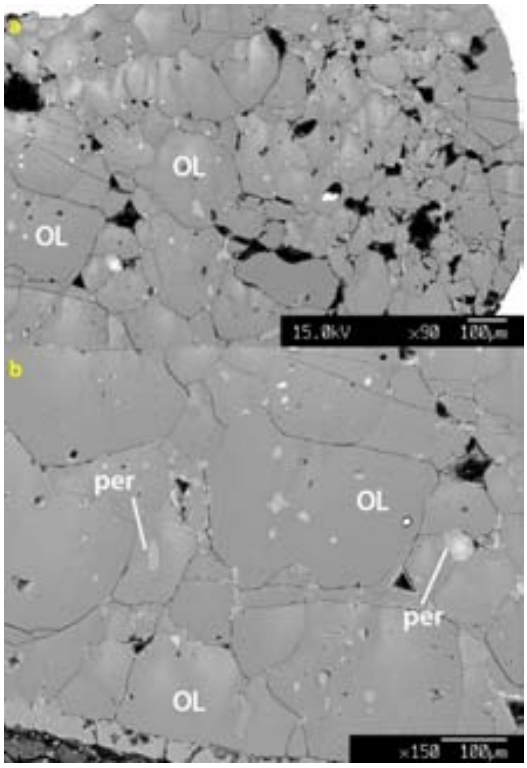

Fig. 4.49. Detail of olivine of dunite rod (a); periclase grounded globules inside the dunite along olivine grain boundaries or inside the olivine grains (b).

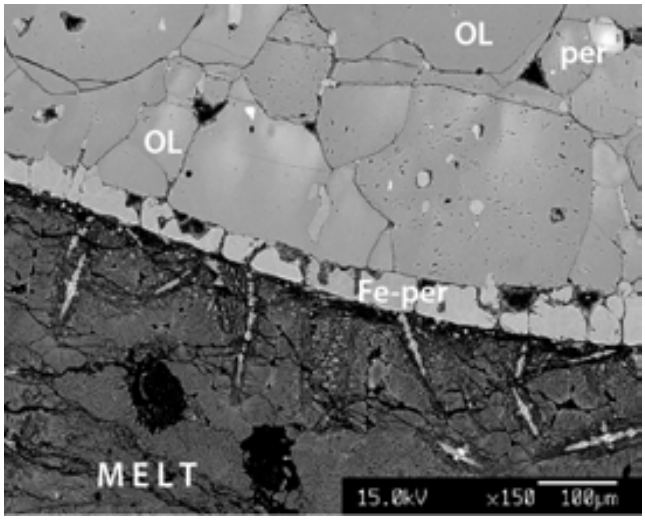

Fig. 4.50. Carbonatite – olivine interface showing a ferropericlase band formation.

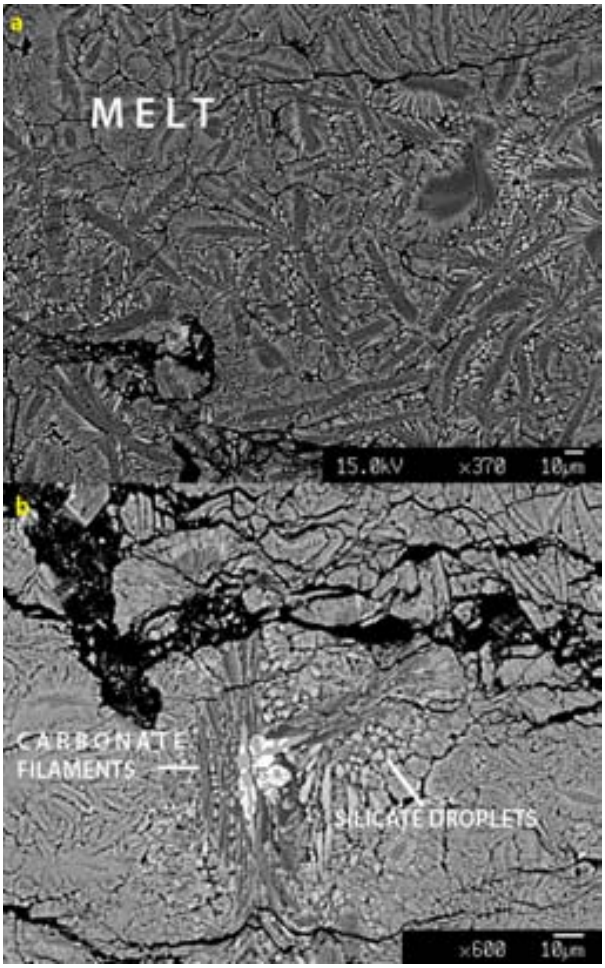

Fig. 4.51. Detail of carbonatitic liquid (a) and the carbonate filaments and silicate droplets structures (b).

LSI_15

LSI_15 experiment was performed using a platinum preconditioned capsule without graphite sleeve. In order to try to avoid the periclase globules we added quartz powder at the starting material to equilibrate the magnesium excess due to the brucite and magnesite presence. To control the oxygen fugacity, we used a graphite stopper at the bottom of the capsule before the welding.

The run time of this experiment was of 30 hours.

We observed olivine, orthopyroxene and carbonatitic liquids as quenched phase in this capsule after run (Fig. 4.52).

The olivine present in the dunite rod shows strong zoning and grain growth having size up to ~ 400 μm. Olivine grains have euhedral and subhedral shape and planar grain boundaries, forming triple junctions at the solid-solid interface. Along the olivine grain boundaries and into the triangular spaces formed by triple junctions it's possible to observe carbonatitic melt pockets infiltrated during the H*P* – H*T* run (Fig. 4.53).

The quenching phase is represented by carbonatitic liquid composition also and orthopyroxene with polygonal shape and size of ~ 10 μm, crystallized by magnesium excess and quartz interaction (Fig. 4.54a and 4.54b in detail). The entire capsule is formed by ~ 80 % of silicate phases (olivine and orthopyroxene) and the rest by carbonatitic liquids and graphite stopper.

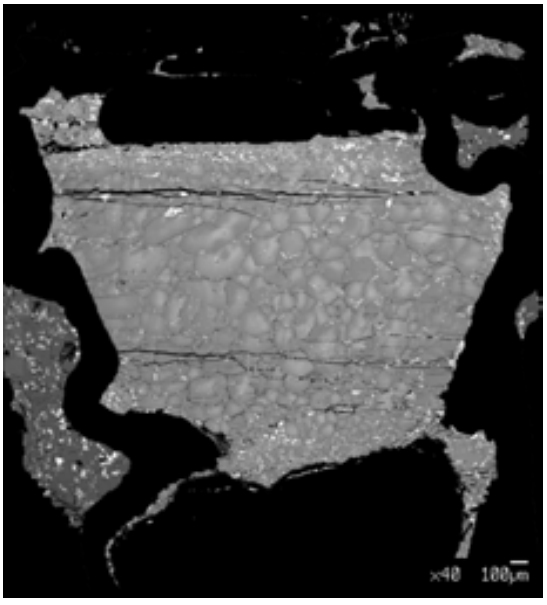

Fig. 4.52. BSE image of experimental run LSI_15.

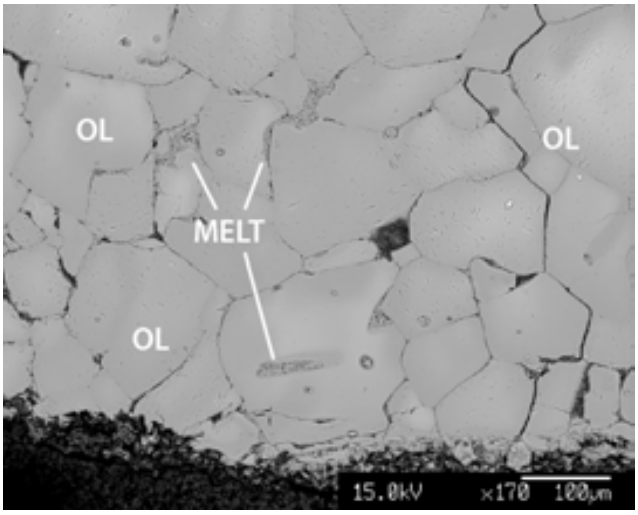

Fig. 4.53. Melt pockets of carbonatitic melt inside the dunite rod.

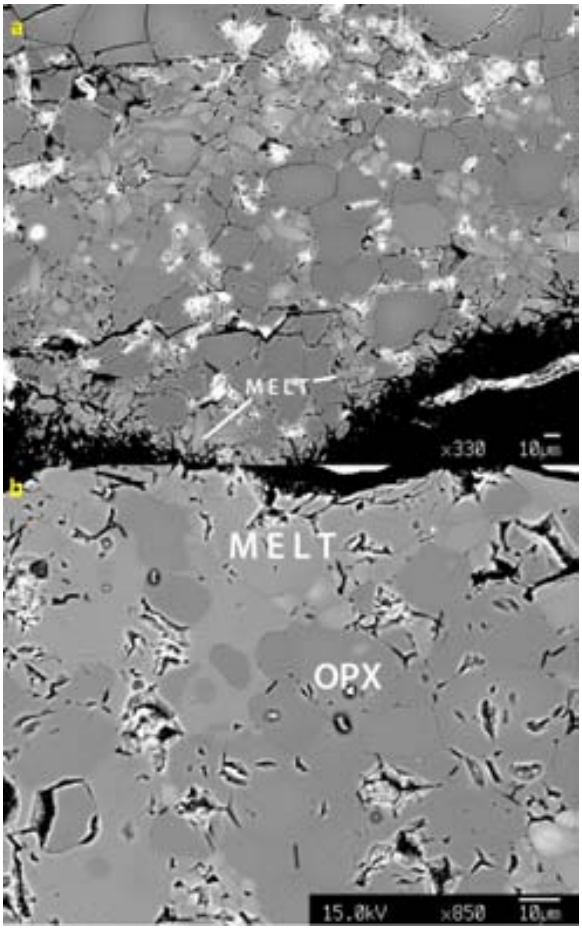

Fig. 4.54. Reaction orthopyroxene with the melts (a) and detail in (b).

LSI_16

The LSI_16 experiment setup was the same of LSI_15 but using a smaller graphite stopper. The products are olivine from the dunite rod, clinopyroxene, Cr-spinel and quenching liquids (Fig. 4.55).

Also in this case olivine grains result strong zoning with size from 50 to > 100 µm. Olivine crystals have subhedral and from lobated to straight shape and the equilibrium conditions are evidenced by triple joints presence (Fig. 4.56a). Perfect euhedral olivine grains with size < 35 µm and without zoning are present at the bottom of the dunite rod into carbonatitic quench products (Fig. 4.56b).

The carbonatitic liquids found in the run charge, representative of 40 vol.% of entire capsule are present at the bottom and at the top of the capsule too and show the typical dendritic texture (Fig.

4.57a). Furthermore, carbonatitic melt pockets were found inside the dunite rod as infiltrated phase (Fig. 4.57b).

By interactions of magnesium in brucite, silica in quartz, and calcium in calcite polygonal clinopyroxene crystals with size < 10 μm cumulated in some portions of the capsule (Fig. 4.58a). Clinopyroxene is present like poikilitic texture (size between 0.3 μm to 8-10 μm) inside oikocrysts of olivine (Fig. 4.58b).

By means Cr X-ray maps it was possible to observe the presence of Cr-spinel.

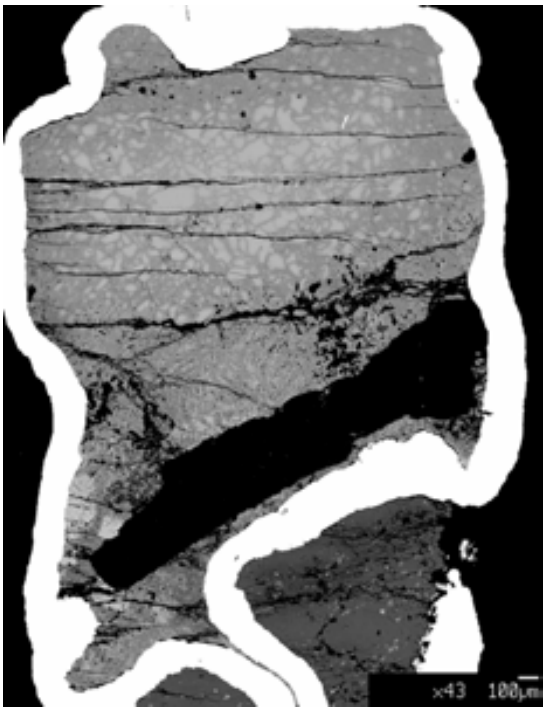

Fig. 4.55. BSE image of experimental run LSI_16.

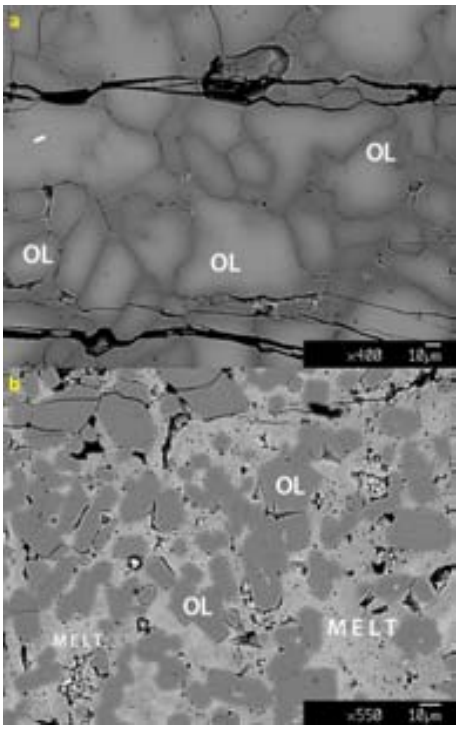

Fig. 4.56. Detail of zoning olivine crysts (a); new euhedral olivine microcrysts into the melt (b).

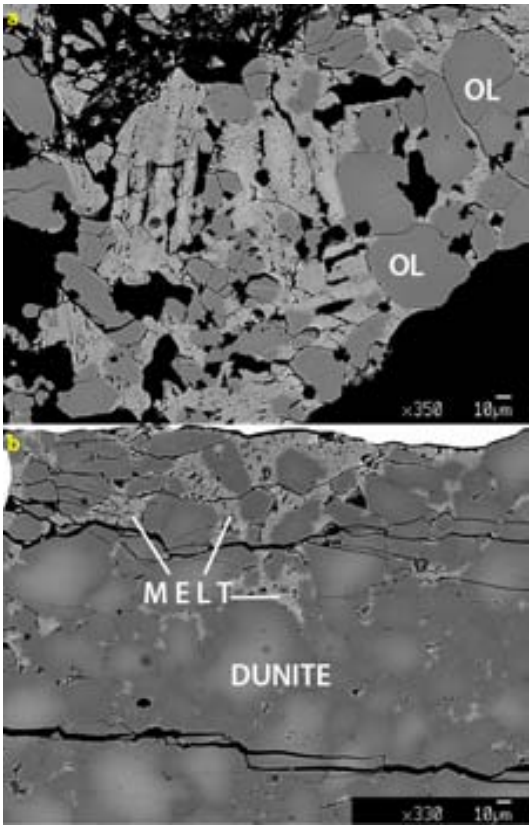

Fig. 4.57. Contact from olivine grains and dendritic liquid (a); carbonatite infiltrated inside the dunite rod (b).

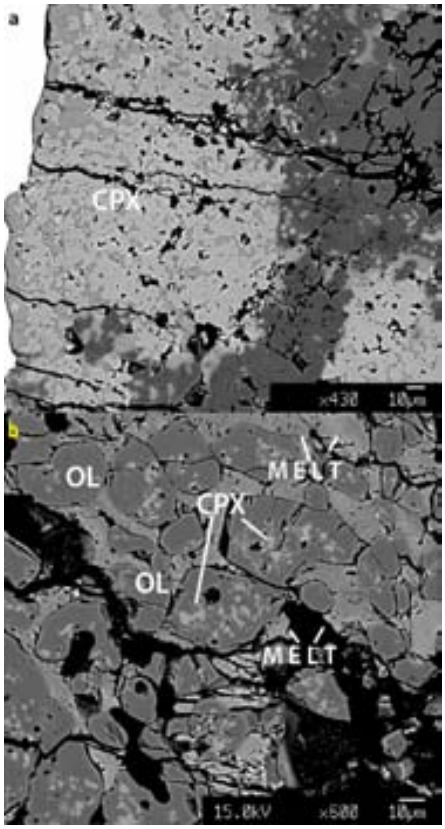

Fig. 4.58. Cumulate of clinopyroxene microcrysts at the edge of the capsule (a); poikilitic clinopyroxene into the olivine oikocrysts (b).

LSI_17

The third experiment with the same capsule setup was LSI_17. The difference compared to the others was the run time, in fact this experiment should have 300-hour duration but it quenched after 164 hours.

By electron microprobe analysis the phases present in this experiment were identified as olivine clinopyroxene, orthopyroxene representative of approximatively 50 vol.% of the entire capsule. The other 50 vol.% is represented by quench phases.

This run is characterized by dissolution-reprecipitation process, in fact the dunite rod is divided into two portions at the top and at the bottom of the capsule (Fig. 4.59). Both above and below the olivine crystals do not show zoning and are characterized by strong grain growth with grains reaching size > 300 μm. These crystals have euhedral and subhedral texture with lobated and planar shape (Fig. 4.60).

Clinopyroxene are present as poikilitic crystals inside olivine grains of dunite at the bottom of the capsule and size of between ~ 4 μm to ~ 35 μm (Fig. 4.61a).

By means of BSE images we could appreciate differences by olivine (light grey) and orthopyroxene (dark grey) and then discriminate these phases by chemical analysis. Orthopyroxene is present at the contact with olivine grains at the bottom of the capsule and also present as big polygonal crystals (until > 600 μm) with planar subhedral shape (Fig. 4.61b).

Carbonatitic liquids are present as quenched products between dunite rods, with typical dendritic texture, and filaments (Fig. 4.62a). In a several cases it is possible to observe elongated olivine phase enveloped by carbonatitic liquids (Fig. 4.62b). Carbonatitic melt pockets were found like infiltrate phase inside the dunite rod also (Fig. 4.63, in yellow).

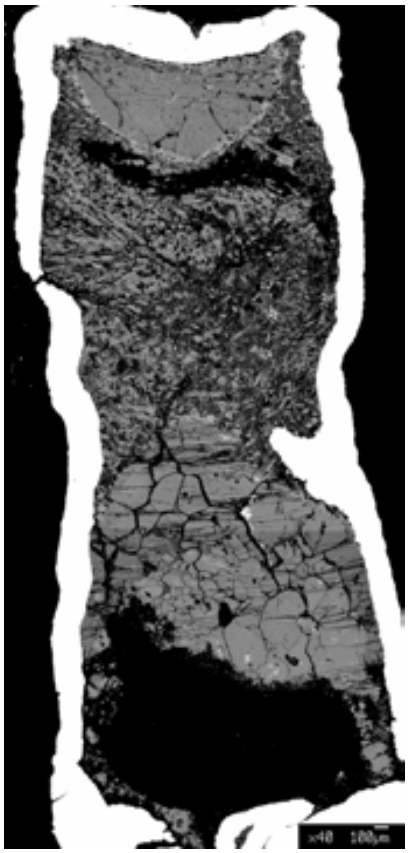

Fig. 4.59. BSE image of experimental run LSI_17.

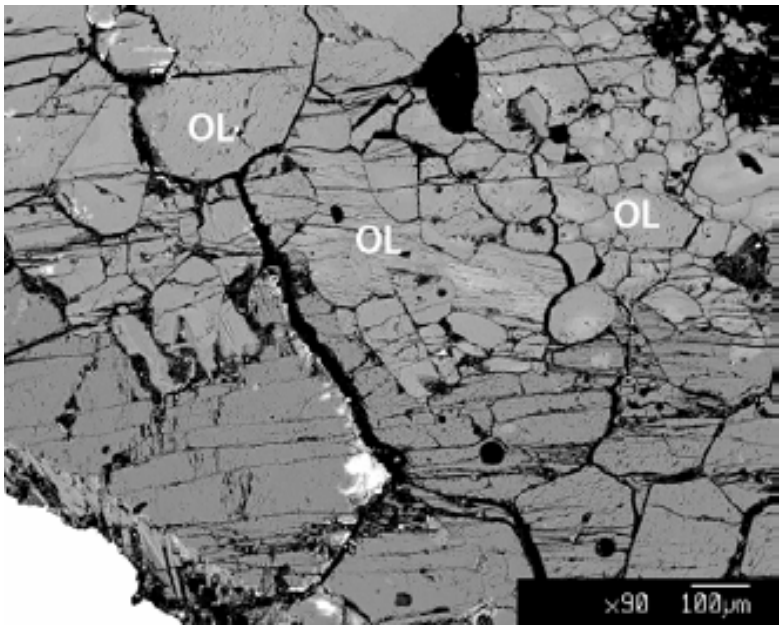

Fig. 4.60. Detail of olivine megacrysts at the bottom of the capsule.

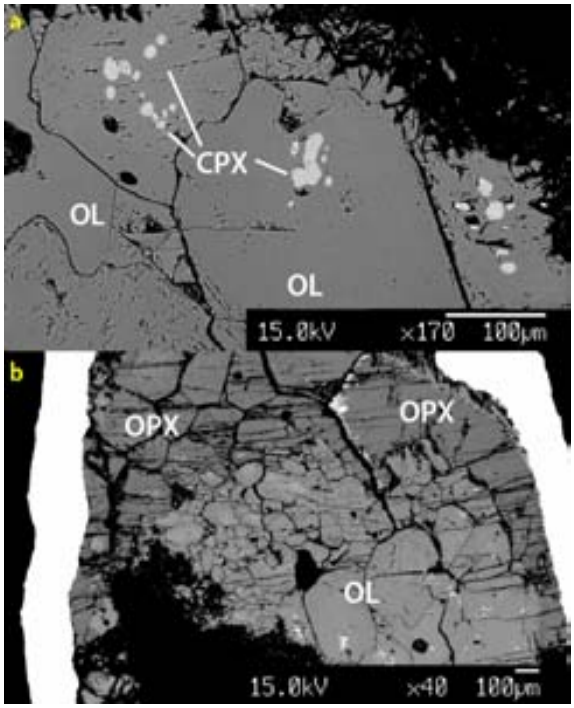

Fig. 4.61. BSE image shows poikilitic clinopyroxene into the olivine grains (a); contact between olivine (light grey) and orthopyroxene (dark grey).

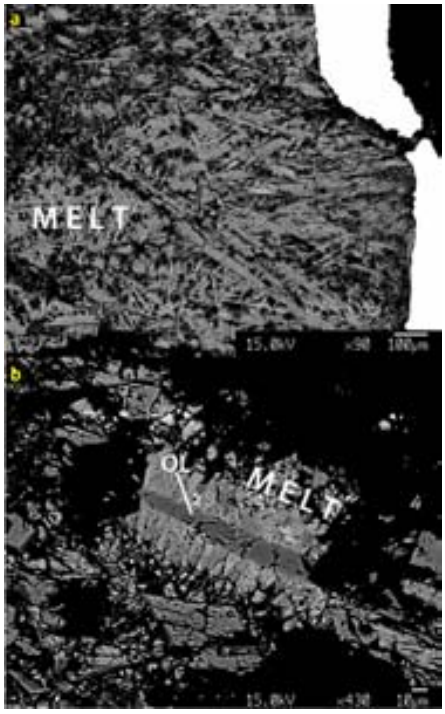

Fig. 4.62. Dendritic texture of carbonatitic liquid (a); elongated ne olivine surrounded by carbonatitic melt (b).

Fig. 4.63. Ca X-ray map that shows the infiltration of carbonatitic melt (yellow) into the olivinic matrix (black).

LSI_18 – LSI_19

LSI_18 and LSI_19 experiments are the same experiments with the same starting material and capsule material and setup and the same run time of 48 hours. For these two experiments we used 30 wt. % of water content. The only difference between LSI_18 and LSI_19 samples was the amount of carbonate mix powder, with the aim of attempting to pierce the capsule at the Capsule Piercing QMS device.

LSI_18 experiment presents olivine grains with minor zoning (Fig. 4.64). These olivine crystals have not suffered much grain growth having size until ~ 100 μm. Crystal shapes are euhedral and planar boundaries and the equilibrium is suggested by presence of triple junctions (Fig. 4.65).

Quench phases are represented by carbonates and silicates with typical dendritic textures (Fig. 4.66). By means of BSE images from EMPA (Fig. 4.67a) and Ca X-ray maps (Liquid phase in yellow/orange colours; Fig. 4.67b) it was possible to appreciate how the carbonate liquid is also present as infiltrated melt pockets phase between 120° triple joints or along olivine grain boundaries forming carbonatitic channel interconnected.

Approximate volume of carbonatitic phase in the run charge, located at the top, at the bottom and at the sides of the dunite rod, is almost 10 vol.% and the rest, represented by the dunite rod is ~ 90 vol.% of the entire capsule.

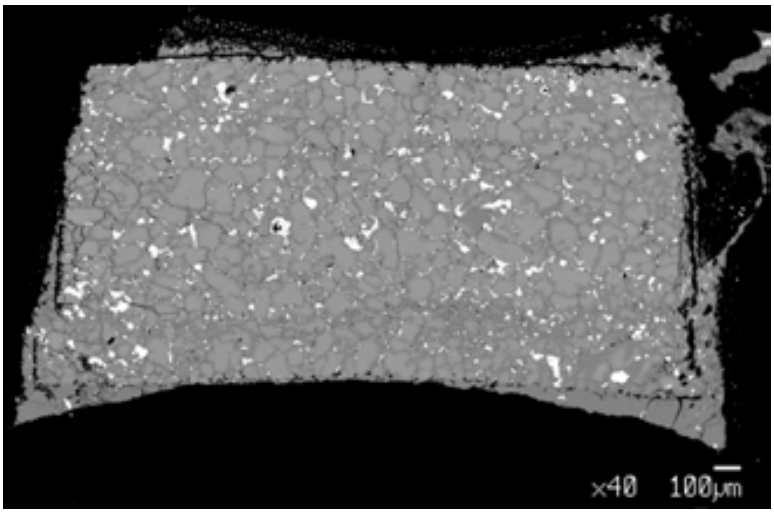

Fig. 4.64. BSE image of experimental run LSI_18.

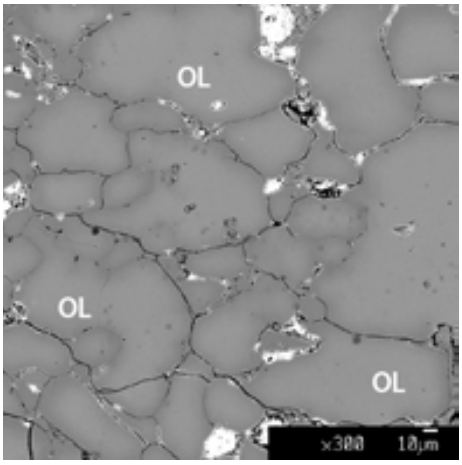

Fig. 4.65. Detail of olivine grains.

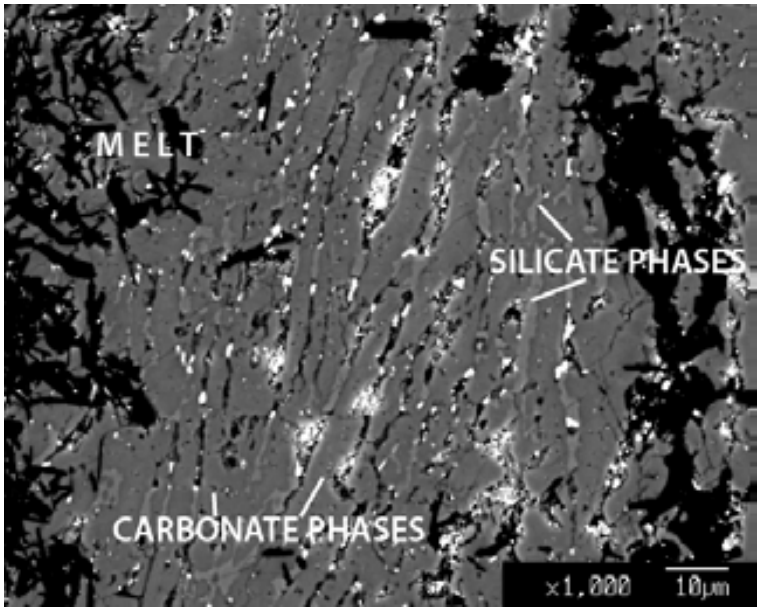

Fig. 4.66. Carbonatitic melts with clear difference between silicate and carbonate phases.

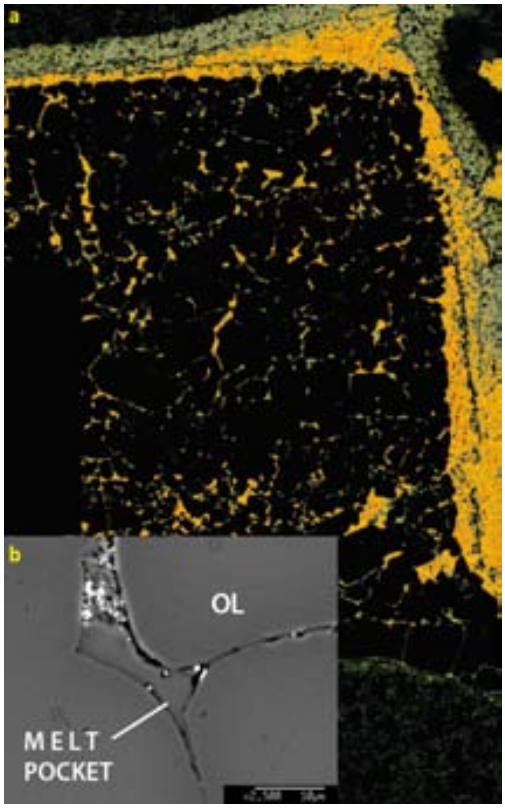

Fig. 4.67. Ca X-ray map that shows carbonatitic liquid infiltrated (a); BSE detail of carbonatitic melt pocket along olivine grain boundaries (b).

Like LSI_18 experiment, LSI_19 sample shows a dunite rod with olivine crystals slightly zoned but with a greater growth, in fact in this case the olivine grains show size up to 500 µm (Fig. 4.68). Also in this case these crystals form a subhedral texture with planar faces and triple joints (Fig. 4.69).

The silicate phases are represented not only by olivine but also by orthopyroxene and clinopyroxene with Al_2O_3 probably due to a presence of spinel inclusions into the original natural San Carlos olivine.

The quench phases, present around the dunite rod like the previous experiment, are represented by skeletal dendritic silicate and carbonate phases (Fig. 4.70). The melt was present inside the dunite matrix along olivine grain boundaries or inside olivine triple junctions (Fig. 4.71a and 4.71b).

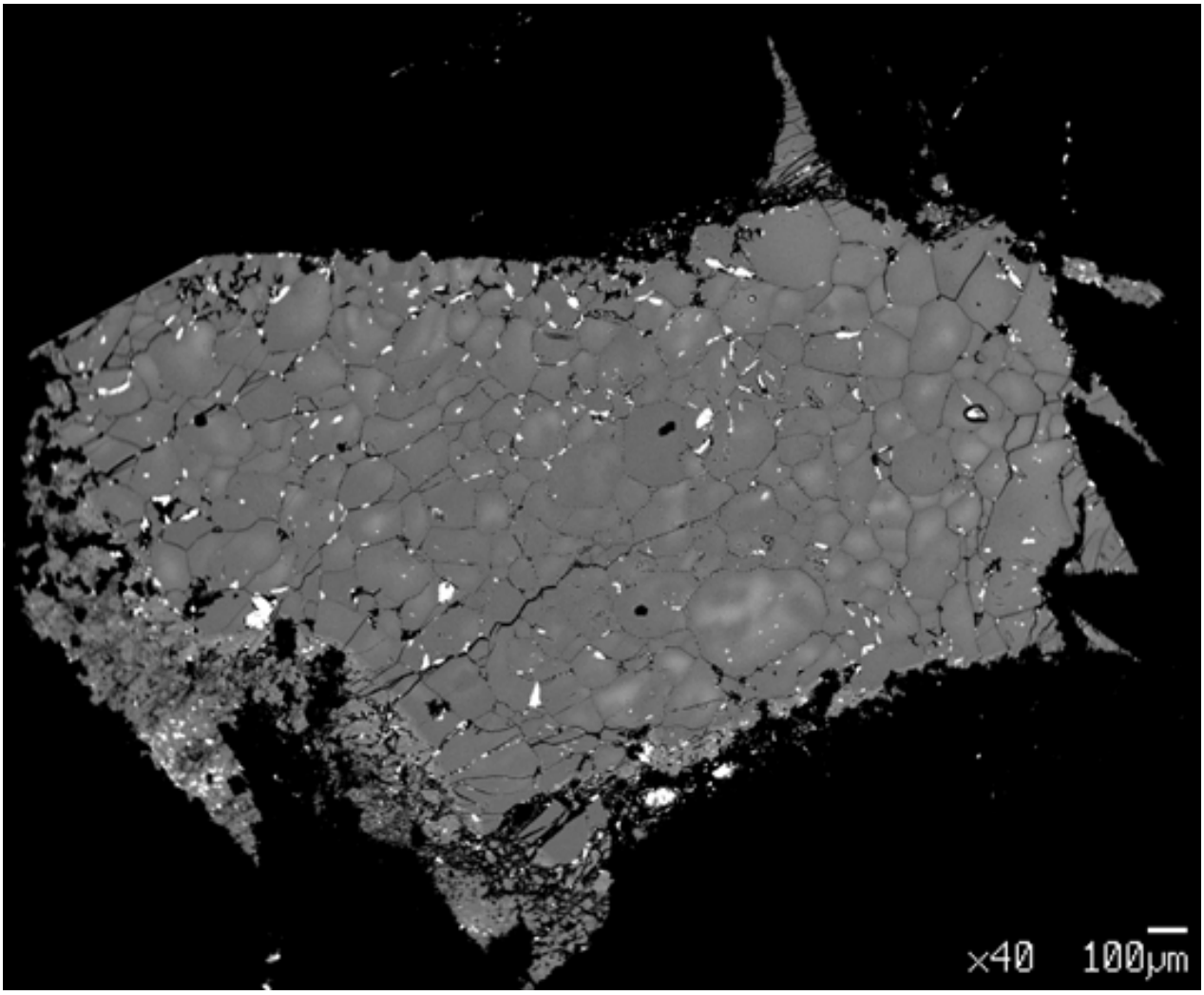

Fig. 4.68. BSE image of experimental run LSI_19.

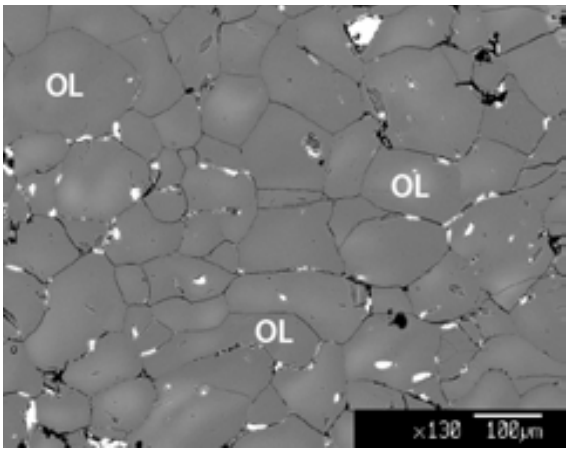

Fig. 4.69. Euhedral and subhedral olivine crystals in LSI_19 sample.

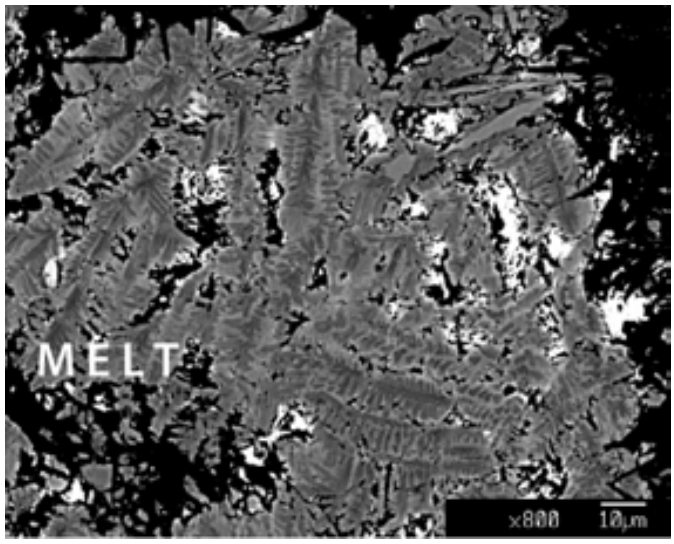

Fig. 4.70. Skeletal dendritic texture of carbonatitic melts in LSI_19 experiment.

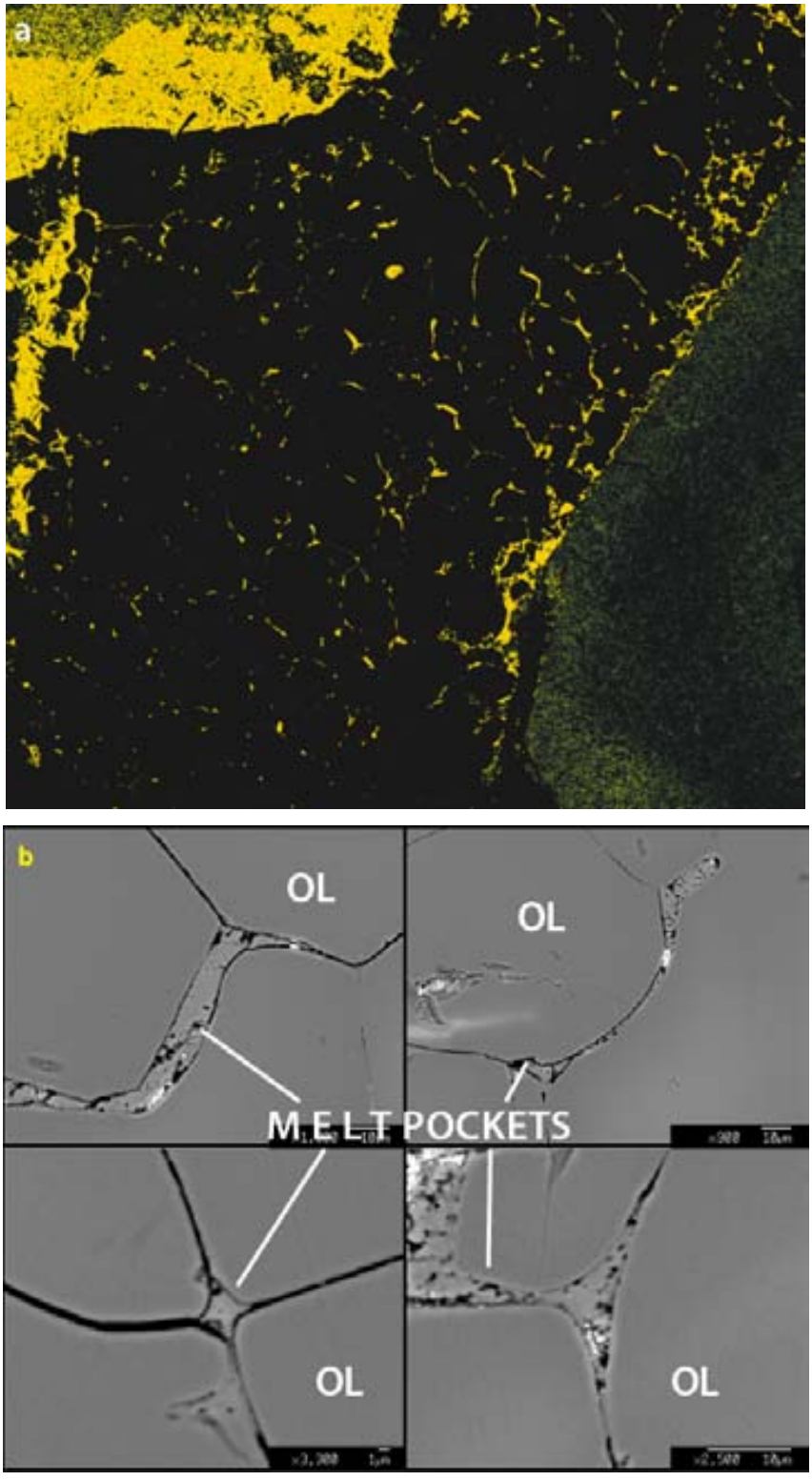

Fig. 4.71. Calcium X-ray map of LSI_19 experiment shows the carbonatite inside the dunite rod (a); four BSE images of carbonatite molten pockets inside the dunite (b).

4.3. Mineral chemistry

4.3.1. Silicate phases

Olivine

Average compositions of olivine crystals from each experimental run are listed in Table 4.2.
Olivine crystals are present in all experiments and are characterized by a Mg composition with a forsterite content ranging from Fo_{82} to Fo_{99}. Compared with San Carlos olivine X_{Mg} value (X_{Mg} = $Mg/Mg+Fe_{tot}$ = 0.898) it is possible to note a large variability mainly for a presence of strong zoning olivine due to a loss of iron of the most analyzed samples (Fig. 4.72).
The highest X_{Mg} values are usually representative of the crystal core that have suffered less iron loss than the crystal rim. The most homogeneous crystals are actually those that lost most of their iron (eg. LSI_17 with FeO ranging from 0.42 to 1.32 wt. % and X_{Mg} of ~ 0.99). FeO average content is 6.86 wt. %, spanning from < 1 (complete loss of iron) to 11 wt. %, the latter value still low respect San Carlos olivine iron content. SiO_2, MgO and CaO average contents in olivine are respectively of 41.25, 51.12 and ~ 0.13 wt. %..

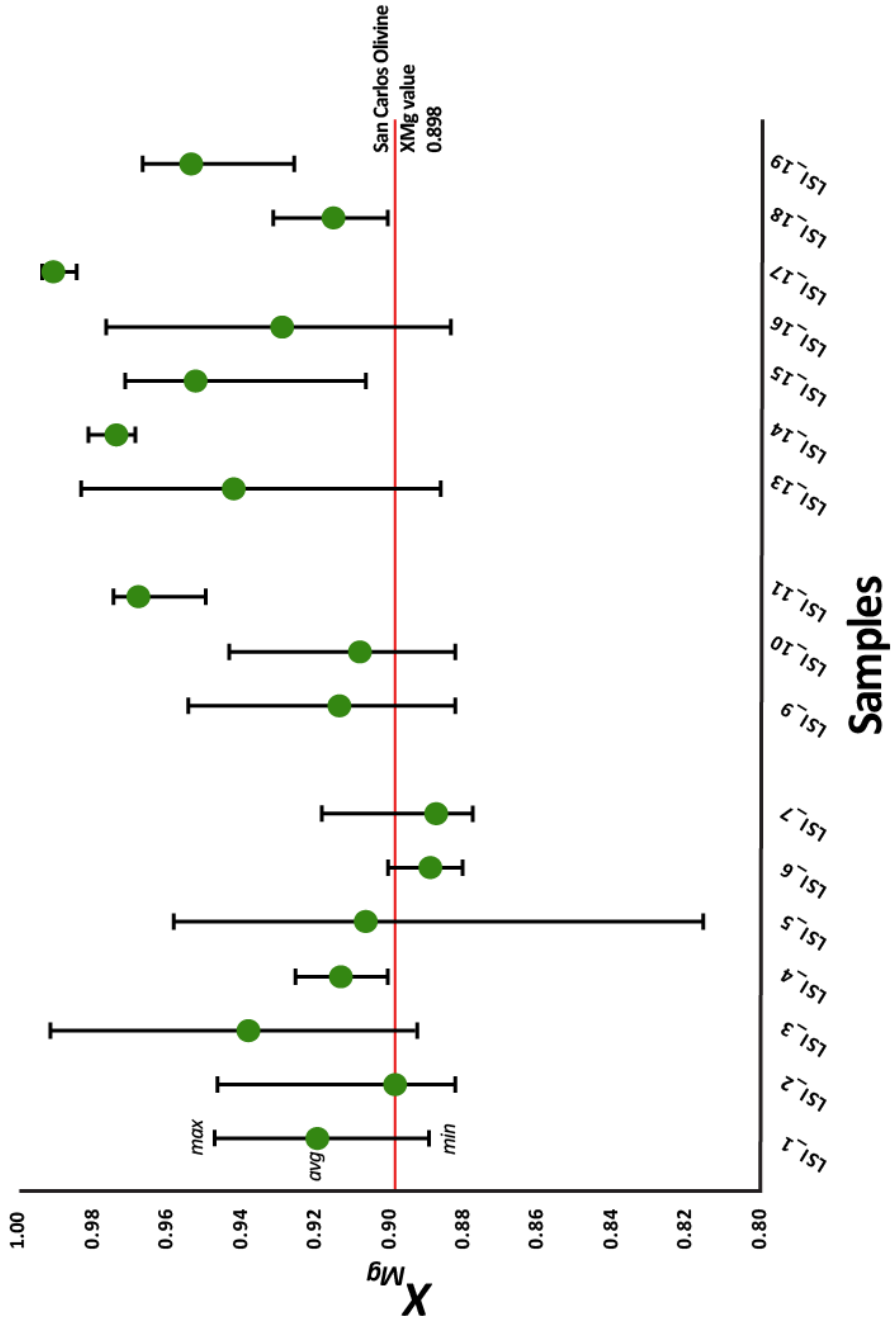

Fig. 4.72. Binary diagram of X_{Mg} values sample by sample related of X_{Mg} San Carlos Olivine value (red line). The ranges represented by black line show the maximum and the minimum forsteritic component and green circles the average values sample by sample.

Run:	LSI_1		LSI_2		LSI_3		LSI_4		LSI_5		LSI_6		LSI_7		LSI_9		LSI_10	
P (GPa)	2.5		2.5		2.5		2.5		2.5		2.5		2.5		2.5		2.5	
T (C)	1200		1200		1200		1200		1100		1200		1200		1200		1200	
	mean	± σ	mean	± σ	mean	± σ	mean	± σ	mean	± σ	mean	± σ	mean	± σ	mean	± σ	mean	± σ
n:	18		27		16		35		19		26		19		17		14	
Oxides (wt.%)																		
SiO_2	41.21	0.88	41.20	0.44	41.56	0.47	40.65	0.53	40.85	0.47	40.59	0.31	39.42	0.35	41.17	0.51	41.33	0.32
Al_2O_3	0.03	0.02	0.02	0.02	0.02	0.02	0.02	0.02	0.02	0.02	0.04	0.02	0.05	0.04	0.02	0.02	0.03	0.02
FeO	7.00	2.15	8.63	1.47	5.79	3.42	7.96	0.59	7.41	1.84	10.16	0.69	10.17	0.88	7.96	3.04	8.38	2.08
MgO	50.99	1.68	49.80	1.32	51.83	2.19	50.10	0.64	49.82	1.64	49.06	0.70	48.60	0.74	50.86	2.26	50.17	1.74
CaO	0.18	0.10	0.11	0.04	0.13	0.11	0.11	0.04	0.07	0.03	0.11	0.03	0.11	0.03	0.09	0.02	0.15	0.22
Na_2O	_	_	0.05	0.05	_	_	_	_	_	_	_	_	0.03	0.03	_	_	_	_
K_2O	_	_	_	_	_	_	_	_	_	_	_	_	_	_	_	_	_	_
TiO_2	_	_	_	_	_	_	_	_	_	_	_	_	0.04	0.05	_	_	_	_
MnO	0.15	0.03	0.14	0.03	0.12	0.04	0.15	0.04	0.16	0.03	0.14	0.03	0.16	0.05	0.19	0.06	0.14	0.06
NiO	0.58	0.42	1.01	0.28	_	_	0.19	0.11	0.33	0.07	0.36	0.04	0.34	0.07	0.24	0.14	0.27	0.09
Cr_2O_3	_	_	_	_	_	_	0.03	0.03	_	_	_	_	0.03	0.03	0.03	0.03	0.03	0.02
Total	100.13	_	101.00	_	99.47	_	99.23	_	98.70	_	100.53	_	98.96	_	100.58	_	100.51	_
a.p.f.u.																		
Si	1.00	0.01	1.00	0.02	1.01	0.02	1.00	0.01	1.01	0.01	0.99	0.00	0.98	0.01	0.99	0.01	1.00	0.00
Al	0.00	0.00	0.00	0.00	0.00	0.00	0.00	0.00	0.00	0.00	0.00	0.00	0.00	0.00	0.00	0.00	0.00	0.00
Fe	0.14	0.04	0.17	0.03	0.12	0.07	0.16	0.01	0.15	0.04	0.21	0.01	0.21	0.02	0.16	0.06	0.17	0.04
Mg	1.84	0.05	1.80	0.03	1.87	0.06	1.83	0.02	1.83	0.04	1.79	0.02	1.79	0.02	1.83	0.06	1.81	0.05
Ca	0.00	0.00	0.00	0.00	0.00	0.00	0.00	0.00	0.00	0.00	0.00	0.00	0.00	0.00	0.00	0.00	0.00	0.01
Na	_	_	0.00	0.00	_	_	_	_	_	_	_	_	0.00	0.00	_	_	_	_
K	_	_	_	_	_	_	_	_	_	_	_	_	_	_	_	_	_	_
Ti	_	_	_	_	_	_	_	_	_	_	_	_	0.00	0.00	_	_	_	_
Mn	0.00	0.00	0.00	0.00	0.00	0.00	0.00	0.00	0.00	0.00	0.00	0.00	0.00	0.00	0.00	0.00	0.00	0.00
Ni	0.01	0.01	0.02	0.01	_	_	0.00	0.00	0.01	0.00	0.01	0.00	0.01	0.00	0.00	0.00	0.01	0.00
Cr	_	_	_	_	_	_	0.00	0.00	_	_	_	_	0.00	0.00	0.00	0.00	0.00	0.00
xMg	0.92	_	0.90	_	0.94	_	0.91	_	0.92	_	0.89	_	0.89	_	0.91	_	0.91	_
xFe	0.07	_	0.09	_	0.06	_	0.08	_	0.08	_	0.10	_	0.10	_	0.08	_	0.09	_

Table. 4.2. Average composition of olivine crystals in selected runs. Fe is reported as total iron. n, number of analysis.

Table. 4.2. Continued.

Run:	LSI_11		LSI_13		LSI_14		LSI_15		LSI_16		LSI_17		LSI_18		LSI_19	
P (GPa)	2.5		2.5		2.5		2.5		2.5		2.5		2.5		2.5	
T (C)	1200		1200		1200		1200		1200		1200		1200		1200	
	mean	± σ	mean	± σ	mean	± σ	mean	± σ	mean	± σ	mean	± σ	mean	± σ	mean	± σ
n:	10		34		10		13		10		10		30		30	
Oxides (wt.%)																
SiO_2	41.09	1.04	41.78	0.78	42.32	0.16	41.72	0.53	41.53	0.64	43.18	0.55	41.00	0.38	41.87	0.44
Al_2O_3	0.02	0.02	0.04	0.02	0.02	0.01	0.02	0.02	0.02	0.01	0.00	0.00	0.02	0.02	0.01	0.02
FeO	2.26	0.98	5.33	3.03	2.36	0.38	4.33	2.01	6.25	3.41	0.61	0.30	8.03	1.21	4.30	1.11
MgO	54.26	0.70	51.08	2.60	55.67	0.47	54.17	1.70	51.82	2.74	55.23	0.32	51.08	0.97	53.53	1.02
CaO	0.53	0.32	0.14	0.13	0.06	0.00	0.02	0.01	0.12	0.04	0.13	0.10	0.14	0.13	0.12	0.16
Na_2O	–	–	0.05	0.11	–	–	–	–	0.05	0.03	–	–	–	–	–	–
K_2O	–	–	–	–	–	–	–	–	–	–	–	–	–	–	–	–
TiO_2	–	–	–	–	–	–	–	–	–	–	–	–	–	–	–	–
MnO	0.17	0.05	0.14	0.03	0.09	0.03	0.13	0.04	0.21	0.05	0.12	0.04	0.17	0.05	0.16	0.04
NiO	0.03	0.03	0.20	0.13	0.11	0.03	0.27	0.09	0.24	0.17	–	–	–	–	–	–
Cr_2O_3	0.04	0.04	–	–	–	–	0.03	0.03	0.04	0.03	0.05	0.06	0.03	0.03	0.03	0.04
Total	98.43	–	98.81	–	100.68	–	100.74	–	100.30	–	99.32	–	100.49	–	100.04	–
a.p.f.u.																
Si	0.99	0.02	1.02	0.01	1.00	0.01	0.99	0.01	1.00	0.00	1.03	0.01	0.99	0.01	1.00	0.01
Al	0.00	0.00	0.00	0.00	0.00	0.00	0.00	0.00	0.00	0.00	0.00	0.00	0.00	0.00	0.00	0.00
Fe	0.05	0.02	0.11	0.06	0.05	0.01	0.09	0.04	0.13	0.07	0.01	0.01	0.16	0.03	0.09	0.02
Mg	1.95	0.03	1.86	0.07	1.95	0.01	1.91	0.04	1.86	0.07	1.96	0.01	1.84	0.02	1.91	0.02
Ca	0.01	0.01	0.00	0.00	0.00	0.00	0.00	0.00	0.00	0.00	0.00	0.00	0.00	0.00	0.00	0.00
Na	–	–	0.00	0.00	–	–	–	–	0.00	0.00	–	–	–	–	–	–
K	–	–	–	–	–	–	–	–	–	–	–	–	–	–	–	–
Ti	–	–	–	–	–	–	–	–	–	–	–	–	–	–	–	–
Mn	0.00	0.00	0.00	0.00	0.00	0.00	0.00	0.00	0.00	0.00	0.00	0.00	0.00	0.00	0.00	0.00
Ni	0.00	0.00	0.00	0.00	0.00	0.00	0.01	0.00	0.00	0.00	–	–	–	–	–	–
Cr	0.00	0.00	–	–	–	–	0.00	0.00	0.00	0.00	0.00	0.00	0.00	0.00	0.00	0.00
xMg	0.97	–	0.94	–	0.97	–	0.95	–	0.93	–	0.99	–	0.91	–	0.95	–
xFe	0.02	–	0.06	–	0.02	–	0.04	–	0.06	–	0.01	–	0.08	–	0.04	–

Pyroxene

In several experimental samples we found orthopyroxene and clinopyroxene. The average compositions of pyroxenes are listed in table 4.3.

The orthopyroxene was present in LSI_5, LSI_10, LSI_15, and LSI_17 experiments and are Mg-rich and can be classified as enstatite following the Morimoto et al. (1988) classification scheme (Fig. 4.74). The X_{Mg} is rather constant and ranges from 0.93 to 0.97. SiO_2 ranges from ~ 54 wt. % to ~ 64 wt. %, MgO from ~ 33 wt. % to ~ 38 wt. % and calcium oxide from <1 wt. % to rather high maximum value of ~ 3 wt. %.

Clinopyroxene was found in LSI_5, LSI_16, LSI_17 and LSI_19 experiments and can be classified as augite except one diopside (Fig. 4.73). Clinopyroxene crystals have X_{Mg} values between 0.86 to 0.99. The SiO_2 content range from 50 to 57 wt. % and MgO from 15 to 24 wt. %. Calcium content values are from 18 to 24 wt. %. Alumina was found only in LSI_5 and LSI_19 clinopyroxene, probably due to spinel inclusions in natural San Carlos olivine and have contents between 2.6 to 9 wt. %, tending to be higher in experiment LSI_19 with 30 wt. % of water content.

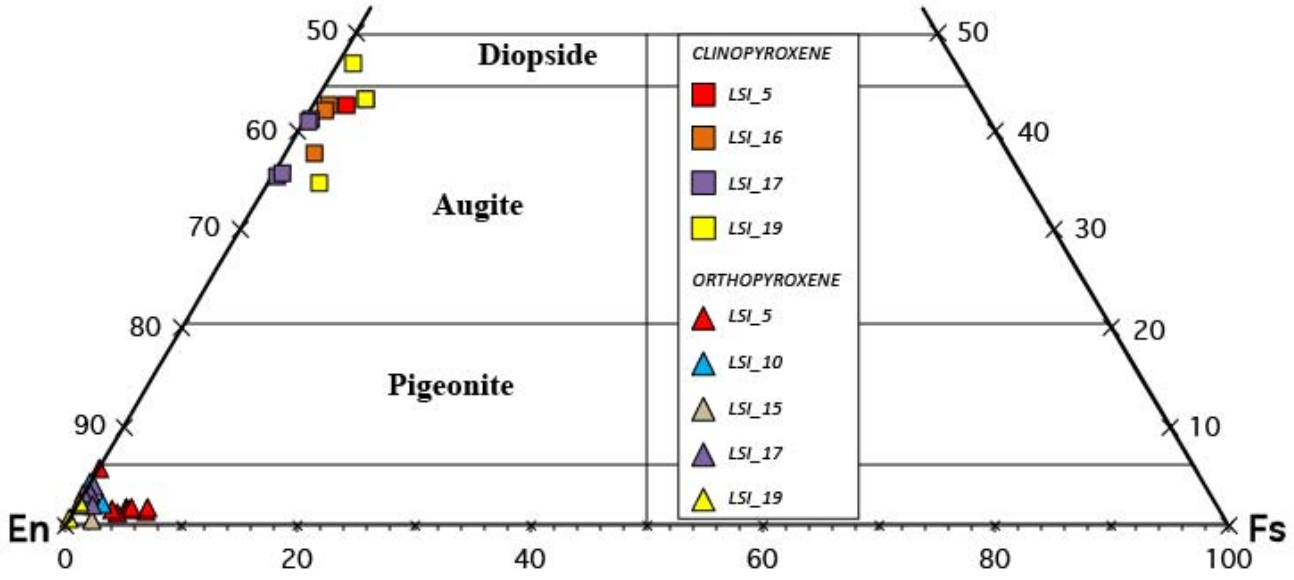

Fig. 4.73. Chemical composition of the experimental orthopyroxene and clinopyroxene crystals in the classification scheme of Morimoto et al. (1988).

Orthopyroxene							Clinopyroxene			
Run:	LSI_5		LSI_10	LSI_15	LSI_17		LSI_5	LSI_16	LSI_17	LSI_19
P (GPa)	2.5		2.5	2.5	2.5		2.5	2.5	2.5	2.5
T (C)	1100		1200	1200	1200		1100	1200	1200	1200
	mean	± σ	mean		mean	± σ		mean	mean	mean
n:	8		2	1	8		1	3	4	3
Oxides (wt.%)										
SiO_2	57.16	1.32	56.89	59.28	60.00	2.05	54.26	55.95	55.95	50.98
Al_2O_3	0.82	0.44	1.09	0.58	0.01	0.02	2.60	0.25	0.25	4.99
Fe_2O_3	0.22	0.61	1.83	0.00	0.14	0.25	_	0.19	0.19	1.66
FeO	2.77	1.29	0.73	1.53	0.38	0.28	1.71	1.20	1.20	2.29
MgO	35.31	0.80	36.48	38.19	37.33	0.66	17.73	21.25	21.25	16.93
CaO	1.10	0.76	1.67	0.21	1.51	0.36	19.98	21.06	21.06	20.92
Na_2O	0.07	0.02	0.21	0.05	_	_	1.10	0.06	0.06	0.16
K_2O	_	_	_	_	_	_	_	_	_	_
TiO_2	_	_	_	0.04	_	_	_	_	_	_
MnO	0.17	0.05	0.10	0.13	0.17	0.03	0.20	0.28	0.28	0.53
NiO	0.06	0.05	_	0.06	_	_	_	_	_	_
Cr_2O_3	0.22	0.16	_	0.19	0.07	0.04	0.68	_	_	0.06
Total	97.89	_	99.01	100.26	99.66	_	98.30	100.30	100.30	98.53
a.p.f.u.										
Si	1.99	0.03	1.95	2.00	2.03	0.05	1.98	2.00	2.00	1.88
Al	0.03	0.02	0.04	0.02	0.00	0.00	0.11	0.01	0.00	0.22
Fe^{3+}	0.01	0.02	0.05	0.00	0.00	0.01	0.00	0.01	0.00	0.05
Fe^{2+}	0.08	0.04	0.02	0.04	0.01	0.01	0.05	0.04	0.01	0.07
Mg	1.83	0.04	1.86	1.92	1.89	0.04	0.96	1.13	1.22	0.93
Ca	0.04	0.03	0.06	0.01	0.05	0.01	0.78	0.81	0.76	0.83
Na	0.00	0.00	0.01	0.00	_	_	0.08	0.00	0.00	0.01
K	_	_	_	_	_	_	_	_	_	_
Ti	_	_	_	0.00	_	_	_	_	_	_
Mn	0.01	0.00	0.00	0.00	0.00	0.00	0.01	0.01	0.01	0.02
Ni	0.00	0.00	_	0.00	_	_	_	_	_	_
Cr	0.01	0.00	_	0.01	0.00	0.00	0.02	_	_	0.00
xMg	0.96	_	0.97	0.98	0.99	_	0.95	0.97	0.99	0.93

Table. 4.3. Average compositions of orthopyroxene and clinopyroxene crystals in selected runs. X_{Mg} values are calculated using Fe_{tot}. n, number of analysis.

4.3.2. Oxide phases

Spinel

Spinel crystals are present in LSI_2, LSI_7, LSI_13 (found by means of Cr X-ray map but not analyzed) and LSI_16 experiments as Chromium-spinel (Fig. 4.74), probably due to inclusion presence in natural San Carlos olivine. These spinel crystals are Al-rich with range from 36 to 41 wt. % and have X_{Mg} of ~ 0.78 and X_{Cr} (X_{Cr} = Cr/Cr+Al) of ~ 0.35, according to chromium number for abyssal peridotites (Fig. 4.75; Dick and Bullen, 1984; Voigt and von der Handt, 2011). Their TiO_2 content is low with < 0.3 wt. %. The Cr average content is 30.3 wt. % and Fe_{tot} ~ 10/11 wt. %. MgO ranging from 18 to 20 wt.%.

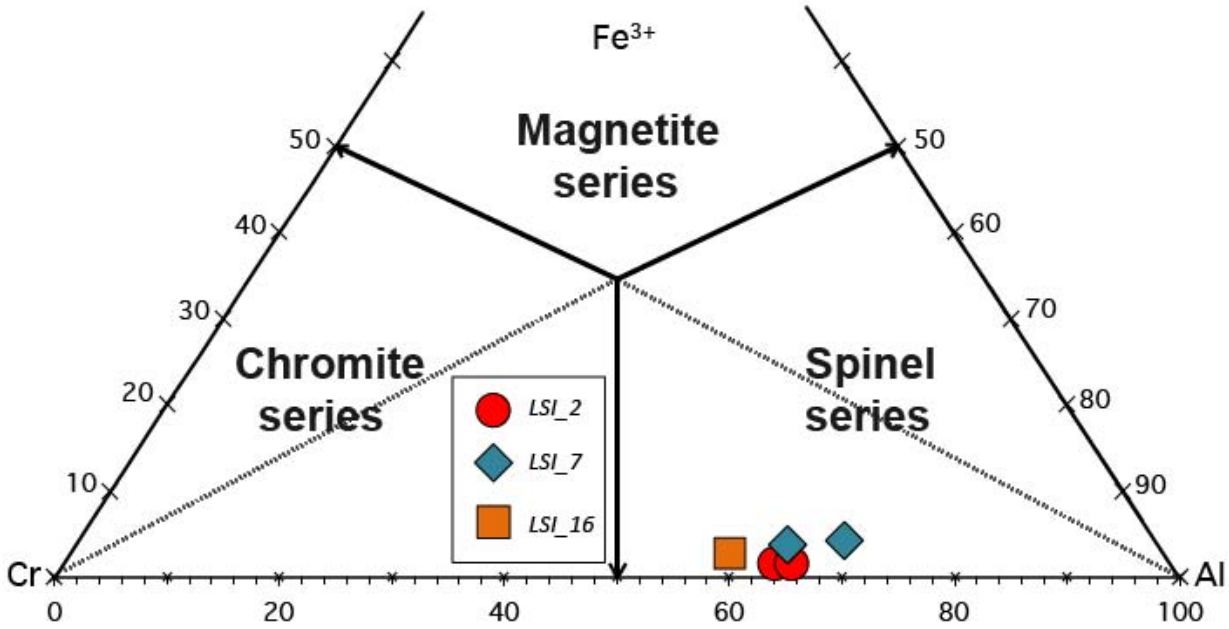

Fig. 4.74. Chemical composition of the experimental Cr-spinel in the classification scheme of Stevens (1944).

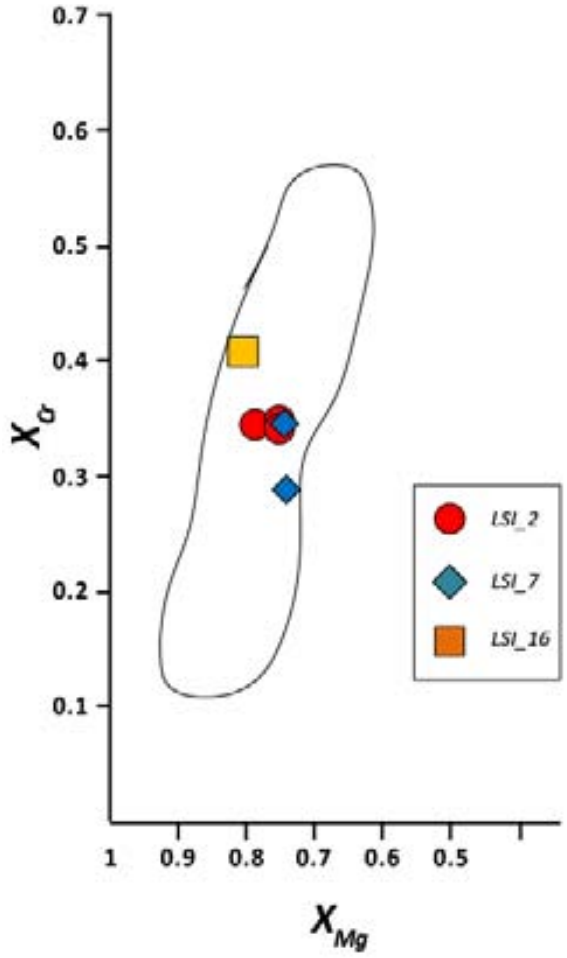

Fig. 4.75. X_{Mg} vs. X_{Cr} spinel composition plotted with X_{Mg}-X_{Cr} abyssal peridotites field closed with black line.

Run:	LSI_2	LSI_7
P (GPa)	2.5	2.5
T (C)	1200	1200
	mean	mean
n:	3	2
Oxides (wt.%)		
SiO_2	0.16	0.44
Al_2O_3	39.07	39.64
Fe_2O_3	1.50	3.69
FeO	9.09	8.78
MgO	18.73	19.59
CaO	–	–
Na_2O	–	–
K_2O	–	–
TiO_2	0.17	0.30
MnO	0.08	0.06
NiO	0.68	0.23
Cr_2O_3	30.46	27.31
Total	99.99	100.07
a.p.f.u.		
Si	0.00	0.01
Al	1.28	1.29
Fe^{3+}	0.03	0.08
Fe^{2+}	0.21	0.20
Mg	0.78	0.81
Ca	–	–
Na	–	–
K	–	–
Ti	0.00	0.01
Mn	0.00	0.00
Ni	0.02	0.01
Cr	0.67	0.60
xMg	0.76	0.74
xCr	0.34	0.32

Table. 4.4. Average compositions of chromium spinel crystals in selected runs. X_{Cr} values are calculated using only alumina. n, number of analysis.

Periclase

Periclase and ferropericlase globules or grains crystallized due to an excess of magnesium from magnesite/dolomite, or as a result of fractionation from brucite decomposition into the run charge; alternatively, it is the result of the loss of iron from olivine crystals and siderite powder mixture to capsule material. The chemical compositions of periclase and ferropericlase crystals are listed in Table 4.5.

Periclase globules were found in LSI_2, LSI_3, LSI_13 and LSI_14 experimental samples. Microprobe analysis performed on several periclase crystals yielded a composition of ~ 91 wt. % MgO and 6.96 wt. % of FeO (average of 22-points analysis) with X_{Mg} from 0.99 to 0.94. MgO and FeO contents ranging from 86.59 to 99.73 wt. % and from 10.17 to 1.72 wt. % respectively (Fig. 4.76). In two-point analysis we found silica content (SiO_2 = 1.34 and 1.81 wt. %) probably representative of two mixed analyses due to little periclase crystals analysed.

Ferropericlase grains were found in LSI_1, LSI_2 and LSI_7 experimental samples (Fig. 4.77). EMPA analysis show a ferropericlase composition of 64 wt. % of MgO and 33.33 wt. % of FeO (average of 22-points analysis). X_{Mg} values ranging from 0.89 to 0.65. Also in the ferropericlase analysis it is possible to find silica, alumina and calcium oxide (SiO_2 = 3.5 – 4.9 wt. %; Al_2O_3 = 0.5 – 1.6 wt. %; CaO = 0.5 – 2 wt. %) representative of mixed analysis.

Periclase							Ferropericlase					
Run:	LSI_2	LSI_3	LSI_13		LSI_14		Run:	LSI_1		LSI_2	LSI_7	
P (GPa)	2.5	2.5	2.5		2.5		P (GPa)	2.5		2.5	2.5	
T (C)	1200	1200	1200		1200		T (C)	1200		1200	1200	
	mean	mean	mean	± σ	mean	± σ		mean	± σ	mean	mean	± σ
n:	2	4	6		6		n:	11		2	9	
Oxides (wt.%)							*Oxides (wt.%)*					
SiO_2	1.58	0.03	0.04	0.02	0.10	0.03	SiO_2	0.21	0.48	0.09	2.41	2.23
Al_2O_3	0.18	0.12	0.09	0.01	0.06	0.01	Al_2O_3	0.28	0.09	0.27	0.91	0.47
FeO	8.66	2.08	6.82	0.50	9.89	0.31	FeO	36.72	4.04	25.97	30.84	11.68
MgO	88.56	98.98	89.37	1.10	89.21	0.49	MgO	63.01	5.26	73.01	63.04	6.36
CaO	0.47	0.17	0.17	0.20	0.02	0.01	CaO	0.34	0.63	0.38	0.74	0.57
MnO	0.25	0.07	0.15	0.03	0.18	0.04	MnO	0.27	0.02	0.30	0.22	0.05
Total	99.68	101.45	96.63	–	99.45	–	Total	100.83	–	100.01	98.16	–
a.p.f.u.							*a.p.f.u.*					
Si	0.01	0.00	0.00	0.00	0.00	0.00	Si	0.00	0.00	0.00	0.02	0.02
Al	0.00	0.00	0.00	0.00	0.00	0.00	Al	0.00	0.00	0.00	0.01	0.00
Fe^{2+}	0.05	0.01	0.04	0.00	0.06	0.00	Fe^{2+}	0.24	0.03	0.16	0.21	0.08
Mg	0.93	0.98	0.95	0.00	0.93	0.00	Mg	0.74	0.04	0.81	0.75	0.06
Ca	0.00	0.00	0.00	0.00	0.00	0.00	Ca	0.00	0.01	0.00	0.01	0.00
Mn	0.00	0.00	0.00	0.00	0.00	0.00	Mn	0.00	0.00	0.00	0.00	0.00
xMg	0.95	0.99	0.96	–	0.94	–	xMg	0.75	–	0.83	0.78	–

Table. 4.5. Average of chemical compositions of periclase and ferropericlase in selected runs.

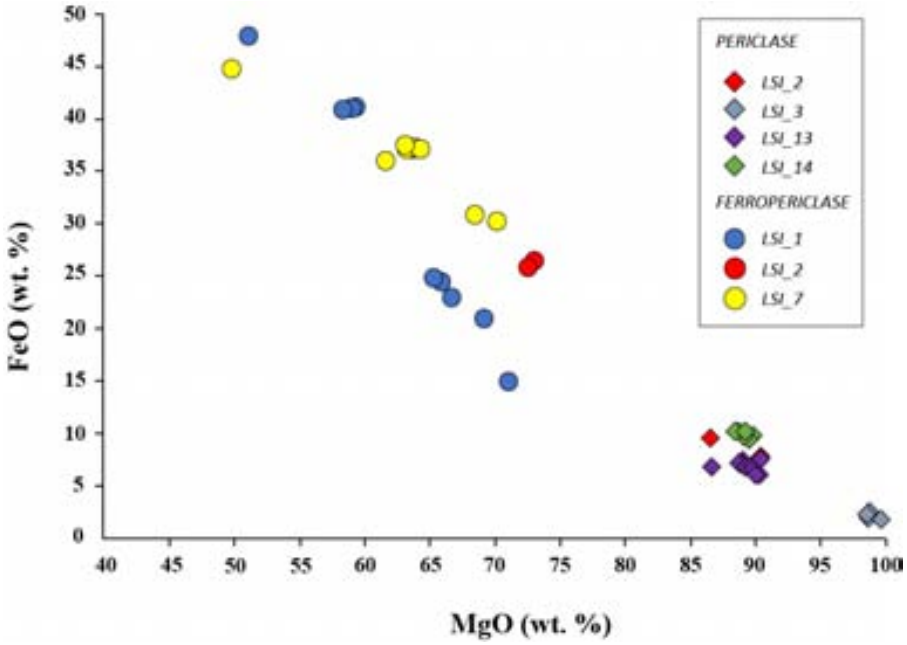

Fig. 4.76. Binary Mg vs. Fe diagram of periclase and ferropericlase analysed showing two different trends between these oxides.

4.3.3. Carbonate phases

Carbonate "phases" are present in all experiments as carbonate crystals, carbonate quenched dendrites/feathers and carbonate/silicate (called carbonatite *in sensu latu* in this thesis work) quenched intergrowths.

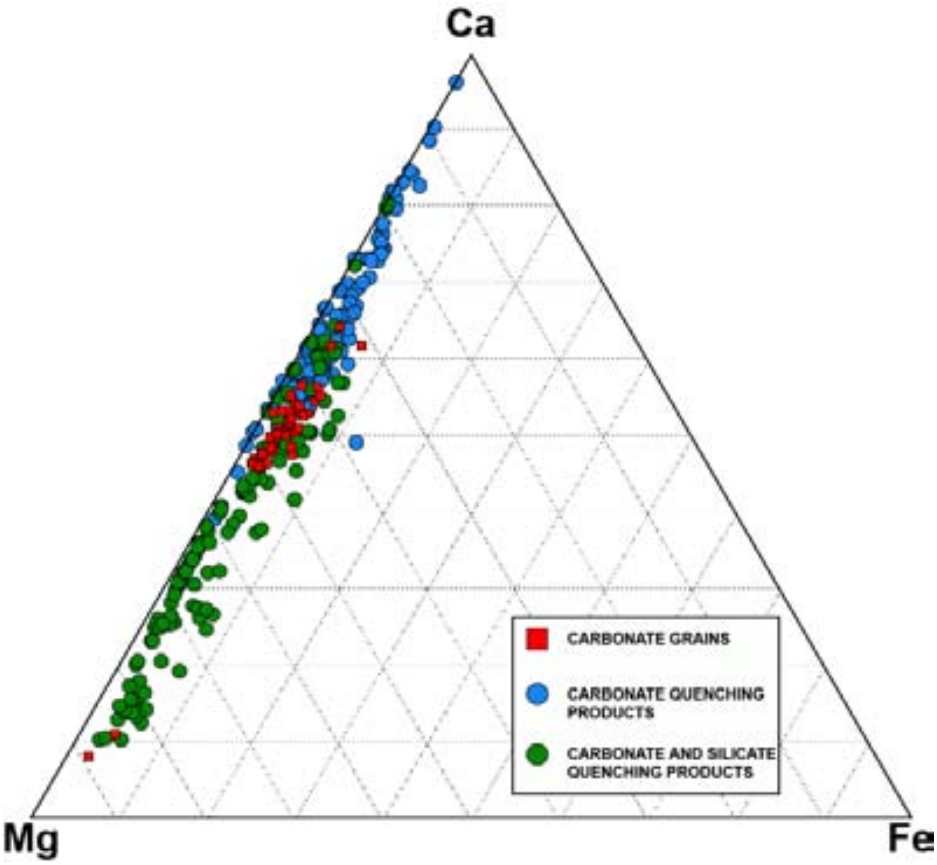

Fig. 4.77. Ca-Mg-Fe diagram of the carbonate grains and carbonate and carbonatitic quenching liquids, showing the large contents of Ca and Mg distribution.

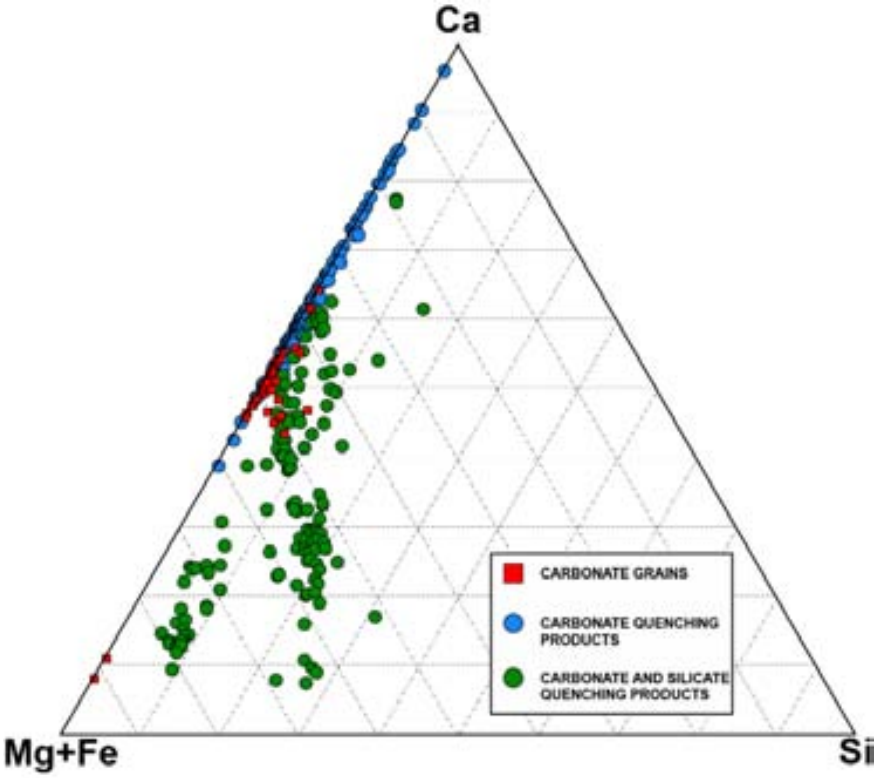

Fig. 4.78. The same analysis points of Fig. 4.78. into the Ca-Mg+Fe-Si diagram that shows the SiO_2 enrichment for the carbonatitic quenching liquids.

Carbonate grains

The compositions of carbonate solid phases in equilibrium are dolomitic and magnesitic. These grains are present in 3 experimental samples (see section 4.2): LSI_5 that is the only experiment performed at T = 1100 °C and LSI_7 and LSI_10.

The average chemistry composition of these carbonates are listed in Table. 4.6.

Dolomitic carbonates in these experiments have a CaO ranging from ~ 28 wt. % to 31 wt.% and MgO from 17.6 to 19.8 wt.%.

Magnesite is present only in LSI_7 sample with > 40 wt.% of MgO and 5.8 wt.% of CaO and it is possible to see them clearly in the triangular diagrams Ca-Mg-Fe and Ca-Mg+Fe-Si (Fig. 4.77 and Fig. 4.78) near the Mg vertex.

Dolomite and magnesite resulting from these experiments have X_{Mg} from 0.91 to 0.97 and X_{Ca} between 0.09 (magnesite) to 0.53.

Run:	LSI_5		LSI_7				LSI_10	
P(GPa)	2.5		2.5				2.5	
T(C)	1100		1200				1200	
n:	14		14		2		9	
Oxides (wt. %)								
	dolomite	± σ	dolomite	± σ	magnesite	± σ	dolomite	± σ
SiO_2	0.27	0.32	0.04	0.06	0.02	0.03	0.03	0.04
Al_2O_3	–	–	–	–	–	–	–	–
FeO	1.86	0.61	2.17	0.73	2.56	0.91	3.28	0.74
MgO	18.79	0.72	19.86	3.45	41.16	1.69	17.69	2.27
CaO	30.07	1.92	28.59	1.15	5.80	1.33	31.01	3.29
Na_2O	–	–	–	–	–	–	0.06	0.04
K_2O	–	–	–	–	–	–	–	–
TiO_2	–	–	–	–	–	–	–	–
MnO	0.18	0.04	0.13	0.05	0.16	0.02	0.41	0.05
NiO	–	–	–	–	–	–	–	–
Cr_2O_3	–	–	–	–	–	–	–	–
Total	51.16	–	50.78	–	49.69	–	52.48	–
a.p.f.u.								
Si	0.00	0.00	0.00	0.00	0.00	0.00	0.00	0.00
Al	–	–	–	–	–	–	–	–
Fe	0.03	0.01	0.03	0.01	0.03	0.01	0.04	0.01
Mg	0.45	0.02	0.45	0.02	0.88	0.03	0.42	0.05
Ca	0.51	0.02	0.51	0.02	0.09	0.02	0.53	0.06
Na	–	–	–	–	–	–	0.00	0.00
K	–	–	–	–	–	–	–	–
Ti	–	–	–	–	–	–	–	–
Mn	0.00	0.00	0.00	0.00	0.00	0.00	0.01	0.00
Ni	–	–	–	–	–	–	–	–
Cr	–	–	–	–	–	–	–	–
xMg	0.95	–	0.95	–	0.97	–	0.91	–
xCa	0.52	–	0.50	–	0.09	–	0.53	–

Table. 4.6. Average of dolomite and magnesite chemical composition analysed by electron microprobe in selected runs.

Carbonate quenched dendrites

Carbonate quenched products are present in almost all runs (except for 2 samples namely LSI_14 and LSI_15). In this section we select the quench products with SiO_2 presence < 1 wt. % where the silicate fraction may be related to beam size compared to thickness of carbonate dendrite.
The average chemistry compositions of these carbonatitic quenched products are listed in Table. 4.7.
The carbonate dendrites analysed present composition from calcite (CaO ~ 50 wt. %; MgO ~ 6 wt. %) to dolomite (CaO ~ 30 wt. % ; MgO ~ 23 wt. %) through magnesium-rich calcite (CaO ~ 40 wt. % ; MgO ~ 10 wt. %) and Ca-magnesite (CaO ~ 25 wt. % ; MgO ~ 26 wt. %). The iron content has ranging from 0 to ~ 5 wt. % (Fig. 4.78). The X_{Mg} and X_{Ca} values ranging between 1.00 (LSI_3 sample do not show iron contents) to 0.90 and between 0.78 to 0.42 respectively.

Run:	LSI_1		LSI_2		LSI_3		LSI_4		LSI_5		LSI_6		LSI_7		LSI_9	
P (GPa)	2.5		2.5		2.5		2.5		2.5		2.5		2.5		2.5	
T (C)	1200		1200		1200		1200		1100		1200		1200		1200	
	mean	± σ	mean	± σ	mean	± σ	mean	± σ	mean	± σ	mean	± σ	mean	± σ	mean	± σ
n:	5		15		12		17		4		8		6		8	
Oxides (wt.%)																
SiO_2	0.05	0.03	0.04	0.03	0.06	0.05	0.08	0.09	0.28	0.08	0.27	0.32	0.02	0.01	0.28	0.21
FeO	1.37	0.48	0.67	0.28	0.00	0.00	2.87	1.87	1.80	0.13	2.40	0.72	0.65	0.22	1.53	0.48
MgO	7.68	1.66	9.29	3.93	15.76	7.27	16.59	1.46	18.92	1.03	16.41	0.75	16.33	1.58	16.84	1.73
CaO	41.60	2.75	43.60	6.22	36.64	7.19	37.31	4.11	30.93	1.08	32.85	1.85	34.99	2.69	33.37	1.59
MnO	0.10	0.02	0.13	0.05	0.04	0.03	0.17	0.05	0.18	0.02	0.15	0.03	0.12	0.06	0.29	0.07
Total	50.80	_	53.73	_	52.50	_	57.03	_	52.10	_	52.08	_	52.11	_	52.30	_
a.p.f.u.																
Si	0.00	0.00	0.00	0.00	0.00	0.00	0.00	0.00	0.00	0.00	0.00	0.01	0.00	0.00	0.00	0.00
Fe	0.02	0.01	0.01	0.00	0.00	0.00	0.04	0.02	0.02	0.00	0.03	0.01	0.01	0.00	0.02	0.01
Mg	0.20	0.04	0.23	0.10	0.35	0.16	0.37	0.04	0.44	0.02	0.39	0.02	0.39	0.04	0.40	0.04
Ca	0.78	0.03	0.76	0.10	0.59	0.14	0.59	0.05	0.52	0.02	0.56	0.03	0.60	0.04	0.57	0.03
Mn	0.00	0.00	0.00	0.00	0.00	0.00	0.00	0.00	0.00	0.00	0.00	0.00	0.00	0.00	0.00	0.00
xMg	0.91	_	0.96	_	1.00	_	0.91	_	0.95	_	0.92	_	0.98	_	0.95	_
xCa	0.78	_	0.76	_	0.64	_	0.59	_	0.53	_	0.57	_	0.60	_	0.58	_

Table. 4.7. Average of carbonate quenching liquid products chemical compositions in selected runs.

Table. 4.7. Continued

Run:	LSI_10		LSI_11		LSI_13		LSI_16		LSI_17		LSI_18		LSI_19	
P (GPa)	2.5		2.5		2.5		2.5		2.5		2.5		2.5	
T (C)	1200		1200		1200		1200		1200		1200		1200	
	mean	± σ	mean	± σ	mean	± σ	mean	± σ	mean	± σ	mean	± σ	mean	± σ
n:	6		3		3		4		2		23		19	
Oxides (wt.%)														
SiO_2	0.26	0.31	0.10	0.07	0.23	0.12	0.29	0.16	0.72	0.16	0.16	0.13	0.39	0.27
FeO	2.51	0.75	0.41	0.03	1.18	0.68	1.09	0.67	0.19	0.16	2.62	0.70	2.21	0.70
MgO	15.93	1.60	15.72	0.93	24.12	2.49	10.23	1.88	12.10	0.93	14.41	2.97	13.37	2.44
CaO	33.11	2.69	36.98	0.73	25.38	1.59	43.79	4.51	42.23	2.69	36.22	1.89	35.77	2.58
MnO	0.35	0.05	0.11	0.02	0.19	0.05	0.24	0.06	0.23	0.09	0.25	0.04	0.36	0.08
Total	52.16	–	53.33	–	51.08	–	55.63	–	55.46	–	53.65	–	52.10	–
a.p.f.u.														
Si	0.00	0.00	0.00	0.00	0.00	0.00	0.00	0.00	0.01	0.00	0.00	0.00	0.01	0.00
Fe	0.03	0.01	0.01	0.00	0.02	0.01	0.01	0.01	0.00	0.00	0.03	0.01	0.03	0.01
Mg	0.38	0.04	0.37	0.02	0.55	0.03	0.24	0.05	0.28	0.03	0.34	0.05	0.33	0.05
Ca	0.57	0.05	0.62	0.01	0.42	0.03	0.73	0.06	0.70	0.03	0.62	0.06	0.63	0.06
Mn	0.00	0.00	0.00	0.00	0.00	0.00	0.00	0.00	0.00	0.00	0.00	0.00	0.01	0.00
xMg	0.92	–	0.99	–	0.97	–	0.95	–	0.99	–	0.91	–	0.92	–
xCa	0.58	–	0.63	–	0.42	–	0.74	–	0.71	–	0.62	–	0.64	–

Carbonatitic quenched intergrowth

Carbonatitic quenched intergrowths are present in eleven experiments and the average of chemical composition is listed in Table. 4.8.

These “liquids” show a large range of silica content between 1 wt. % to ~ 30 wt. % (Fig. 4.79) depending on the position of EMPA large beam in the analysis.

In these samples it is possible to note a large range of iron content as well from FeO = 0.23 wt. % to FeO = 6.96 wt. %.

These carbonatitic liquids analyzed show a calcium content range from ~ 7 to ~ 50 wt. % and MgO from ~ 46 to ~ 4 wt.%.

The X_{Mg} and X_{Ca} values range from 0.87 to 0.98 and from 0.15 to 0.70, respectively.

Run:	LSI_5	LSI_6	LSI_9		LSI_10		LSI_11		LSI_13		LSI_14		LSI_16	LSI_17		LSI_18	LSI_19	
P (GPa)	2.5	2.5	2.5		2.5		2.5		2.5		2.5		2.5	2.5		2.5	2.5	
T (C)	1100	1200	1200		1200		1100		1200		1200		1200	1200		1200	1200	
	mean	mean	mean	± σ	mean	± σ	mean	± σ	mean	± σ	mean	± σ	mean	mean	± σ	mean	mean	± σ
n:	5	3	9		14		25		19		17		4	8		6	27	
Oxides (wt.%)																		
SiO_2	9.62	5.80	6.37	3.25	4.70	2.27	15.80	2.17	6.36	4.65	6.83	0.89	3.24	9.31	5.58	14.70	8.97	9.21
FeO	2.16	4.13	2.51	0.88	4.90	1.13	1.12	0.15	2.23	1.32	3.53	0.42	0.91	0.46	0.21	4.95	2.91	1.21
MgO	26.47	19.79	24.17	3.60	18.13	3.33	31.10	2.04	34.19	5.33	42.41	2.06	12.57	20.42	6.91	30.06	23.01	9.95
CaO	23.48	29.46	27.07	3.43	28.29	2.96	22.46	2.04	17.26	4.37	10.56	1.08	42.60	32.76	6.41	21.35	25.33	10.25
MnO	0.14	0.20	0.35	0.05	0.40	0.05	0.15	0.03	0.21	0.08	0.24	0.05	0.21	0.28	0.05	0.24	0.31	0.08
Total	61.88	59.37	60.47	_	56.42	_	70.63	_	60.25	_	63.58	_	59.53	63.22	_	71.29	60.53	_
a.p.f.u.																		
Si	0.12	0.08	0.08	0.03	0.07	0.03	0.18	0.02	0.08	0.04	0.08	0.01	0.05	0.12	0.06	0.15	0.11	0.09
Fe	0.02	0.05	0.03	0.01	0.06	0.01	0.01	0.00	0.02	0.01	0.03	0.00	0.01	0.00	0.00	0.05	0.03	0.01
Mg	0.51	0.41	0.48	0.03	0.39	0.06	0.53	0.02	0.65	0.07	0.74	0.02	0.27	0.40	0.10	0.50	0.45	0.09
Ca	0.34	0.46	0.40	0.07	0.44	0.05	0.28	0.03	0.24	0.07	0.13	0.01	0.67	0.48	0.12	0.30	0.40	0.18
Mn	0.00	0.00	0.00	0.00	0.00	0.00	0.00	0.00	0.00	0.00	0.00	0.00	0.00	0.00	0.00	0.00	0.00	0.00
xMg	0.96	0.90	0.95	_	0.87	_	0.98	_	0.96	_	0.96	_	0.97	0.99	_	0.91	0.93	_
xCa	0.38	0.49	0.43	_	0.50	_	0.34	_	0.26	_	0.15	_	0.70	0.54	_	0.34	0.44	_

Table 4.8. Average of carbonatitic quenching liquid products chemical compositions in selected runs.

4.3.4. Fluid phase

The volatile phase in the experiments LSI_19, characterized by a starting H_2O content of 30 wt.% (83 micromoles), has been analysed using the capsule-piercing technique (see section 3.2.3). Absolute and relative micromoles of H_2O, CO_2, CH_4, CO, and H_2 are shown in Table. 4.9.

Least squares

	LSI_19_micromoles
(O_2)	0.0117267
(H_2O)	0.126494
(H_2)	0.0194136
(CO)	0.0206206
(CO_2)	1.01962
(CH_4)	0.0646726
(air)	0.871562

(2.1343095) Total of µmol of evolved gas

	LSI_19_percent
(O_2)	0.549437
(H_2O)	5.92671
(H_2)	0.909598
(CO)	0.966152
(CO_2)	47.7821
(CH_4)	3.03015
(air)	40.8359
[total]	100
XCO_2	0.889651065

	LSI_19_percent air free
(O_2)	0.928666
(H_2O)	10.0174
(H_2)	1.53741
(CO)	1.633
(CO_2)	80.7619
(CH_4)	5.1216

Table. 4.9. Composition of the fluid phase in sample LSI_19. QMS data reduction; measured volatile species are given as absolute micromoles, relative micromoles (percent) and relative micromoles on an air-free basis (percent air free)

In this run we measured 2.13 micromoles of volatiles. The fluid phase is mainly composed by CO_2 (80.8 mol.%), H_2O (10.0 mol.%) and methane (CH_4 = 5.1 mol.%). Carbon monoxide, hydrogen and oxygen are present in low amounts <2 mol.%. The fluid composition plots close to the graphite saturation surface (Connolly and Cesare, 1993) in the C–O–H ternary diagram (red dot in Fig. 4.79), suggesting equilibration with graphite.

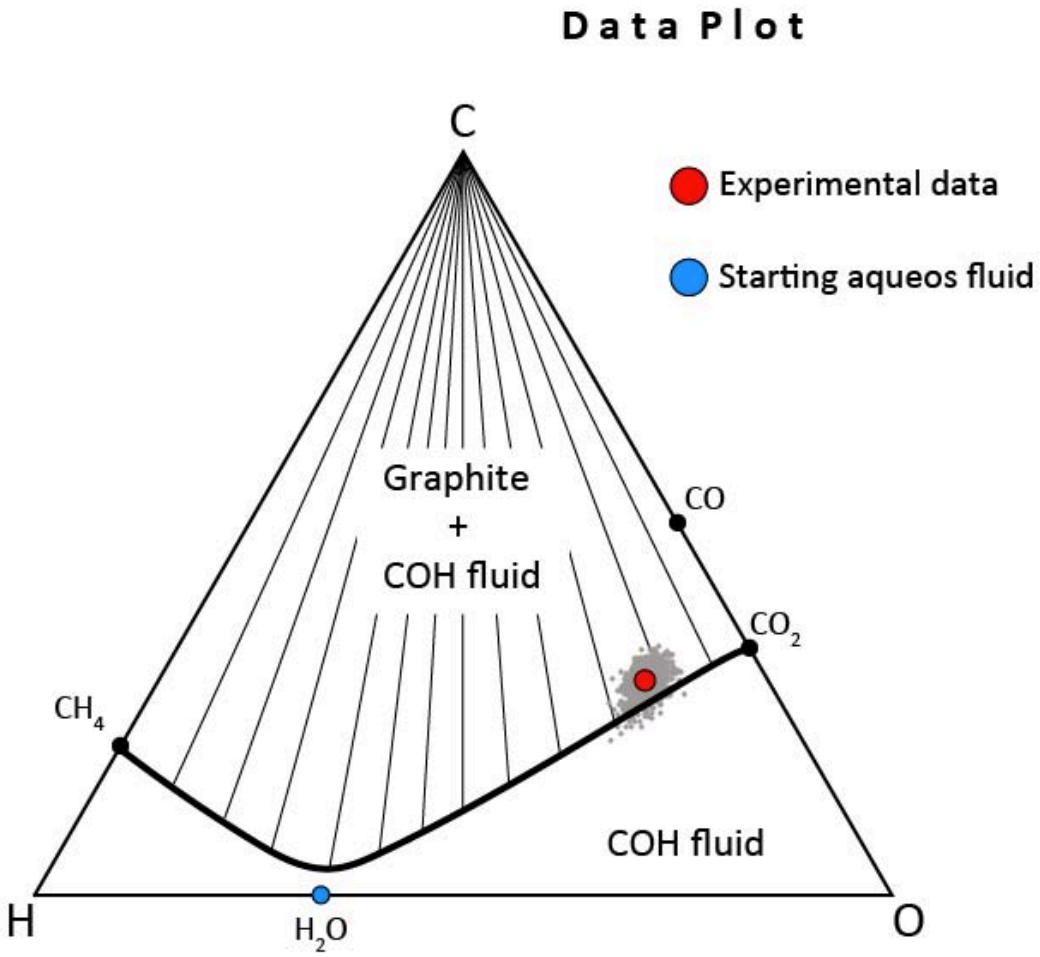

Fig. 4.79. COH ternary diagram showing the composition of the measured fluid phase (red dot), with the analytical uncertainty cloud (grey dots). The starting fluid composition (water) is shown by a blue dot. The graphite saturation surface (black solid line), calculated by thermodynamic modelling using the COH fluid equation of state of Connolly and Cesare (1993), represents all possible compositions of graphite-saturated COH fluids at fixed 2.5 GPa, 1200 °C and variable fO_2 conditions.

The post-quench volatile phase coexisting with olivine, graphite and a dolomite-rich carbonate–silicate melt at P = 2.5 GPa and T = 1200 °C (run LSI_19) is characterised by a XCO_2 ($=CO_2/H_2O+CO_{2molar}$) of 0.89. Although the redox conditions in this experiment are not constrained, and keeping in mind that water (and likely also some molecular CO_2) partitioned into the melt, at least partially, as suggested by EMPA analyses, we can compare the composition of this post-quench fluid phase with that of a theoretical graphite-saturated fluid, retrieved through thermodynamic modelling using the Perple_X software (Connolly, 1990; http://www.perplex.ethz.ch/), using the routine "fluids" and the MRK EoS for of Connolly and Cesare (1993) (Perple_X equation of state n°11).

```
Enter p(bar), T(K), X(O)    :
25000   1473   .896


Fluid equation of state: X(O) GCOH-fluid MRK Connolly & Cesare 1993

         p(bar)     =   25000.
         T(K)       =   1473.0

         log[f(O2)] =  -7.5536
         log[f(S2)] =  -9999.0
         a(gph/dia) =   1.0000


                  Speciation/Fugacities

          H2O          CO2          CO           CH4
x     0.10802      0.86646      0.25259E-01  0.20872E-04
f      21243.      0.85479E+07  0.16656E+06   208.06

          H2
x     0.24473E-03
f      166.10

Sum of species fractions:    1.000000000


                  Atomic Proportions

     C           H           O           S           N           Si
0.29979      0.72822E-01  0.62739      0.0000      0.0000      0.0000

Back-calculated X(O) =  0.896000000
Back-calculated X(C) =  0.299789810

Molar Volume (cm3/mol) =   33.967
```

Fig. 4.80 Thermodynamic modelling of a graphite-saturated fluid at 2.5 GPa and 1200°C. Oxygen fugacity has been adjusted in order to match the measured fluid XCO_2 (0.89).

In order to obtain a fluid characterized by $XCO_2 = 0.89$, $\log fO_2$ must be fixed at a value of -7.55, corresponding to a ΔFMQ ($= \log fO_2^{sample} - \log fO_2^{FMQ}$) value of -1.16.

Ulmer and Luth (1991) provided an estimate of the fO_2 for experiments performed in graphite capsules run without external buffer in the range 1 – 3 GPa:

$$log\, fO_2 = \frac{-22324 + 189P - 1.41P^2}{T} + 4.62 \qquad \text{(Eq. 4)}$$

with T in K, and P in kbar and an uncertainty of $\log fO_2 \pm 0.1$.

Using this equation with P-T conditions of run LSI_19, i.e. 2.5 GPa and 1200°C, we obtain $\log fO_2 = -7.92 \pm 0.1$, which is relatively close to the $\log fO_2$ value (-7.55) retrieved from measured XCO_2. However, even by considering the maximum possible $\log fO_2$ estimate of -7.82, the COH fluid composition predicted by thermodynamic calculations would display an $XCO_2 = 0.51$ (Table 4.10), which is considerably lower (-43 mol. %) if compared with the post-quench volatile phase analysed through mass spectrometry.

Perple_X calculation with X(O) = 0.896		
	species (mol. %)	H_2O-CO_2 norm
H_2O	48.534	49.35025319
H_2	0.13789	–
CO	1.4346	–
CO_2	49.812	50.64974681
CH_4	0.081244	–
XCO_2		0.506497468
fO_2	-7.8259	

Table. 4.10. Predicted volatile composition of a graphite-saturated COH fluid (mol. %) using log fO_2 estimated at 2.5 GPa and 1200°C using Eq. 4 from Ulmer and Luth (1991).

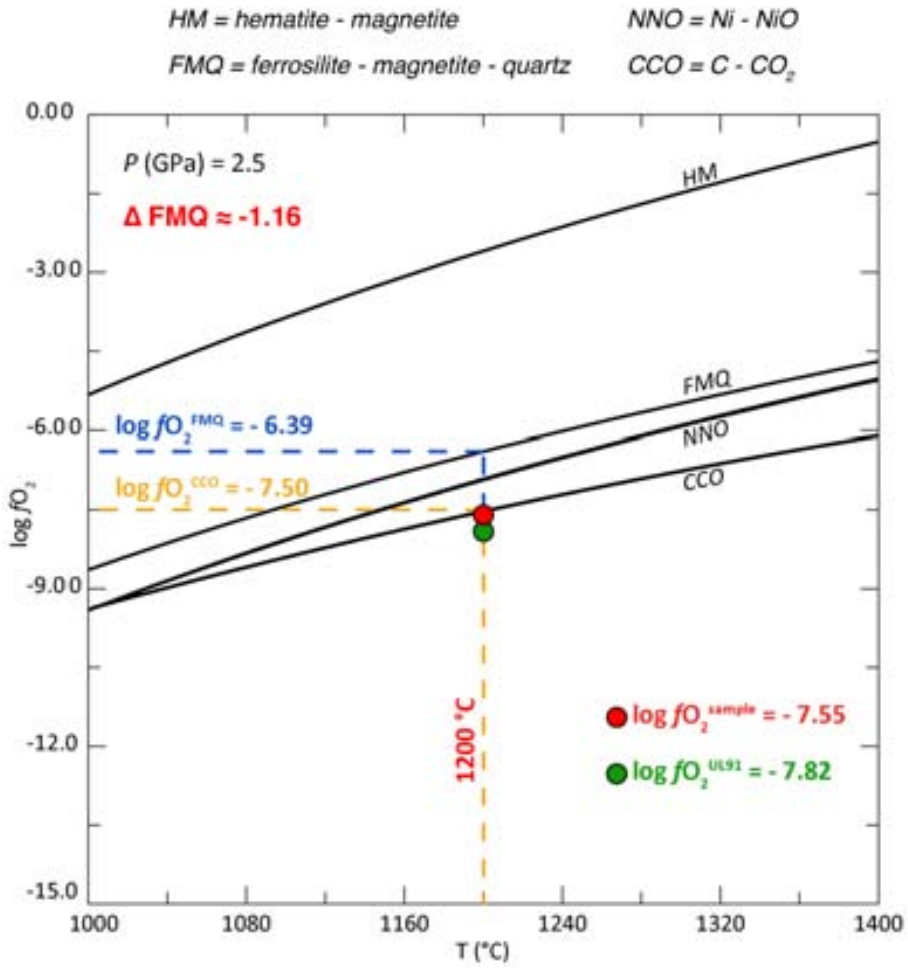

Fig. 4.81. T vs. log fO_2 diagram showing the location of some buffering equilibria. The red dot represents sample LSI_19; the green dot shows the predicted oxygen fugacity at 2.5 GPa and 1200 °C for a experiments performed in a graphite capsule without external buffers (UL91; cf. Ulmer and Luth, 1991).

In order to explain this apparent discrepancy, we propose the following hypotheses:

- problems related to the uncertainties or the applicability of the model of Ulmer and Luth (1991) at our experimental conditions;
- water (hydrogen) loss from the capsule (Truckenbrodt and Johannes, 1999) due to the high hydrogen permeability of platinum;
- unconstrained partitioning of water and/or molecular CO_2 into the carbonatitic melt;
- silicate dissolution in the fluid, which could affect the XCO_2 in particular enhancing the CO_2 content up to ± 30% (Tumiati et al., 2017);
- carbonate dissolution in the fluid, which has not been investigated yet in experimental studies.

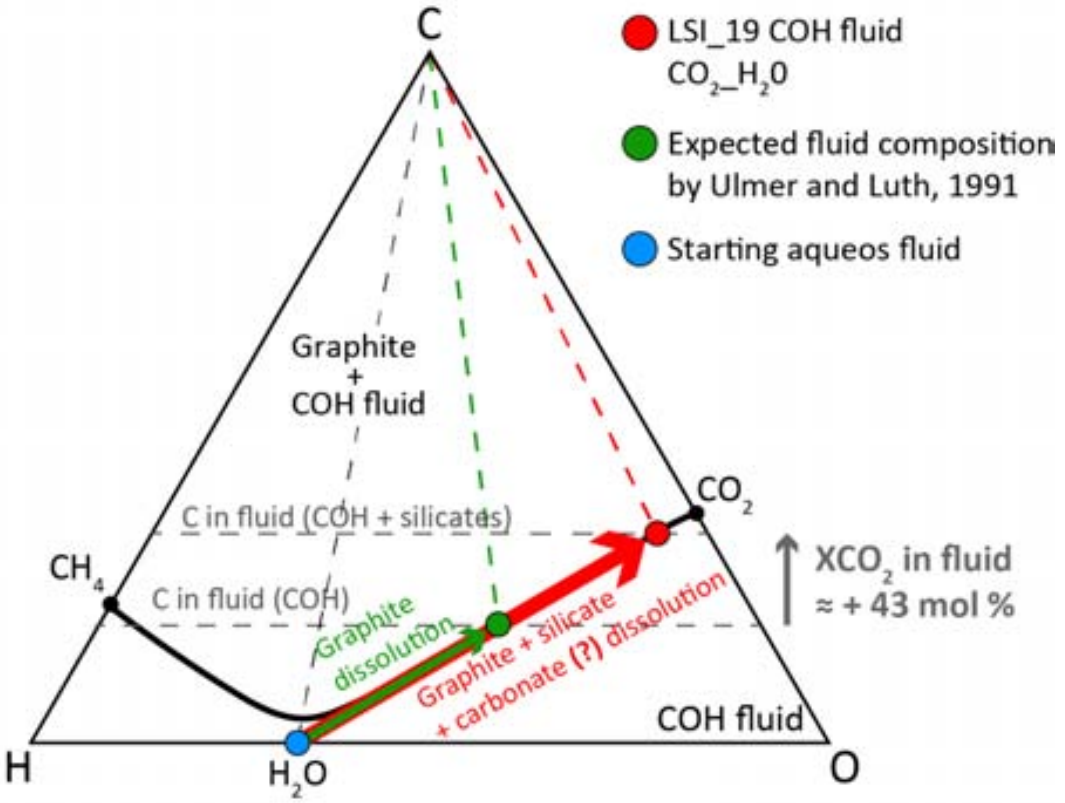

Fig. 4.82. Evolution of pure water (blue dot) interacting with graphite alone (green dot; predicted composition by thermodynamic modelling) and graphite+olivine+carbonate-silicate melt (red dot; this study). Post-quench fluids display an increase in XCO_2 up to 43 mol.% if compared with fluids interacting with graphite alone, which could result from the dissolution of olivine (cf. Tumiati et al., 2017) and/or carbonates.

4.4. Liquid distribution in the olivine matrix

4.4.1. The shape of liquid pockets

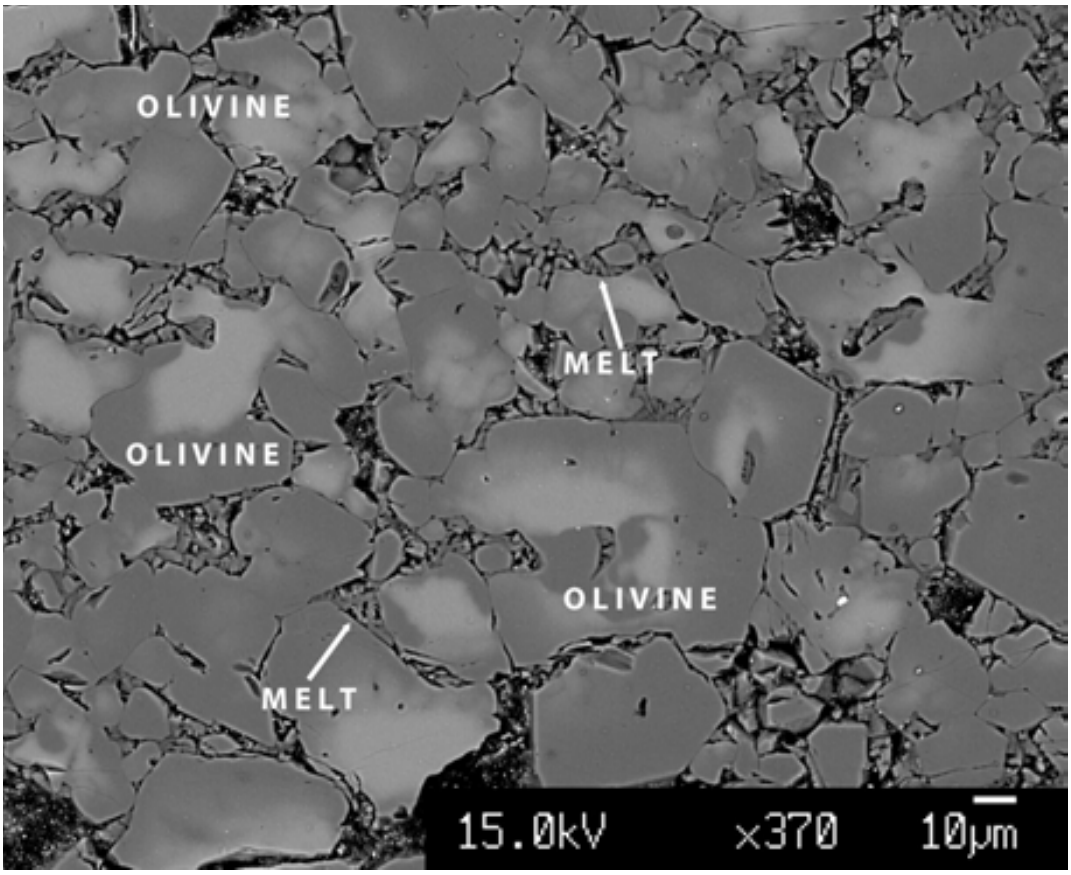

Fig. 4.83. BSE image showing a olivinic matrix infiltrated by carbonatitic melt with different liquid microstructure representative of all experimental products infiltrated (BSE image of LSI_13 experiment).

During the infiltration experiments at high temperature the polycrystalline aggregated continues to evolve by grain growth and melt distribution driven by the interfacial energy.

During this stage in these infiltrations experiments some microstructure may be created by growth and by melt mobility into the charge (Fig. 4.83). These microstructures called by Cmiral et al. (1998) large interserts, triple junctions and layers occurred in our experimental samples.

In most cases the infiltrated melt resides in large interserts involving more than three olivine crystals (four or more) with elongated planar or rounded edges (Fig. 4.84a,b,c).

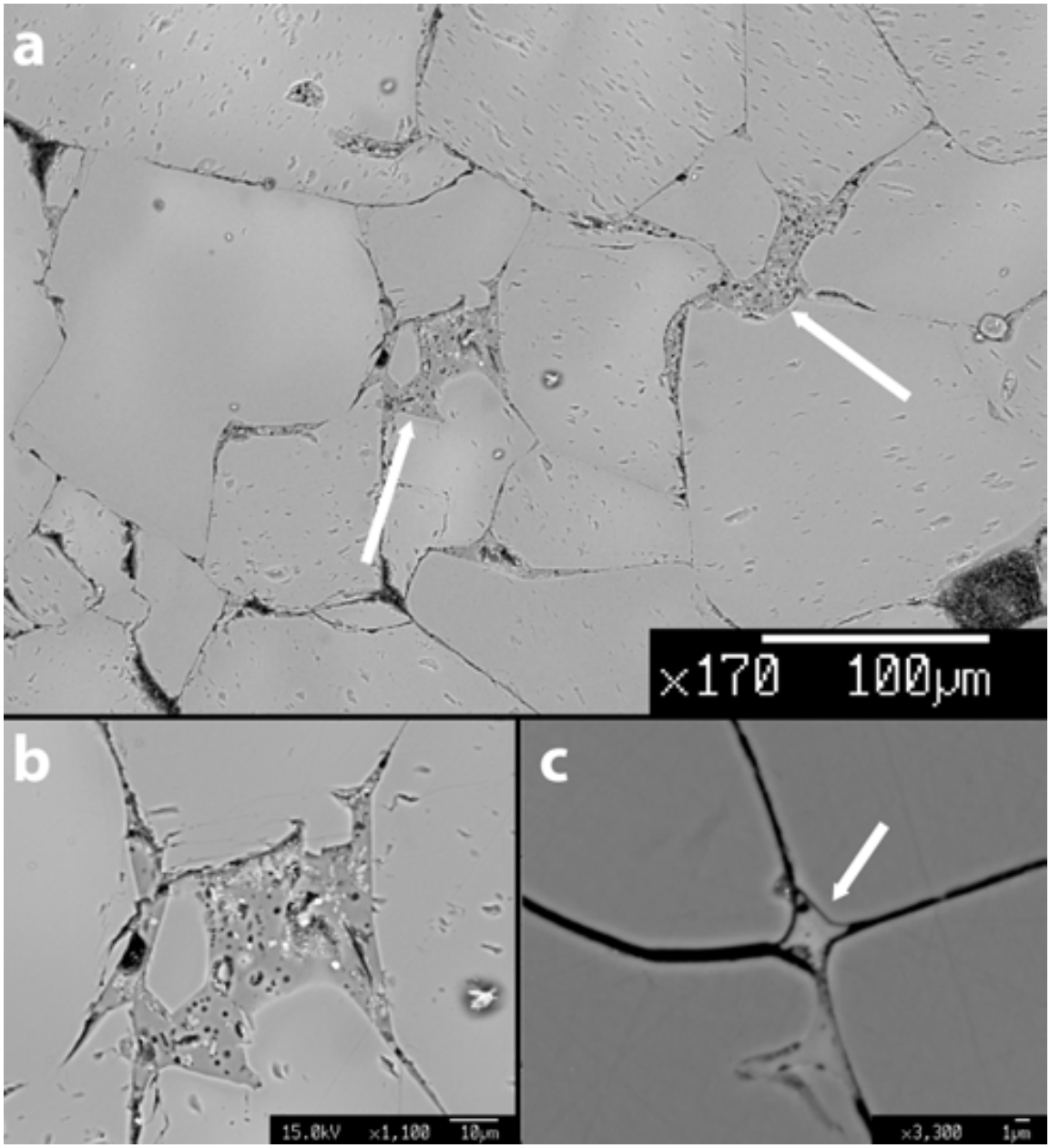

Fig. 4.84. (a) Back scattered image showing dunite infiltrated by carbonatitic melts forming large intersects between olivine grain boundaries (LSI_15 experiment); (b) detail of one of large intersert of (a); (c) carbonatitic melt pocket involving four olivine crystals (LSI_19).

In many cases these infiltrated liquids are inferred in triple junctions between three olivine grain boundaries. In several cases these melt pockets into the triple junctions present smoothly curved grain edges (Fig. 4.85a). More often the olivine grains present a faceting with planar edge. Grain develops a planar face there frequently is a more isometric rounded olivine grain next to it (Fig. 4.85b and 4.85c). These triple junctions could be curved and planar as mentioned above or could show curved edges with one or more planar edges (Fig. 4.85d) and in some cases forming a kind of intersects between three olivine grains (Fig. 4.85e).

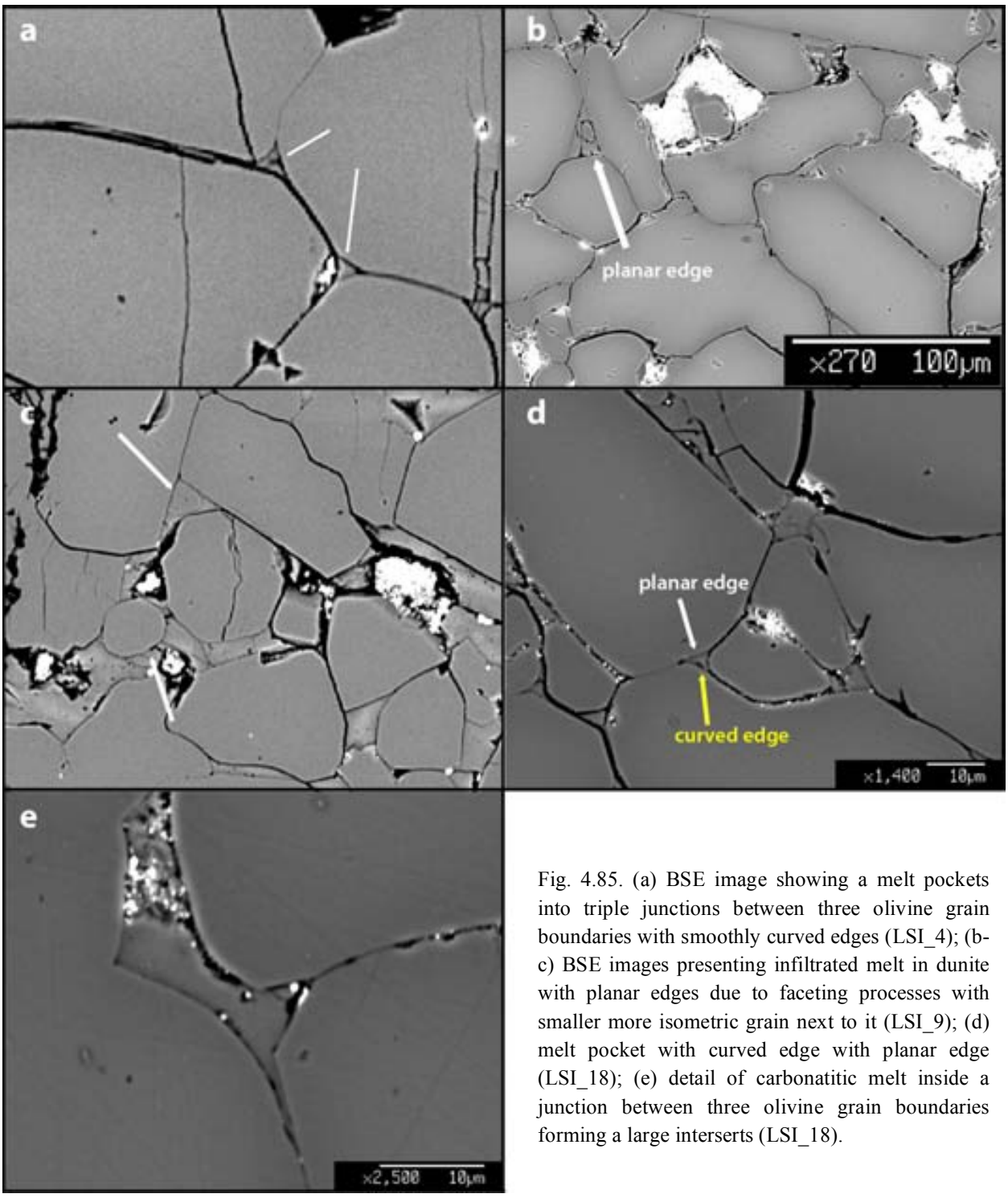

Fig. 4.85. (a) BSE image showing a melt pockets into triple junctions between three olivine grain boundaries with smoothly curved edges (LSI_4); (b-c) BSE images presenting infiltrated melt in dunite with planar edges due to faceting processes with smaller more isometric grain next to it (LSI_9); (d) melt pocket with curved edge with planar edge (LSI_18); (e) detail of carbonatitic melt inside a junction between three olivine grain boundaries forming a large interserts (LSI_18).

Very often you can note how the infiltrated liquids form layers connecting two or more melt pockets or placing along the olivine grin boundaries. These layers occur between flat as well as between curved grain surfaces and are abundant in samples with largest olivine grains and they present thickness of << 1 µm (Fig. 4.86).

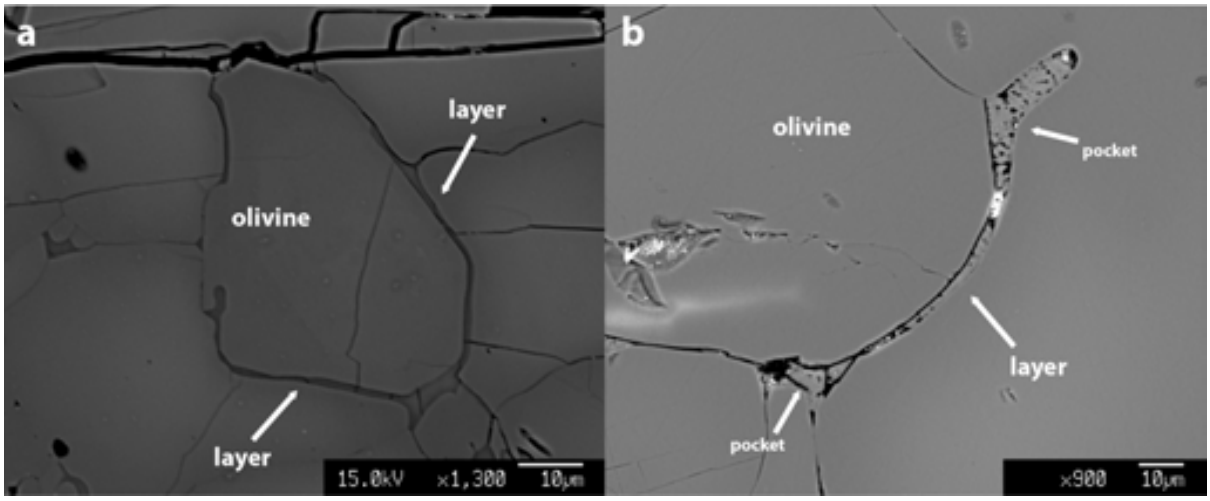

Fig. 4.86. (a) BSE photographs of melt layer along olivine grin boundary (LSI_16); (b) melt layer connecting two melt pockets (LSI_19). Black features are cracks from quench and post run sample preparation.

4.4.2. Liquid channelization

In our samples it is possible to observe different liquid distribution at different run time, bulk or geometry capsule setup. Several samples show melt more evenly distributed over the whole charge and some areas contain the melt in separated pocket like in LSI_3 sample with dunite rod below carbonatitic reservoir and brucite as hydrous source, or short run experiment (3 hours duration) with 5 wt. % of free water and dunite rod above the carbonate mixture powder (LSI_6, Fig. 4.87a and Fig. 4.87b).

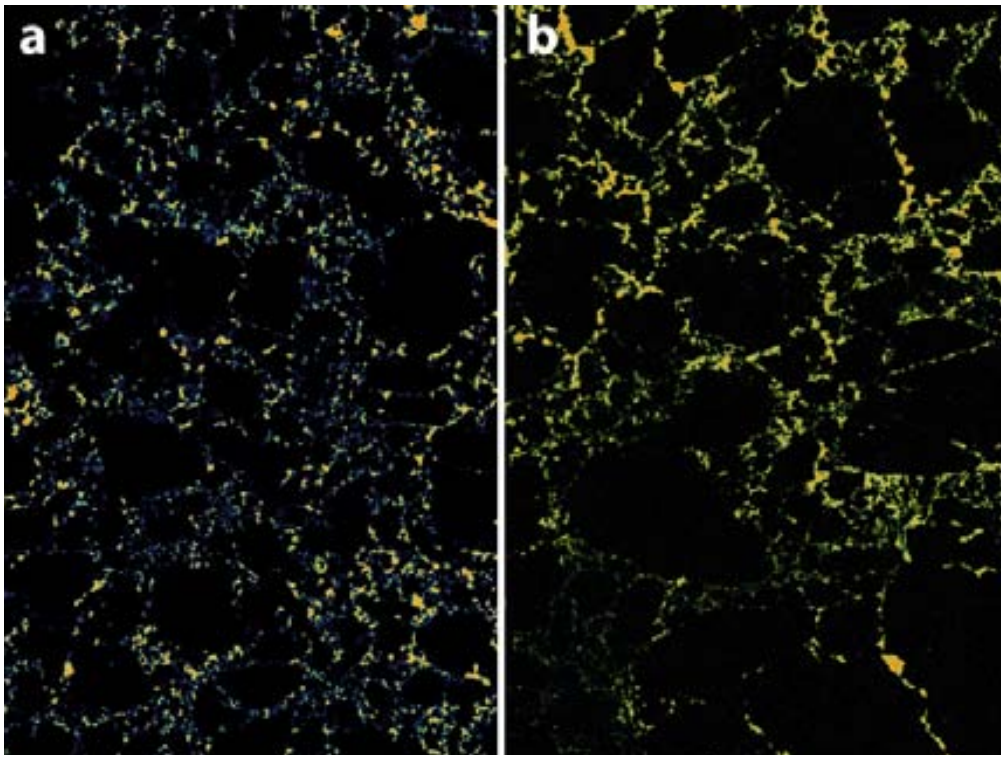

Fig. 4.87. Calcium X-ray maps of experiments with small melt pockets inside the dunite rod. (a) LSI_3; (b) LSI_6. Black = Dunite rod; Yellow/Orange = infiltrated liquids.

In most cases the infiltrated melts form an interconnected channel of layers between two or more melt pocket in triple junction or in large interserts giving rise to a thrust channelization saw in a long run duration experiment (300 h) with brucite and dunite rod below carbonatitic reservoir (Fig. 4.88a); the run charge in this example is divided into a portion with channelization (close to dunite-carbonate interface) and a portion below with porous flow infiltration (see 4.2 section – Fig. 4.16). A less pronounced channelization is noted in experiments of 48 hours and with water content of 30 wt. % (Fig. 4.88b).

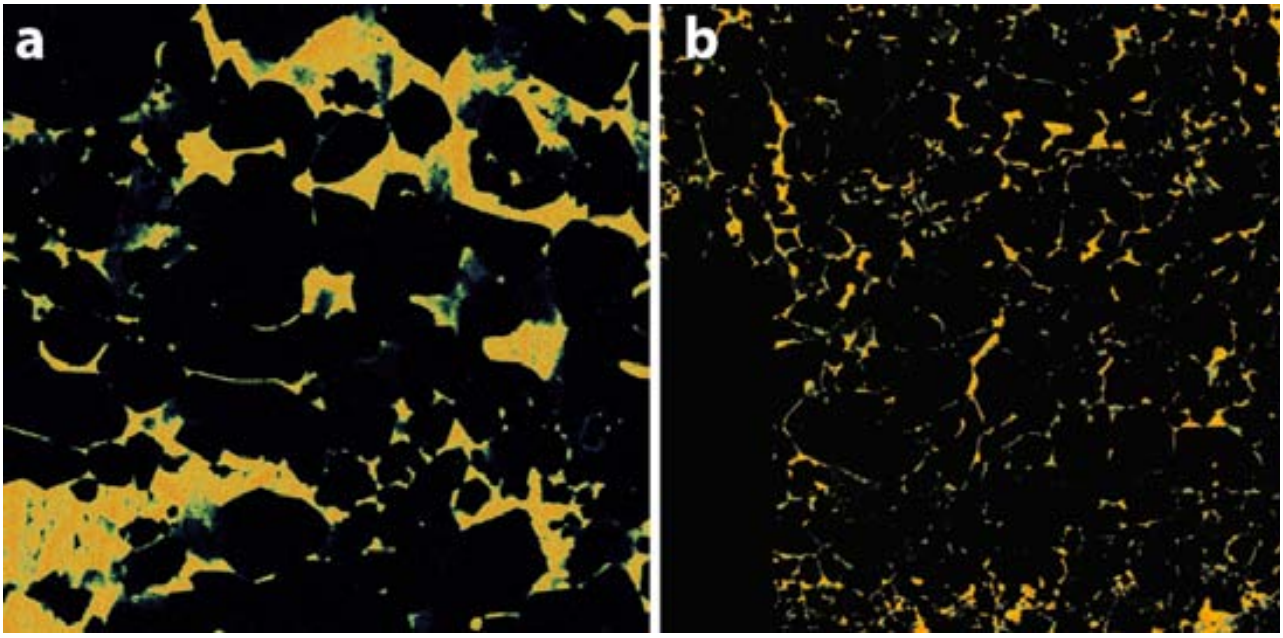

Fig. 4.88. Channelization inside the dunite rod (black) by means of infiltrated carbonatitic melts. (a) LSI_4 sample; (b) LSI_18 experiment.

4.5. Image analysis

4.5.1. Dihedral angle: characterization and measurements

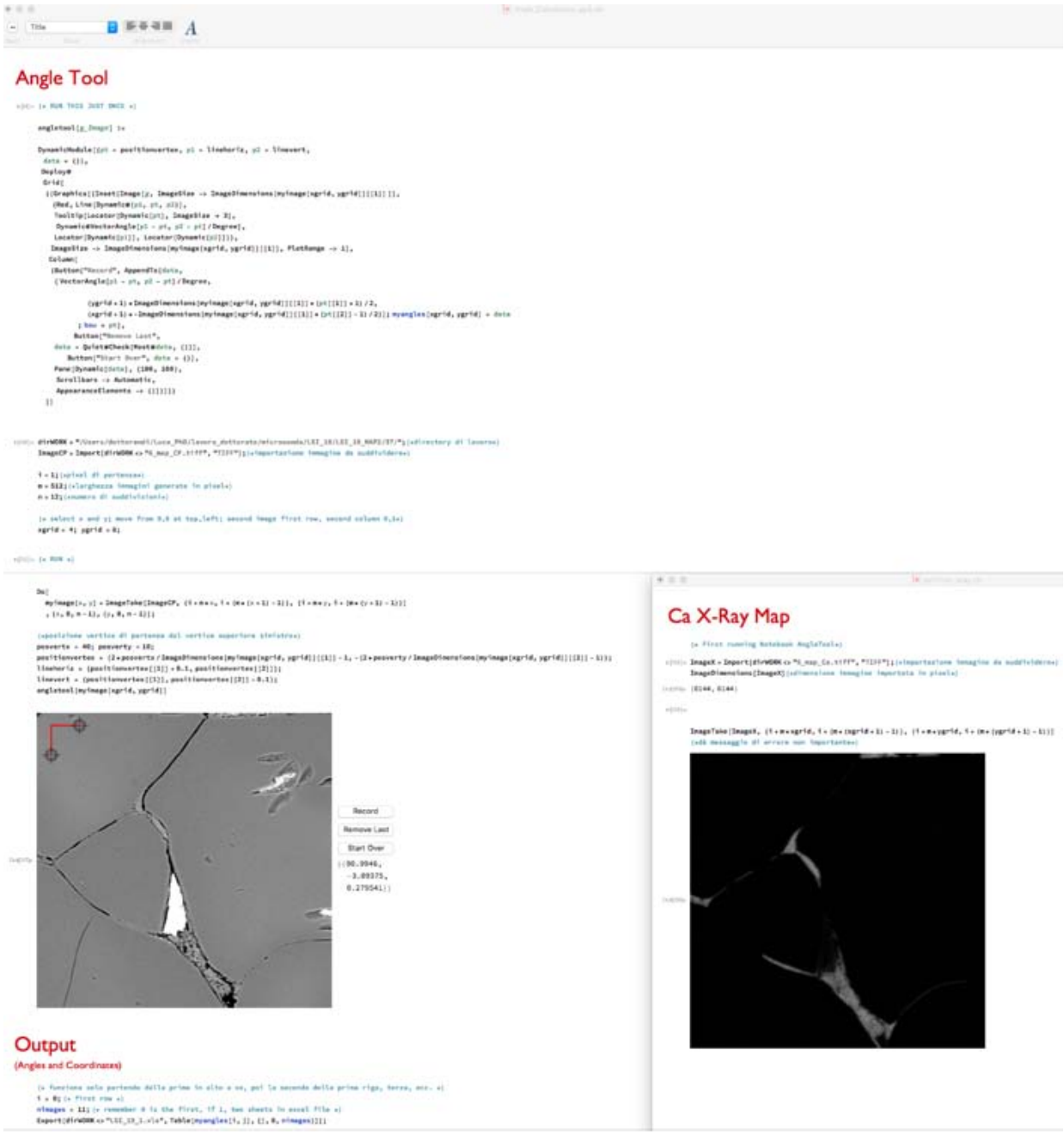

Fig. 4.89. Representative image of the two Mathematica® routine allowed us to measure apparent dihedral angles in selected experimental runs.

The first step in the characterization of melt dihedral angles and in the measurement of melt wetting was simply to examine the sample at high resolution in BSE images combined with calcium X-ray map (Ca) in order to discriminate olivine grains from quench products derived from the liquid because, despite the different grey tone, the high resolution BSE image were insufficient to highlight the phase boundaries.

We first chose the representative areas of the polished sample surface. To obtain the resulting high resolution maps we set the EMPA maps program as "*guide net map*" with a pixel size of 0.30 μm, which is lower than the area excited by the electron beam for X-rays but large enough to inspect the BSE signal in reasonable time.

Tessellation and processing of the compositional map images and measurement of the dihedral angle is performed using a customized dynamic routine developed as Mathematica® notebook combined with another routine to make the corresponding Ca X-ray map visible (Fig.4.89).

The dynamism of this Mathematica® routine allows us to measure manually the apparent dihedral angle values and related *x* and *y* spatial coordinates. The measurements are then grouped into output file for Microsoft® excel program.

To validate our Mathematica® routine we performed measurements on literature images of melt pockets of fluorite – H_2O, fluorite – K-rich silicate melts systems and quartz – H_2O from Yoshino et al. (2005) and of schematic image from Hunter and McKenzie (1989) (Table. 4.11). By these measurements we obtain a dihedral angle values almost equal related to dihedral angle values measured by the author cited above for the considered systems.

	Considered Systems	Dihedral Angle measured (°)	Our Measurements number	Our Measurements Dihedral Angle (°)
Hunter and McKenzie, 1989	Olivine + dolomite	28	30	28.84
	Fluorite + H_2O	66	11	65.44
Yoshino et al., 2005	Fluorite + K-rich silicate	20	18	19.7
	Quartz + H_2O	55	16	56.15

Table. 4.11. Dihedral angle values measured by Hunter and McKenzie and Yoshino et al., 2005 for different systems compared with our measurements on their pictures (number = number of measurements).

The dihedral angle measurements were carried out in six experiments with different capsule geometry, run time and bulk compositions and are listed in Table 4.12.

LSI_4 experiment, lasting 300 hours run time, was performed using Mix 1 (see section 3.1.1; Table. 3.2) and capsule geometry setup placing the dunite rod below the Mix 1 put into platinum and graphite thick capsule. In this experiment we carried out four hundred apparent dihedral angle measurements.

LSI_9 and LSI_10 experiments durations was 30 and 3 hours respectively and they were performed with the same capsule materials than LSI_4 but with Mix 2 as carbonatitic reservoir adding 5 wt. % of free water and using the reversal geometry capsule setup, placing the dunite rod above the carbonate mix powder. In LSI_9 and LSI_10 experiments we performed respectively 127 and 303 measurements.

LSI_13 sample was an experiment conducted for 3 hours in a capsule of preconditioned platinum without graphite thick using Mix 2 but brucite as hydrous source and graphite powder, placing the dunite rod in the upper part of the run charge. For this run we performed 176 measurements.

Finally, 424 and 257 apparent dihedral angle measurements were carried out on two experiments of 48 hours run time, same capsule setup of LSI_4, Mix 2 as carbonatitic reservoir but with 30 wt. % of water as hydrous source. The only difference between LSI_18 and LSI_19 was the carbonate amount related to rod weight (30 wt. % and 70 wt. % respectively).

Run	Capsule	Starting Material	Water content (wt. %)	Run time (h)	Geometry From top to bottom	Number of measurements	TRUE dihedral angle value (°)
LSI_4	Pt+grph	Mix 1	5	300	Mix - Dunite	400	40.8
LSI_9	Pt+grph	Mix 2	5	30	Dunite - Mix	127	34.1
LSI_10	Pt+grph	Mix 2	5	3	Dunite - Mix	303	31.5
LSI_13	Pt	Mix 2	5	3	Dunite - Mix	176	32.6
LSI_18	Pt+grph	Mix 2	30	48	Mix - Dunite	424	49.8
LSI_19	Pt+grph	Mix 2	30	47	Mix - Dunite	257	48.1

Table. 4.12. Run table of the six experiments considered to measure the dihedral angles related with capsule material, bulk composition, water content, run time duration and capsule geometry setup.

Histograms and cumulative frequency curves are reported in Fig. 4.90a-f. Although the error in measuring dihedral angles from BSE images may be as 5°, the use of cumulative curve reduces the apparent observational error by a factor of 10. The likely error is thus ± 0.5 ° on the mean value (Hunter and McKenzie, 1989).

Considering that the two-dimensional surface of the polished mount represents a plane through a three-dimensional microstructure, the dihedral angles measured in the plane of the section do not represent true dihedral angle but the apparent dihedral angle. The true dihedral angle can be obtained from the median value (Riegger and Van Vlack, 1960), represented by green line on cumulative frequency diagrams (Fig. 4.90a-f), on a cumulative frequency curve constructed from measurements of observed apparent dihedral angles (Hunter and McKenzie, 1989).

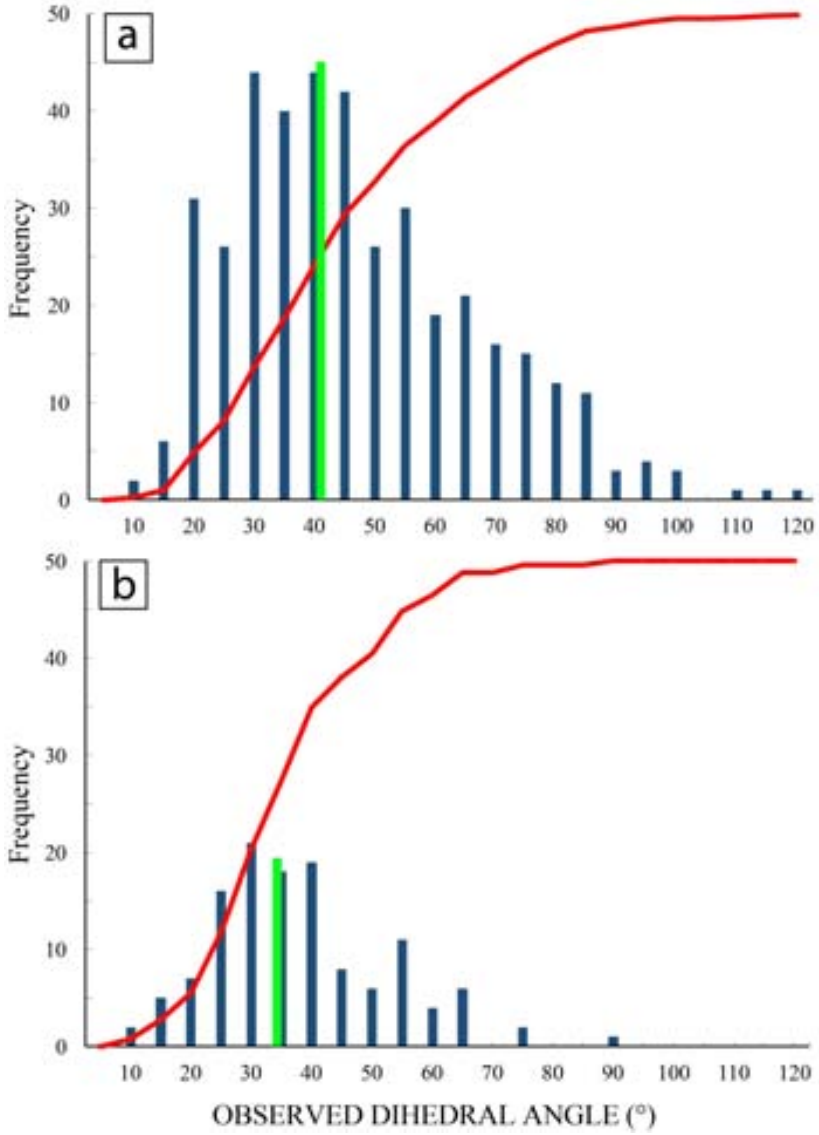

Fig. 4.90. The histogram of the relative frequencies of apparent dihedral angle measured. The data are plotted as 10° intervals. The median point on the curve represented by green line yields a true dihedral angle values. Cumulative frequency curves (red curve) refer to 0-100% scale, are also plotted.
a = LSI_4 (300h and H_2O = 5 wt. %); b = LSI_9 (30h and H_2O = 5 wt. %); c = LSI_10 (3h and H_2O = 5 wt. %); d = LSI_13 (3h and H_2O = 5 wt. %); e = LSI_18 (48h and H_2O = 30 wt. %); f = LSI_19 (47h and H_2O = 30 wt. %).

Fig. 4.90. Continued

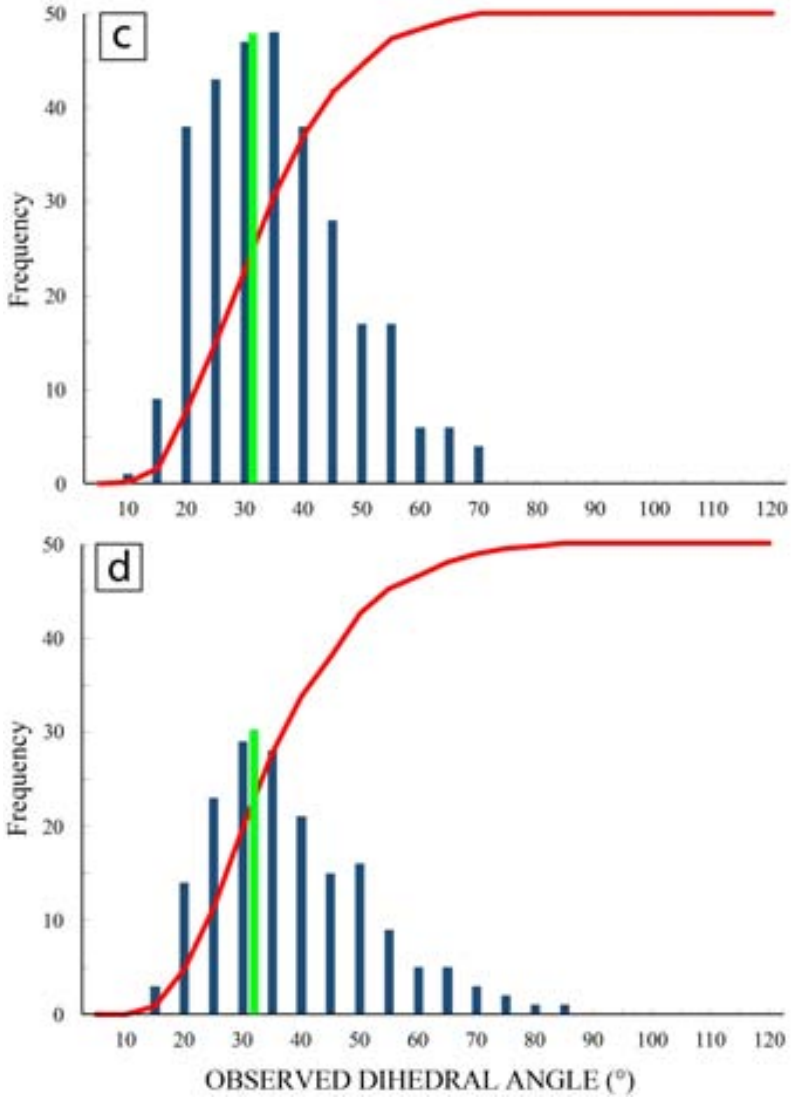

Fig. 4.90. Continued

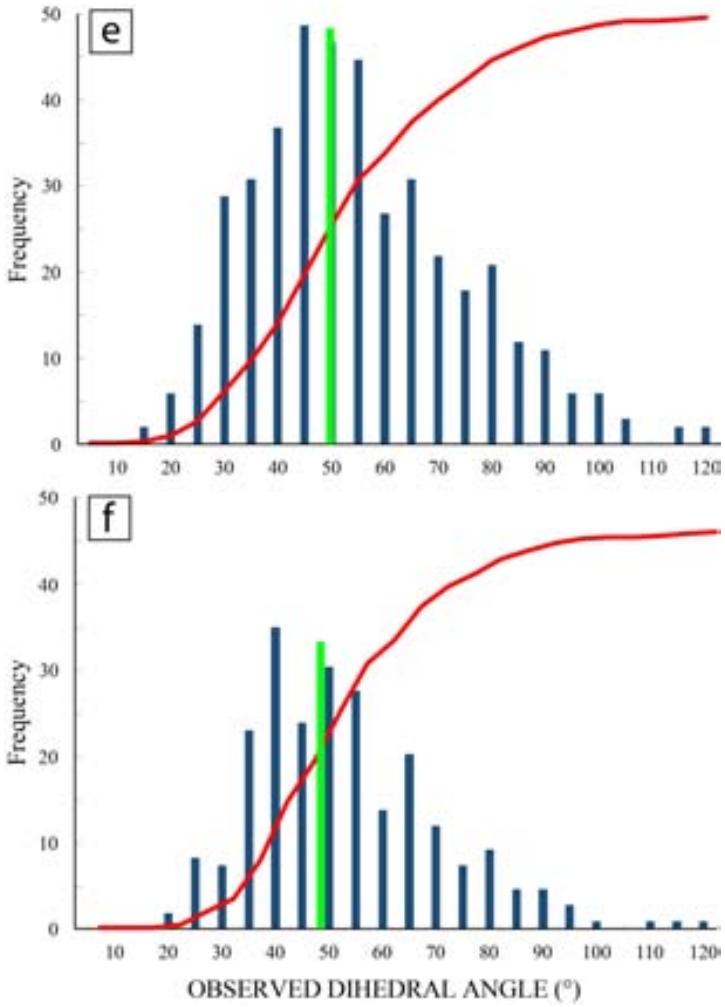

In LSI_4 experiment, the longest run performed in this study, the resulting data were plotted adopting binning in ten degrees interval and the median point on the curve indicates a value of true dihedral angle of 40.8° (Fig. 4.90a).

In the 30 hours run (LSI_9) the median point yields a lower value of θ of 34.15° (Fig. 4.90b).

The two short run experiments considered here devoted to measurement of dihedral angles (LSI_10 and LSI_13) show the true values of 31.5° and 32.6°, values that are strictly comparable, and that are lower than 30 hours run time experiment (Fig. 4.90c-d).

Finally, the experiments performed with 30 wt. % of water content (LSI_18 and LSI_19) have highlighted true dihedral angle much larger, reaching almost 50° (Fig. 4.90e-f).

The dihedral angles measured in the experimental samples cited above clearly show different values from each other related to run time experiment, capsule geometry setup and water content differences. The lowest true dihedral angle values are representative of the shorter run time experiment independently from the different bulk carbonatitic reservoir composition. The

experimental run at 300 hours duration shows a higher value of true θ therefore suggesting the increase of wetting angle value with run time duration, although the different geometries used are not strictly comparable.

The water content instead seems to be related to higher true wetting angle value measured; runs with 30% H_2O present show values that are higher compared to 300 hours run experiment, notably with the same geometry capsule setup.

4.5.2. Grain boundary wetness: characterization and measurements

The geometry of melt filled pores was investigated quantitatively by measuring the grain boundary wetness, which is defined as the ratio of solid – liquid boundary area over the total area of interphase boundaries (see section 1.5).

In LSI_4 sample we performed EBSD analysis at Géosciences Montpellier, University of Montpellier (see section 3.2.2) and this analysis allow us to define clearly the olivine grain boundaries and liquid "grain" boundaries too.

By means the Matlab® toolbox MTEX 4.1 (Bachmann et al., 2010) modified by David Mainprice and Benoit Ildefonse we could process the EBSD output data to have an higher resolution map of olivine grain boundaries (Fig. 4.91a) and carbonatitic melt boundaries (Fig. 4.91b).

In order to calculate the grain boundary wetness, the EBSD output image data of olivine grain boundaries, and calcium X-ray map of carbonatitic "liquid" boundaries were combined with using Photoshop to ensure that the grain boundaries of two different images fit perfectly, and to eliminate artefacts from EBSD image. For this process these images were manually edited and superimposed (Fig. 4.92).

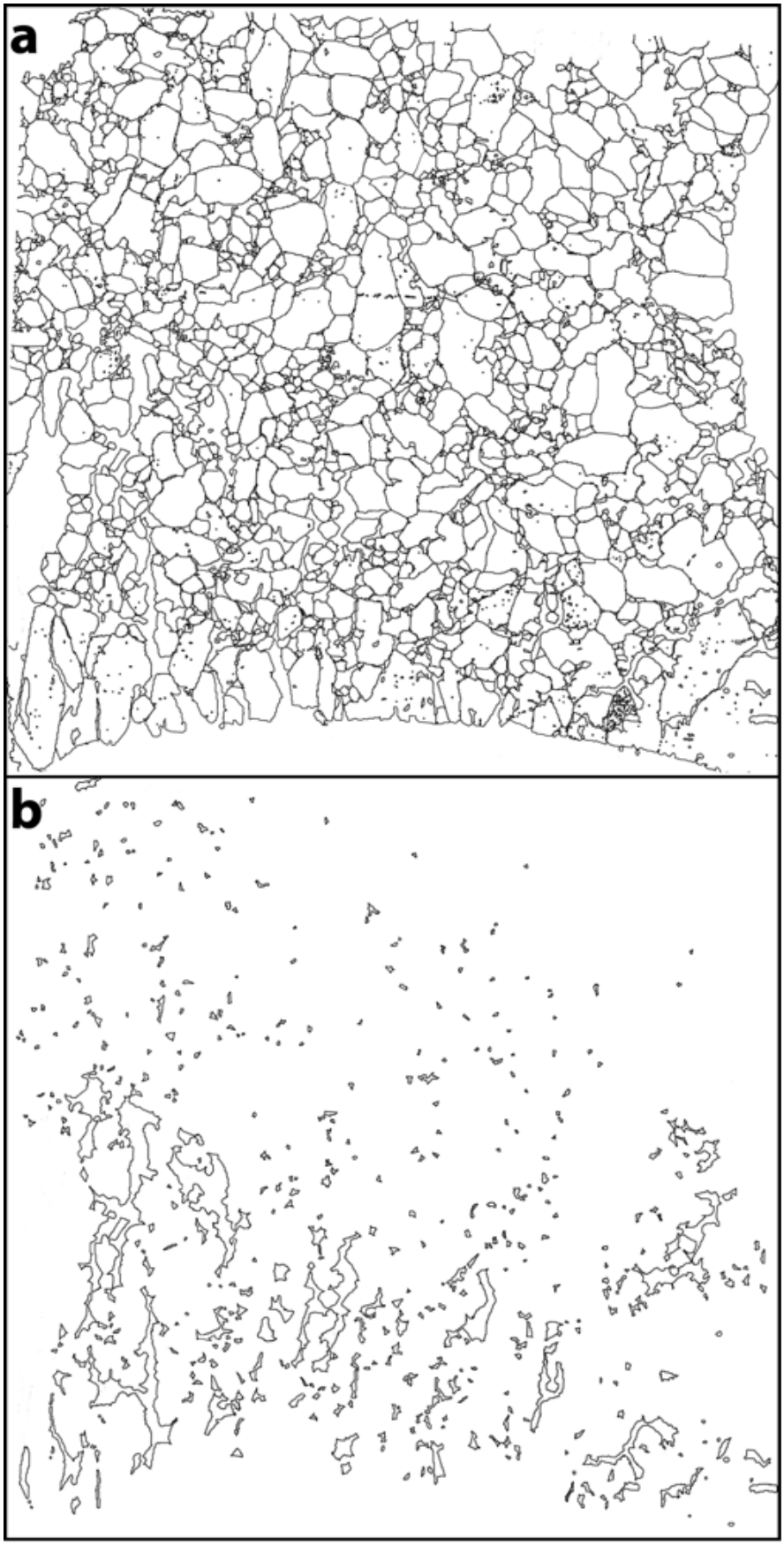

Fig. 4.91. EBSD output images from MTEX 4.1 routine of Matlab®. (a) olivine grain boundaries only; (b) carbonatitic liquids boundaries only.

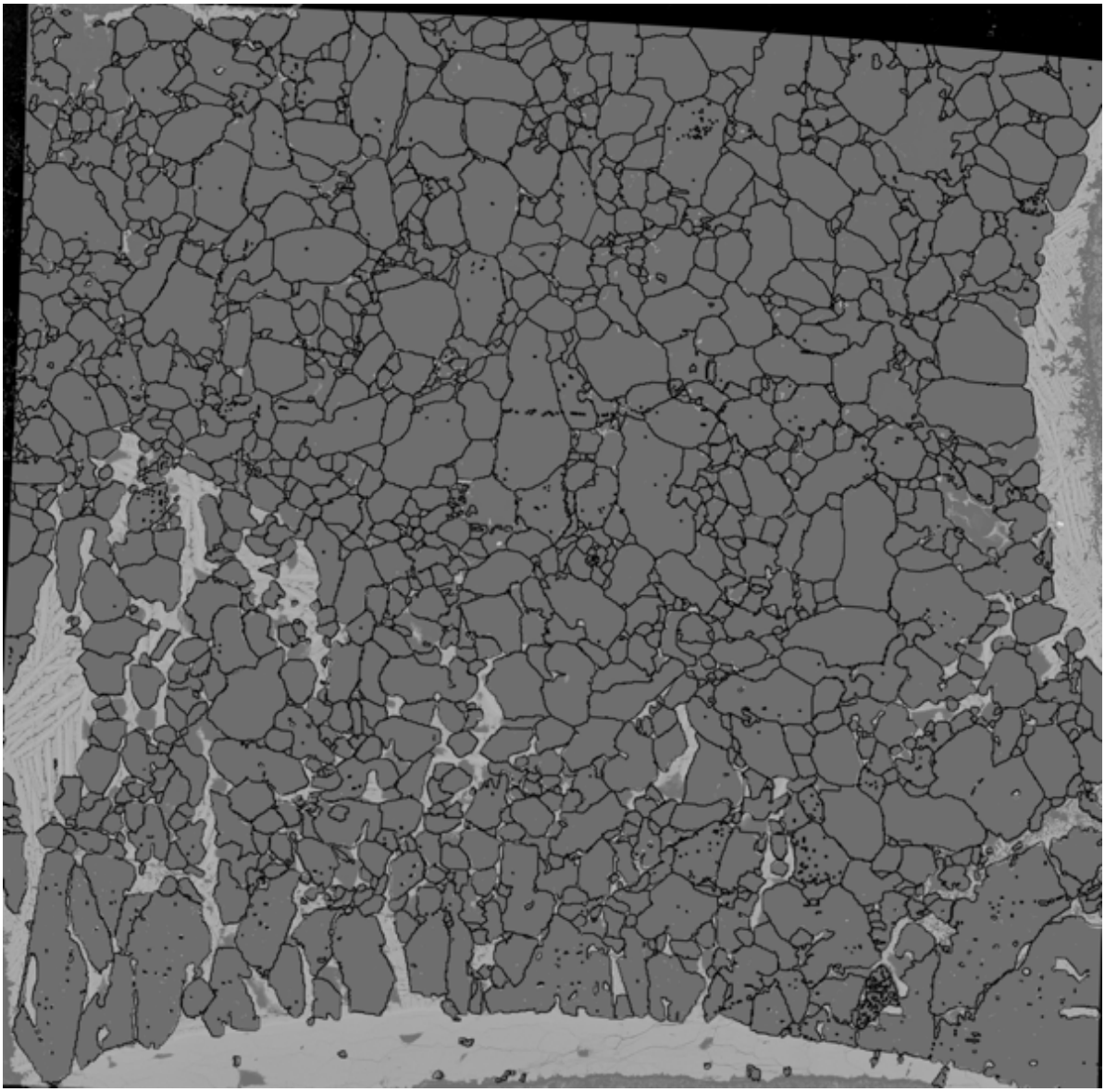

Fig. 4.92. EBSD output images superimposed on Ca X-ray map corresponding.

By means of Photoshop the EBSD olivine grain boundaries and liquids boundaries images were arbitrarily subdivided into two different images to be treated, because LSI_4 sample analysed, as mentioned before, is characterized by two distinct portions where different amounts of infiltrated liquid are differently distributed, here organized in melt pockets (in the far olivine dunite – carbonatitic reservoir interface) or in interconnected channels near the carbonatitic reservoir (Fig. 4.93a-d).

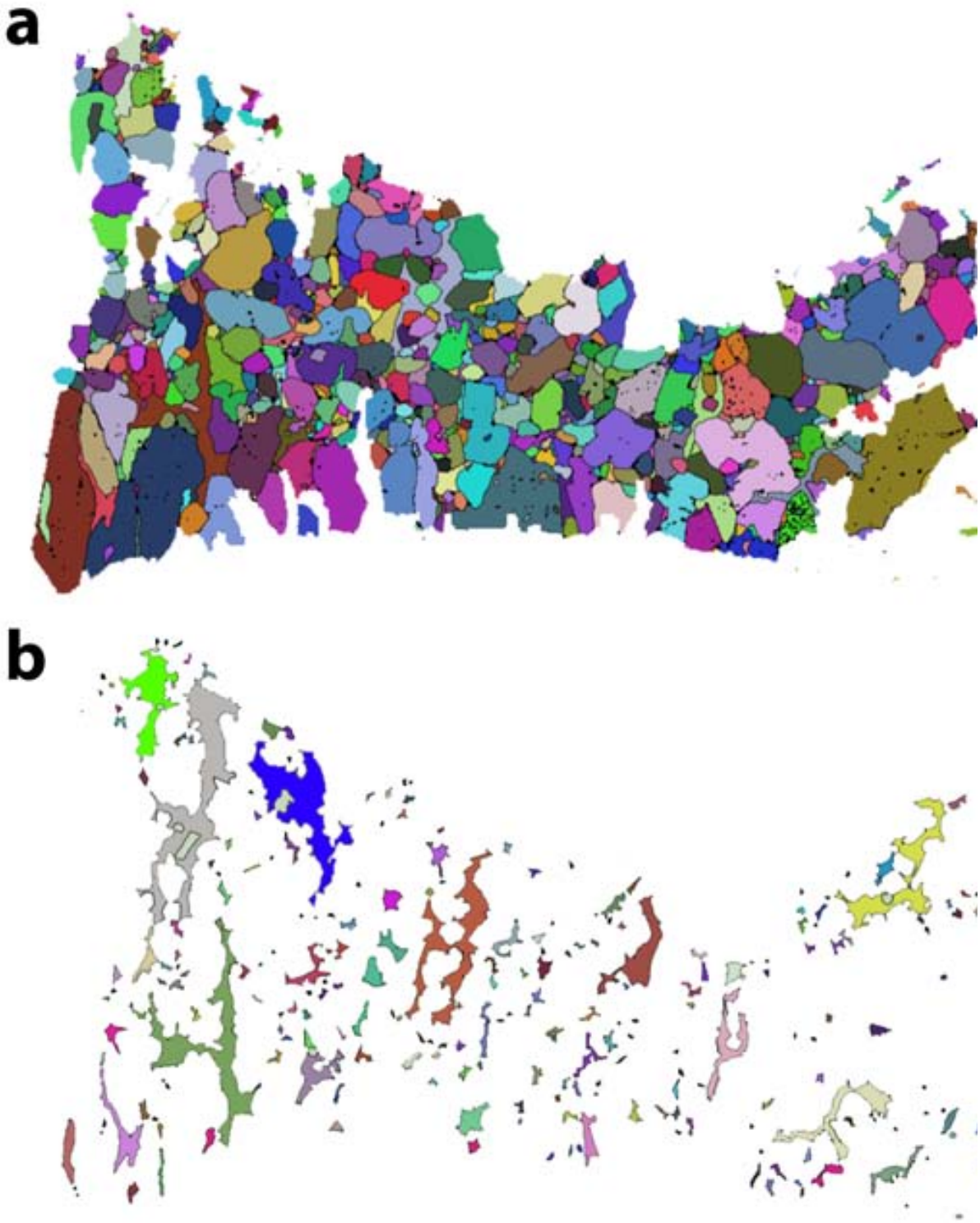

Fig. 4.93. EBSD output images from Matlab® showing LSI_4 sample olivine and liquids boundaries. (a) olivine grain boundaries close to the interface olivine – carbonatitic reservoir; (b) liquid interconnected channels related with the olivine in (a); (c) and (d) are two images representative respectively of olivine and liquid melt pockets boundaries in the bottom of the charge (far from olivine – carbonate powder interface).

Fig. 4.93. Continued

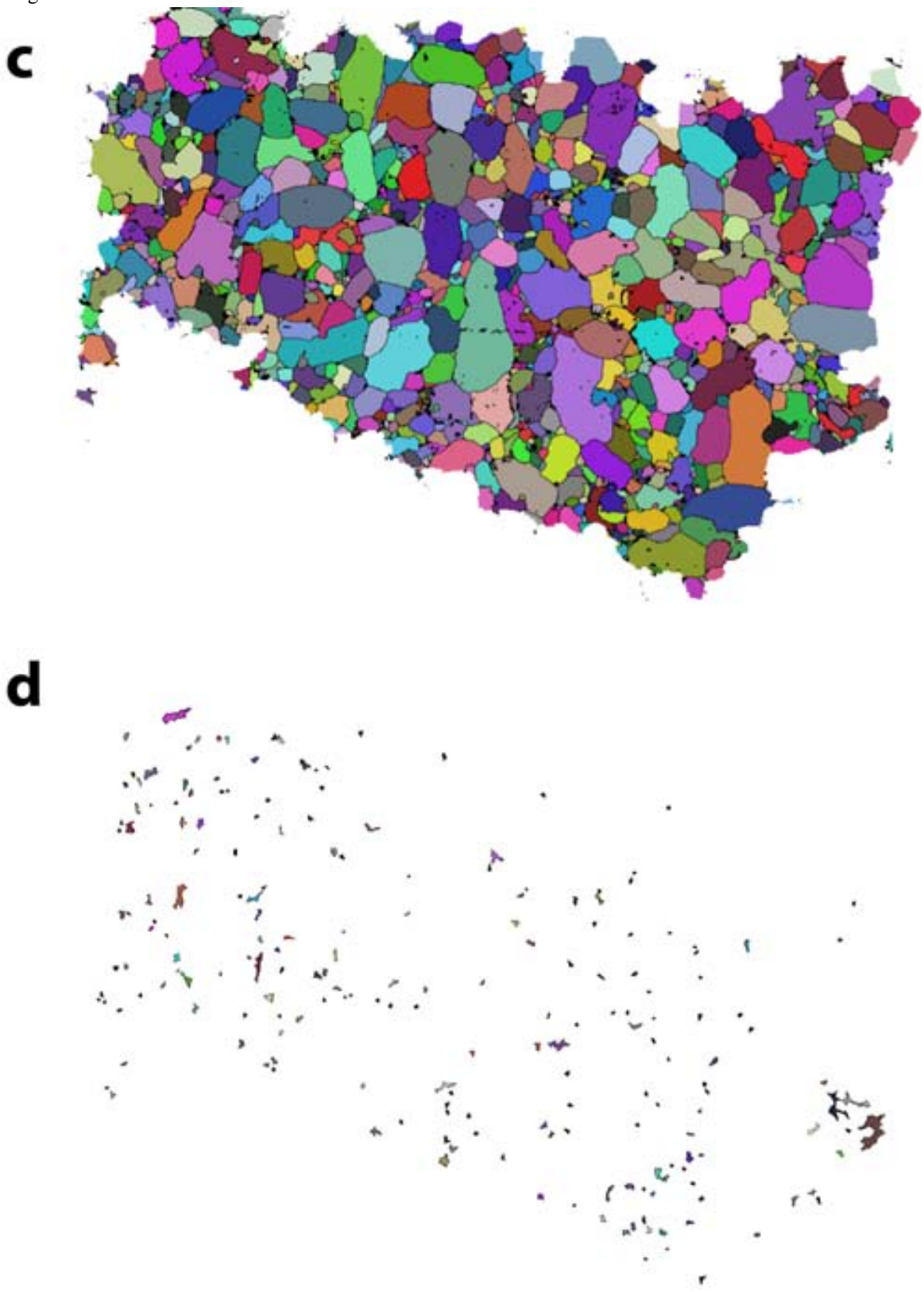

After this first image analysis approach, we wrote a Mathematica® routine to eliminate stray pixels that were interpreted as "noise" and that are not present into the calcium X-ray map and to remove any internal pixels aggregates into the olivine or liquid. A different Mathematica® script allow us to count and summarize all contiguous black pixel considered to represent solid or liquid boundaries and therefore to calculate A_{SS} (solid-solid interfacial area) for the two images of olivine grain boundaries and to calculate A_{SL} (solid-liquid interfacial area) for the image with melt pockets boundaries and with interconnected channel boundaries.

Remembering that the grain boundary wetness is the defined as the ratio of solid – liquid boundary area over the total area of interphase boundaries we measured two different grain boundary wetness values.

In the sample portion characterized by high carbonatitic liquid content in connected channel we have measured a grain boundary wetness value of 0.144 and 0.025 by means equation (3) in section 1.5.

4.5.3. Infiltrated liquid fraction

The volume liquid fraction infiltrated into the peridotitic matrix was calculate by processing the Ca and Si X-ray maps, using a Mathematica® routine to enhance the distinction between melt (characterized by calcium presence) and solid.

The contrast of the images was elevated in order to transform it into a binary image where by means of the erosion – dilation morphological operator we obtain a black and white image where the white representing calcium and silicon component for the Ca and Si X-ray maps respectively (Fig.4.94a-c).

These images were used to determine the percentage of white pixels in an image representative of the effective area of liquid and solid fractions.

This procedure was carried out in LSI_4 (300h), LSI_9 (30h), LSI_10 (3h) and the two experiments with 30 wt. % water content LSI_18 and LSI_19 samples.

After calculations of silica and calcium percentage in each experiment we have obtained a percentage of volume liquid fraction infiltrated in our experimental sample and these values are listed in Table 4.13. These calculations were performed only for the samples with the complete sample X-ray maps.

LSI_4 sample was divided into two portions as was be done previously due to the different liquid amount into the run charge.

Run	Ca	Si	Ca/(Ca+Si) %
LSI_4 (more infiltrated)	4.76	25.34	15.81
LSI_4 (less infiltrated)	1.08	45.04	2.35
LSI_9	9.25	79.13	10.47
LSI_10	6.05	66.07	8.39
LSI_18	6.97	73.71	8.64
LSI_19	1.77	60.99	4.00

Table. 4.13. Our calculations of percentage of volume of COH liquid infiltrated into the dunite matrix represented here by the Ca/(Ca+Si) ratio in selected runs.

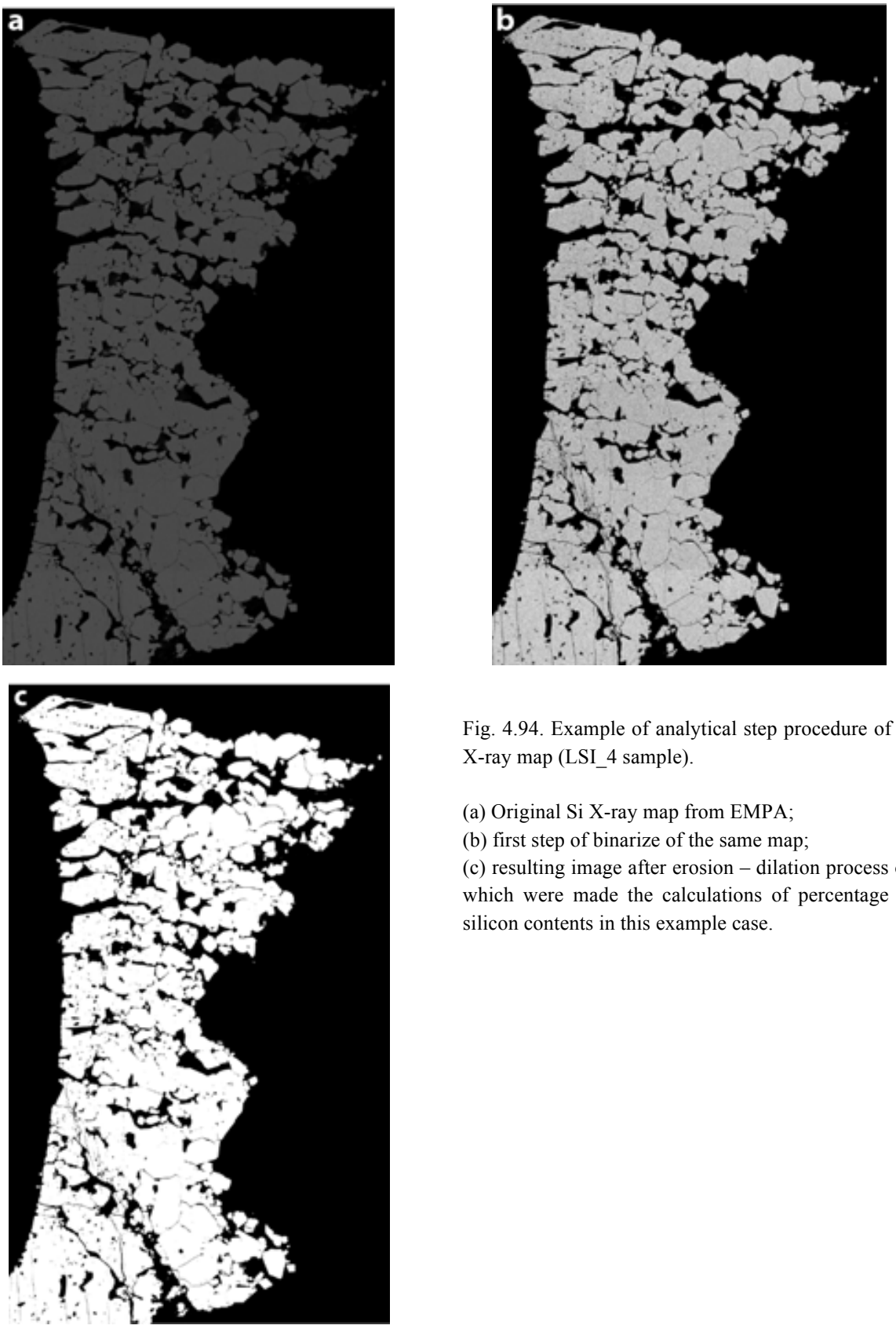

Fig. 4.94. Example of analytical step procedure of Si X-ray map (LSI_4 sample).

(a) Original Si X-ray map from EMPA;
(b) first step of binarize of the same map;
(c) resulting image after erosion – dilation process on which were made the calculations of percentage of silicon contents in this example case.

These results can be compared to the volume liquid fraction obtained by Hammouda and Laporte (2000) infiltrating a dunite with carbonatitic melts. Hammouda and Laporte (2000) measured a volume of Na_2CO_3 liquid infiltrated into dunite of 18% related with a wetting angle of 30°. Overall, the values found in our work are invariably lower.

Comparing the portion characterized by porous flow infiltration of LSI_4 sample with anhydrous samples present in literature seems to be a dependence by water presence and run duration. In fact, the volume of hydrous carbonatitic liquid infiltrated results to be lower than anhydrous liquids.

The 2 vol.% of hydrous carbonatitic liquids infiltrated in long run duration experiment results to be lower than medium and short run experiments with ~ 8-10 vol.%. For this reason, seems to be a dependence between volume infiltrated melts and run duration experiments.

Furthermore, the experiments with high water content (30 wt.%) and 48 duration present a volume of liquid infiltrated into the dunite between 4 to 9 vol.% with higher wetting angles measured (almost 50°).

Chapter 5

Discussion

5.1. The variability of wetting angle of volatile-rich liquids and fluids

	Capsule material	Run Time (h)	Starting Material	θ measured (°)	Pressure (Gpa)	Temperature (°C)
Hunter and McKenzie (1989)	Pt	92	sp-lherz + $MgCa(CO_3)_2$	28	3	1290
Watson et al. (1990)	Pt	24 - 144	S.C.ol + Na_2CO_3 S.C.ol + K_2CO_3 S.C.ol + $CaCO_3$+H_2O	23 - 26	1-3	1300
Minarik and Watson (1995)	Ti+grph	10 - 20	S.C.ol + Na_2CO_3	25 - 30	1	1300
Hammouda and Laporte (2000)	Pt	0.16 - 95	S.C.ol(+MgO-SiO_2) + Na_2CO_3	30	1	1300

Table. 5.1. Previous experimental dihedral angle measured in literature between peridotitic matrix and carbonatitic reservoir. See Table. 4.9. to compare with our experiments.
Abbreviations:
Pt = platinum; Ti = titanium; grph = graphite; sp-lherx = spinel lherzolite; S.C.ol = San Carlos olivine.

The behaviour of carbonate melts has been previously investigated and the experimental characterizations considering dihedral angle of liquids infiltrated in a peridotitic matrix with their results are listed in Table 5.1. From the wetting angle measurements (see section 4.5.1) we can state that the true θ values for hydrous carbonatitic liquids are higher compared to anhydrous wetting angles reported in literature (Table. 5.1).

These differences may be due to the bulk carbonate compositions, but also experimental run durations. Possibly, the most crucial factor is the presence and amount of water content in the experimental setup as seen in our results.

Hunter and McKenzie (1989) performed experiments with anhydrous iron-free dolomite in a spinel lherzolite from San Carlos matrix with 79 vol.% of olivine, 15 vol.% of orthopyroxene and 3 vol.% both clinopyroxene and spinel, at pressure of 3 GPa and 1290 °C of temperature using a Pt capsule without graphite sleeve for 92 hours and they have measured six sets of melt – matrix dihedral angles, i.e., olivine-olivine-melt, olivine-orthopyroxene-melt, olivine-garnet-melt, orthopyroxene-orthopyroxene-melt, orthopyroxene-garnet-melt and garnet-garnet-melt; overall, they have obtained a wetting angle value of 28°. Furthermore, Hunter and McKenzie

(1989) present the only cumulative frequency curve available in literature on carbonatitic liquids. They have constructed this curve from 100 measurements of apparent dihedral angles for only ol-ol-melt set of melt matrix and the correspondence of the cumulative distribution with the theoretical distribution of apparent dihedral angles for a given true wetting angle demonstrates that the local textural equilibrium was achieved and the anisotropic surface are negligible (Fig. 5.1).

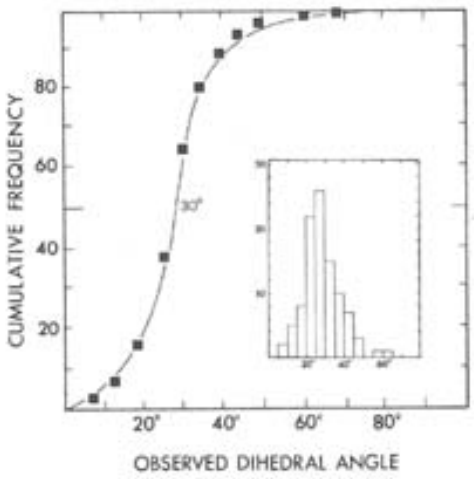

Fig. 5.1. Cumulative frequency curve of ol-ol-melt wetting angles with data plotted as 5° intervals. The metian point yelds a value of 28 ° for the true dihedral angle from Hunter and McKenzie (1989). They have shown the theoretical distribution of apparent dihedral angle for a true angle of 30 °.

Watson et al. (1990) investigated a San Carlos olivine with anhydrous alkali carbonate (Na_2CO_3 and K_2CO_3) and hydrous $CaCO_3$ at $P - T$ conditions from 1 to 3 GPa and 1300 °C respectively (it is important to remember that calcite is not expected in a peridotite matrix at these pressure and temperature conditions). They performed experiments with platinum capsule without graphite in a range of run time between 24 to 144 hours obtaining a narrow range of dihedral angle from 23° to 26° observing no systematic dependence upon intensive variables like temperature and pressure. Their results confirm the low dihedral angle value for anhydrous carbonatite melts measured by Hunter and McKenzie (1989) indicating that the carbonate melt in an olivine – rich mantle will be interconnected in three dimensions.

Minarik and Watson (1995) investigated the interconnectivity of anhydrous carbonate melt at low melt fraction carrying out experiments at 1 GPa and 1300 °C using as starting material the San Carlos olivine mixed against Na_2CO_3 carbonate powder. This mixture was contained within a graphite liner inside a titanium outer capsule covered by platinum disk at the top and run time between 10 to 20 hours. They measured a carbonate – olivine dihedral angle between 25° to 30°.

These wetting angles are far less than the critical dihedral angle of 60°, and their experiments show that a low melt fractions (0.03 – 0.07) demarcates a lower limit to melt interconnectivity. Finally, Hammouda and Laporte (2000) performed infiltration experiments at the same $P - T$ conditions of Minarik and Watson (1995) on couples consisting of a synthetic dunite placed against a carbonatite reservoir (at the top of dunite) made of sodium carbonate saturated with forsterite ($MgO+SiO_2$) at experimental conditions using a simple Pt capsule from ten minutes to 95 hours. They obtained a value computed for a dihedral angle of 30 °. They estimated a volume fraction of carbonatitic melt in the dunite of 0.18. By means of the different run time of their experiments they estimated the impregnation processes and then the infiltration rate of carbonatite melt in mantle lithologies evaluating the velocity of this process by means of the distance of infiltrated melt from liquid reservoir to the most distant portions from it and the relative mobility occurring in three different steps: dissolution, transport and precipitation (see section 2.1; Fig. 2.4).

	Run Time (h)	Starting Material	θ measured (°)	Pressure (Gpa)	Temperature (°C)
Waff and Balau (1979)	160	ol + basalt	50	1	1240
Toramaru and Fujii (1986)	300	sp-lherz	49	1	1300
Daines and Kohlstedt (1993)	6–32	ol + basalt/ol-opx+basalt	27 - 38	3	1250
Cmiral et al. (1998)	240-612	ol+basalt	10	1	1360
Yoshino et al. (2005)	–	ol+MORB	34	1	1350
	–	sp-lherz	34	1	1200-1350
Faul and Scott (2006)	168	ol+basalt	12	1	1250-1450
Yoshino et al. (2009)		ol+MORB	12	1	1200-1350

Table. 5.2. Previous experimental dihedral angle measured in literature between olivinic matrix and MORB/basaltic melt source and in partially molten peridotite. See Table. 4.9. to compare with our experiments.

The description of dihedral angle as a key parameter to interpret the behaviour of liquids in solid matrix (mantle or crustal lithologies) has been of primary concern not only in systems involving carbonate or carbonatitic melts, as mentioned above, but obviously also using silicate melts as liquid fraction.

The most extensively investigated system is olivine + basaltic melt (Table. 5.2). The dihedral angles in this system were first measured on a light microscope (Waff and Balau, 1979) with a reported value of 50°. They performed experiments in a single stage piston cylinder apparatus at 1 GPa and 1240 °C of pressure and temperature for 160 hours of duration and they observed a

completely interconnected network of channels glass phase along intergranular edge intersections.

Measurements on relatively low-magnification backscattered electron images resulted in a median angle of 49° for experiment carried out by Toramaru and Fujii (1986) at 1 GPa and 1300 °C $P - T$ conditions for 300 hours using a spinel lherzolite (ol = 58%, opx = 25%, cpx = 15% and sp = 2%) from Kilborne Hole, New Mexico.

Daines and Kohlstedt (1993) in their study to estimate experimentally the melt migration to investigate the dependence of permeability on melt fraction on opx content for a partially molten aggregate of olivine + basalt and olivine-orthopyroxene reported wetting angle values between 27° to 38° from SEM images in their experiments performed at 1250° C and 3 GPa of pressure in a run time duration ranging from 6 to 32 hours.

In order to investigate quantitatively melt – filled pore geometry in texturally equilibrated aggregates by means of the grain boundary wetness measurements, Yoshino et al. (2005) analysed San Carlos olivine + MORB melt and partially molten fertile spinel lherzolite systems. These two systems were investigated at 1 GPa of pressure and 1350 °C for olivine and from 1200 °C to 1350 °C for the spinel lherzolite and, despite the relevant temperature differences, the median point of apparent dihedral angle values measured was the same of 34° associated at low melt fraction between 0.02 to 0.31 vol.%. On the other hand, using higher resolution images Yoshino et al., 2009 for a sample in runs ranging from 1200 °C to 1350 °C and 1 GPa show the cumulative frequencies of apparent dihedral angles comparing it with theoretical cumulative distribution of the median obtained from each run, the measure angles deviate from the theoretical curve when apparent angles are large (Fig. 5.2). Furthermore, they show how the dihedral angle values decreased until 12° with increasing of temperature at 1 GPa, approaching to 0° at solidus temperature of mantle peridotite at higher pressure, 5 GPa and approximatively 1550 °C (Fig. 5.3).

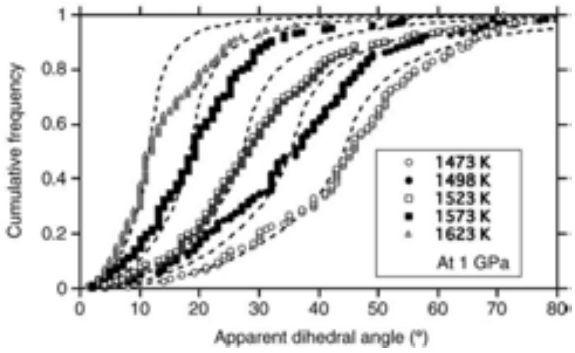

Fig. 5.2. Cumulative frequency distributions of apparent wetting angle of olivine – melt dihedral angle at 1 GPa with different temperature (In kelvin degrees). The dashed curves represent the theoretical distributions calculated by Jurewicz and Jurewicz, 1986 (Yoshino et al., 2009).

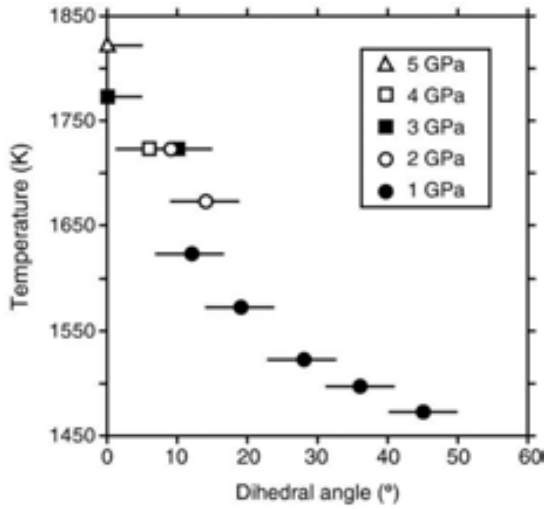

Fig. 5.3. Dihedral angle variation as a function of temperature in partially molten peridotite (Yoshino et al., 2009).

This value measured by Yoshino et al. (2009) is in fair agreement with values reported by Cmiral et al. (1998) and by Faul and Scott (2006).

In fact, Cmiral et al. (1998) performed high resolution analysis in experimental samples at 1 GPa and 1360 °C in a range of time between 240 to 612 hours and they obtained a dihedral angle of 10°, because TEM magnification reflects a small amount of quench growth during cooling experiments.

Faul and Scott (2006) in experiments with olivine + basalt system at fixed durations of 168 h in a range of temperature between 1250 to 1450 °C by means EBSD mapping and BSE images reported true wetting angle values of 12°. From these literature data it is possible to appreciate not only the differences in temperature and pressure, but also the crucial importance of the image resolutions on which measured angles and that these measured values are smaller in relation to this.

The study of dihedral angles extended to relationships between fluid and mineral interfaces both considering aqueous fluids (or pure water) and CO_2-rich fluids.

In their study, Watson and Brenan (1987) determined experimentally the characteristics of pure water and CO_2-rich fluids along with their implications for fluid transport in synthetic rock samples (dunite and quartzite).

After experiments at 1 GPa and in a range of temperature from 950 °C to 1150 °C for 5 days they measured a wetting angle of 57° for aqueous fluids in equilibrium with synthetic quartzite, and of ~ 90°in CO_2-rich fluids (Xco_2 ~ 0.9). The behaviour for aqueous and carbon dioxide rich

fluids in equilibrium with a matrix made of dunite is substantially the same. In fact, they reported the wetting angle values of 65° and 90° respectively.

The results of Mibe et al. (1998) after annealing experiments on forsterite aggregate at pressure from 3 to 5 GPa and 1000 °C, in equilibrium with aqueous fluid show wetting angle values between 48° to 40°. These values are smaller than 60°, which indicates that also aqueous fluid forms interconnected network along grain boundaries at high pressure (Fig. 5.4). However, Mibe et al. (1999), performing experiments at 800 °C, again at pressure from 3 to 5 GPa, found dihedral angle values greater than 60° at low *P*, and lower than 60° at higher pressure. The observations by Mibe et al. (1998, 1999) show that the wetting angle values decrease with both an increase of pressure and of temperature. They have obtained a median of dihedral angle values of 62° (3 GPa) and 57° (5 GPa) (Fig. 5.5a and b).

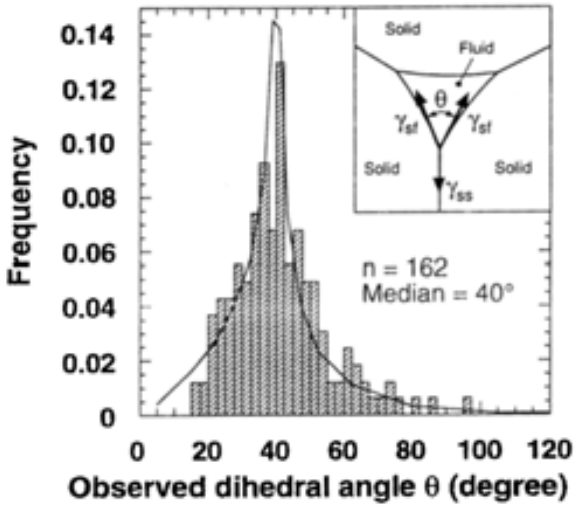

Fig. 5.4. Relative frequency distribution of apparent dihedral angle values at H_2O – rich fluid in equilibrium with forsterite at 1000 °C and 5 GPa (Mibe et al., 1998).

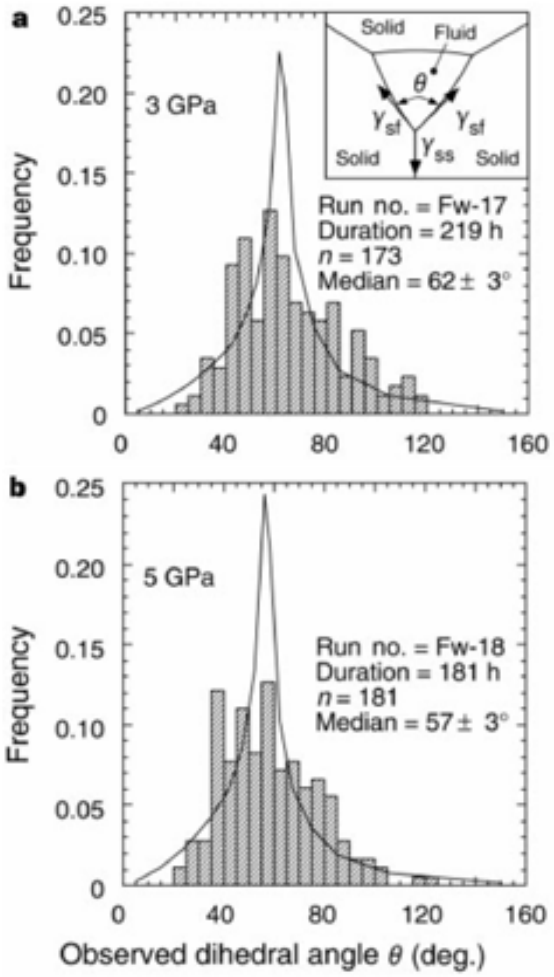

Fig. 5.5. Relative frequency distribution of apparent dihedral angle values at H_2O – rich fluid in equilibrium with forsterite at 3 GPa (a) and 5 GPa (b) (Mibe et al., 1999).

Lower temperatures and high pressure experiments involving H_2O-rich fluids but in equilibrium with an eclogite composition show the same measured results of Watson and Brenan (1987) (Mibe et al., 2003). They performed experiments using synthetic gel with MORB composition adding 6 wt. % of water from $Al(OH)_3$ using the multianvil high-pressure apparatus at range of temperature between 700 °C to 800 °C and pressures of 3, 4 and 5 GPa. They measured a wetting angle for cpx-fluid, garnet-fluid and garnet-cpx-fluid reporting values range from 62° to 68° in fair agreement with dihedral angles of aqueous fluids with olivine and quartzite lithologies from Watson and Brenan (1987).

5.2. The evolution of pore geometry with time

Liquid – phase – sintering (LPS) is a process for forming multiphase dense materials from powder aggregates. LSP involve the sintering process where liquid and solid phases coexist (German et al., 2009).

It is widely accepted that when the liquids form in LPS the resulting microstructure is made of solid, liquid and vapour. The balance of the interfacial energies of these three state conditions governs the dihedral angle. A typical wetting liquid tends to move into the boundary with lowest energy configuration flowing between small grains into the pores.

In LPS case involving both liquids and vapours again with solid phase, the solid – vapour dihedral angle is at the intersection between grains and vapour phases but where liquid phase is involved the angle is within the intersection of the grains contacts with liquid phase.

Microstructures are constantly evolving with time during the sintering process and the final structure with prolonged sintering evolves until a single grain, or crystal, configuration with a structure well developed by time (Fig. 5.6).

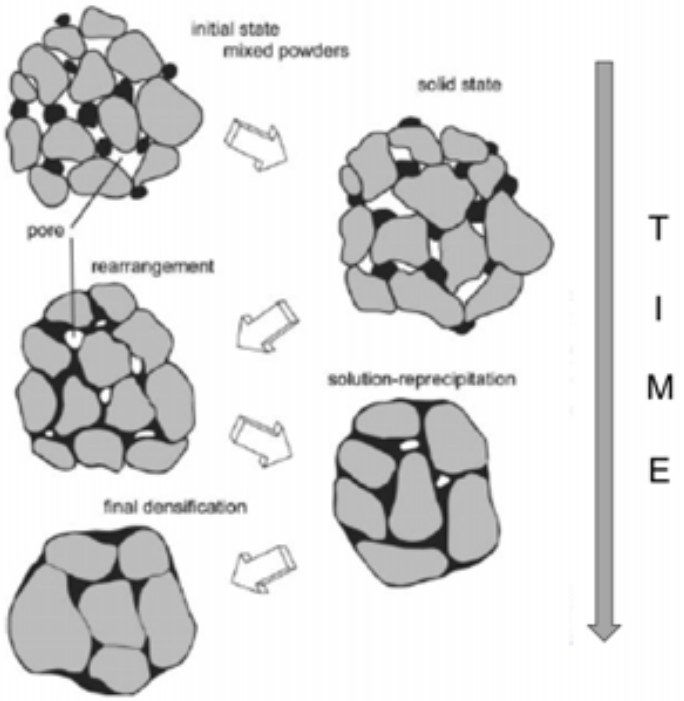

Fig. 5.6. Schematic microstructure changes with time increasing during sintering process with mixed powder and pores between grains (mod. from German et al., 2009).

Small changes in the solid – liquid surface energy are able to give liquid penetration of grain boundary, spreading to fill small pores (Brada and Clarke, 1997).

This reaction decreases the solid liquid interface below the equilibrium causing a variation of dihedral angle values. In the first step of sintering the dihedral angles and the whole system tends to the equilibrium condition with a decrease in wetting angle values with time (Fig. 5.7, left side of the curve).

In the late stage of densification (see Fig. 5.6), grain boundary development and annealing processes move the interfaces toward equilibrium, with a progressive growth of sintering necks, migration of grain boundaries and reduction of interstitial liquid fraction.

Our experiments, representative of a wetting liquid, can be interpreted in this theoretical frame. The increase of dihedral angle values with run time is representative of a sintering process, where the first stages of vapour-filled pore reorganization, liquid spreading and neck formation are omitted because infiltration in our experiments occur in a previously sintered compact.

After liquid formation the low dihedral angle values enables liquid penetration of the grain boundaries, therefore the solid-liquid system and also the evolution of dihedral angles discussed in section 4.5.1 is an expected evolution tending to equilibrium condition as a function of time (Fig. 5.7).

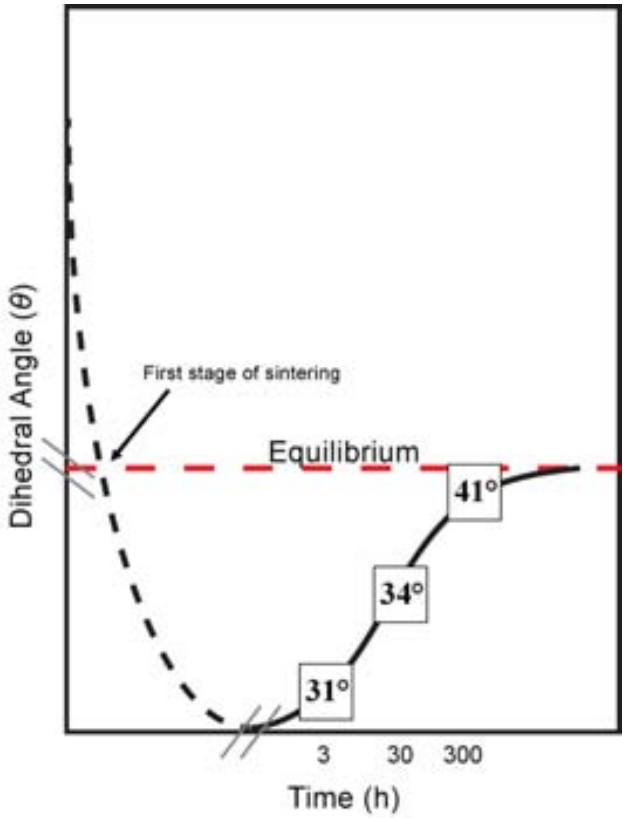

Fig. 5.7. Schematic diagram that shows the relation between dihedral angle values with time. The first stage of sintering, not occurring in our experiments, highlights a decrease of wetting angle values with time (ramp down), while in the ramp up it is possible to observe an increasing of wetting angle with run time experiment underlined by our measured true dihedral angle values in our experiments (mod. from German et al., 2009).

5.3. Channelization and grain boundary wetness

Strictly related to evolution of pore geometry we observed the channelization of pores, mainly due to gradients in temperature or chemical composition of intergranular fluid or melt at lithospheric mantle conditions. The channelization of pores varies with lithology and it was found to be stronger for calcite + quartz + wollastonite with H_2O-CO_2-rich fluid, and decreases for aqueous fluid in olivine. Channelization process changes the modality of migration of metamorphic fluids or melts, increasing permeability without advection (Wark and Watson, 2002). Fluids and melts occupy micropores with geometries dictated by interfacial energy (Smith, 1969), assuming the fluid or melt distribution uniform despite some differences in the microstructure of pores (Wark and Watson, 2002). However, in a deep-seated rocks contest we expected non-uniform fluid or melt distribution and this may be modified by mineralogy variations (Watson, 1999) and consequently by chemistry, by grain size (Wark and Watson, 2000) and consequently by pores microstructure.

Wark and Watson (2002) point their interest in the channelization of pores as a process promoted by strong gradients in fluid composition (XCO_2 specifically). In their experimental samples, they observed differences of pores microstructures due to gradients of fluids and melts compositions thus modifying the channels morphology varying the mineral-fluid or melt.

Characterizing LSI_4 experiment performed at 2.5 GPa and 1200 °C, and run time duration of 300 hours (see section 4.1 and 4.2), we noted two different infiltrated melt behaviour from top to bottom of the run charge we have interpreted the run charge part characterized by interconnected channels as result of channelization process (Fig. 5.8).

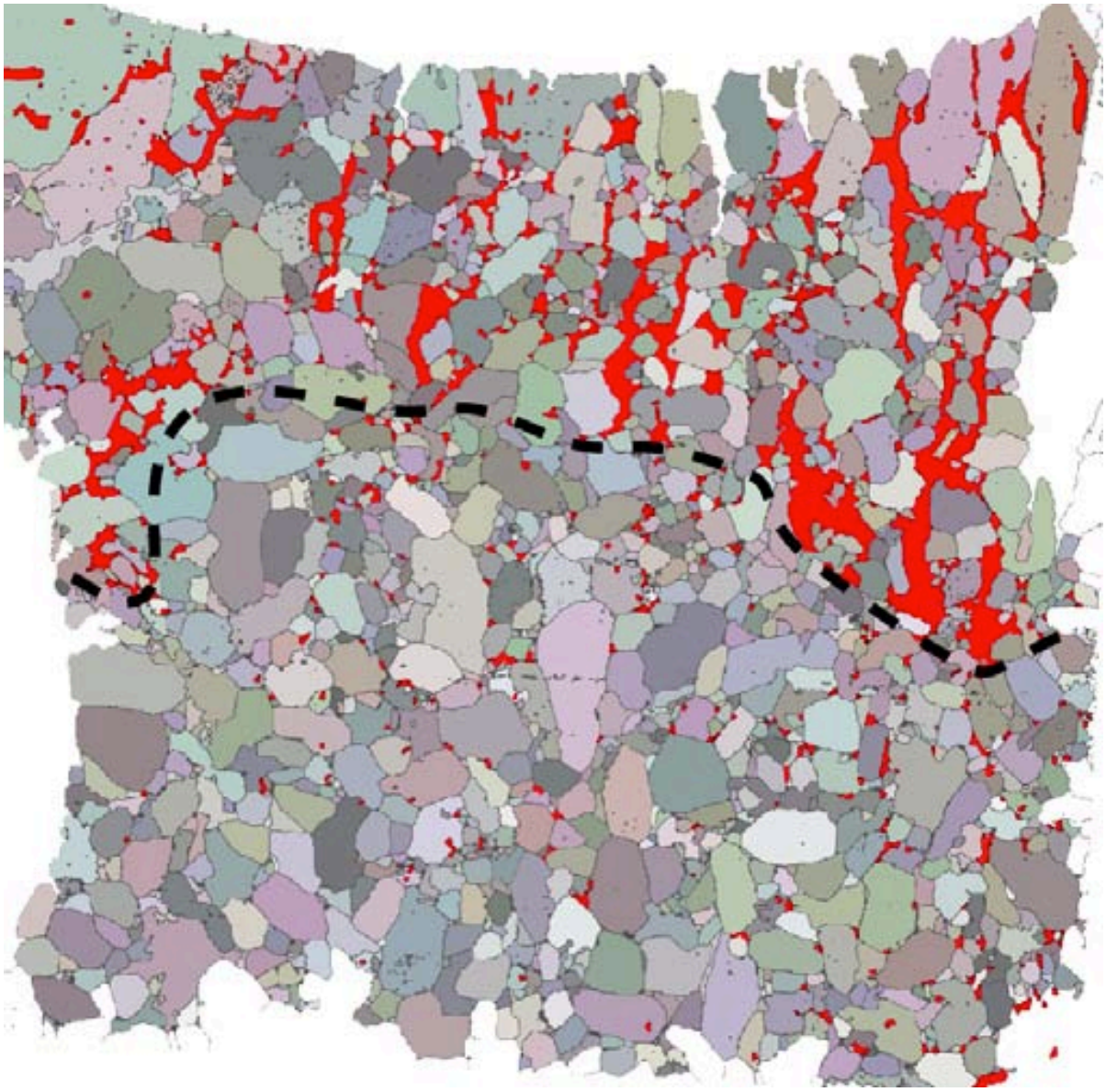

Fig. 5.8. EBSD image modified by Photoshop program showing clearly (in red) the liquid portion strongly channelized at the top of the run charge compared with the bottom of it separated by black dotted line.

Channelization is highlighted when grain boundary wetness is compared to the fraction of liquid infiltrated in the solid matrix. The obtained relationship between grain boundary wetness ψ and

volume liquid fraction φ infiltrated in the solid matrix can be fitted well to the formulae $\psi = A\varphi^{1/2}$ with fitting parameter "A" indicating that the three-dimensional pore shape is a tabular one (Fig. 5.10). Also shown in Fig. 5.10 the theoretical results obtained by Riley and Kohlstedt (1991), von Bargen and Waff (1986) and Takei (2002) assuming a tube geometry without corner effects (Fig. 5.9a), tetrakaidecahedral grains with coordination number (Nc) of 14 (Fig. 5.9b) and rhombic dodecahedral grains with Nc = 12 (Fig. 5.9c), respectively. In these models the isotropic interfacial energy and uniform melt distribution are assumed, and the ψ - φ relationship is derived as a function of wetting angle θ.

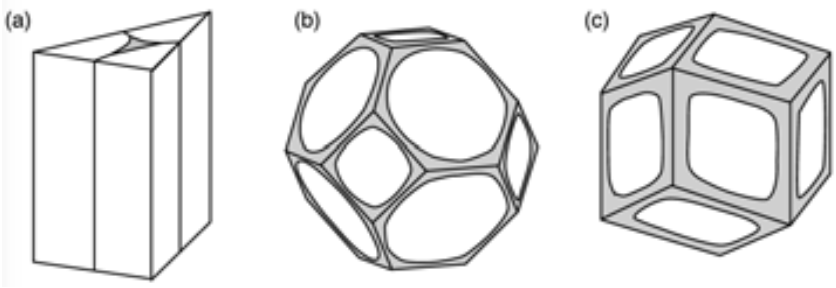

Fig. 5.9. Scheme of grain packing geometry. (a) tube model of Riley and Kohlstedt (1991); (b) tetrakaidecahedral grain of von Bargen and Waff (1986); and (c) rhombic dodecahedral grain of Takei (2002). White part represent grains and grey part the liquid phase.

We have therefore compared the volume liquid fractions infiltrated into the dunite rod, measured (see section 4.5.3) for the two different parts of the sample, with the calculated grain boundary wetness in this sample (see section 4.5.2). As LSI_4 displays a $\theta \sim 41°$, we performed such comparison with grain boundary wetness values measured by Yoshino et al. (2005) in olivine + basalt and partially molten peridotite at the closest θ value, i.e. $\theta \sim 35°$.

Fig. 5.10 shows that very low values of grain boundary wetness are related to volume of liquid infiltrated for carbonatitic melt in our study, both for the sample portion that shows interconnected channels and for the portion characterized by carbonatitic liquid pockets.

Such low grain boundary wetness measured in our experiment may be due to an underestimation of liquid amounts, but this is unlikely because with a relatively high wetting angle we do not expect liquid films, hardly detectable with routine BSE analysis, on grain-grain interfaces. As a consequence, low wetness should be attributed to relatively low liquid-solid interfaces, which develop if the liquid is channelized. Similarly, the portion of the run charge characterized by the carbonate liquid pockets is not representative of porous flow infiltration but should be also

related to a channelization processes promoted by chemical gradient, possibly evolving to macroscopic channelization of pores with time (Wark and Watson, 2002).

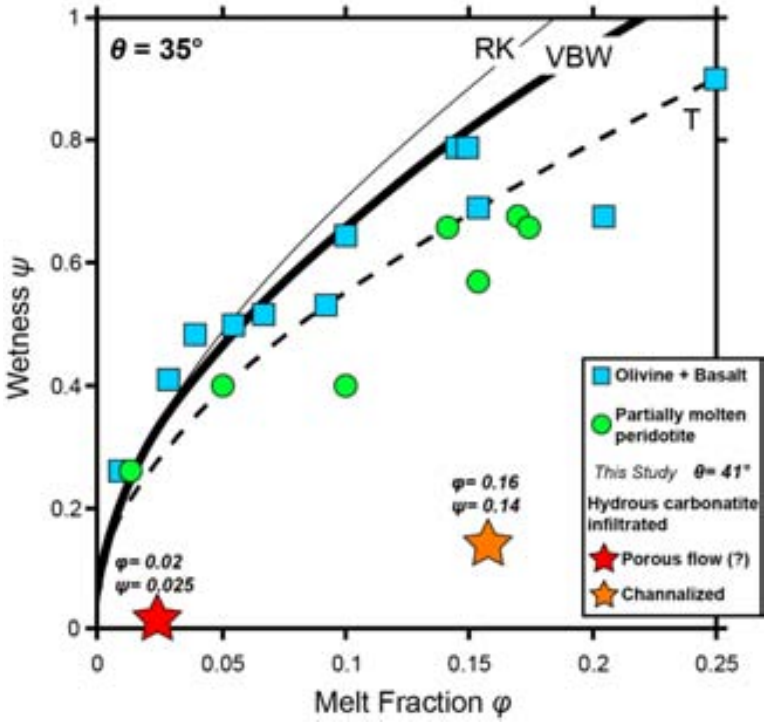

Fig. 5.10. Plot of wetness and melt fraction related of olivine + basalt and partially molten peridotite systems from Yoshino et al., 2005 with our experiment measured values. Thin, thick and dotted curves represent ψ-ϕ relations of tube geometry (RK - Riley and Kohlstedt, 1991), tetrakaidecahedral grain packing geometry (VBW - von Bargen and Waff, 1986), and rohombic dodecahedral grain packing geometry (T - Takei, 2002) at 35° of wetting angle (mod from Yoshino et al., 2005).

5.4. A reversal in the wettability of carbonatitic vs. silicate magmas

Several studies conducted by Waff and Balau (1979 and 1982) and Toramaru and Fujii (1986) concerning the morphology of liquids in partial molten peridotites show, as previously summarized, that the wetting angle of basaltic melts in olivine is between 30° to 50° in the uppermost mantle close to solidus conditions.

In order to assess the wetting angle variation between olivine matrix and a morb melt, Yoshino et al. (2009) fitted the experimental data through parabolic equation. Then they calculated the melt composition in equilibrium with olivine using pMELTS program (Ghiorso et al., 2002) and constructed a contour map of wetting angle for different temperatures and pressures. Their results illustrate the dependence of dihedral angle on melt structure in partially molten peridotite, and demonstrate that temperature is the variable mostly controlling variations in dihedral angle.

As the solidus for carbonatitic magmas is located at relatively low temperature (see Chapter 1), it is therefore a common assumption that carbonatitic liquids are more wetting than basaltic melts, and therefore more mobile.

Nonetheless, as widely described in the first chapter, water is believed to be an important component of carbonatitic liquids and it plays a crucial role in many carbonatite magma models (Veksler and Keppler, 2000). It was assumed that the water solubility in the carbonate melts was in order of 14 wt. % at low pressure and relatively high temperature (0.225 GPa and 900 °C; Keppler, 2003) and 10 wt. % at even lower pressure of 0.1 GPa and temperature between 700 °C to 900 °C (Veksler and Keppler, 2000), which is two to three times higher than the value observed for most silicate liquids under same or similar pressure and temperature conditions (Behrens, 1995).

For these reasons, according to Keppler (2003) we can safely assume that water partitions preferably into carbonatitic melts compared to silicate melts at similar $P - T$ conditions.

Having said that, the comparison of the true wetting angle measured for our runs at high water content (experiments with 30 wt. % of water at 2.5 GPa and 1200 °C pressure and temperature conditions) with olivine + morb melt systems studied by Yoshino et al. (2009) shows how the wetting angles of silicate melts have much lower values than those carbonatitic liquids which are unexpectedly high (Fig. 5.11). The Fig. 5.11 shows clearly the dependence of dihedral angle on melt structure and composition in partially molten peridotites highlighting how the dihedral angle values tend to be small in a system in which the liquid phase (Morb) has a similar

composition with the solid phase (olivine). Melt structures are related by the degree of polymerization and its increase approaches the melt structure to that solid structure (Yoshino et al., 2009).

Considering the inability to polymerize to form network structures of carbonate ions and the presence of water in the system involving hydroxyl bonds highlighting negative effect on stability structures and polymerization, our experimental results can be also explained in this frame.

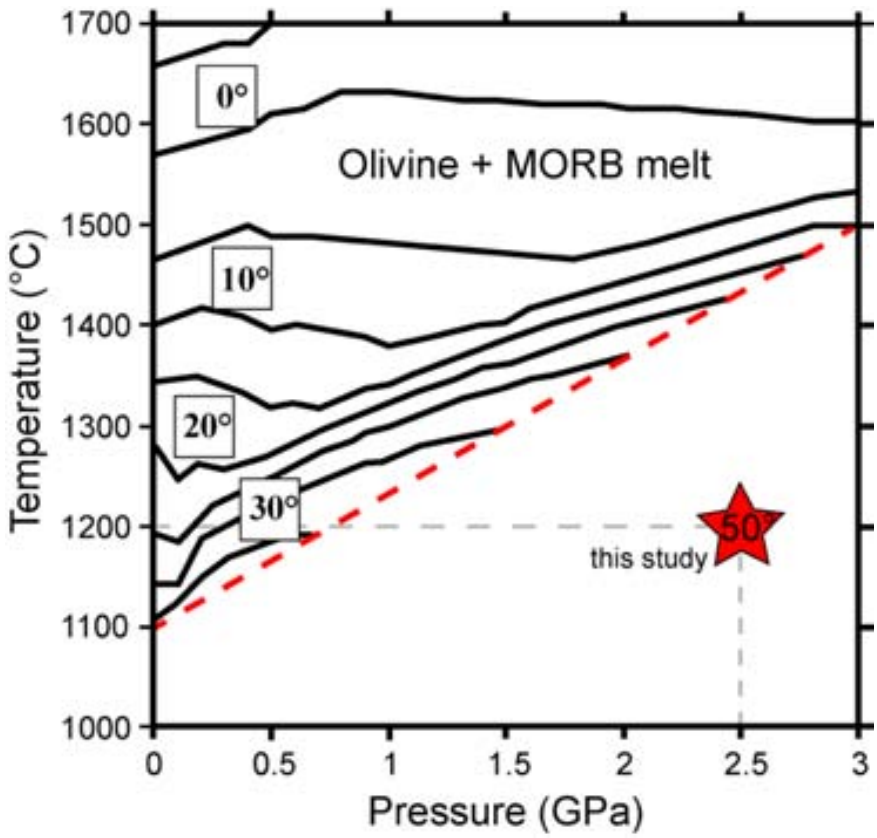

Fig. 5.11. Isopleths diagram of the dihedral angles values in olivine – MORB liquid system for the model mantle compositions (Ringwood, 1966) in $P - T$ space. Dashed – red line represents the solidus curve in the peridotite system from Herzberg et al., 2000. Red star represents the P – T conditions of our experiments performed with 30 wt. % of water content of this study with true dihedral angle measured of ~ 50°.

Chapter 6

Summary and Conclusions

Knowledge of pore geometry is essential to understanding bulk physical properties, interconnectivity and mobility mechanisms of melts in partially molten rocks.

It is widely accepted that the melt- or fluid-filled pore geometry in texturally equilibrated aggregates is controlled by the interfacial energies (Smith, 1964; Bulau et al., 1979; Waff and Balau, 1979; Watson, 1982; Jurewicz and Jurewicz, 1986).

The equilibrium of pore geometry can be determined by knowing the porosity and the dihedral angle, which is determined by the ratio of solid-solid and solid-liquid interfacial energies (von Bargen and Waff, 1986).

Measurements of the dihedral angle has been the most common way to assess the geometry and connectivity of intergranular liquids by researchers that have investigated the dihedral angles of the geometry of anhydrous carbonatitic melts (Hunter and McKenzie, 1989; Watson et al., 1990; Minarik and Watson, 1995; Hammouda and Laporte, 2000), C-O-H fluids (Watson and Brenan, 1987) and silicate melts (Bulau et al. , 1979; Waff and Balau, 1979; Toramaru and Fujii, 1986; Daines and Kohlstedt, 1993; Cmiral et al., 1998; Faul and Scott, 2006; Yoshino et al. (2005 and 2009) in various silicate mineral aggregates at various pressure and temperature conditions.

Because experimental studies demonstrated that dihedral angles are independent of melt fraction (Waff and Faul, 1992; Faul, 1997; Garapic et al., 2013), another parameter is needed to account the variability of melt geometry in partially molten rocks as grain boundary wetness which is a parameter that relate solid-liquid and solid-solid interfacial areas (Yoshino et al., 2005).

Our experimental results in the hydrous carbonatitic liquids in the dunite matrix system at P = 2.5 GPa and T = 1200 °C at different run experimental durations suggest several differences between our systems and silicate or anhydrous carbonatitic melts in different silicate aggregates in terms of dihedral angle values and grain boundary wetness.

The variability of wetting angle suggests that the addition of water into a carbonatitic melt solution (5 or 30 wt.% of mixture of starting carbonates) compared with silicate and anhydrous carbonatitic melts, or compared with volatile-rich fluids, shifts the dihedral angle toward values significantly higher than 30°, up to 48-50° for liquids with high dissolved H_2O. Such values,

although much higher than the upper limit found by previous researchers for anhydrous carbonatitic liquids, are still lower than the threshold of 60°, i.e. the value required to inhibit the interconnected network for a carbonatitic systems (Hunter and McKenzie, 1989).

Considering that the evolution of pore geometry changes with time (German et al., 2009) we demonstrated that our experiments can be represented in this frame presenting similar behavior.

An increase of dihedral angle values with time is expected to follow a first stage of sintering process where a decrease of wetting angle is observed; the increase of dihedral angle with time is then the result of a path toward final equilibration of interfacial energies (Fig. 5.7).

Experimental results also demonstrate an evolution of the pore geometry; we observe different stages of channelization of pores filled by hydrous carbonatitic liquid due to gradient of temperature and chemical composition. We noted different infiltration behaviors underlined comparing the grain boundary wetness with volume liquid infiltrated into the dunite rod. We have interpreted this difference due to a channelization process evolving from "micro-channelization" of pore with time.

Last, although it is widely assumed that carbonatitic liquids are more wetting and more mobile than silicate magmas, if H_2O is available, we expect that H_2O partitions into carbonatitic liquids rather than in silicate liquids at the same *P*-*T* conditions. As a result, hydrous carbonatitic form, their dihedral angle may evolve up to 50°, a value, as shown, significantly higher than that characterizing silicate melts at similar mantle conditions (see Chapter 5, section 5.4, Fig. 5.11). In conclusion, if silicate and carbonatitic maintain immiscibility, hydrous carbonatitic liquid may preferentially segregate and conserve their identity in an olivine mantle solid matrix.

Acknowledgments

I would like to thank my PhD supervisor Stefano Poli. I am deeply greateful to him for teaching me how to live the laboratory and to introduce me to experimental petrology.
His support has been an invaluable asset to my growth as a researcher and I am thankful for the time he has dedicated to me beyond my academic endeavour.
A big thank you also goes to my co-supervisors Patrizia Fumagalli and Simone Tumiati. Over the last three years, they have always shown a sincere interest in my research and gave me precious feedbacks. I truly appreciate their constant presence in my short life in Milan.
I would like to thank Benoit Ildefonse (University of Montpellier) for the assistance provided during EBSD sessions at the University of Montpellier.
Thanks to Andrea Risplendente (University of Milan) for his support during electron microprobe analyses.
Thanks to Giulio Borghini (University of Milan) for his support and helpfulness in the experimental petrology laboratory.
Thanks to Massimo Coltorti (University of Ferrara), Carmelo Ferlito (University of Catania) and Matteo Alvaro (University of Pavia) for their support and help in my university life.
Thanks to the reviewers S. Conticelli and M. Scambelluri to a significant tips of the thesis.
I am grateful to Carla Tiraboschi for her crucial scientific contribution and “psychological” sympathy, especially in the “lament moments”.
I also want to thank my PhD fellows and the “kitchen” colleagues Simone Tumiati, Gianluca Sessa, Alessandro DaMommio, Davide Comboni, Marilena Moroni, Elena Ferrari, Giovanni Grieco, Mattia Bonazzi, Micol Bussolesi and Enrico Cannaò for sharing some good laughs with me.
I am grateful to the members of the “CAVALLO” group Simone Tumiati, Carla Tiraboschi and Andrea Risplendente (yes, it’s always them) and Francesca Miozzi, Irene Fantone and Paolo Lotti for being great friends to me.

I treasure the presence in my life of people that I have felt deeply close in spite of physical distance, like my friends and colleagues from Rome Psarakis, Giulio, Simone, Queengliarini, Claudia, and from Ferrara Beatrice, Pierpaolo, Maria, whom I thank for their invaluable friendship.
Thanks to my “cugy” Adele for her great English support and for being there for me in these three years, as well as Marzia in the “sushi-time”.
Thanks also to Alessia G. for the “beer and volleyball” moments and for her healthy and lovely dose of craziness.
There is a person who has been important for me in these three years. I thank Laura C.D., who has recently undertaken the crazy geology path, for the complicated but exciting communications and for much more than this.
I would like to thank my friends forever Ileana and Alessandra SjuSju. When it comes to them, distance is just a number and I do not add anything else because these would be unnecessary words.
Thanks to Nano, Marcella V., Silvia ”blablablabla” M., Caterina M., Laura D.G. and “crazy Claudia F.”, the “petro-speleologist”, for their constant presence in all kinds of situations.
A special thanks to Antonella A. who has been essential for my personal growth.

Finally, I would like to thank my family…Mom and Dad and Manu for always being part of my existence, the most important people in my life again, this personal accomplishment would have never been possible without their support…and this is for them.

References

Bachmann, F., Hielscher, R., Schaeben, H. (2010) Texture analysis with MTEX – free and open source software toolbox. *Solid State Phenomena, 160*, 63 – 68.

Bailey, D.K. (1960) Carbonatites of the Rufunsa Valley, Feira District. *Bullettin 5, Geological Survey of Northern Rhodesia*.

Bailey, D.K. (1984) Kimberlite: "The mantle sample" formed by ultra – metasomatism. *In J Kornprobst, Ed., Kimberlites, vol. I: Kimberlites and related rocks. Proceedings of the Third International Kimberlite Conference*, 323 – 333.

Bailey, D.K. (1989) Carbonate melt from the mantle in the volcanoes of south – east Zambia. *Nature, 388*, 415 – 418.

Bailey, D.K. (1993) Carbonate magmas. *Journal of the Geological Society, London, 150*, 637 – 651.

Balau, J.R., Waff, H.S., Tyburczy, J.A. (1979) Mechanical and thermodynamic constraints on fluid distribution in partial melts. *Journal of Geophysical Research, 84*, 6102 – 6108.

Becker, M., Le Roex, A.P. (2006) Geochemistry of South African On- and Off- craton, Group I and Group II Kimberlites: Petrogenesis and Source Region Evolution. *Journal of Petrology, 47(4)*, 673 – 703.

Behrens, H. (1995) Determinations of water solubilities in high – viscosity melts: An experimental study on $NaAlSi_3O_8$ melts. *European Journal of Mineralogy, 7*, 905 – 920.

Best, M.G. (1982) Igneous and Metamorphic Petrology. *Brigham Young Univeristy. Blackwell Science Ltd.*

Boettcher, A.L., Kerrick, D.M. (1971) Temperature calibration in cold – seal pressure vessels. *In G.C. Ulmer, Ed., Research Techniques for High Pressure and High Temperature*, 179 – 193.

Bose, K., Ganguly, J. (1995) Quartz – coesite transition revisited: Reversed experimental determination at 500 – 1200 °C and retrieved thermochemical properties. *American Mineralogist, 80*, 231 – 238.

Boyd, F.R., England, J.L. (1960) Apparatus for Phase – Equilibrium measurements at pressures up to 50 kilobars and temperatures up to 1750 °C. *Journal of Geophysical Research, 65(2)*, 741 – 748.

Brada, M. P., Clarke, D.R. (1997) A thermodynamic approach to the wetting and dewetting of grain boundaries. *Acta Materialia, 45 (6)*, 2501 – 2508.

Brey, G.P., Bulatov, V.K., Girnis, A.V., Lahaye, Y. (2008) Experimental melting of carbonated peridotite at 6 – 10 GPa. *Journal of Petrology, 49*, 797 – 821.

Buob, A., Luth, R.W., Schmidt, M.W., Ulmer, P. (2006) Experiments solid solutions at high pressure and temperature. *American Mineralogist, 91*, 435 – 440.

Byrnes, A.P., Wyllie, P.J. (1981) Subsolidus and melting relations for the join $CaCO_3$ – $MgCO_3$ at 10 kbar. *Geochimica et Cosmochimica Acta, 45*, 321 – 328.

Canil, D., Scarfe, C.M. (1990) Phase relations in peridotite + CO_2 systems to 12 GPa: Implications for the origin of kimberlites and carbonate stability in the earth's upper mantle. *Journal of Geophysical Research, 95*, 15805 – 15816.

Circone, S., Agee, C.B. (1996) Compressibility of molten high-Ti mare glass: Evidence for crystal-liquid density inversions n the lunar mantle. *Geochimica et Cosmochimica Acta, 60*, 2709 – 2720.

Cmiral, M., Fitz Gerald, J.D., Faul, U.H., Green, D.H. (1998) A close look at dihedral angles and melt geometry in olivine – basalt aggregates: a TEM study. *Contribution to Mineralogy and Petrology, 130*, 336 – 345.

Connolly, J.A.D. (1990) Multivariable phase diagrams; an algorithm based on generalized thermodynamics. *American Journal of Science, 290*, 666 – 718.

Connolly, J. A. D., Cesare, B. (1993) C-O-H-S Fluid Composition and Oxygen Fugacity in Graphitic Metapelites. *Journal of Metamorphic Geology, 11*, 379 – 388.

Daines, M.J., Kohlstedt, D.L. (1993) A laboratory study of melt migration. *Philosophical Transactions of the Royal Society of London, 342*, 43 – 52.

Dalou, C., Koga, K.T., Hammouda, T., Poitrasson, F. (2009) Trace element partitioning between carbonatitic melts and mantle transition zone minerals: Implications for the source of carbonatites. *Geochimica et Cosmochimica Acta, 73(1)*, 239 – 255.

Dalton, J.A., Presnall, D.C. (1998) The continuum of primary carbonatitic – kimberlitic melt composition in equilibrium with lherzolite: data from the system $CaO\text{-}MgO\text{-}Al_2O_3\text{-}SiO_2\text{-}CO_2$ at 6 GPa. *Journal of Petrology, 39*, 1953 – 1964.

Dasgupta, R., Hirschmann, M.M., Stalker, K. (2006) Immiscible transition from carbonate – rich to silicate – rich melts in the 3 GPa melting interval of eclogite + CO2 and genesis of silica – undersaturated ocean island lavas. *Journal of Petrology, 47*, 647 – 671.

Dasgupta, R., Hirschmann, M.M., Smith, N.D. (2007a) Water follows carbon: CO_2 incites deep silicate melting and dehydration beneath mid – ocean ridges. *Geology, 35*, 135 – 138.

Dasgupta, R., Hirschmann, M.M., Smith, N.D. (2007b) Partial melting experiments of peridotite + CO_2 at 3 GPa and genesis of alkali ocean island basalts. *Journal of Petrology, 48*, 2093 – 2124.

Dasgupta, R., Hirschmann, M.M., McDonough, W.F., Spiegelman, M., Withers, A.C. (2009) Trace element partitioning between garnet lherzolite and carbonatite at 6.6 and 8.6 GPa with applications to the geochemistry of the mantle and of mantle – derived melts. *Chemical Geology, 262*, 57 – 77.

Dasgupta, R., Hirschmann, M.M. (2010) The deep carbon cycle and melting in Earth's interior. *Earth and Planetary Science Letters, 298*, 1 – 13

Dawson, J.B. (1962) Sodium carbonate lavas from Oldoinyo Lengai, Tanganyika. *Nature, 195*, 1075 – 1076.

Dawson, J.B., Hawthorne, J.B. (1973) Magmatic sedimentation and carbonatitic differentiation in kimberlite sill at Benfontein, South Africa. *Journal of the Geological Society, London, 129*, 61 – 85.

Dawson, J.B., Smith, J.V. (1977) The MARID (mica-amphibole-rutile-ilmenite-diopside) suite of xenoliths in kimberlite. *Geochimica et Cosmochimica Acta, 41*, 309 – 323.

Dawson, J.B. (1989) Sodium carbonatitic extrusions from Oldoinyio Lengai, Tanzania: implications for carbonatite complex genesis. In Bell, K. (Ed.), *Carbonatites: genesis and evolution. Unwin – Heyman, London.*

Dawson, J.B., Smith, J.V. (1988) Metasomatized and veined upper – mantle xenoliths from Pello Hill, Tanzania: evidence for anomalously – light mantle beneath the Tanzanian sector of the East African Rift Valley. *Contributions to Mineralogy and Petrology, 100(4)*, 510 – 527.

Dawson, J.B., Smith, J.V. (1992) Potassium loss during metasomatic alteration of mica pyroxenite from Oldoinyo Lengai, northern Tanzania: contrasts with fenitization. *Contributions to Mineralogy and Petrology, 112(2)*, 254 – 260.

Dawson, J.B., Smith, J.V., Steele, I.M. (1995) Petrology and mineral chemistry of plutonic igneous xenoliths from the carbonatite volcano, Oldoinyo Lengai, Tanzania. *Journal of Petrology, 36(3)*, 791 – 826.

Dick, H.J.B., Bullen, T. (1984) Chromian spinel as a petrogenetic indicator in abyssal and alpine-type peridotites and spatially associated lavas. *Contributions to Mineralogy and Petrology, 86(1)*, 54 – 76.

Dobson, D.P., Jones, A.P., Rabe, R., Sekine, T., Kurita, K., Taniguchi, T., Kondo, T., Kato, T., Shimomura, O., Urakawa, S. (1996) In – situ measurement of viscosity and density of carbonate melts at high pressure. *Earth and Planetary Science Letters, 143*, 207 – 215.

Eberius, E. (1958) Wasserbestimmung mit Karl – Fischer – Lösung. Verlag Chemie, Weinheim.

Eggler, D.H. (1989) Carbonatites, primary melts, and mantle dynamics. In Bell, K. (Ed.), *Carbonatites: genesis and evolution. Unwin – Heyman, London.*

Faul, U.H. (1997) The permeability of partially molten upper mantle rocks from experiments and percolation theory. *Journal of Geophysical Research, 102*, 10299 – 10311.

Faul, U.H., Scott, D. (2006) Grain growth in partially molten olivine aggregates. *Contributions to Mineralogy and Petrology, 151*, 101 – 111.

Foley, S.F., Yaxley, G.M., Rosenthal, A., Buhre, S., Kiseeva, E.S., Rapp, R.P., Jacob, D.E. (2009) The composition of near – solidus melts of peridotite in the presence of CO_2 and H_2O between 40 and 60 kbar. *Lithos, 112*, 274 – 283.

Foustoukos, D.I., Mysen, B.O. (2015) The structure of water – saturated carbonate melts. *American Mineralogist, 100*, 25 – 46.

Fredriksson, P., Sundmann, B. (2001) A thermodynamic assessment of the Fe – Pt system. *Calphad, 25*, 535 – 548.

Garapić, G., Faul, U.H., Brisson, E. (2013) High resolution imaging of the melt distribution in partially molten upper mantle rocks: evidence for wetted two – grain boundaries. *Geochemistry Geophysics Geosystems, 14(3)*, 556 – 566.

Genge, M.J., Jones, A.P., Price, G.D. (1995a) An infrared and Raman study of carbonate glasses: Implications for the structure of carbonatite magmas. *Geochimica et Cosmochimica Acta, 59*, 927 – 937.

Genge, M.J., Price, G.D., Jones, A.P. (1995b) Molecular – dynamics simulations of $CaCO_3$ melts to mantle pressures and temperatures. Implications for Carbonatite Magmas. *Earth and Planetary Science Letters, 131*, 225 – 238.

German, R. M., Suri, P., Park, S.J. (2009) Review: liquid phase sintering. *Journal of Materials Science, 44*, 1 – 39.

Ghiorso, M.S., Hirschmann, M., Reiners, P.W., Kress, V.C. (2002) The pMELTS: A revision of MELTS for improved calculation of phase relations and major element partitioning related to partial melting of the mantle to 3 GPa. *Geochemistry, Geophysics, Geosystem, 3(5)*, doi: 10.1029/201GC000217.

Gudfinnsson, G., Presnall, D.C. (2005) Continuous gradations among primary carbonatitic, kimberlitic melilititic, basaltic, picritic and komatitic melts in equilibrium with garnet lherzolite at 3 – 8 GPa. *Journal of Petrology, 46*, 1645 – 1659.

Hamilton, D.L., Bedson, P., Esson, J. (1989) The behavior of trace elements in the evolution of carbonatites. In Bell, K. (Ed.), *Carbonatites: genesis and evolution. Unwin – Heyman, London,* 405 – 427.

Hammouda, T., Laporte, D. (2000) Ultrafast mantle impregnation by carbonatite melts. *Geology, 28(3)*, 283 – 285.

Hammouda, T. (2003) High – pressure melting of carbonated eclogite and experimental constraints on carbon recycling and storage in the mantle. *Earth and Planetary Science Letters, 214*, 357 – 368.

Herzberg, C., Raterron, P., Zhang, J. (2000) New experimental observations on the anhydrous solidus fo peridotite KLB-1. *Geochemistry, Geophysics, Geosystems, 1*, doi: 10.1029/2000GC000089.

Hirose, K. (1997) Partial melt composition of carbonated peridotite at 3 GPa and role of CO_2 in alkali – basalt magma generation. *Geophysical Research Letters, 24*, 2837 – 2840.

Holland, T.J.B. (1980) The reaction albite: jadeite + quartz determined experimentally in the range 600 – 1200 °C. *American Mineralogist, 65*, 129 – 134.

Humphreys, F.J. (1999) Quantitative metallography by electron backscattered diffraction. *Journal of Microscopy, 195(3)*, 170 – 185.

Hunter, R.H., McKenzie, D. (1989) The equilibrium geometry of carbonate melt in rocks of mantle composition. *Earth and Planetary Science Letters, 92*, 347 – 356.

Ihinger, P.D., Hervig, R.I., McMillan, P.F. (1994) Analytical methods for volatiles in glasses. *Reviews in Mineralogy, 30*, 67 – 121.

Irving, AJ., Wyllie, P.G. (1975) Subsolidus and melting relationship for calcite, magnesite and the join $CaCO_3$ – $MgCO_3$ to 36 kb. *Geochimica et Cosmochimica Acta, 39*, 35 – 53.

Jakobsson, S. (2012) Oxygen fugacity control in piston – cylinder experiments. *Contribution to Mineralogy and Petrology, 164*, 397 – 406.

Jarosewic, E., Nelen, J.A., Norberg, J.A. (1980) Reference samples for Electron Microprobe Analysis. *Geostandards Newsletter, 4(1)*, 43 – 47.

Johannes, W., Bell, P.M., Mao, H.K., Boettcher, A.L., Chipman, D.W., Hays, J.F., Newton, R.C., Seifert, F. (1971) An interlaboratory comparison of piston-cylinder pressure calibration using the albite-breakdown reaction. *Contributions to mineralogy and Petrology, 32(1)*, 24 – 38.

Johannes, W., Bode, B. (1978) Loss of iron to the Pt – container in melting experiments with basalt and a method to reduce it. *Contribution to Mineralogy and Petrology, 67*, 221 – 225.

Jones, A.P., Dobson, D.P., Genge, M. (1995) Comment on Physical – properties of carbonatite magmas inferred from Molten – salt data and Application to extraction patterns from carbonatite – silicate magma chambers - Discussion. *Geological Magazine, 132*, 121 – 121.

Jones, A.P., Genge, M., Carmody, L. (2013) Carbonate Melts and Carbonatites. *Reviews in Mineralogy and Geochemistry, 75*, 289 – 322.

Jurewicz, S.R., Jurewicz, A.J.G. (1986) Distribution of Apparent Angles on Random Sections with Emphasis on Dihedral Angle Measurements. *Journal of Geophysycal Research, 91*, 9277 – 9282.

Keppler, H. (2003) Water solubility in carbonatite melts. *American Mineralogist, 88*, 1822 – 1824.

Kono, Y., Kenney-Benson, C., Hummer, D., Ohfuji, H., Park, C., Shen, G., Wang, Y., Kavner, A., Manning, C.E. (2014) Ultralow viscosity of carbonate melts at high pressures. *Nature Communications, 5, DOI: 10.1038/ncomms6091*.

Koster van Groos, A.F. (1990) High – pressure DTA study of the upper three – phase region in the system Na_2CO_3 – H_2O. *American Mineralogist, 75*, 667 – 675.

Le Bas, M.J. (1987) Nephelinites and carbonatites. *Geological Society London Special Publications, 30(1),* 53 – 83.

Le Maitre, R.W. (2002) Igneous Rocks: A Classification and Glossary of Terms. *Cambridge University Press, Cambridge, UK.*

Lesher, C.E., Walker, D. (1986) Solution properties of silicate liquids from thermal diffusion experiments. *Geochimica et Cosmochimica Acta, 50*, 1397 – 1411.

Lesher, C.E., Walker, D. (1988) Cumulate maturation and melt migration in a temperature gradient. *Journal of Geophysical Research, 93*, 10295 – 10311.

Liu, Q., Lange, R.A. (2003) New density measurements on carbonate liquids and the partial molar volume of the $CaCO_3$ component. *Contribution to Mineralogy and Petrology, 146*, 370 – 381.

Liu, Q., Tenner, T.J., Lange, R.A. (2007) Do carbonate liquids become denser than silicate liquids at pressure? Constraints from the fusion curve of K_2CO_3 to 3.2 GPa. *Contribution to Mineralogy and Petrology, 153*, 55 – 66.

Lupini, L., Stoppa, F. (1993) Mineralogy and Petrology of the Polino Monticellite Calciocarbonatite (Central Italy). *Mineralogy and Petrology, 49*, 213 – 231.

Mariano, A.N., Roeder, P.L. (1983) Kerimasi: A neglected carbonatite volcano. *Journal of Geology, 91*, 449 – 455.

Martin, L., Schmidt, M., Mattsson, H., Guenther, D. (2013) Element partitioning between immiscible carbonatite and silicate melts for dry and H_2O – bearing systems at 1 – 3 GPa. *Journal of Petrology, 54*, 2301 – 2338.

Melekhova, E., Schmidt, M.W., Ulmer, P., Pettke, T. (2007) The composition of liquids coexisting with dense hydrous magnesium silicates at 11 – 13.5 GPa and the endpoints of the solidi in the $MgO – SiO_2 – H_2O$ system. *Geochimica et Cosmochimica Acta, 71(13)*, 3348 – 3360.

Menzies, M.A., Wass, S.Y. (1983) CO_2 and LREE – rich mantle below eastern Australia: A REE and isotopic study of alkaline magmas and apatite – rich mantle xenoliths from the Southern Highland Province, Australia. *Earth and Planetary Science Letters, 65*, 287 – 302.

Mibe, K., Fujii, T., Yasuda, A. (1998) Connectivity of aqueous fluid in the Earth's upper mantle. *Geophysical Research Letters, 25(8)*, 1233 – 1236.

Mibe, K., Fujii, T., Yasuda, A. (1999) Control of the location of the volcanic front in island arcs by aqueous fluid connectivity in the mantle wedge. *Nature, 401*, 259 – 262.

Mibe, K., Yoshino, T., Ono, S., Yasuda, A., Fujii, T. (2003) Connectivity of aqueous fluid in eclogite and its implications for fluid migration in the Earth's interior. Journal of Geophysical Research, 108

Minarik, W.G. (1998) Complications to carbonate melt mobility due to the presence of an immiscible silicate melt. *Journal of Petrology, 39*, 1965 – 1973.

Minarik, W.G., Watson, E.B. (1995) Interconnectivity of carbonate melt at low melt fraction. *Earth and Planetary Science Letters, 133*, 423 – 437.

Mitchell, R.H. (2005) Carbonatites and carbonatites and carbonatites. *Canadian Mineralogist, 43(6)*, 2049 – 2068.

Moore, K.R., Wood, B.J. (1998) The transition from carbonate to silicate melts in the CaO-MgO-SiO_2-CO_2 system. *Journal of Petrology, 39*, 1943 – 1951.

Morimoto, N., Fabries, J., Ferguson, A.K., Ginzburg, I.V., Ross, M., Seifert, F.A., Zussman, J., Aoki, K., Gottardi, G. (1988). Nomenclature of clinopyroxenes. *American Mineralogist, 73*, 1123 – 1133.

Mysen, B.O. (1983) The structure of silicate melts. *Annual Review of Earth and Planetary Sciences, 11(1)*, 75 – 97.

Mysen, BO. (2012) High pressure and high – temperature titanium solution mechanism in silicate – saturated aqueous fluids and hydrous silicate melts. *American Mineralogist, 97*, 1241 – 1251.

Mu, S., Faul, U.H. (2016) Grain boundary wetness of partially molten dunite. *Contribution to mineralogy and Petrology, 171* (40)

Nelson, D.R., Chivas, A.R., Chappel, B.W., McCulloch, M.T. (1988) Geochemical and isotopic systematics in carbonatites and implications for the evolution of ocean – island sources. *Geochimica et Cosmochimica Acta, 52*, 1 – 17.

Nesbitt, B.E., Kelly, W.C. (1977) Magmatic and Hydrothermal inclusions in carbonatite of Magnet Cove Complex, Arkansas. *Contributions to Mineralogy and Petrology, 63*, 271 – 294.

Park, H.H., Yoon, D.N. (1985) Effect of Dihedral Angle on the morphology of grains in a matrix phase. *Metallurgical Transactions A, 16A*, 923 – 928.

Rhodes, J.M., Dawson, J.B. (1975) Major and trace element chemistry of peridotite inclusions from the Lashaine volcano, Tanzania. *Physics and Chemistry of the Earth, 9*, 545 – 557.

Riegger, O.K., Van Vlack, L.H. (1960) Dihedral angle measurements. *AIME Transactions, 218*, 933 – 5.

Riley, G.N.Jr., Kohlstedt, D.L. (1991) Kinetics of melt segregation in upper mantle-type rocks. *Earth and Planetary Science Letters, 105*, 500 – 521.

Ringwood, A.E. (1966) The chemical composition and origin of the Earth. *Advances in Earth Science*. Mit press, Cambridge, USA, 287 – 356.

Roden, M.F., Murthy, V.R. (1985) Mantle metasomatism. *Annual Review of Earth and Planetary Science Letters, 13*, 269 – 296.

Rudnick, R.L., McDonough, W.F., Chappell, B.W. (1993) Carbonatite Metasomatism in the Northern Tanzanian Mantle: Petrographic and Geochemical Characteristics. *Earth and Planetary Science Letters, 114(4)*, 463 – 475.

Sakamaki, T., Suzuki, A., Ohtani, E., Terasaki, H., Urakawa, S., Katayama, Y., Funakoshi, K., Wang, Y., Hernlund, J.W., Ballmer, M.D. (2013) Ponded melt at the boundary between the lithosphere and asthenosphere. *Nature Geoscience, 6*, 1041 – 1044.

Schmidt, M.W., Ulmer, P. (2004) A rocking multianvil: elimination of chemical segregation in fluid – saturated high – pressure experiments. *Geochimica et Cosmochimica Acta, 68(8)*, 1889 – 1899.

Shaw, H.R. (1980) The fracture mechanisms of magma transport from the mantle to the surface. In *RB Hargraves, Ed., Physics of magmatic processes: Princeton, N.J., Princeton University Press*, 201 – 264.

Smith, C.B. (1983) Pb, Sr, and Nd isotopic evidence for sources of African Cretaceous kimberlite. *Nature, 304*, 51 – 54.

Smith, C.S. (1969) Some elementary principles of polycrystalline microstructure. *Metallurgical Reviews, 9*, 1 – 47.

Sokol, A.G., Kupriyanov, I.N., Pal'yanov, Y.N. (2013) Partitioning of H_2O between olivine and carbonate – silicate melts at 6.3 GPa and 1400 °C: Implications for kimberlite formation. *Earth and Planetary Science Letters, 383*, 58 – 67.

Sokol, A.G., Kruk, A.N. (2015) Conditions of kimberlite magma generation: experimental constraints. *Russian Geology and Geophysics, 56(1-2)*, 245 – 259.

Soret, C. (1879) Sur l'ètat d'èquilibre que prend au point de vue de sa concentration une dissolution saline primitivement homogène dont deux parties sont portèes à des temperatures differentes. *Archives de Geneve, 2*, 48 – 61.

Spera, F.J. (1980) Aspects of magma transport. In *RB Hargraves, Ed., Physics of magmatic processes: Princeton, N.J., Princeton University Press*, 265 – 323.

Spera, F.J. (1987) Dynamics of translithospheric migration of metasomatic fluid and alkaline magma. *In M.A. Menzies and C.J. Hawkesworth, Eds., Mantle metasomatism*, 1 – 20.

Stalder, R., Ulmer, P. (2001) Phase relations od a serpentine composition between 5 and 14 GPa: significance of clinohumite and phase E as water carriers into the transition zone. *Contribution to Mineralogy and Petrology, 140(6)*, 670 – 679.

Stevens, R.E. (1944) Composition of some chromites of the western Hemisphere. *American Mineralogist, 29*, 1 – 34.

Streckeisen, A. (1980) Classification and nomenclature of volcanic rocks, lamprophyres, carbonatites and melilitic rocks. IUGS Subcommission on the systematics of Igneous Rocks. *Geologische Rundschau, 69*, 194 – 207.

Sweeney, R.J., Thompson, A.B., Ulmer, P. (1993) Phase relations of a natural MARID composition and implications form MARID genesis, lithospheric melting and mantle metasomatism. *Contribution to Mineralogy and Petrology*, 115, 225 – 241.

Sykes D., Baker, M.B., Wyllie, P.J. (1992) Viscous properties of carbonate melts at high pressure. *Eos, 73*, 72.

Takahashi, E. (1986) Melting of a dry peridotite KLB-1 up to 14 GPa: Implications on the origin of peridotitic upper mantle. *Journal of Geophysical Research, 91*, 9367 – 9382.

Takei, Y. (2002) Effect of pore geometry on Vp/Vs: From equilibrium geometry to crack. *Journal of Geophysical Research, 107*, 2043, doi: 10.1029/2001JB000522.

Takei, Y., Shimizu, I. (2003) The effects of liquid composition, temperature, and pressure on the equilibrium dihedral angles of binary solid – liquid system inferred from a lattice – like model. *Physics of the Earth and Planetary Interiors, 139*, 225 – 242.

Terry, R.D., Chilingar, G.V. (1955) Summary of "concerning some additional aids in studying sedimentary formations" by M.S. Shevetsov. *Journal of Sedimentary Petrology, 25(3)*, 229 – 234.

Tiraboschi, C., Tumiati, S., Recchia, S., Miozzi, F., Poli, S. (2016) Quantitative analysis of COH fluids synthesized at HP – HT conditions: an optimized methodology to measure volatiles in experimental capsules. *Geofluids, 16(5)*, 841 – 855.

Toramaru, A., Fujii, N. (1986) Connectivity of melt phase in a partially molten peridotite. *Journal of Geophysical Research, 91*, 9239 – 9252.

Treiman, A.H., Schedl, A. (1983) Properties of Carbonatite Magma and Processes in Carbonatite Magma Chamber. *Journal of Geology, 91*, 437 – 447.

Treiman, A.H. (1989) Carbonatite magmas: properties and processes. In Bell, K. (Ed.), *Carbonatites: genesis and evolution. Unwin – Heyman, London.*

Treiman, A.H. (1995) Ca – Rich carbonate melts – a Regular – Solution model, with applications to Carbonatite Magma plus Vapor Equilibria and Carbonate lavas on Venus. *American Mineralogist, 80*, 115 – 130.

Truckenbrodt, J., Johannes, W. (1999) H_2O loss during piston-cylinder experiments. *American Mineralogist, 84(9)*, 1333 – 1335.

Tumiati, S., Fumagalli, P., Tiraboschi, C., Poli, S. (2013) An Experimental Study on COH – bearing Peridotite up to 3.2 GPa and Implications for Crust – Mantle Recycling. *Journal of Petrology, 54(3)*, 453 – 479.

Tumiati, S., Tiraboschi, C., Sverjensky, D.A., Pettke, T., Recchia, S., Ulmer, P., Miozzi, F., Poli, S. (2017) Silicate dissolution boots the CO_2 concentrations in subduction fluids. *Nature Communications, 8(1)*, doi: 10.1038/s41467-017-00562-z.

Ulmer, P., Luth, R.W. (1991) The graphite-COH fluid equilibrium in P, T, fO_2 space. An experimental determination to 30 kbar and 1600 °C. *Contribution to Mineralogy and Petrology, 106*, 265 – 272.

Veksler, I.V., Keppler, H. (2000) Partitioning of Mg, Ca, and Na between carbonatite melt and hydrous fluid at 0.1 – 0.2 GPa. *Contributions to Mineralogy and Petrology, 138*, 27 – 34.

Veksler, I.V., Dorfman, A.M., Dulski, P., Kamenetsky, V.S., Danyushevsky, L.V., Jeffries, T., Dingwell, D.B. (2012) Partitioning of elements between silicate melt and immiscible fluoride, chloride, carbonate, phosphate and sulfate melts, with implications to the origin of natrocarbonatite. *Geochimica et Cosmochimica Acta, 79*, 20 – 40.

Voigt, M., von der Handt, A. (2011) Influence of subsolidus processes on the chromium number in spinel in ultramafic rocks. *Contributions to Mineralogy and Petrology, 162*, 675 – 689.

von Bargen, N., Waff, H.S. (1986) Permeabilities, interfacial areas and curvatures of partially molten system: results of numerical computations of equilibrium microstructures. *Journal of Geophysical Research, 91*, 9261 – 9276.

Waff, H.S., Balau, J.R. (1979) Equilibrium fluid distribution in an ultramafic melt under hydrostatic stress conditions. *Journal of Geophysical Research, 84*, 6109 – 6114.

Waff, H.S., Balau, J.R. (1982) Experimental determination of near – equilibrium textures in partially molten silicates at high pressure. *In Akimoto S., Manghnani MH. (eds). High pressure research in geophysics. Adv Earth Planetary Science, 12*, 229 – 236.

Waff, H.S., Faul, U.H. (1992) Effects of crystalline anisotropy on fluid distribution in ultramafic partial melts. *Journal of Geophysical Research, 97*, 9003 – 9014.

Walker, D., Delong, S. (1982) E. Soret separation of mid-ocean ridge basalt magma. *Contribution to Mineralogy and, 79*, 231 – 240.

Walker, D., Jurewicz, S., Watson, E.B. (1988) Adcumulus dunite growth in a laboratory thermal gradient. *Contribution to Mineralogy and Petrology, 99*, 306 – 319.

Wallace, M.E., Green, D.H. (1988) An experimental determination of primary carbonatite magma composition. *Nature, 335*, 343 – 346.

Wang, F., Doi, S., Hosoiri, K., Watanabe, T. (2004) Microstructure of electrodeposited Fe – Pt binary alloy films. *Material Science and Engineering, A375-377*, 1289 – 1293.

Wark, D.A., Watson, E.B. (2000) Effect of grain size on fluid and melt distribution in mantle and deep crustal rocks. *Geophysical Research Letters, 27*, 2029 – 2032.

Wark, D.A., Watson, E.B. (2002) Grain – scale channelization of pores due to gradients in temperature or composition of intergranular fluid or melt. *Journal of Geophysical Research, 107*, 5-1 – 5-15.

Watson, E.B. (1982) Melt infiltration and magma evolution. *Geology, 10*, 236 – 240.

Watson, E.B., Brenan, J.M. (1987) Fluids in the lithosphere. Experimentally – determined wetting characteristics of CO_2 – H_2O fluids and their implications for fluid transport, host – rock physical properties, and fluid inclusion formation. *Earth and Planetary Science Letters, 85*, 497 – 515.

Watson, E.B., Brenan, J.M., Baker, D.R. (1990) Distribution of fluids in the continental mantle. *In Continental Mantle (ed. M.A. Menzies), Clarendon Press, Oxford*, 111 – 124.

Watson, E.B. (1999) Lithologic partitioning of fluids and melts. *American Mineralogist, 84*, 1693 – 1710.

Wendlandt, R.F., Eggler D.H. (1980) The origins of potassic magmas; Stability of phlogopite in natural spine lherzolite and in the system $KAlSiO_4$ – MgO – SiO_2 – H_2O – CO_2 at high pressures and high temperatures. *American Journal of Science, 280(5)*, 421 – 458.

Wendlandt, R.F. (1984) An experimental and theoretical analysis of partial melting in the system $KALSiO_4$ – CaO – MgO – SiO_2 – CO_2 and application to the genesis of potassic magmas, carbonatites and kimberlites. *In J Kornprobst, Ed., Kimberlites, vol. I: Kimberlites and related rocks. Proceedings of the Third International Kimberlite Conference*, 359 – 369.

Wolff, J.A. (1994) Physical – properties of carbonatite magmas inferred from Molten – salt data and Application to extraction patterns from carbonatite – silicate magma chambers. *Geological Magazine, 131*, 145 – 153.

Woolley, A.R., Kempe, D.R.C. (1989) Carbonatites: Nomenclature, average chemical compositions and element distribution. In Bell, K. (Ed.), *Carbonatites: genesis and evolution. Unwin – Heyman, London.*

Woolley, A.R., Church, A.A. (2005) Extrusive carbonatites: A brief review. *Lithos, 85(1-4)*, 1 – 14.

Woolley, A.R., Kjarsgaard, B.A. (2008) Carbonatite occurrences of the world: map and database. *Geological Survey od Canada, 5796*, 28

Wyllie, P.J. (1987) Transfer of subcratonic carbon into kimberlites and rare earth carbonatites. *In B.O. Mysen, Ed., Magmatic processes*, 500.

Wyllie, P.J. (1989) Origin of Carbonatites: Evidence from phase equilibrium studies. In: Carbonatites: genesis and evolution. *Unwin Hyman London*, 500 – 545.

Wyllie, P.J. (1995) Experimental petrology of upper – mantle materials, process and products. *Journal of Geodynamics, 20(4)*, 429 – 468.

Wyllie, P.J., Lee, W.J. (1998) Model system controls on conditions for formation of magnesiocarbonatite and calciocarbonatite magmas from the mantle. Journal of Petrology, 39, 1885 – 1893.

Yaxley, G.M., Brey, G.P. (2004) Phase relations of carbonate – bearing eclogite assemblages from 2.5 to 5.5 GPa: implications for petrogenesis of carbonatites. *Contributions to Mineralogy and Petrology, 146(5)*, 606 – 619.

Yoshino, T., Takei, Y., Wark, D.A., Watson, E.B. (2005) Grain boundary wetness of texturally equilibrated rocks, with implications for seismic properties of the upper mantle. *Journal of Geophysical Research, 110*, B08205. doi:10.1029/2004JB003544.

Yoshino, T., Yamazaki, D., Mibe, K. (2009) Well – wetted olivine grain boundaries in partially molten peridotite in the asthenosphere. *Earth and Planetary Science Letters, 283*, 167 – 173.